University of Nottingham
UK | CHINA | MALAYSIA

Developing Unique Nanoporous Titanate Structures for Biomedical Applications: Mechanisms, Conversion and Substitution

Matthew D. Wadge, BSc. (Hons)

Thesis submitted to the University of Nottingham for the degree of Doctor of Philosophy

Supervisors: Prof. David Grant, Dr. Ifty Ahmed & Dr. Reda Felfel

June 2020

Declaration

I, Matthew D. Wadge, herby certify that this thesis has been composed by myself and that it is a record of my own work over the period from October 2017 to June 2020.

Except where specific reference is made to other sources or collaborators, the work presented in this thesis is the original work of the author. It has not been submitted, in whole or in part, for any other degree.

Matthew D. Wadge

Dedicated to the memory of my late Grandad John

You taught me to always persevere with a problem or challenge, no matter how difficult, and if something was wrong or did not work, to try again and never give up. I hope I have made you proud.

Acknowledgements

I would like to express my sincere gratitude to my supervision team; Prof. David Grant, Dr. Ifty Ahmed, and Dr. Reda Felfel. Their guidance throughout both my undergraduate and postgraduate studies has been second to none. I would not have been able to achieve half of the achievements I have during this time without their understanding, dedication, and endless support. I would also like to thank all the technical and research staff in the department for their expertise, and whose support and kindness has enabled this work to flourish. Particularly, Kathryn Thomas for conducting cellular and microbiological assessments; Nigel Neate & Hannah Constantin for their help with XRD & RHEED; James Murray for profilometry assistance; Saul Vazquez Reina for help with ICP analysis; Chris Parmenter for aiding in FIB-SEM training and guidance; Chris Mellor for extensive ellipsometry assistance; Bryan Stuart & Ben Hanby for their guidance on magnetron sputtering; and Graham Rance for their expertise in Raman spectroscopy.

In addition, I would like to take the opportunity to thank everyone who has made my PhD studies at Nottingham a wonderful experience. I won't name everyone individually as this section would be longer than the thesis, however, I have met some amazing friends during this time in Wolfson and the Biomaterials Research Group; both past and present. They have helped me during the low times and made the highs even more enjoyable. Thank you all. Particularly, Kathryn, Teo, Tom, The Matts, Jamie, Vinnie, Bryan, and Ben, thank you for the office laughs and the coffee breaks, even if they took up most of the day!

Last but certainly not least, I want to sincerely thank my family for their constant support, and for always believing in me. To Phil, for all your help over the years, for the long chats about my work on the car journeys back to Nottingham, and for painstakingly proofreading my thesis – thank you. To Harry, the best brother anyone could wish for, thanks for the laughs and for always knowing how to cheer me up; I'm very proud of the young man you are becoming! To Nanny Hazel, for your love and support, even when Grandad and I painted the kitchen with either mud or bubbles, for the tea and biscuits every time I come round, and for your encouraging letters – thank you. To Aunty Julie, for always listening and supporting me and for always putting a smile on my face – thank you. To my partner, Alice, for standing by me with love, kindness, and support, and for always pushing me to achieve my goals whilst you are also pushing to achieve yours; I'm very proud of you – thank you. To Mom, thank you for everything, for always telling me "*Do your best, as that's the best that you can do.*", for bringing me up during the difficult times to be the person I am today; I know how proud you are of me, and I hope everyone knows how proud I am of you.

Abstract

Titanate structures have been of interest in many sectors, including healthcare, due to their ease of manufacture (low processing temperature and simplistic equipment), ion exchange potential to produce multifunctional (bioactive and antibacterial) surfaces, as well as their nanoporosity. However, their use has been limited to only Ti-containing materials due to the specific wet chemical methodology employed.

The work presented in this thesis demonstrates one of the first studies to generate gallium-doped titanate structures as a multifunctional surface, specifically to assess their cytocompatibility and antibacterial potential for biomedical applications. Successive wet chemical (5 M NaOH; 60 ^{o}C; 24 h), ion exchange (4 mM $Ga(NO_3)_3$; 60 ^{o}C; 24 h), and heat treatment (700 ^{o}C; 1 h) stages were employed on Cp-Ti surfaces. Gallium was shown to be fully incorporated (*ca.* 9 at.%) into the nanoporous titanate structure, and completely replaced sodium (initial Na content *ca.* 3 at.%). The heat treatment stage crystallised the amorphous titanate layer, which increased the stability and reduced the maximum level of Ga^{3+} released (*ca.* 2.76 *vs.* 0.68 ppm for pre- and post-heat-treated gallium titanate samples, respectively) into DMEM over 7 d. Finally, the heat-treated gallium titanate samples were shown to be cytocompatible, compared to the non-heat-treated samples, which demonstrated a significant ($p < 0.0001$) reduction compared to the TCP control. Unfortunately, neither gallium titanate samples exhibited robust antibacterial properties against *S. aureus*.

The applicability of titanate structures was furthered in this thesis through the optimisation and characterisation of novel wet chemical (5 M NaOH; 60 ^{o}C; 24 h) titanate-converted Ti thin films deposited *via* DC magnetron sputtering. The films produced were deposited onto 316L SS to function as thin coatings for orthopaedic applications. This was in lieu of the ‘gold standard’ plasma sprayed hydroxyapatite

(HA) coatings, due to their inherent shortfalls such as residual internal stresses and long-term delamination. An understanding of the titanate growth mechanism through thickness and oxygen variations was also detailed.

Tailorable coating properties (structural, morphological, *etc.*) were achieved *via* modification of the sputtering parameters used (target power, substrate biasing, and *in situ* substrate heating). Graded coating structures from columnar (T_c for the α-Ti (002) plane = 3.39) to more equiaxed ($T_{c(002)}$ = 1.54) coatings were produced, with their influence on titanate formation being investigated. Equiaxed coatings generated the thickest titanate structures (*ca.* 1.63 *vs.* 1.12 μm for columnar grown films) due to a reduction in oblique angle crystal growth because of the decreased surface roughness (R_a: *ca.* 32.6 *vs.* 26 nm). This was contrary to the hypothesis that more columnar structures would allow greater NaOH penetration, and hence further conversion. It was also found the titanate structures formed even on 50 nm thick Ti films, as well as oxygen limiting the titanate formation mechanism.

Finally, sodium and calcium titanate-converted thin (*ca.* 500 nm) Ti coatings (both columnar and equiaxed) were applied to Mg substrates to tailor its corrosion resistance for biomedical applications. The columnar calcium titanate coatings performed the best of all the coatings tested compared to Mg in terms of their corrosion resistance (E_{corr} = *ca.* -1.33 *vs.* -1.49 V; i_{corr} = *ca.* 0.06 *vs.* 0.31 mA.cm^{-2}, respectively).

The novel method outlined in this thesis has demonstrated consistent production of tailorable nanoporous titanate structures on non-Ti containing materials. Furthermore, the produced titanate structures enabled ion substitution of Ca ions, which have previously only been achieved in titanate structures produced on Ti substrates. The results detailed not only enhances the understanding of the titanate

growth mechanism, but also demonstrates the broad applications enabled through this platform technology.

Table of Contents

Glossary of Abbreviations & Nomenclature

% (w/w)	Weight Concentration of a Solution or Weight for Weight
(v/v)	Volume per Volume
$\emptyset_f$	Work Function
$\emptyset_{inner}$	Inner diameter
u_e	Electrophoretic Mobility ($m^2V^{-1}s^{-1}$)
ε_0	Permittivity of a Vacuum
ε_r	Dielectric Constant
316L SS/316L	Stainless Steel (Low Carbon)
AES	Auger Electron Spectroscopy
AFM	Atomic Force Microscopy
ALP	Alkaline Phosphatase
B	Magnetic Field Strength (T)
B/150	-100 V Bias/150 ^oC *In Situ* Heater
B/300	-100 V Bias/300 ^oC *In Situ* Heater
B/NH	-100 V Bias/No Heater
BCC	Body Centred Cubic
BMP	Bone Morphogenetic Protein
ca.	Circa (Latin, '*about'*)
Ca:P	Calcium Phosphate
CaTC	Calcium Titanate Conversion
Cp-Ti	Commercially Pure Titanium
DC	Direct Current
DCPD	Dicyclopentadiene
DLC	Diamond-like Carbon
DMEM	Dulbecco's Modified Eagle's Medium
E	Electric Field Strength (NC^{-1})
E	Electron Energy (J)
$E_{binding}$	Binding Energy (eV)
ECM	Extracellular Matrix
EDX	Energy Dispersive X-ray Spectroscopy
EIS	Electrochemical Impendence Spectroscopy
$E_{kinetic}$	Kinetic Energy (eV)
E_{photon}	Photon Energy (eV)

eV	Electronvolt
FDA	Food and Drug Administration
FIB-SEM	Focused Ion Beam Scanning Electron Microscopy
FTIR	Fourier Transform Infrared Spectroscopy
h	Height (m)
HA	Hydroxyapatite
HCP	Hexagonal Closed Packing
HT	Heat-Treated
HVOF	High Velocity Oxygen Fuel
ICP	Inductively Coupled Plasma
ISO	International Organisation for Standards
M	Molarity
MAO	Microarc Oxidation
MHz	Megahertz
MRSA	Multidrug Resistant *Staphylococcus Aureus*
NaTC	Sodium Titanate Conversion
NB/NH	No Bias/No *In Situ* Heater
P4H	Prolyl 4-hydroxylase
PBS	Phosphate Buffered Saline
PLA	Polylactic Acid
PLGA	Poly(lactic glycolic) Acid
PLLA	Poly(l-lactic) Acid
PMMA	Polymethyl Methacrylate
PPC	Potentiodynamic Polarisation Curve
PPM	Parts Per Million
PVD	Physical Vapour Deposition
RF	Radio Frequency (13.56 MHz)
RHEED	Reflective High-Energy Electron Diffraction
S0: Cp-Ti	Commercially Pure Titanium
S1: Na_2TiO_3	Sodium Titanate before Heat treatment
S2: $Ga_2(TiO_3)_3$	Gallium Titanate before Heat treatment
S3: $Ga_2(TiO_3)_3$-HT	Heat-Treated Gallium Titanate
S4: Cp-Ti-HT	Heat-Treated Commercially Pure Titanium
SBF	Simulated Body Fluid
SEM	Scanning Electron Microscopy/Microscope
S^o	Thermodynamic Saturation Level
SSE	Sum of Squared Errors or

	Standard Error of the Mean
TC	Titanate Converted (Sodium)
TCP	Tri-calcium Phosphate
TEM	Transition Electron Microscopy
UHMWPE	Ultrahigh Molecular Weight Polyethylene
v	Velocity (ms^{-1})
W	Watts
XPS	X-ray Photoelectron Spectroscopy/Spectrometer
XRD	X-ray Diffraction
ζ	Zeta Potential (V)
η	Solution Viscosity (Pa.s)
λ	Mean Free Path (m)/Wavelength (m)

Table of Figures

Table of Tables

Publications & Conferences

Publications in Thesis

1. **Wadge, M. D.**, *et al.* "*Generation and characterisation of gallium titanate surfaces through hydrothermal ion exchange processes*". Materials & Design, 2018.
2. **Wadge, M. D.**, *et al.* "*Developing Highly Nanoporous Titanate Structures via Wet Chemical Conversion of DC Magnetron Sputtered Titanium Thin Films*". Journal of Colloid and Interface Science, 2020.
3. **Wadge, M. D.**, *et al.* "*Tailoring the Degradation Rate of Magnesium through Biomedical Nanoporous Titanate Coatings*". Journal of Magnesium and Alloys, 2020.
4. **Wadge, M. D.**, *et al.* "*Adapting Titanate Surfaces for Biomedical Applications: A Review*". International Materials Reviews (Under Review), 2020.

Additional Publications

1. Parsons, A. J., Felfel, R. M., **Wadge, M. D**., Grant, D. M., "*Improved Phosphate-Based Glass Fibre Performance Achieved Through Acid Etch/Polydopamine Treatment*". International Journal of Applied Glass Science, 2020.
2. Arafat, A., Samad, S. A., **Wadge, M. D**., Islam, M. T., Lewis, A. L., Barney, E., Ahmed, I., "*Thermal and Crystallisation Kinetics of Yttrium-Doped Phosphate-Based Glasses*". International Journal of Applied Glass Science, 2020.
3. Coe, S. C., **Wadge, M. D**., Felfel, R. M., Ahmed, I., Walker, G. S., Scotchford, C. A., Grant, D. M., "*Production of High Silicon-Doped Hydroxyapatite Thin Film Coatings via Magnetron Sputtering: Deposition, Characterisation, and In Vitro Biocompatibility*". Coatings, 2020.
4. Felfel, R. M., Parsons, A. J., Chen, M., Stuart, B. W., **Wadge, M. D.**, Grant, D. M., "*Towards Robust, Water Resistant Fibre-Matrix Interface: Polydopamine as a Coupling Agent for Phosphate Glass Fibre Composites*". (Under Review), 2020.

Conferences

1. Surfex Conference, Coventry, UK – Jun. 2021 (Invited Speaker: Postponed)
2. 11th World Congress for Biomaterials, Glasgow, UK – Dec. 2020 (Oral & Poster Presentations: Postponed)
3. STEM for Britain 2020, House of Commons, London, UK – Mar. 2020 (Poster)
4. Future Materials Conference, IOM3, University of Leeds, UK – Dec. 2019 (Oral Presentation – *Best Presentation Prize*)
5. 30th Annual European Society for Biomaterials Conference, Dresden, Germany – Sep. 2019 (Poster Presentation - *Best Presentation Prize*)

6. Tissue and Cell Engineering Society (TCES)/UK Society for Biomaterials (UKSB) 1st Joint Conference, University of Nottingham – June 2019 (Poster Presentation)
7. UK Society for Biomaterials 17th Annual Conference, University of Bath – June 2018 (Oral Presentation - *Best Presentation Prize*)

Chapter 1. Introduction

A biomaterial is broadly defined as a "*substance* [*or material*] *that has been engineered to take a form which, alone or as part of a complex system, is used to direct, by control of interactions with components of living systems, the course of any therapeutic or diagnostic procedure, in human or veterinary medicine*." [1]. More specifically, biomaterials are described by Black (adapted from the definition presented by The European Society for Biomaterials) as "*a material intended to interface with biological systems to evaluate, augment, or replace any tissue, organ, or function of the body."* [2]. The field of biomaterials encompasses a diverse range of application types, from dentistry to tissue engineering, each with their specific requirements for materials and their active properties (bioactivity, antifouling, antibacterial, etc.). One key area of research within the biomaterials field is orthopaedics, which focuses on the alleviation of disease and injuries of the musculoskeletal system [3].

Generation and improvement of orthopaedic biomedical materials from fracture fixation plates and bone screws [4, 5], to total hip replacements such as those developed by Charnley (*Figure 1:1*) [6], have resulted in reduced convalescence periods and improved treatment of degenerative orthopaedic conditions. Despite this, considerable improvements, such as infection alleviation/prevention, reduced stress shielding, and improved bioactivity, are still needed in many areas of biomedical materials science.

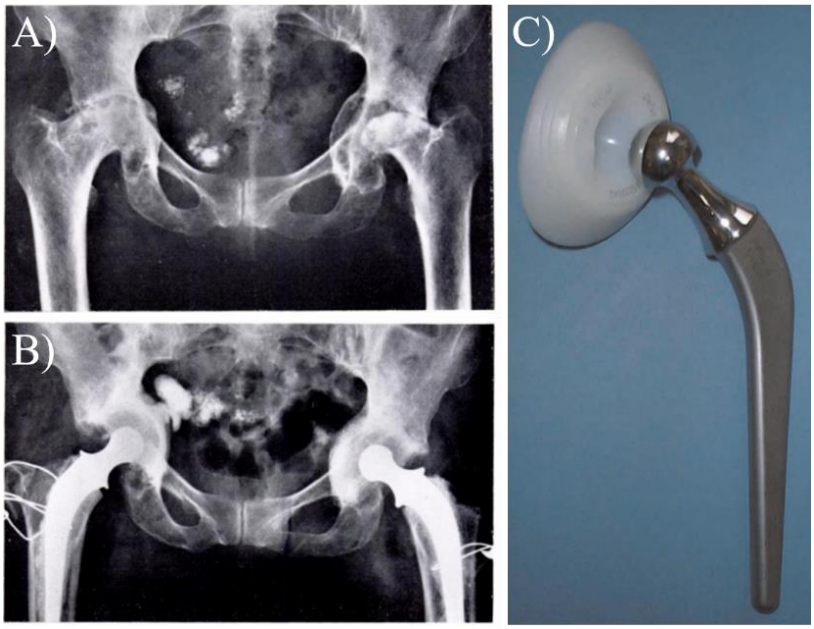

Figure 1:1 X-ray radiographs A) Pre- and B) Post-implantation of the Charley low-friction arthroplasty (C). Images taken from Charnley (A & B) and Jackson (C) [7, 8].

The prevalence of hip replacements in the United Kingdom has continually increased year on year, with 97,792 primary hip replacements (not including revisions) out of 106,116 total hip replacement procedures (including revisions) being conducted in 2018, compared to 89,288 primary replacements (98,401 in total including revisions) in 2015 [9]. The vast majority (87%) of these procedures are a direct result of osteoarthritis, with an average BMI for patients being 28.3, which classifies them as 'overweight' [9]. Furthermore, the average age for both female and male patients in 2018 undergoing primary hip arthroplasties was 70.0 and 67.6 years, respectively (*Figure 1:2*). In addition, instances of fractures for long bones dramatically increased with age (>50 years), as well as females experiencing a higher prevalence, due to higher incidence of osteoporosis [10]. For women aged 80-84 years between 1988 and 2012, the prevalence of hip/femur fractures was 89.4/10,000 per year, compared to 40.1/10,000 per year in men of the same age [11].

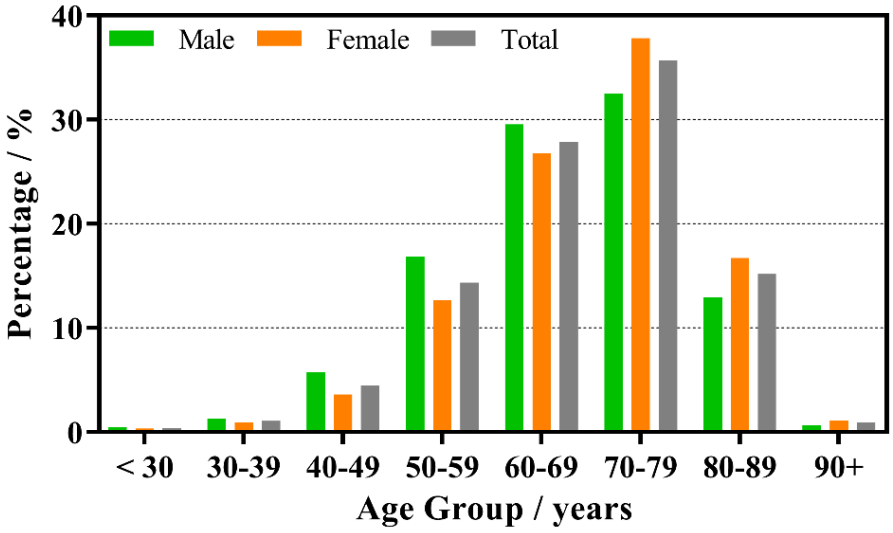

Figure 1:2 Distribution by age and sex of total primary hip prosthesis operations during 2018 from the National Joint Registry [9].

With an ever-ageing population that is experiencing higher prevalence of obesity, tighter scrutiny is imposed on successful implantation of medical devices. Biomedical hip implants have experienced evolution from the original ivory implants used in the late 19th century [12] to metals and polymers by the 1960s, which were deemed the 'gold standard' materials used to provide appropriate anchorage and articulation of the replaced joint [13]. Anchorage of these components, as is still the case with *ca.* 28% of total hip replacements in 2018, has been *via* polymethyl methacrylate (PMMA) bone cement; a polymer which is polymerised *in situ* to form a paste which hardens over time, anchoring the implant in place [9].

Most implant designs are produced through varying combinations of metals, polymers and ceramics to match target properties and functions. The major components of total hip replacements have not considerably changed since they were introduced by Charnley [14]. The general design consists of a metallic stem; ceramic/metallic femoral element; articulating in a low coefficient of friction acetabular component [13, 15]. The metallic femoral stem is now usually made from

Ti6Al4V alloy, or derivatives thereof, compared to earlier stainless steel (316L) or Co-Cr(-Mo) alloys, due to its better corrosion resistance, superior biocompatibility, and substantially lower density and modulus (*Table 1:1*) [16]. The acetabular cup, usually made of the same metal as the stem, is lined with an ultra-high molecular weight polyethylene (UHMWPE) surface to reduce friction and allow self-lubrication between itself and the femoral head, usually produced from metal (Co-Cr-Mo) or ceramic (alumina or zirconia) [17].

*Table 1:1 Mechanical properties of common metals used in replacement hip implants for the femoral stem and acetabular cup casing compared to natural cortical and cancellous bone. *indicates orientation dependency due to anisotropy. Values outside brackets are the most common, with values inside giving full literature ranges.*

Material	Young's Modulus (E) / GPa	U.T.S / MPa	Density (ρ) / g.cm^{-3}	Poisson's Ratio (ν)	Max. Elongation / %	Reference(s)
316L Stainless Steel	189-210	465-950 (207-1160)	7.9-8.1	0.30	40-55	[3, 18-24]
Ti Alloys (e.g. Ti6Al4V (F136))	105-117	960-970 (780-1050)	4.4-4.7	0.32-0.33	10-17	[3, 18-25]
Co-Cr Alloys (e.g. CoNiCrMo (F562))	200-240	600-1795 (430-1795)	7.2-9.2	0.30	8-50	[3, 18-21, 23-25]
Cortical (Lamellar) Bone	3-20 (1-40*)	90-140 (50-150*)	1.8-2.1	0.30	1.3-1.7	[3, 18-22, 24, 26, 27]
Cancellous (Trabecular) Bone	0.01-3 (0.01-13*)	1-20	0.05-0.1	0.3-0.4	N/A	[20-22, 28-31]

Anchorage or fixation of the femoral stem within the femoral canal (the central portion of bone consisting of cancellous "spongy" bone surrounded by compact cortical bone; *Figure 1:3*), as well as the acetabular cup within the acetabulum, has seen a perceptible shift over the lifetime of total hip replacements. Originally, all

implants were cemented in place, however, improvements to implant design and patient needs have caused a transition to more natural adhesion through porous, coated or surface modified uncemented implants [32].

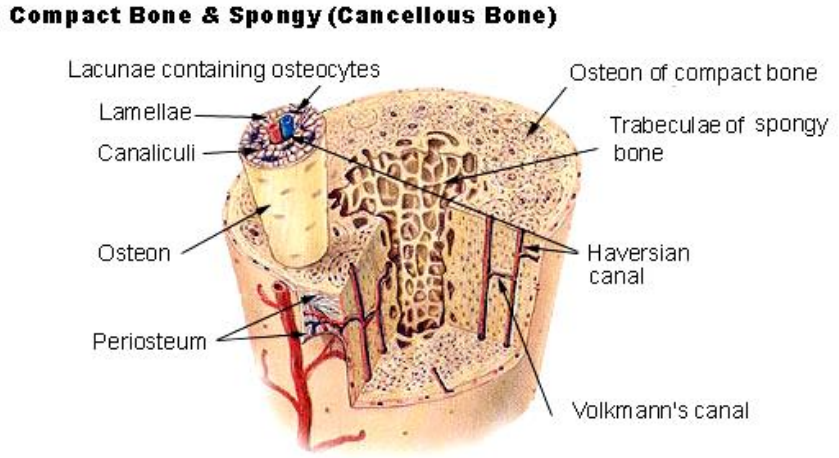

Figure 1:3 Structure of typical long bones, demonstrating locations of cancellous (spongy/trabecular) and cortical (compact) bone [33].

Currently, failure of hip implants occurs predominantly through aseptic loosening (*Figure 1:4*) accounting for 24.3% of revisions between 2003 and 2018, with infection resulting in 14.5% of revisions [9]. Aseptic loosening is defined as "*osteolysis* [*resorption of bone matrix due to osteoclast activity*] *resulting in loosening of the implant whether linear, focal, or a combination of the two"* [34]. The main cause often proposed, from a multifactorial list, is the generation of wear debris from frictional motion between the femoral head and the acetabular lining. These particles are subsequently phagocytosed by macrophages, with recent studies discussing the role of endotoxin attachment resulting in macrophage activation. These induce inflammatory cascades, which eventually generate the activation of osteoclasts, enabling bone resorption [34, 35].

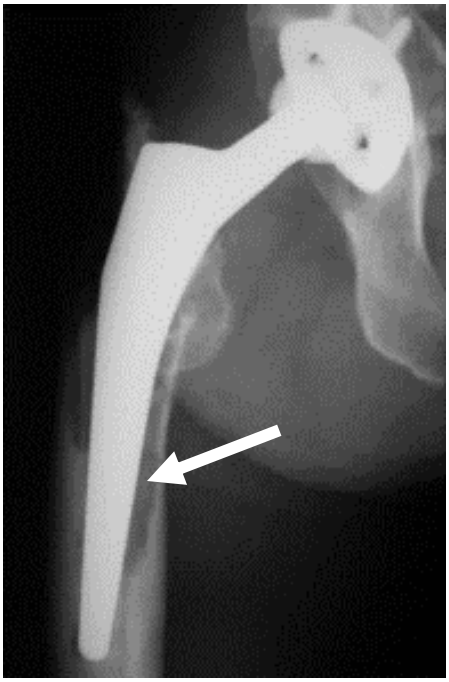

Figure 1:4 Aseptic loosening of the femoral component of a total hip replacement (indicated by the white arrow). Image taken from Miletic et al. [36].

1.1 Implant coatings and surface modifications

1.1.1 Current methods

A key research area for orthopaedic implants is the modification of surfaces to enable greater adhesion to surrounding bone tissue [37, 38]. Durability and *in vivo* success of an implant are dependent upon osteoconductive growth around an implant through osteoblastic recruitment. Presently, surface improvements to implants are conducted through a high-temperature (>10,000 ºC for the flame centre; >1500 ºC for particle temperature [39]) plasma spraying methodology, which is the only FDA approved method for providing hydroxyapatite (HA) coatings on implants. Other coating methods have been tested, however, their regulatory status has not been approved [40-43]. HA is a form of calcium phosphate, which mimics the main mineral component, crystal and chemical structure of cortical bone: $Ca_{10}(PO_4)_6(OH)_2$ [39]. However, despite these coatings being ideal for improving implant biocompatibility, they suffer from inherent issues such as residual stresses and cracking resulting from the high manufacturing temperatures used [44, 45]. This ultimately results in coating

spallation, and in turn, generation of aseptic loosening (sustained osteolysis and failure between the implant and bone in the absence of infection [35]) *in vivo* through macrophage activation and subsequent inflammatory responses [35, 44-47]. Macrophages are phagocytic (ingest and destroy foreign particles [48]) cells with responsibilities in maintaining tissue homeostasis [49]. Improvements are hence required to enhance implant surfaces without resulting in long-term performance issues.

1.1.2 Alkali titanates: An alternative to plasma sprayed HA

To negate the limitations of implant coatings, surface modifications have been considered, such as the production of sodium titanate layers. By directly modifying the surface, the issue of coating spallation can be minimised. Around the mid-1990s, Kokubo *et al.* demonstrated that sodium titanate, which occupies a perovskite structure (*Figure 1:5*), generated apatite *in vitro* and could be synthesised at 60 ^{o}C; much lower than conventional plasma-spraying methods. The sodium modifier in the Ti—O framework, allowed for ion exchange reactions to take place with Ca^{2+} ions in the extracellular environment/simulated body fluid, which over time could produce the necessary apatite that can lead to bone maturation [50].

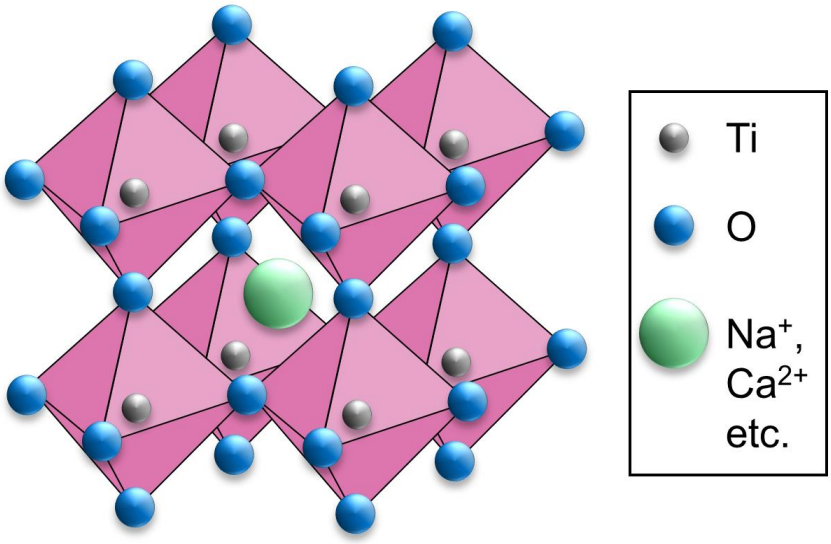

Figure 1:5. Perovskite crystal structure of titanate materials. Adapted from Chilvery et al. [51].

Generation of such surface layers, as demonstrated by Kokubo *et al.* results from immersion of commercially pure titanium (Cp-Ti) in 5 M NaOH solution at 60 ^{o}C for 24 h. This process is then followed by heat treatments at 600 ^{o}C for 1 h at a ramp rate of 5 ^{o}C min^{-1}, in order to densify and crystallise the resulting titanate structure. Samples are then left to dwell in the furnace until they have reached room temperature [52-54]. The successful studies both *in vitro* and *in vivo* resulted in implantation of NaOH treated Ti-6Al-2Nb-Ta alloy femoral stems and acetabular cups into 10,000 patients in Japan (*Figure 1:6*) [55].

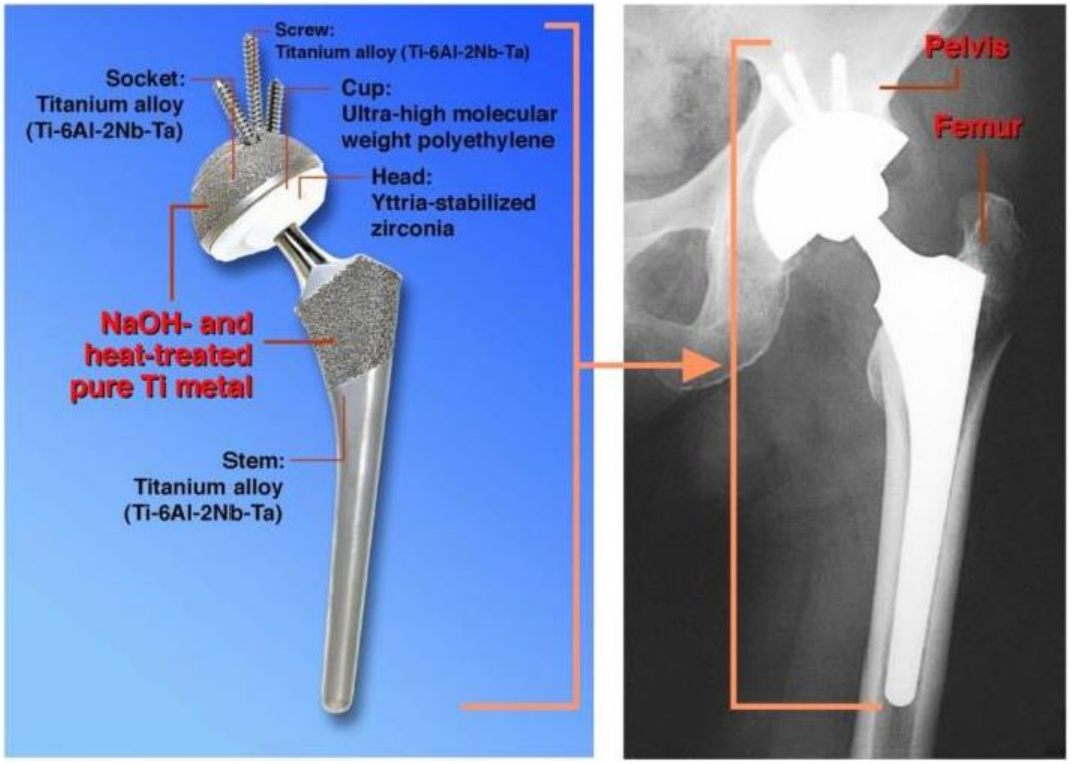

Figure 1:6. Deployment of hydrothermal sodium hydroxide treatment on porous titanium alloy hip stem for improved osseointegration. The implant was deployed in over 10,000 patients [55].

Further work by Kizuki *et al.*, Yamaguchi *et al.* and others have demonstrated the ability for incorporating various ions into the titanate structure through solution based ion exchange reactions [56-58]. Calcium (Ca) ions were shown to preferentially exchange with the sodium modifier, allowing generation of a calcium titanate. Other elements such as magnesium (Mg), silver (Ag) and strontium (Sr) have also been successfully incorporated into the titanate structure, allowing for improved bioactivity and antibacterial properties, as well as improved tailoring for specific applications [57-59].

1.2 Medical material generations: 1st, 2nd and 3rd

1.2.1 1st Generation biomaterials

Historically, as described by Hench *et al.*, the majority of implants can be categorised into one of three different implant 'generations'. Prior to the development of first generation biomaterials during the 1960s and 70s, most biomedical materials

used were those readily available in other industrial sectors. This was regardless of their cytotoxicity, due to the facile understanding of the immune system's reaction to foreign materials at the time. The goal of first generation biomaterials was *"to achieve a suitable combination of physical properties to match those of the replaced tissue with a minimal toxic response in the host."* [60]. Today, these materials have been referred to as biologically 'inert'. Many of these materials are still commonly used, such as titanium (Ti). Ti and its alloys (Ti6Al4V) have been widely used as orthopaedic implant materials, specifically hip stems and acetabular components, due to their mechanical properties (Young's modulus *ca.* 110 GPa [61]) and their bioinertness. However, their lower hardness (*ca.* 200 H_v [62, 63]), wear resistance, shear strength (*ca.* 300 MPa [64]) and cytotoxic alloying additions (V and Al [65]), as well as their limited capacity to confer bonding to bone, have resulted in the need for alternative materials to be considered.

1.2.2 2nd Generation biomaterials

Despite the improvement to patient survivability, bioinert materials were unable to adhere to the surrounding tissue, meaning highly exothermic bone cements (40-110 ^oC [66]) and other damaging fixation mechanisms were used. Second generation biomaterials were developed to be 'bioactive', whereby they elicit a controlled response in physiological media, which is favourable to tissue growth. An example of such a material is 45S5 Bioglass® composed of Na_2O-CaO-P_2O_5-SiO_2 (*Figure 1:7*), invented by Hench, which upon dissolution forms a surface layer of carbonated HA [67]. These materials facilitate interfacial bonding between the implant surface and the host tissue, which ultimately allows hard tissue formation.

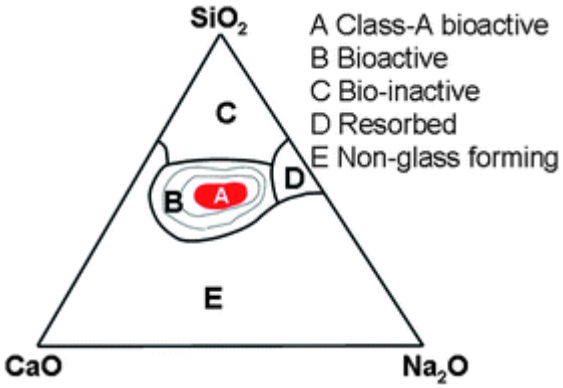

Figure 1:7. Ternary phase diagram demonstrating the various properties achieved through varying glass composition [68].

1.2.3 3rd Generation biomaterials

Third generation biomaterials, also known as cell- and gene-activating materials, are the intersection between bioactive and resorbable materials. These materials facilitate cellular pathway stimulation down at the molecular level [69]. Once the material has induced a cellular response, resulting in growth and maturation of hard tissue, the material resorbs allowing the hard tissue to replace the implant, removing the need for implant removal and the associated difficulties [70].

1.3 Degradable metallic biomaterials

A class of materials that has received significant attention over the last few decades are biodegradable metallic implants. These materials impinge on 3rd generation biomaterials, and allow implantation, without the need for secondary surgery to remove the implanted device. Furthermore, their high mechanical properties allow them to be used in load bearing applications, improving on previous 3rd generation biomaterials. This does not only reduce surgical costs, but also reduces the morbidity and convalescence for patients [71]. However, degradable metals such as magnesium have issues regarding their corrosion rate, since it is quicker than the healing rate for bone (*ca.* 12-18 weeks [72, 73]). Furthermore, the corrosion products (*i.e.* hydrogen gas evolution) that are formed result in alterations to the local environmental pH, hence causing issues for surrounding cellular processes. Therefore, surface

modifications could potentially reduce/control their degradation rate to meet the required healing time of fractures. However, careful production must be observed due to breaches in the coating resulting in localised rapid degradation.

1.4 Aims and objectives

Despite the proven clinical track record of HA plasma sprayed coatings over the last 30 years, the increasing ageing population combined with clinical challenges (antibiotic resistance and aseptic loosening) results in increased demand for alternative biomaterials to enhance natural adhesion whilst delivering therapeutic ions for antibacterial or bioactive properties. Furthermore, investigations into 3rd generation biomaterials, which also negate issues surrounding revision surgery, are also an attractive research avenue.

Alkali titanate structures are an interesting class of materials, which so far have revealed promising properties regarding orthopaedic applications, as well as delivering bioactive and antibacterial properties through cationic exchange within their structure. To date, their use as a coating/surface in a biomedical setting has been limited to titanium and its alloys due to the wet chemical production methodology, which relies on direct modification of the substrate through reaction with NaOH. Magnetron sputtering seems a suitable methodology, to be combined with the conventional chemical processing route in order to achieve such coatings, with tailored morphology, crystallinity and chemistry for biomedical applications.

The aim of this project was to develop novel, highly tailorable titanate surfaces, which can be applied to a variety of different medical materials for a wide range of applications, from fracture fixation to total joint replacement implants. This is achieved through generation of novel bioactive and antimicrobial titanate layers produced *via* hydrothermal processes, both on Ti substrates, as well as, for the first

time, magnetron sputtered Ti thin films, for biomedical applications. Specifically, the aim of these surfaces is to improve the biocompatibility and antimicrobial properties of specific biomaterials (316L SS, magnesium, etc.), as well as potentially reduce the degradation rate of magnesium for a more appropriate resorption window.

The objectives to be achieved for this project are as follows:

1. Generate an antibacterial gallium titanate layer *via* solution-based hydrothermal routes onto Cp-Ti substrates.
2. Investigate the antibacterial efficacy of gallium titanate as an antibacterial biomedical surface.
3. Apply, investigate and optimise through ellipsometry and SEM measurements, the coating parameters of magnetron sputtered Ti films onto various substrates (316L SS, magnesium, etc.).
4. Characterise the structural and chemical properties of the produced bioactive titanate layers *via* modified hydrothermal routes onto sputtered titanium films.
5. Investigate the adhesion of the thin films through scratch/pull off testing.
6. Characterise the optimised, minimum thickness of sputtered Ti films required for the titanate conversion, as well as the influence of oxygen content *via* Ti *vs.* TiO_2 microspheres, in order to produce titanate structures.
7. Understand the required chemical and structural properties of Ti films to produce titanate structures on a range of substrates.
8. Investigate the effect of Ti and titanate-converted coatings on the corrosion rate of degradable metal (Mg) substrates for degradable biomedical implants.

The following chapter (*Chapter 2*) is a detailed literature review covering bioactive and antimicrobial titanate layers; coatings used in orthopaedic and fracture fixation applications; utilisation of magnetron sputtering for coatings; and degradable metallic biomedical materials.

Chapter 2. Literature Review

Titanate structures have been extensively used within the field of materials science, with a notable example being ferroelectrics [74-76]. However, within the last 20 years, Kokubo *et al.* have demonstrated the suitability of titanates for use in biomedical applications to facilitate bone formation *in vivo* through ion exchange reactions [55, 77-80]. For biomedical applications, this ability is advantageous as it could allow more 'natural' integration of implants within the osseous environment, as well as improving osseous-growth in patients suffering from osteoporosis [81]. Expansion and improvement of bioactive titanate layers by Kokubo *et al.* has led to the use of sodium titanate surface modifications on titanium hip stems for improved implant integration [82]. Further improvements of the ion exchange ability of titanate structures has led to antimicrobial sub-categories, opening up additional avenues of infection negation for such surfaces [83]. Utilisation of bioactive and antimicrobial titanate layers have the potential to be used on substrates other than titanium and its alloys. This could be achieved through titanate conversion of sputtered titanium thin films, to improve biocompatibility and potentially reduce the degradation rate of biodegradable materials, such as magnesium, all of which have been conducted within this thesis. The following chapter reviews the literature pertaining to bioactive and antimicrobial titanate layers (*Section 2.1*); biodegradable metallic materials (*Section 2.2*), specifically magnesium and its alloys (*Section 2.2.2*); as well as physical vapour deposition (PVD) of titanium thin films *via* magnetron sputtering (*Section 2.3*).

2.1 Bioactive and antibacterial titanium-based surfaces and current uses

In the field of orthopaedics, varying types of materials are used in order to 'mimic' the *in vivo* biomechanics exhibited in the human skeleton during typical daily movements. These materials have been discussed in *Chapter 1*, however, of the

different classes of materials used, metals and their alloys are of particular interest to biomaterial scientists, due to their superior mechanical properties [84]. As previously explained (*Chapter 1*), various metallic materials are used for femoral and acetabular components, such as Co-Cr(-Mo) alloys; medical grade stainless steel (316L SS); and Ti and its alloys (Ti6Al4V). In particular, Ti and its alloys are becoming more frequently sort after in orthopaedic applications. *Section 2.1.1* below will detail Ti and its alloys used in orthopaedic settings, with *Section 2.1.2* investigating the requirement for surface modification prior to implantation, from the 'gold standard' method of plasma spraying HA (*Section 2.1.2*) to the potential alternative of titanate structures produced *via* wet chemical treatments (*Sections 2.1.3-2.1.8*).

2.1.1 Titanium and its alloys: A prevalent biomaterial

Titanium (Ti) is a lustrous transition metal found in group 4, period 4 of the periodic table. Despite finding applications in many fields, including aerospace and automotive industries, its prevalence in biomaterials has increased significantly over the past few decades [21, 85, 86]. A key feature of Ti, due to the amorphous passivated surface, is its bio-inertness; bioinert materials are defined as materials, by which, *"no chemical reactions occur between the implant and the tissue...*[and] *no direct bonding with the adjacent bone tissue* [is observed]*"* [87]. Its excellent corrosion resistance, and minimal allergenic and immunogenic potential when implanted, compared to Co-Cr-Mo or Cr-Ni-Mo, make it an ideal candidate for biomedical applications [88]. Furthermore, its Young's modulus (105-117 GPa; *Table 1:1*, however, still higher than cortical bone: 10-30 GPa [89]) results in lower amounts of stress shielding compared to 316L SS and Co-Cr-Mo; a common issue resulting from the mismatch in mechanical properties of implanted materials and the surrounding bone, leading to bone resorption/osteolysis (*Figure 2:1*) [90]. Julius Wolff, in the late 19th century,

investigated the effect of external forces on bone growth, producing a law which bears his name; *"the law of bone remodelling is the law according to which alterations of the internal architecture clearly observed and following mathematical rules, as well as secondary alterations of the external form of the bones following the same mathematical rules, occur as a consequence of primary changes in the shape and stressing ... of the bones"* [91]. However, historical evidence has shown Wolff's interpretation was flawed, due to inaccurate modelling and disregard for bone resorption, therefore, observations by Wilhelm Roux provide a more scientific perspective [92]; functional stimulus is paramount in the shaping of bone, evidenced by thickened fibula due to tibial absence [93]. If a material with a higher stiffness to bone is implanted, the higher stiffness material will ultimately carry the load exerted, meaning the bone will remodel itself due to the lack of load experienced.

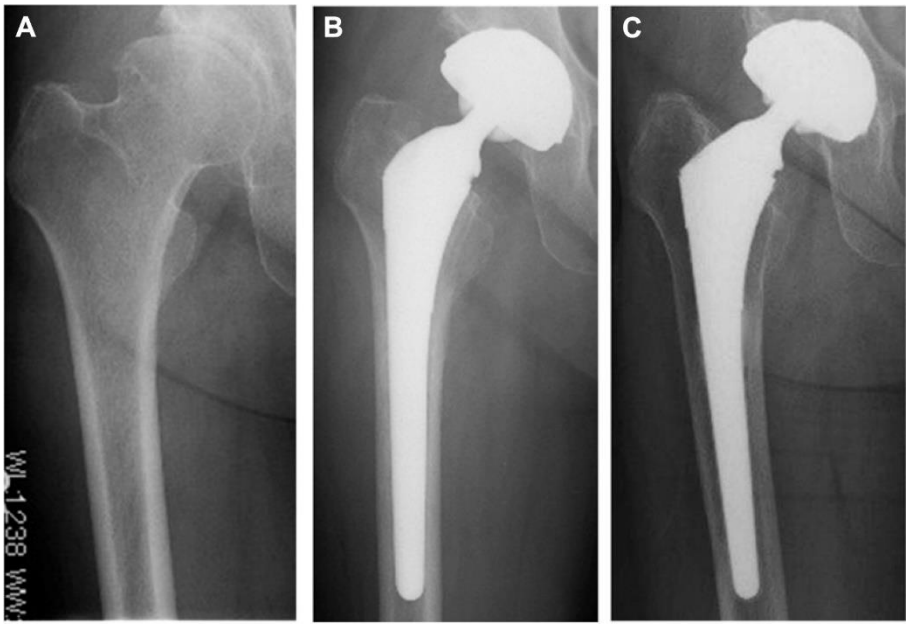

Figure 2:1 A) Preoperative image of a patient's hip, B) 1 week post-operation, with C) showing 11 years post-operation with significant osteolysis occurring due to high amount of stress shielding (darker regions). Image taken from Kusano et al. [94].

Despite Ti's excellent properties, fundamental issues remain regarding its deployment as a biomaterial. Firstly, its lower hardness (*ca.* 200 H_v [62, 63]) and wear

resistance; and its lack of shear strength (*ca.* 300 MPa [64]), results in an inability to be used for articulating and rotation applications, such as the femoral head or for bone screws [95]. Secondly, prior to any surface modification, Ti cannot confer a bond to living bone (the native amorphous passivated oxide is not considered to be bioactive [96]), and therefore, over time, its fixation *in vivo* is not stable.

2.1.2 Background of titanium and other metallic surface modifications

To address the issue of bioactivity, many researchers have investigated the ability to confer bond-bonding to previously bioinert implant metals and alloys (reviewed by Jäger [97] in *Table 2:1* & *Table 2:2*). One method, which has received a great deal of attention, is the coating of metallic stems with a ceramic layer, such as hydroxyapatite (HA), which is inherently bioactive [98]. HA, as a coating material has been used since 1972, since the main mineral (inorganic) component of bone is a calcium phosphate, making up 70-90% of the dry mass of bone [99, 100]. Getter *et al.* implemented the first calcium phosphate coated implant in 1972, which consisted of a slurry of high purity β-TCP (Tri-Calcium Phosphate), applied to high density Alumina endosteal root dental implants [101]. In theory, osteogenic cells that are in contact with the surface of the implant, no longer 'identify' a foreign, metallic surface of an uncoated implant, but one which is akin to the cortical bone in which the implant is located, due to the HA coating. Therefore, the tissue that is generated, will incorporate the coating layer, and will result in stable tissue fixation [102-104]. Despite the lack of success from the initial *in vivo* study in monkeys, subsequent research improved upon the use of HA-coated implants (*Figure 2:2*) [105]. This resulted in successful clinical trials such as the first HA-coated primary hip prostheses being implanted by Furlong in 1985 [106]. Presently, clinical survival rates are > 93% after over 10 years post-implantation [107-109].

Table 2:1 Review of the various techniques that have been explored to improve the performance of titanium materials for biomedical applications. Table adapted from Jäger et al. [97].

Type	Technique	Modified Layer	Objective
Mechanical	- Grinding - Polishing - Machining - Grit blasting	Rough or smooth surface formed by the subtraction process	- Produce specific surface topographies - Clean and roughen surface - Improve bonding adhesion
	- Attrition (shot peening, sand blasting, etc.)	To fabricate nanophase surface layers on Ti, which improve the tensile properties and surface hardness	- Produce materials with nanometre grain size (1-100 nm) - Produce rough morphology and higher hydrophilicity
Chemical	- Acid-treatment	< 10 nm surface oxide	- Remove oxide scales and contamination - Improve biocompatibility, bioactivity or bone-conductivity
	- Alkali-treatment	*ca.* 1 μm sodium titanate gel	- Improve biocompatibility and bioactivity
	- Hydrogen peroxide treatment	*ca.* 5 nm inner oxide and porous outer layer	
	- Sol-gel	*ca.* 10 μm of thin film. E.g. Ca-P, TiO_2, SiO_2.	
	- Chemical Vapour Deposition (CVD)	*ca.* 1 μm of TiN, TiC, TiCN, DLC thin films	- Improve wear and corrosion resistance, and blood compatibility
	- Anodic oxidation	*ca.* 0.01-40 μm TiO_2, plus electrolyte anion adsorption and incorporation	- Produce specific surface topographies - Improve corrosion resistance - Improve biocompatibility and bioactivity
	- Biochemical methods	Coating deposition, modification through salinized Ti, photochemistry, Self-assembled monolayers (SAMs), protein-resistance etc.	- Induce specific cell and tissue response through surface immobilised peptides, proteins, or growth factors

Table 2:2. Continuation of Table 2:1.

Type	- Technique	Modified Layer	- Objective
Physical	- Thermal spray	*ca.* 30-200 μm Ti, HA, calcium silicate, Al_2O_3, ZrO_2, TiO_2 etc.	- Improve wear and corrosion resistance, and biological properties (osteoblast adhesion)
	- *Flame spray*		
	- *Plasma spray*		
	- *High-velocity oxy-fuel*		
	- *Others*		
	- PVD	*ca.* 1 μm of TiN, TiC, TiCN, DLC. HA coating by sputtering	- Improve wear and corrosion resistance, and blood compatibility
	- *Evaporation*		
	- *Ion plating*		
	- *Sputtering*		
	- Ion implantation and deposition	*ca.* 10 nm surface modified layer/thin film	- Modify surface composition - Improve wear/corrosion resistance/biocompatibility
	- Glow discharge plasma treatment	*ca.* 1-100 nm surface modified layer	- Cleaning, sterilising, or oxidising surface - Surface nitridation - Removal of oxide layer

Figure 2:2 Mallory-Head Porous femoral component (Biomet); a collarless, Ti femoral stem with a plasma sprayed Ti coating (left), with a HA coating applied on the right hand stem. Image taken from Ellison et al. [110].

Of the techniques used and researched, plasma spraying remains as the primary method for depositing bioactive hydroxyapatite coatings [111]. Plasma spraying utilises a carrier gas (usually argon, or a mixture with other gases) to carry HA particles through a low voltage (60-80 V [112]), high current (300-400 A [112]) electrically discharged plasma, as described by Herman (*Figure 2:3*) [113]. This melts the particles sufficiently, that upon impingement on the substrate surface, they solidify into a coating. Plasma spraying offers rapid deposition rates (1×10^6 particles $m^{-2}s^{-1}$) and sufficiently low costs (for atmospheric plasma spraying; *Figure 2:4*). Despite these advantages, plasma spraying has inherent disadvantages including poor adhesion [43]; non-uniform coating density [114]; and excessive temperatures (Particle temperature *ca.* 1500 K [39]) leading to undesired phase transformations and residual

internal stresses [115, 116], which can result in micro-crack formation [117]. Their brittle nature, coupled with weak mechanical adhesion (55-62 MPa; slightly above the FDA's minimum requirement of 50.8 MPa) [98, 111], can result in delamination, as well as spalled particles *in vivo*. Issues regarding spalled particles have previously been described in *Section 1.1.1*. Alternative coating methods for generating HA on implants have been reviewed by Yang *et al.*, which details the advantages and disadvantages of each coating method (*Table 2:3*) [118]. However, substantive issues remain within all techniques mentioned, especially regarding biomedical coatings, resulting in alternative lines of enquiry.

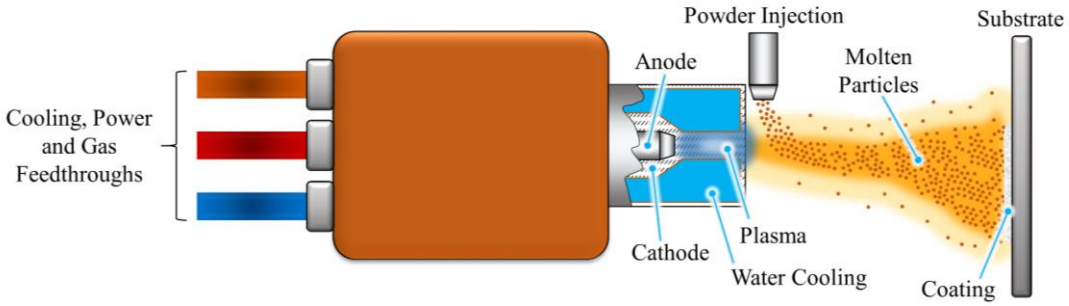

Figure 2:3 Schematic of plasma spraying set up. Powder particles are melted in the plasma flame, before being projected and quenched onto the substrate surface to form a coating.

Table 2:3. Comparison of HA coatings techniques explored within the literature. Table adapted from Yang et al. [118].

Technique	Thickness / µm	Advantages	Disadvantages
Thermal spraying	30-200	- High rate of deposition - Low cost	- Line of sight - Decomposition induced through high temp. - Amorphous coating (rapid cooling)
Sputter coating	0.5-5	- Uniform coating thickness - Dense coating	- Line of sight - Expensive & time consuming - Amorphous coatings
Pulsed laser deposition	0.05-5	- Crystalline & amorphous coatings - Dense and porous coatings	- Line of sight
Dynamic mixing method	0.05-1.3	- High adhesive strength	- Line of sight - Expensive - Amorphous coatings
Dip coating	50-500	- Inexpensive - Quick deposition - Complex substrates possible	- High sintering temp. - Thermal expansion mismatch
Sol-gel	< 1	- Complex shapes possible - Low processing temp. - Cheap coatings (very thin)	- May require controlled atmosphere - Expensive raw materials
Electrophoretic deposition	100-2000	- Uniform coating thickness - Rapid deposition - Complex substrates possible	- Difficult to prevent cracking - High sintering temp.
Biomimetic coating	< 30	- Low processing temp. - Can form bone-like apatite - Complex shapes possible - Can incorporate bone growth stimulating factors	- Time consuming - Requires replenishment - Constant pH necessary (SBF)
Hot isostatic pressing	200-2000	- Dense coatings	- Cannot coat complex structures - High temp. - Thermal expansion mismatch - Elastic property differences - Expensive - Removal/interaction of encapsulated material

Further techniques have been researched to improve various surface properties of titanium, with ion implantation and electrochemical reactions having been investigated to try to induce apatite *in vitro* in SBF (Simulated Body Fluid). Principally, these modifications were designed to negate issues surrounding the coating techniques and their produced coatings described both above, and in *Table 2:3*. The hypothesis being that if appropriate metallic ions, which are present and utilised during bone maturation and healing, such as calcium (Ca^{2+}), magnesium (Mg^{2+}), and strontium (Sr^{2+}), are incorporated into the surface, they theoretically should improve the bioactivity of the metallic substrate. Mg^{2+} homeostasis, as reviewed by Castiglioni *et al.*, is essential for optimum bone health, with decreased ionic concentrations resulting in osteoporosis through multifactorial pathways [119]. Ca^{2+} that is found in bone makes up approximately 99% of all body calcium, due to being a key component of apatite, and is essential for growth and development [120]. Furthermore, Sr^{2+}, in low concentrations, has been known to increase trabecular bone volume in animals, due to inhibition of bone resorption, and stimulation of bone formation [121-124].

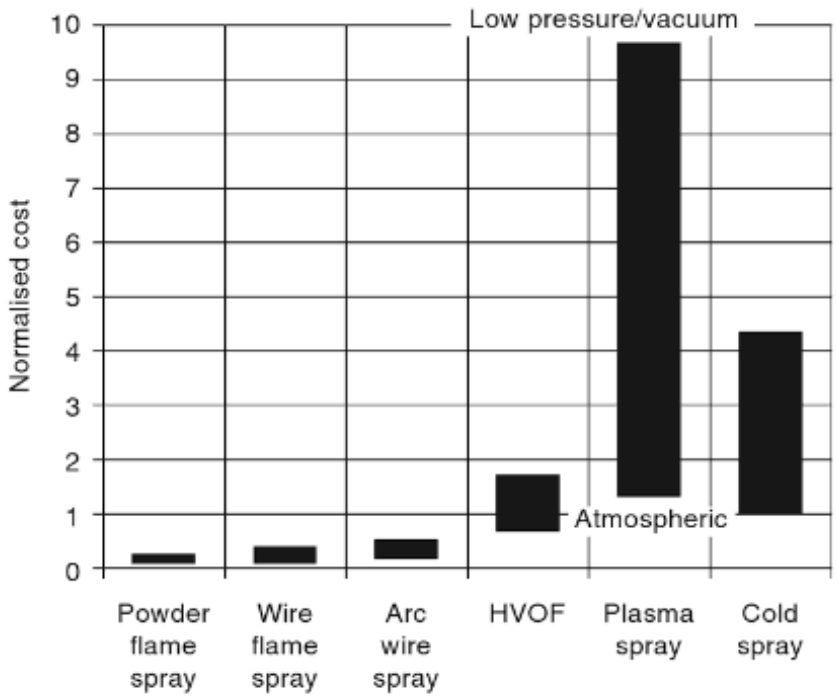

Figure 2:4 Normalised cost comparison of various hot and cold spraying techniques currently available in industry. Figures normalised to HVOF (High Velocity Oxygen Fuel) at ca. $10 (ca. £8) per part. Image taken from Celotto et al. [125].

Ion implantation (*Figure 2:5*), in a facile sense, relies on an ion source, an accelerator, and a target. The source, usually in the form of a Freeman ion source [126], generates ions, which are accelerated to a very high energy through electrostatic attraction *via* the accelerator, where they impinge onto the chosen target material [127, 128]. This technique has been of considerable interest regarding modification of Ti, specifically in the field of corrosion resistance for orthopaedic applications [129, 130]. Buchanan *et al.* detailed a 100-fold increase in wear resistance due to nitrogen ion implantation in a biomedical Ti6Al4V alloy, in comparison to a virgin implant [131]. Furthermore, dose levels of 4-7 × 10^{16} ions.cm^{-2} were shown to generate optimum corrosion resistance in Ringer's solution, as demonstrated by Sundararajan *et al.* [132].

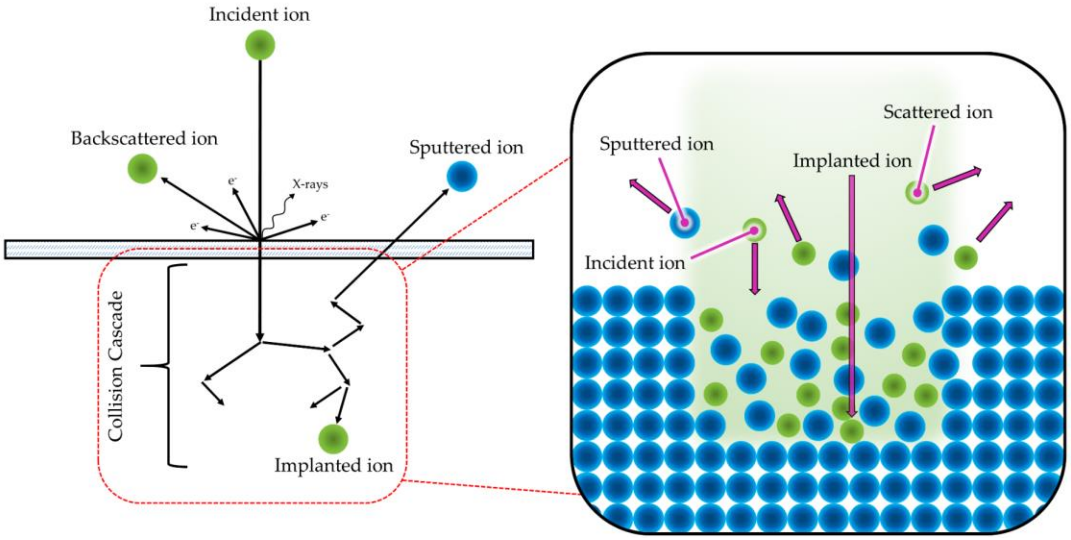

Figure 2:5 Schematic representation of ion-solid interactions, which is the principal mechanism employed in ion-implantation.

It has been reported that, under specifically high-dosages, the Ti 'picks up' carbon, generating carbonitrides at a rate proportional to the fluence (measure of particle flux) of nitrogen [133], which, as delineated by Leitao *et al.* resulted in undesirable effects on corrosion resistance [134, 135]. Therefore, optimum ion dosage is necessary for maximum expected corrosion resistance. Furthermore, Sundararajan *et al.* demonstrated in a separate study, again through nitrogen implantation at a dose of 1×10^{17} ions.cm^{-2}, a Ti-modified 316L SS alloy exhibited a 3-fold increase in resistance to corrosion [136]. Collectively, the inclusion of nitrogen results in the formation of a passivated film, as well as oxynitride formation within the material and passivated layers. Additionally, passivation thickness is greatly increased due to ion implantation, resulting in improved surface properties [136].

In addition to the improvement in corrosion resistance, improved bioactivity has also been considered through ion implantation. Armitage *et al.* and Nayab *et al.* both demonstrated the implantation of Ca ions into the surface of Ti [130, 137]. Varying degrees of success have been noted due to Ca ion implantation, with some studies showing no detrimental effect on human derived bone cells [138], whereas Nayab *et*

al., in a series of studies, demonstrated significant effects. For example, Ca-Ti inhibited cellular attachment within 4 h, whilst adhered cells exhibited enhanced spreading, with 24 h cultures showing significant increase in cell number compared to Ti controls [139-141]. A review of ion implantation into Ti and its alloys conducted by Rautray *et al.* detailed different ionic inclusions, including Na, F, Ar, N, Ag etc. [142]. Despite the advantages of ion implantation, as well as electrochemical methods detailed elsewhere [143-150], specialist, costly equipment is required in order to confer these properties. Additionally, these techniques are unable to coat complex shapes successfully, meaning an inability to coat porous femoral stems. Chemical treatments on the other hand, such as those producing titanate structures, do not have these limitations, and are therefore more applicable to complex, porous femoral stems.

2.1.3 Simple chemical treatments to improve titanium bioactivity

Since the work of Li *et al.* in 1994, on the induction of bone-like HA on titanium substrates through the generation of gel-like titania on its surface, surface modification through chemical routes has been considered of great practical importance [151]. Their study demonstrated that the hydroxyl groups formed on the surface were bioactive in nature, in addition to the negative surface potential. Therefore, if such groups could be generated on titanium, whilst ensuring a negative surface charge, it would hypothetically induce apatite formation both *in vitro* and *in vivo* [151].

Formation of osteoconductive HA, through submersion in SBF, is a well-known technique utilised in *in vitro* assessment of a material's bioactivity (ISO 23317:2014) [152]. In comparison to the *in vivo* environment, SBF solutions are regarded as supersaturated, as demonstrated by Lu *et al.* (SBF ionic concentrations noted in *Table 2:4*) [153]. It is well known that the higher the supersaturation of a solution, the greater the probability of molecular collision, which ultimately can lead to formation of stable

nuclei and, therefore, crystal growth [154]. As SBF is supersaturated with respect to Ca^{2+} and HPO_4^{2-} ($S^o_{(HA)} = 1.42$; S^o, is defined as the thermodynamic saturation level, where $S^o > 0$ indicates the compound will precipitate [155]), spontaneous apatite growth has been known to occur from nucleation points within the SBF container, such as cracks/scratches. Furthermore, it is a metastable system that thermodynamically will form apatite crystals to increase the system's stability [155]. Significant studies have contraindicated the use of SBF as an *in vitro* predictor of *in vivo* bioactivity, for example, *β*-TCP has extensively been shown to bond to bone *in vivo*, yet did not demonstrate a bioactive response in SBF [156]. This, as well as other studies, have brought into question the reliability of such a test, and therefore should be quantified with additional *in vitro* assessments (such as measuring proliferation and osteogenic differentiation of human mesenchymal stromal cells) prior to *in vivo* testing.

Table 2:4 Ionic concentrations of varying SBF solutions with respect to human blood plasma. Table adapted from Kokubo et al. [157].

Solution Type	**Ion concentration / mM**							
	Na^+	**K^+**	**Mg^{2+}**	**Ca^{2+}**	**Cl^-**	**HCO_3^-**	**HPO_4^{2-}**	**SO_4^{2-}**
Human blood plasma [158]	142.0	5.0	1.5	2.5	103.0	27.0	1.0	0.5
Original SBF	142.0	5.0	1.5	2.5	148.8	4.2	1.0	0.0
Corrected SBF (*c*-SBF)	142.0	5.0	1.5	2.5	147.8	4.2	1.0	0.5
Revised SBF (*r*-SBF)	142.0	5.0	1.5	2.5	103.0	27.0	1.0	0.5
Newly improved SBF (*n*-SBF)	142.0	5.0	1.5	2.5	103.0	4.2	1.0	0.5

Chemical surface modifications can be categorised into three distinct classifications: acidic, alkali, and combinatory, all of which have been considered in this review. Acidic treatments have often been employed as a pre-treatment for titanium materials, with a 10-30 vol.% HNO_3 and 1-3 vol.% HF (with distilled water) being the common standard solution. Wang *et al.* detailed the production of an amorphous titania gel, formed on Ti substrates through a mixed 8.8 M hydrogen peroxide (H_2O_2)/0.1 M hydrochloric acid (HCl) solution, held at 80 ^oC for specific time periods between 5 to 60 min [159]. The substrates were then heat-treated between 300 to 800 ^oC in air for 1 h. As delineated in *Table 2:5*, subsequent immersion in SBF led to apatite formation on samples heat-treated between 400 and 500 ^oC, following chemical treatment for greater than 15 min. If the soaking time used was less than this, then the titania gel layer that formed was insufficiently thick to form apatite, despite the heat treatment stage. The minimum gel thickness necessary for apatite formation was found to be *ca.* 0.2 μm. Additionally, the drop off in apatite formation above 600 ^oC attributed to the densification of the gel layer formed [159]. At the same temperature inflection-point, the dominant phase transformed from anatase to rutile, however, it must be noted that this does not confirm that rutile would lack bioactivity, since appropriate porosity/surface area is also a necessary property for bioactivity in some materials (*Figure 2:6*) [151]. Traditionally, the titania gel layer is generated *via* sol-gel methodologies. However, the process required to produce these layers is more complicated than the chemical treatment presented by Wang *et al.* [159]. Furthermore, sol-gel coatings tend to crack at thickness > 380 nm, whereas this study proved that layers of < 0.5 μm did not, suggesting stronger adhesion [160, 161].

Table 2:5 Apatite deposition as a function of length of chemical treatment time, and heat treatment temperature. Apatite generation (yes or no) was measured through FTIR techniques after soaking in SBF for various periods of time. Table modified from Wang et al. [159].

8.8 H_2O_2/0.1 M HCl @ 80 °C treatment time / min	**Heat treatment / °C at 1 h**	**Period of soaking in SBF / day(s)**				
		1	**2**	**3**	**5**	**7**
5	400	No	No	No	No	No
10	400	No	No	No	No	No
15	400	No	No	No	Yes	Yes
20	400	No	Yes	Yes	Yes	Yes
60	400	No	Yes	Yes	Yes	Yes
30	-	No	No	No	No	No
30	300	No	No	No	No	No
30	400	No	Yes	Yes	Yes	Yes
30	500	No	Yes	Yes	Yes	Yes
30	600	No	No	Yes	Yes	Yes
30	700	No	No	No	No	No
30	800	No	No	No	No	No

Figure 2:6 Extent of integration due to macro- and micro-structured titanium implants. It is clear that the higher surface area leads to higher implant-to-bone strength, resulting in intra-bone fracture during removal. Images taken from Jäger et al. [97].

Wu *et al.* explained varying complex chemical modifications in H_2O_2 (termed the oxidising stage) and subsequently HCl (labelled the ageing stage) [162]. Initially a 1:1.5:6 (vol.) mixture of HF, HNO_3, and distilled water, was used to immerse the substrates for 2 min at 60 °C. Substrates then experienced subsequent treatment in

10 mL of H_2O_2, 70% H_2O_2/30% $TaCl_5$ (mass), 1:1 H_2O_2/$TaCl_5$ (mass), or 30% H_2O_2/70% distilled water at 80 ^oC for either 8 or 72 h. The second treatment consisted of either nothing, distilled water (72 or 360 h), or 0.25 M HCl (72 h), all at 80 ^oC. Crystalline titania layers, which consisted of both rutile and anatase with a ratio of *ca.* 2:1, were generated *via* a 30 mass% H_2O_2/3 mM $TaCl_5$ solution for 72 h. Amorphous titania with varying ratios of anatase and rutile were produced *via* the other processing routes mentioned above, however, subsequent aging in either distilled water or 0.25 M HCl was required to crystallise the gel [162]. This study showed that regardless of the processing route, the obtained crystalline titania films generated approximately the same amount of apatite in SBF. The induction time for apatite formation was less than 24 h. A key difference in this study is the low-temperature processing route used (80 ^oC), in order to induce crystallisation. Uchida *et al.* demonstrated in a similar way to Wu *et al.*'s study, that apatite formation has a structural dependence, whereby amorphous titania gels will not form apatite, however, crystalline titania consisting of anatase and/or rutile phases are significantly more bioactive [163].

Zhao *et al.* researched nano- and conventional-TiO_2 powders that had been plasma sprayed onto Ti6Al4V substrates, generating 100 μm films, followed by treatment in solutions of 3 M hydrochloric and 1 M sulfuric acid [164]. It was found that the acid-treated coatings of both nano- and conventional-titania induced carbonate-containing HA. This study also revealed that the acidic solution, containing an abundance of H^+ ions, bridge the oxygen bonds found within the titania layers, resulting in formation of Ti—OH groups. Yu *et al.* corroborated these results and demonstrated that the acid-treated titania surface resulted in a higher hydroxyl content compared to untreated titania [165]. During submersion in SBF, negative functional groups (Ti—O^-) are

formed, attracting Ca^{2+} to the surface, and enabled apatite formation. Further details on the mechanism of apatite formation are detailed in *Section 2.1.5*.

Takeuchi *et al.* investigated the combined treatment of sulfuric and hydrochloric acids (10.6% and 66.3% (w/w: weight for weight), respectively), and the effect of such a treatment on the cytocompatibility of rat bone marrow derived osteoblastic cells [166]. It was seen that the treatment resulted in differing surface topographies, which intrinsically possessed different biomechanical properties for the mineralised tissue. This produced tissue, which was measured *via* 5 μm deep indentations, exhibited an elastic modulus and hardness 3.5 and 2.5 times higher, respectively, than standard machined Ti surfaces. Furthermore, not only did the elastic modulus fall slightly above the range of normal healthy bone, but also the quantity of all extracellular matrix (ECM)-related gene expression for bone, including osteocalcin (non-collagenous hormone located in bone/dentin); P4H (key enzyme in collagen synthesis); and Collagen I & III, was higher for the acid-treated substrates compared to as-machined Ti, as seen in *Figure 2:7* [166].

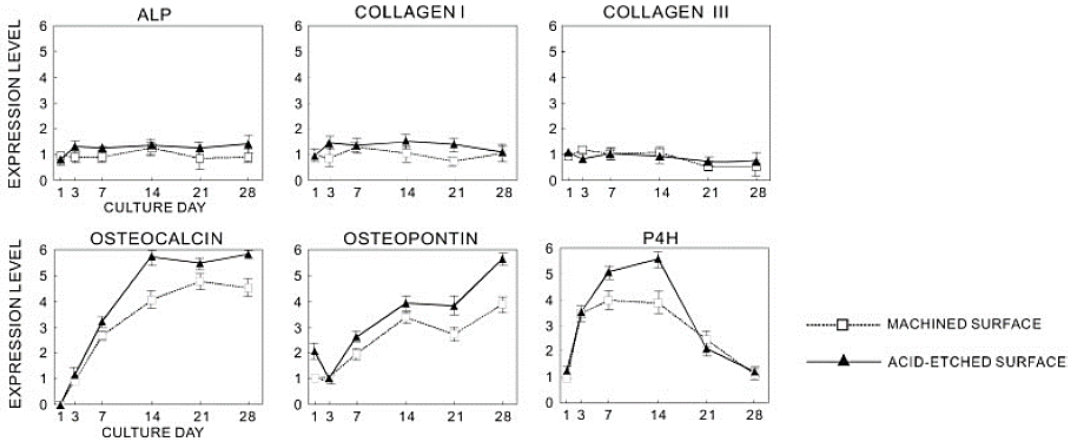

Figure 2:7 Expression of bone ECM-related genes as a measure of bone mineralisation on the surface of acid-treated and as-machined Ti substrates. ALP = alkaline phosphatase, and P4H is a gene required during collagen synthesis. Figure taken from Takeuchi et al. [166].

Continuing the thematic research into acid-treated substrates, Lee *et al.* demonstrated that a Ti metal substrate, immersed in a 1:1 (vol.%) ratio of 97% H_2SO_4 and 30% H_2O_2 (40 ^oC, 1 h) and heat-treated (400 ^oC, 1 h), produced a reduction in the inflammatory response *in vivo* [167]. The samples were implanted into the abdominal connective tissue of mice for a period of 28 days, with the average fibrous capsule size surrounding the implant material being 47.1 ± 23.7 μm. This is in comparison to untreated Ti, Al, and 316L SS, whose average capsule thickness was 52.2 ± 13.4, 168.7 ± 45.1, and 101.9 ± 30.5 μm, respectively. Fibrous capsule formation is indicative of poor tissue healing post-trauma; a form of 'wall' to barrier the implant from the host, hence the smaller the capsule, generally the better the *in vivo* response [168]. Previous studies by Lee *et al.* and Kim *et al.* demonstrated, similar to above, that titanium alloy and stainless steel generate thicker fibrous capsules (21.0 and 36.7 μm, respectively) when compared to pure Ti (19.5 μm), indicating the former materials exhibit lower biocompatibility (*Figure 2:8*) [169-171]. Since the treated-Ti generated a thinner fibrous capsule compared to the untreated-Ti, the biocompatibility is therefore improved as a result of the acid-treatment.

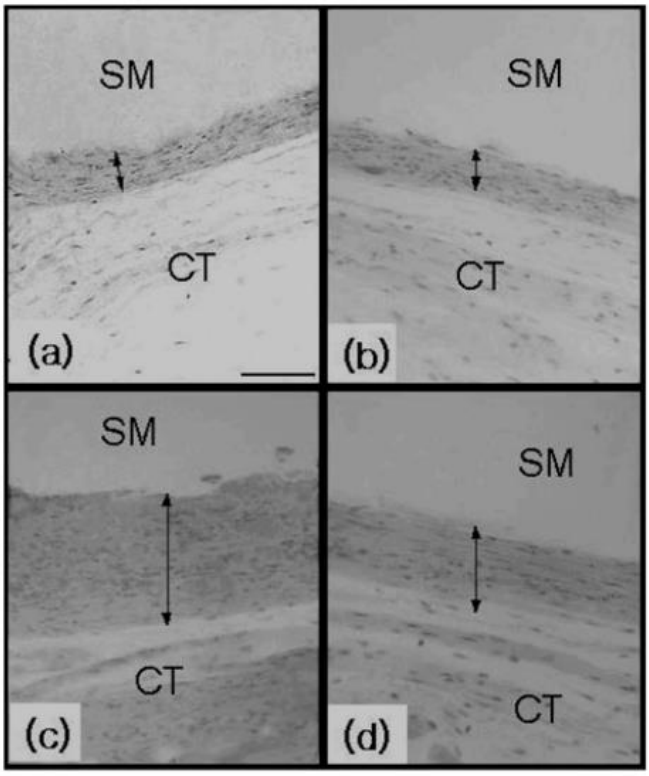

Figure 2:8 Comparison of the fibrous capsule formation surrounding (A) untreated Ti, B) acid-treated Ti, C) untreated Al, and D) untreated 316L SS. CT = Connective tissue; SM = Site of implanted metal. Image taken from Lee et al. [167].

Further acidic treatments were studied by Lu *et al.* with nitric acid being tested as an alternative treatment to sulfuric or hydrochloric acids used previously [172]. In a similar trend to those presented above, the nitric acid treatment not only provided enhanced surface passivation, but also demonstrated its efficacy as an alternative method to the two-step acidic methods presented previously. A calcium phosphate layer consisting of globules (*ca.* 1-5 μm in diameter) was seen on the 60 ^{o}C, 10 h nitric acid treated substrate, following submersion in SBF after 1 day. It was found that a minimum acid treatment time of 1 h was needed to confer apatite formation, with a proportional trend between acid treatment time and rate of calcium phosphate formation (*Table 2:6*). The optimum conditions were found to be 60 ^{o}C for 10 h [172]. Nitric acid treatment differs from the other acid treatments in a fundamental way. Instead of dissolving the passivated oxide layer, and generating a rougher surface

morphology, nitric acid has been shown to decrease the thickness of the oxide layer formed, whilst also increasing the surface energy [172]. Surface energy can be calculated through varying methods [173-179], and is defined as *"the excess free energy per unit area"* [180]. The surface energy for untreated Ti compared to nitric acid treated Ti, as calculated using the Owens-Wendt (or Kaelble) method [173], were 61.37 and 76.26 mJ/m^2, respectively [172].

Table 2:6 Ca-P deposition on treated Ti substrates from the study by Lu et al. [172], *demonstrating a clear link between HNO_3 treatment time, and rate of calcium phosphate deposition. Table adapted from Lu et al.* [172].

Ti surface treatment	Treatment temperature (°C)	Treatment time / min	SBF immersion time / day(s)			
			1	3	7	10
H_2SO_4/HCl	60	300	No	No	No	No
H_2SO_4/HCl + HNO_3	25	20	No	No	No	No
		60	No	No	No	No
		300	No	No	No	No
		600	No	No	No	No
	60	20	No	No	No	No
		60	No	No	Yes	Yes
		300	No	Yes	Yes	Yes
		600	Yes	Yes	Yes	Yes
Polished Ti	-	-	No	No	No	No
Polished Ti + HNO_3	60	600	Yes	Yes	Yes	Yes

Zhao *et al.* further explored the application of nitric acid treatments, through comparing varying molarities of sulfuric and nitric acid, on plasma sprayed Ti layers on Ti6Al4V alloys [181]. Both acid treated surfaces generated bone-like apatite upon the surface in SBF. However, at lower concentrations (0.01 M), the bioactivity was not improved. As previously mentioned, the acid treatment is necessary to generate Ti—OH bonds, which are essential for the formation of apatite, irrespective of the acid used. Furthermore, the treatment resulted in enhanced mesenchymal stem cell adhesion and proliferation, potentially as a result of increased surface roughness due

to the sulfuric acid treatment, or due to the increased hydrophilicity from the nitric acid.

Similarly, Turkan and Guden studied nitric acid (1:1 vol. ratio of 65% HNO_3 and H_2O, 60 ^oC, 5h) treatment on Ti6Al4V open-cell foams, which were 60% porous, with an average pore size of 300-500 nm [182]. Porous surface morphologies for implant materials aid in the degree of bone in-growth into the surface structure, enabling more natural adhesion between the implant and surrounding tissue [183]. This ultimately resulted in improved fixation of the implant into the medullary canal; an essential requirement for total joint replacements. The study by Turkan and Guden confirmed that the nitric acid-treatment, although it did not alter the surface roughness significantly, the treatment generated nanoscale undulations, resulting in increased surface area [182]. Additionally, the treated surfaces were able to produce a continuous thin Ca-P coating after submersion in SBF. Interestingly, foams generated from smaller Ti6Al4V powder sizes (*ca.* 66 *vs.* 94 μm average particle size, respectively) resulted in a more pronounced surface area difference, as well as generating Ca-P coatings with a reduced induction time; 5 *vs.* 14 days, respectively, indicating enhanced bioactivity for the foams produced with smaller particles sizes. In comparison to untreated specimens, Ca-P layer development occurred after 14 days. The decrease in the time for Ca-P formation were attributed to a reduction in the heterogeneous nucleation barrier (energy required for nucleation to occur from a surface or impurity), due to an increase in the surface energy (24% increase in nitric acid-treated Ti *vs.* un-treated [172]).

Cooper *et al.* examined the effect of fluoride ion treatment on TiO_2 grit-blasted Ti substrates on their *in vitro* osteogenesis, and the degree of bone formation *in vivo,* through endosseous (dental) implantation [184]. It was determined that the benefits of

such a treatment were two-fold. Firstly, osteoconduction at the interface between the metallic implant and bone was improved. Secondly, the healing period after implantation was reduced, whilst simultaneously increasing the amount of bone formation during that period. The fluoride treated surfaces enhanced proliferation of human mesenchymal stem cells, as well as increased expression of Bone Morphogenetic Protein (BMP-2), and bone sialoprotein. The contact area between the bone and the implant increased from 34.2% for the solely grit-blasted surface, to 55.5% for the fluoride treated, grit-blasted samples [184].

Further studies have been conducted by Ferraris *et al.* [185]; Karthega and Rajendran [186]; Li *et al.* [187]; and Sugino *et al.* [188], however, their scope is similar to the studies presented above, hence to avoid repetition their content will not be discussed further in this literature review.

2.1.4 Alkali titanate formation and its apatite forming ability

Although all the studies mentioned in *Section 2.1.3* attempted to induce apatite formation on Ti metal and its alloys within SBF through acidic treatments, the mechanism by which apatite formation occurs, was not fully focussed on in these studies. Furthermore, acid treatments lack the ability to incorporate additional ions to aid in bone maturation or conferring additional properties such as being antibacterial. Systematic studies conducted by Kokubo and his team, have elucidated the basic principles of this mechanism, as well as optimal parameters necessary for apatite formation. The first studies that introduced alkali and heat treatment processes in order to improve Ti biocompatibility were by Kokubo *et al.* and Kim *et al.* in April and November 1996, respectively [77, 189]. Their work followed on from corrosion studies by Revie *et al.* [190], Hurlen *et al.* [191], Arsov *et al.* [192], and Prusi *et al.* [193], who suggested that in alkaline solutions (*e.g.* KOH used by Arsov *et al.* and

Prusi *et al.*), hydrated TiO_2 would be produced; similar to the acid treatments as previously mentioned in *Section 2.1.3* [151]. Kim *et al.* hypothesised that if such layers could be subsequently generated *in vivo*, bone-like apatite may be generated, enhancing the bioactivity of the Ti surface [77]. The method proposed by Kim *et al.*, enables the formation of bone-like apatite on the surface of the alkali-modified titanium, akin to structures formed on bioactive materials such as 45S5 Bioglass® [168], HA [194], and A/W glass ceramic (MgO-CaO-SiO_2 glassy matrix, which contains apatite and wollastonite), developed by Kokubo *et al.* [195].

The initial alkali-treatment outlined by Kim *et al.*, consisted of a 5-10 M NaOH or KOH (5 mL, 60 °C) treatment of Ti or Ti alloy substrates for 24 h, followed by rinsing in distilled water, ultrasonic cleaning for 5 min, and 40 °C air drying. Initially the passivated surface layer, TiO_2, was partially dissolved by the alkali solution, as detailed by the below equation:

$$TiO_2 + OH^- \rightarrow HTiO_3^-$$

As demonstrated by numerous studies [191, 192, 196-199], the above reaction occurs concurrently with the hydration of the Ti metal, causing oxygen penetration into the top *ca.* 1 μm of the surface [200].

$$Ti + 3OH^- \rightarrow Ti(OH)_3^+ + 4e^-$$

$$Ti(OH)_3^+ + e^- \rightarrow TiO_2.H_2O + \left(\frac{1}{2}H_2\right)\uparrow$$

$$Ti(OH)_3^+ + OH^- \rightarrow Ti(OH)_4$$

The negatively charged $HTiO_3^-$ anions generated through the alkali attack combine with the alkali cations (M_x) present within the solution, most notably Na^+, which results in an alkali titanate gel layer, with the chemical formula:

$M_xH_{2-x}Ti_yO_{2y+1}; 0 < x < 2$ and $y = 2, 3,$ or 4 (*Figure 2:9*). The depth of penetration for both sodium and oxygen is *ca.* 1 μm with 8 at.% Na at the surface, as demonstrated by Kim *et al.*, and is shown in *Figure 2:10* [201].

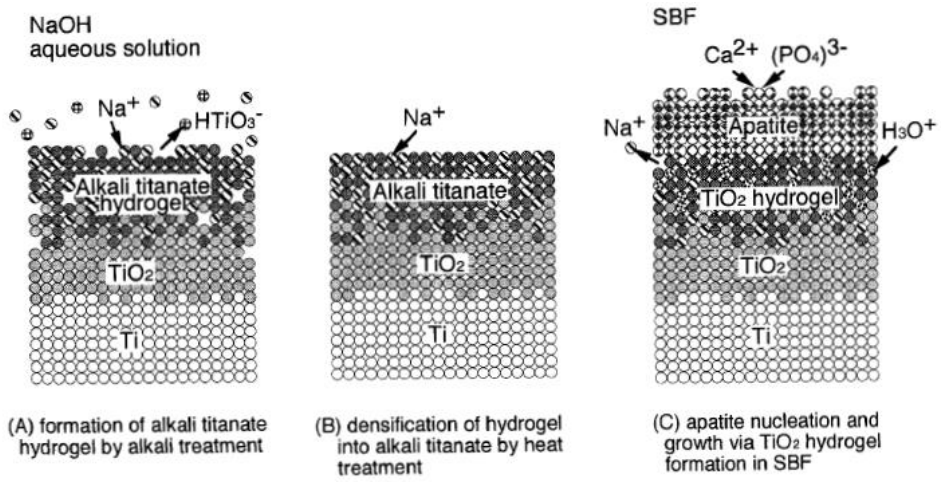

Figure 2:9. Representation of the chemical reactions occurring on the surface of the titanium substrate during (A) alkali- and (B) heat treatments, as well as subsequent apatite nucleation in SBF (C). Image taken from Kim et al. [77].

Heat treatment of the samples was then performed between 400-800 °C for 1 h to assess the effect heat has on the formed hydrogel layer [77]. Following heat treatment at varying temperatures, it was noted through XRD that the original amorphous sodium titanate that was formed during the NaOH treatment, partially converted into crystalline sodium titanate by 600 °C, with small quantities of rutile also being formed. At 800 °C, large amounts of rutile (TiO_2) and sodium titanate with the formula $Na_2Ti_yO_{2y+1}; y = 5, 6,$ etc. had formed, with no amorphous layers present (*Figure 2:11*). The sodium titanate formed following heat treatment was isomorphic to the sodium hydrogen titanate hydrogel formed prior. It is clear from the Auger Electron Spectroscopy (AES) data presented in *Figure 2:10* that oxygen exhibits further penetration into the substrate following heat treatment [201]. Not only can this process occur on pure Ti, but subsequent studies by Kokubo *et al.*, Kim *et al.*, Ueno *et al*, and

Tsukimura *et al.* have demonstrated its applicability to Ti alloys, such as: Ti6Al4V, Ti-6AL-2Nb-Ta, and Ti-15Mo-5Zr-3Al alloys [77, 189, 202, 203].

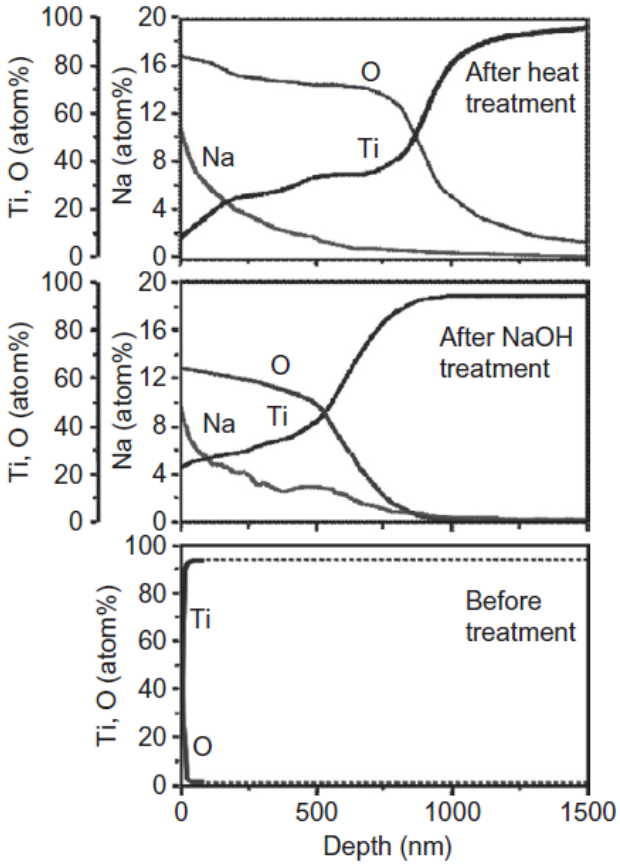

Figure 2:10 Auger electron spectroscopy (AES) of Ti substrates that have been treated in sodium hydroxide and subsequently heat-treated. Graph taken from Kim et al. [201].

Titanate layers have previously been commended on their ease of ion exchangeability [204-206], allowing their use as ion exchangers in fixing radioactive metal ions [207]. Once generated, the sodium titanate layers are able to perform ion exchange reactions within aqueous solutions. The level of electrostatic attraction of Na^+ within the sodium titanate layer is not enough to hold it in place when H_3O^+ ions are in solution. Therefore, exchange of H_3O^+ with Na^+ results in Ti—OH bonds forming on the surface. Furthermore, this reaction causes an increase in the pH of the environment surrounding the surface, which in turn causes the surface to become negatively charged, as detailed by Gold *et al.* [208]. The significance of surface charge

will be described in further detail in *Section 2.1.5*. Further reactions occur within the aqueous SBF solution, whereby, the negative surface attracts Ca^{2+}, forming an amorphous calcium titanate surface. The accumulation of Ca^{2+} ions results in an overall positive surface charge, which subsequently attracts PO_4^{3-} (phosphate) ions, forming an amorphous calcium phosphate. This surface is metastable and subsequently matures into apatite, which was found to occur within 3 days in SBF [209]. Representation of the ion exchange reactions is detailed in *Figure 2:12*.

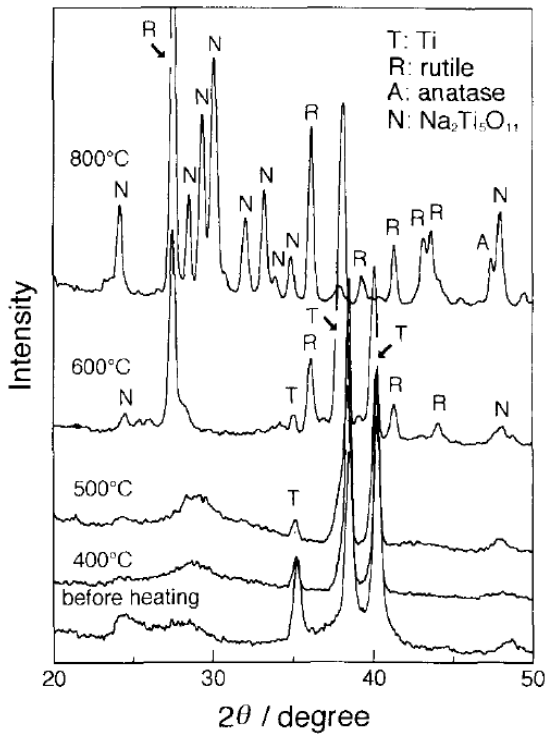

Figure 2:11 XRD spectra of NaOH treated Ti substrates after varying heat treatment temperatures. T = Ti, R = rutile, A = anatase, N = $Na_2Ti_5O_{11}$. Figure taken from Kim et al. [77].

The mechanism of apatite formation outlined above was a result of a collection of research data conducted by various research groups [50, 210, 211]. Notably, Takadama *et al.* used X-ray Photoelectron Spectroscopy (XPS) and X-ray Diffraction (XRD) to quantify the composition of the top surface layers of the substrate [210]. It was found, as outlined in *Figure 2:13*, that HA formation began at around day 2, with

complete conversion occurring within 3 days. Furthermore, high resolution scans of Ca 2p, O 1s, Na 1s, and P 2p all corroborated the initial findings. From the Na 1s spectra, Na^+ began eluting within 30 mins, whilst Ca 2p peaks were found as early as 30 min (deconvoluted as calcium titanate: $Ca_3Ti_2O_7$). The Ca 2p peaks exhibited a slight shift in binding energy at 2 days, which was deconvoluted as hydroxyapatite. P 2p did not exhibit a peak until 48 h submersion in SBF, indicating Ca had ion exchanged into the surface prior to attraction of phosphate ions onto the surface. However, the most significant piece of data was the formation of Ti—OH bonds within 30 min of SBF immersion. This partially confirmed the hypothesis that these bonds were essential for indirect apatite formation through calcium titanate formation [210].

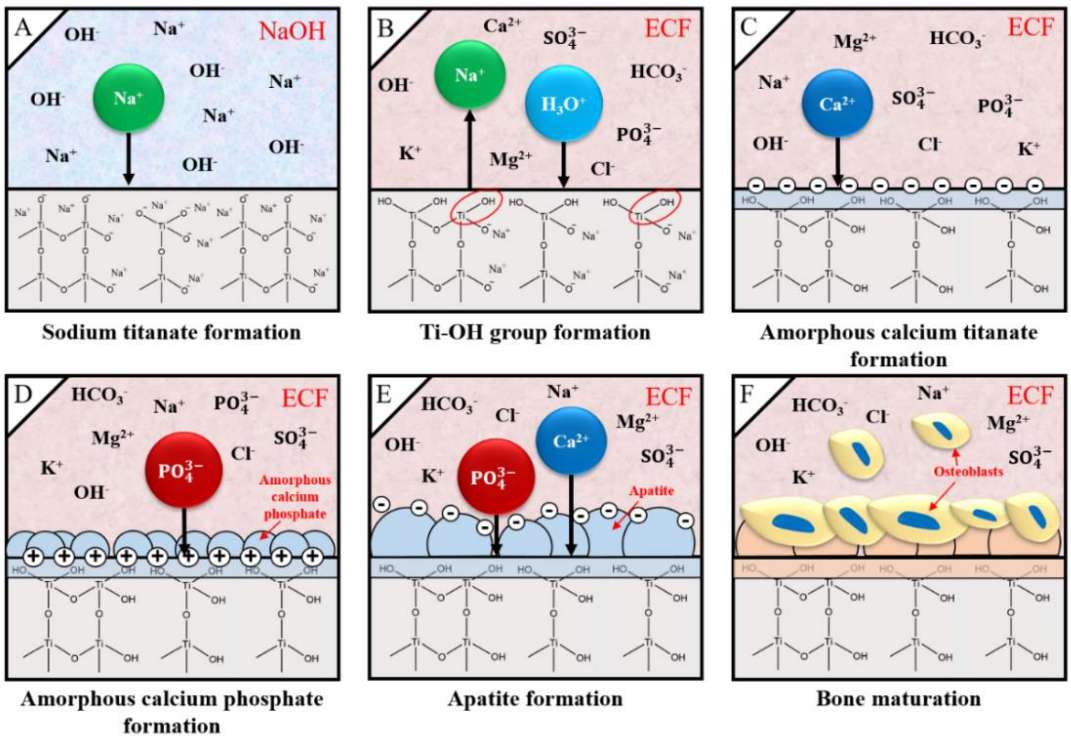

Figure 2:12 Ion exchange reactions that facilitate apatite formation in SBF. ECF denotes extracellular fluid, however, this process was initially discovered utilising SBF.

XPS results were corroborated in a further study by Takadama *et al.* whereby Transition Electron Microscopy (TEM) combined with Energy Dispersive X-ray

(EDX) analysis was employed to understand the structural alteration during apatite formation [50]. Initially, a fine network structure of *ca.* 500 nm was observed on the alkali- and heat-treated samples. Upon immersion in SBF, Ca inclusion was noted within 0.5 h, with an amorphous calcium titanate and calcium phosphate (Ca:P = 1.4) forming within 24 and 36 h, respectively. By 72 h, the Ca:P ratio was approximately 1.65, close to stoichiometric HA (1.67) [50]. Yamaguchi *et al.* further demonstrated the morphological changes that occurred during submersion of sodium titanate layers within SBF, producing apatite as seen in *Figure 2:14* [209].

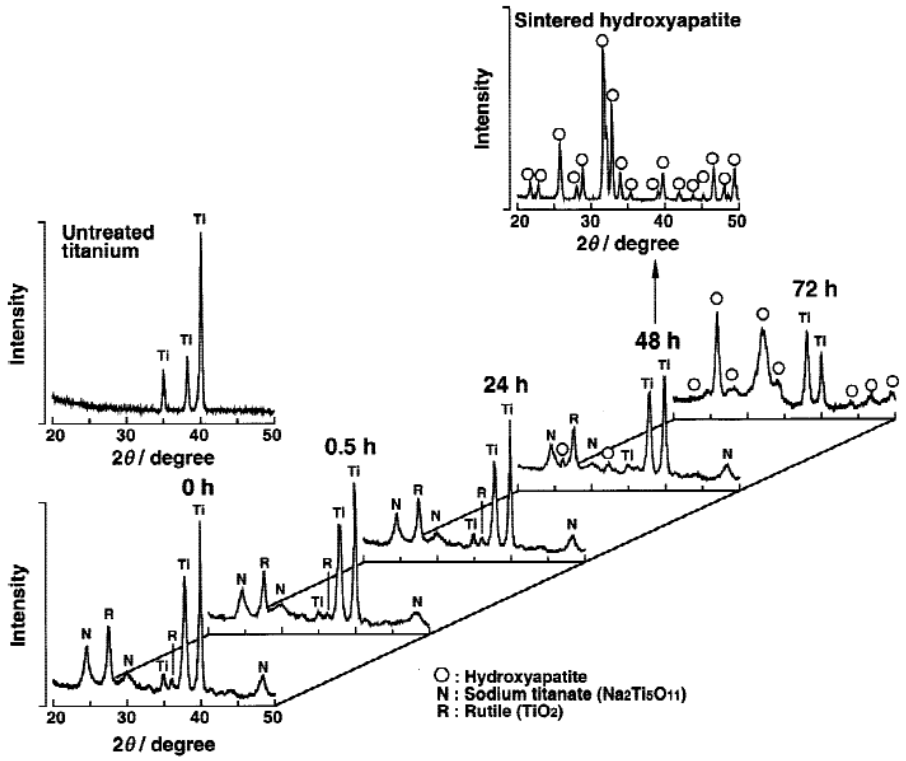

Figure 2:13 XRD spectra of sodium titanate surfaces and their transformation into apatite following submersion in SBF over 72 h. Figure taken from Takadama et al. [210].

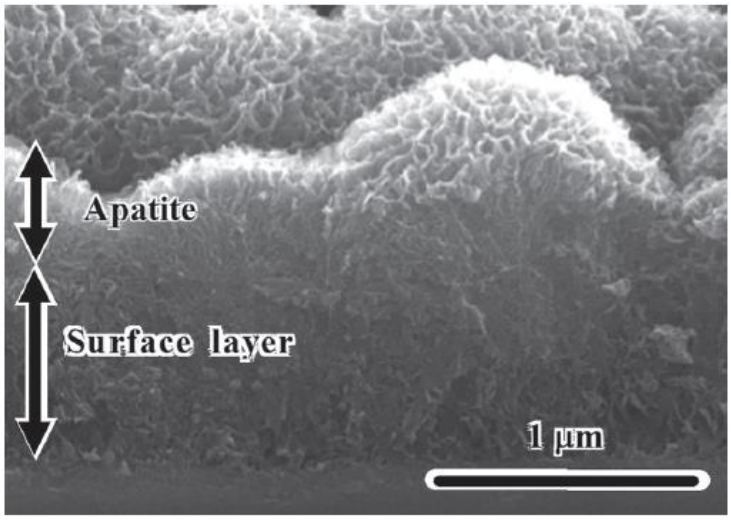

Figure 2:14 SEM image of the formation of apatite on the surface of alkali- and heat-treated titanium surfaces after 1-day immersion in SBF. Figure taken from Yamaguchi et al. [209].

A recent study by Li *et al.*, detailed the effect of different pressures during the heat treatment process (*ca.* 10^{5}-10^{-3} Pa) [212]. Their results showed that at higher vacuum pressures, the structure exhibited larger pores sizes, whilst improving the HA formability in SBF [212].

2.1.5 pH and surface charge dependence on apatite formation

It was proposed by Takadama *et al.* that formation of apatite on alkali-treated titanium occurred through electrostatic interactions between the surface, and specific ions within the aqueous solution [50]. Kim *et al.* investigated these effects through understanding the surface potential, also known as the Zeta (ζ) potential, in regard to soaking time in SBF [211]. The ζ potential (V) was quantified using the Smoluchowski equation [213], seen below:

$$\zeta = \frac{\eta u_e}{\varepsilon_r \varepsilon_0}$$

where u_e = electrophoretic particle mobility ($m^2V^{-1}s^{-1}$), η = solution viscosity (Pa.s (or $N.s.m^{-2}$)), ε_r = relative permittivity/dielectric constant, and ε_0 = permittivity of a vacuum (8.8 x 10^{-12} Fm^{-1} (or NV^{-2})). The results presented corroborated the

mechanism outlined in *Section 2.1.4*, that ion exchange reactions between Na^+ and H_3O^+ occurred first, generating negative Ti—OH bonds (negative ζ potential), which then attracted positive Ca^{2+} (increasing the ζ potential), followed by negative phosphate ions, forming calcium titanate (formed within 0.5 h) and calcium phosphate (formed within 42 h), respectively (*Figure 2:15*) [211]. Within 72 h, apatite had been formed on the surface, which was due to the much lower solubility of HA with respect to calcium phosphate in the body environment. Furthermore, it is well known that HA has a negative charge in the body environment due to the presence of hydroxyl and phosphate groups on its surface, as demonstrated by the potential at 72 h (*Figure 2:15*) [214]. Interestingly, a common trend that has been seen in a few studies [211, 215], is the incorporation of carbonate, sodium and magnesium into the apatite layer formed in SBF, which is more akin to that of bone-like apatite. This is due to the SBF being supersaturated with respect to apatite even under normal conditions [216].

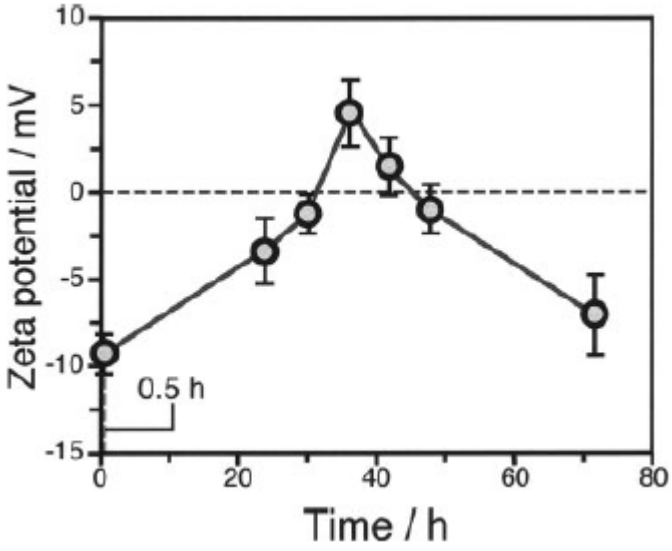

Figure 2:15 Zeta (ζ) surface potential as a function of soaking time in SBF. Figure taken from Kim et al. [211].

In order to completely assess the dependence of pH of the treatment medium on apatite formation, systematic alteration of NaOH and HCl solution pH from 0 to 14,

was conducted at 60 °C for 24 h, followed by heat treatment at 600 °C. The study by Pattanayak *et al.* elucidated that a pH of $1.1 \leq x \leq 13.6$ inhibited the occurrence apatite formation, whilst pH values below 1.1 and above 13.6 generated apatite within 3 days (*Figure 2:16A*) [217]. It was also demonstrated in this study that apatite formation depends on surface charge, rather than surface roughness and specific crystalline phases. When Ti metal is subjected to acid-treatment, as outlined previously, followed by subsequent heat treatment, the surface ζ potential is positive (*Figure 2:16B*). Conversely, for alkali-treated substrates, the ζ potential is negative. The theory that ζ potential affects apatite formation, is further substantiated through the fact that natural Ti, despite the same heat treatment process, does not generate apatite on its surface, since the surface ζ potential is neutral (*Figure 2:16C*) [217].

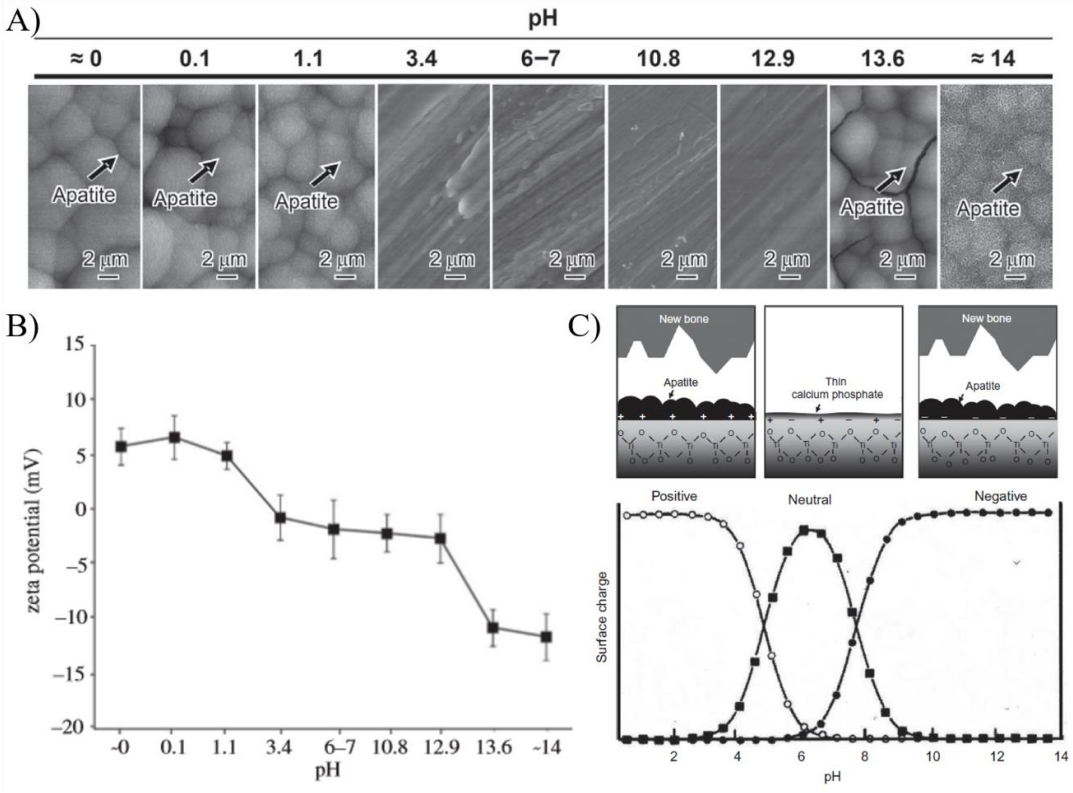

Figure 2:16 (A) Morphological changes as a function of solution pH during alkali-/acid-treatment of Ti substrates. (B) Zeta (ζ) potential measurements as a function of solution pH. (C) Representation of surface charge with respect to solution pH, and its effect on apatite formation on the surface. Figures adapted from Pattanayak et al. [217].

2.1.6 Issues and improvements to titanate generation

Despite their simplicity and significant beneficial improvements to the bioactivity/antimicrobial properties of Ti and its alloys, issues regarding alkaline titanates have resulted in the need for further studies. This has been initiated within the literature regarding changes to the current production methodologies.

Kizuki *et al.* systematically reviewed various reagents, as well as their compositions, in order to assess issues regarding reduced apatite formation with respect to increased NaOH volume [218]. This study demonstrated that even 0.0005% of Ca ions present within the initial NaOH solution used, would preferentially enter into the sodium titanate layers formed, inhibiting apatite formation, since sodium ions will not be released from the structure. However, even some reagents, which have a nominal purity of 97%, produced apatite *in vitro* due to having no calcium contamination. The reduction in apatite formation was a direct correlation to the increase in NaOH volume used, since a larger volume resulted in greater abundance of Ca^{2+} ions. It was found that just 2 ppm of Ca^{2+} was enough to reduce Na^{+} release from 1.21 to 0.87 ppm [218]. Ultimately, there is a need for very careful planning of the type of reagent used, since contamination on this scale is what would normally be considered negligible.

Another significant issue was outlined by Kawai *et al.,* which concerns the lack of stability of sodium titanate structures in humid environments [219]. The substrates were kept in 95% humidity at 80 ^{o}C, for 7 days. Since humid environments inherently contain H_3O^{+} within the water vapour [220], ion exchange reactions can still persist, causing a decrease in the sodium content present prior to intended use, such as SBF or implantation. This is a significant issue regarding medical implants, since there is a substantial storage period between manufacture and implantation. The ion exchange

reactions reduced the Na^+ content of the sodium titanate, and hence reduced apatite formation. Ultimately, these surfaces, unless otherwise modified, require dry controlled conditions (vacuum bags) in order for apatite to form once implanted [219].

Finally, Yamaguchi *et al.* outlined a particular issue regarding Ti-Zr-Nb-Ta alloys [221]. Despite their lack of cytotoxic elements, the alkali-treatments detailed are not effective to produce apatite-forming abilities in this new family of Ti alloys. Specifically, the Ti-15Zr-4Nb-4Ta alloy investigated by Yamaguchi *et al.* has superiorly high ultimate tensile strength (*ca.* 453 MPa) [222]. However, subsequent investigations negated all the issues outlined above and are detailed in *Section 2.1.7* below.

2.1.7 Ion exchanged Titanate Structures

A large proportion of studies, as outlined in previous sections, have detailed the applicability of sodium titanate surface for biomedical applications. However, additional scope regarding further ion exchange of these surfaces needed exploring, since all the ion exchange reactions detailed occurred post-implantation, through the *in vivo* apatite formation. By incorporating an additional step into the hydrothermal treatment, which soaks the samples in 100 mM $CaCl_2$ (40 ^oC, 24 h), Kizuki *et al.* demonstrated the ability of sodium titanate surfaces to incorporate alternative ions (Ca^{2+}) into the structure, that in themselves can be used to generate apatite [56, 57]. Although calcium titanate is generated following this additional step (crystallographically detailed in *Figure 2:17*), apatite formation does not occur unless an additional hot water (80 ^oC, 24 h) soaking treatment is conducted. Apatite was found to be supressed due to minimal Ca^{2+} leaching from the untreated calcium titanate layer. The water-treatment generates a calcium-deficient titanate layer on the surface due to ion exchange with H_3O^+ ions, which facilitates calcium release. This allows

subsequent apatite formation, through ion exchange reactions detailed previously. Furthermore, studies by Yamaguchi *et al.* demonstrated that not only does this additional treatment prevent issues regarding humidity affecting apatite formation, but also this treatment is effective at generating apatite formation on Ti-Zr-Nb-Ta alloys [223, 224].

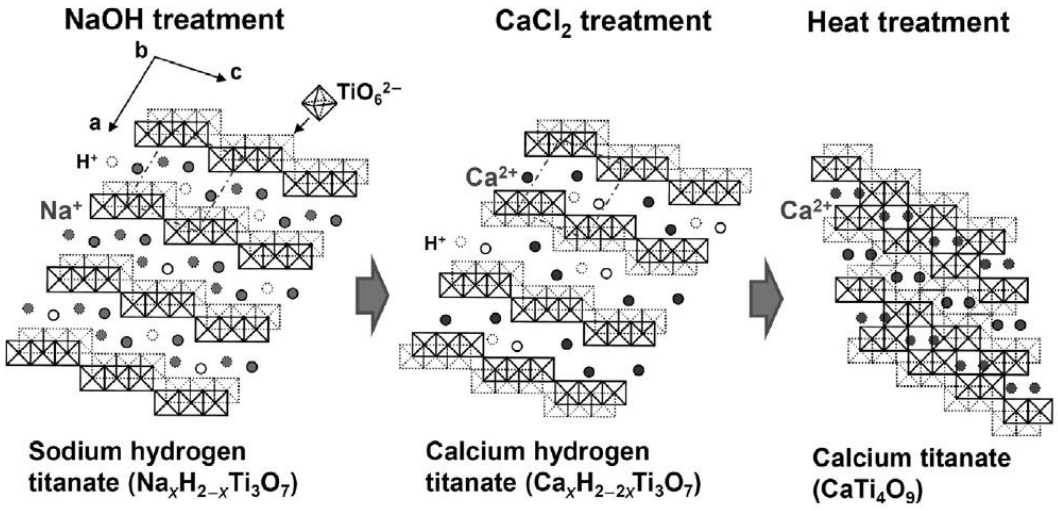

Figure 2:17 Crystallographic representation of the sodium and calcium hydrogen titanate layers, as well the as the calcium titanate formed from the heat treatment. Figure taken from Kokubo et al. [225].

Bone bonding of NaOH, $CaCl_2$, heat- and water-treated Ti metal and Ti alloys, specifically Ti-Zr-Nb-Ta alloys, were investigated by Fukuda *et al.* and Tanaka *et al.* [226, 227]. Fukuda *et al.* investigated Ti-15Zr-4Nb-4Ta and Ti-29Nb-13Ta-4.6Zr alloys, whilst Tanaka *et al.* studied gum metal (Ti-36Nb-2Ta-3Zr-0.3O). Both studies investigated the effect of NaOH, $CaCl_2$, heat- and water-treatments on the bone-bonding ability of the above alloys as rabbit tibial implants [226, 227]. All implants demonstrated successful bone bonding without fibrous encapsulation. Furthermore, during detachment/removal testing, fracture occurred within the main bone portion, as opposed to the implant-bone interface, meaning the interfacial bond strength is sufficient to prevent delamination (*Figure 2:18*). It was postulated by this thesis's

author that developing better bone-bonding capabilities on alloys that are free of cytotoxic elements, will result in a new generation of implant materials that can potentially replace the current generation of Ti alloys.

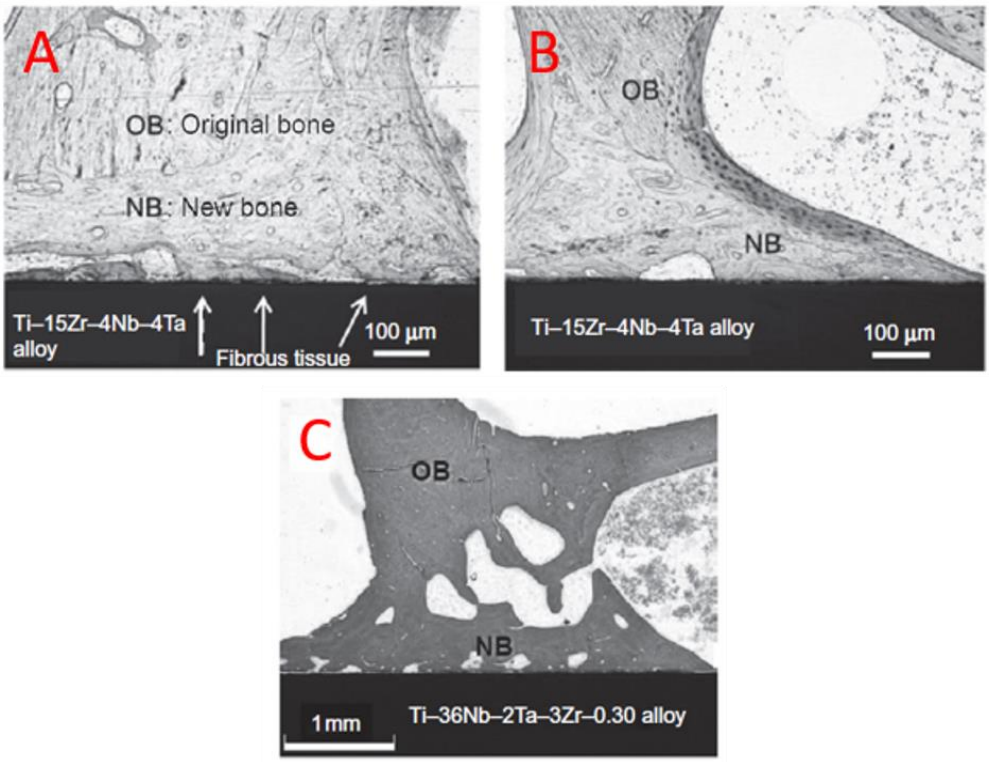

Figure 2:18 Optical micrographs of A) untreated Ti-15Zr-4Nb-4Ta alloy, and B) NaOH, $CaCl_2$, heat- and water-treated Ti-15Zr-4Nb-4Ta, and C) Ti-36-Nb-2Ta-3Zr-0.3O alloys after implantation in rabbit tibias. A & B are 16 weeks post-implantation, with C being 26 weeks post-implantation. Figure adapted from Fukuda et al. and Tanaka et al. [226, 227].

A more recent study by Ferraris *et al*. [228], tested the bioactive potential, specifically looking at the mechanical and chemical stability of the interface, of a variety of different chemically treated Ti and Ti6Al4V substrates, compared to a bioactive glass (48% SiO_2, 18% Na_2O, 30% CaO, 3% P_2O_5, 0.43% B_2O_3, 0.57% Al_2O_3 (mol%)). The 4 treatments; including a Ti6Al4V substrate subjected to a 5 M NaOH (95 ^oC/24 h) treatment, followed by 100 mM $CaCl_2$ (40 ^oC/24 h) treatment, before being subjected to heat treatment (600 ^oC/1 h) and hot water (80 ^oC/24 h) stages, all demonstrated globular HA formation at 1 d, with a continuous layer (similar to the

bioactive glass) *ca.* 11 μm after 28 d [228]. Further exemplifying the bioactive potential of chemical surface modifications.

In addition to Ca incorporation into titanate structures, other ions, which have been proven to promote bone growth, have also been investigated. Ions such as Mg^{2+} (Yamaguchi *et al.* [58]), Sr (Yamaguchi *et al.* [59]), and Zn (Yamaguchi *et al.* [229]) have all been successfully included in the Ca-titanate structure, generating Mg-, Sr-, and Zn-doped calcium titanate surfaces. By varying the mixture of solutions used within the ion exchange processes, or by replacing the water-treatment with ion-containing solutions, one can successfully incorporate additional ions into the titanate structure. Furthermore, this will allow elution into the surrounding environment, generating beneficial effects during bone remodelling. All of the ion incorporated calcium titanate layers were found to form apatite in SBF, and allow slow release of the ions into the surrounding aqueous environment (phosphate buffered saline; PBS) at concentrations of 0.43, 0.92, and 0.03 ppm for Mg, Sr, and Zn, respectively [58, 59, 229].

As well as bioactive ion incorporation into alkali titanate structures, antibacterial ions have also been considered to negate issues regarding implant infection rates. Additionally, it allows scope for generating ‘two-in-one biointerfaces’, whereby bioactive and antibacterial properties are combined in one surface [83]. One of the main antibacterial ions, which is widely prevalent in the literature, is silver (Ag) [230, 231]. During hip-replacement arthroplasties, infection remains as a significant issue, as outlined in *Chapter 1*. Conventional strategies employ topical or oral antibiotics, however, this approach does not prevent every infection [232, 233]. Furthermore, issues surrounding the formation of antibiotic-resistant bacteria requires alternative antibacterial methodologies in clinical settings [234]. Apatite and calcium phosphates

containing antibiotics have been suggested, however, their stability regarding HA layers, as outlined previously in *Section 1.1*, is insufficient for long term applications [235].

Studies by Inoue *et al.*, Lee *et al.*, and Kizuki *et al.* investigated the ion exchangeability of Ag^+ with Na^+ in the titanate structure [57, 236, 237]. The initial study by Inoue *et al.* described the formation of titanate nanotubes through 10 M NaOH treatment at 160 ^oC for 3 h, followed by heat treatment at 300 ^oC for 1 h. The nanotubes were submersed in 12 mL, 0.05 M silver acetate, generating nanostructured silver titanates with loaded silver nanoparticles (metallic colloids). The surfaces produced also generated an antibacterial effect that was proven to be due to Ag-ion elution, which due to its greater elution speed, would speculatively have greater and more rapid antibacterial effects than previously reported metallic silver against Multidrug Resistant *S. aureus* (MRSA) [236].

Kizuki *et al.* furthered the study by Inoue *et al.* in order to produce a silver titanate layer, on Ti and a Ti-15Zr-4Nb-4Ta alloy, without forming metal colloids on the surface, as well as understanding the effect on apatite-forming and bone-bonding abilities of the resultant products [57]. All samples experienced an $AgNO_3$ solution step at varying molarities (0.01-25 mM) following previous NaOH, $CaCl_2$ (optional), and heat- and water-treatments. A further recent study by Yamaguchi *et al.*, detailed a Sr and Ag-doped Ca-deficient titanate surface, through various wet chemical treatments, exhibited a release of 1.29 and 1.69 ppm of Sr and Ag, respectively over 14 days in FBS. This surface demonstrated an increase (*ca.* 10%) in cell (MC3T3-E1) viability after 3 d, whilst generating a 5.9-log reduction in *E. coli* activity, in comparison to untreated Ti substrates [238].

However, conflicting results surrounding silver, demonstrating both *in vitro* cytotoxicity of keratinocytes and fibroblasts in some studies [239, 240], whilst no cytotoxicity in some *in vivo* studies [239], have resulted in alternative antibacterial ions being considered [230]. Gallium (Ga) has been previously reported to be an ideal substitute for Ag in antibacterial settings, due to successful antibacterial studies [241, 242]. Its history in the field of medicine is expansive, having been notably used in chemotherapeutic drugs [243]. Its similarity to Fe(III) in ionic radius and charge, allows replacement within target molecules, which has resulted in an ideal antimicrobial agent, whose presence can cause Ga(III)-induced bacterial metabolic distress [241, 244]. Furthermore, inhibition of bone resorption through reduced Ca release from bone, makes it an ideal element for incorporation in orthopaedic devices [245]. Investigations into gallium titanate surfaces in a biomedical setting were not published until 2017. Yamaguchi *et al.* published an article describing a 'two-in-one' biointerface, whereby gallium ions were incorporated into calcium titanate structures [83]. This particular study followed the principle outlined by Cochis *et al.*, by doping gallium into the surface of titanium through electrodeposition [242]. Cochis *et al.* demonstrated that these surfaces are antibacterial against *Acinetobacter Baumannii* (MRAB12); a Multi Drug Resistant (MDR) nosocomial (originating in a hospital) pathogen, which is rapidly emerging in implant-related infections, with a higher efficacy compared to silver [246]. The study by Yamaguchi *et al.* demonstrated the successful incorporation of gallium into the calcium titanate structure through a mixture of $CaCl_2$ and $GaCl_3$, as well as purely $GaCl_3$ treatment (with additional water-treatments post-heat treatment), generating Ga-doped calcium titanate and gallium titanate surfaces, respectively. The proposed structures were intended to utilise Ga's antibacterial ability, as well as its inhibitory effect on bone resorption, to generate a

surface that not only disrupts bacteria, specifically *A. baumannii* due to its higher Ga susceptibility (2-100 μM [241]), but also increasing the bioactivity of the Ti surface; a surface combining two ideal biomaterial properties in one. Described in the study, Yamaguchi *et al.* demonstrated the ability for both Ga-containing calcium titanate and gallium titanate surfaces to kill *A. baumannii*, with Ga^{3+} release rates of 0.35 and 3.75 ppm, respectively, whilst also producing apatite in SBF. However, this study only focussed on *A. baumannii* as the bacterial pathogen in question, which is remarkably susceptible to Ga ions; 2-100 μM *vs.* 0.32-5.12 mM for *S. aureus* [241, 247]. The claim of antimicrobial resistance is somewhat speculative, since no other pathogen, or microbe, has been considered on such a surface. Hence, there is a significant gap in the literature, which requires additional testing of alternative pathogens, both Gram-negative and Gram-positive, in order to fully elucidate its antimicrobial efficacy. A summary of some of the potential cations that can be included in titanate structures, and their benefits, have been summarised in *Figure 2:19*.

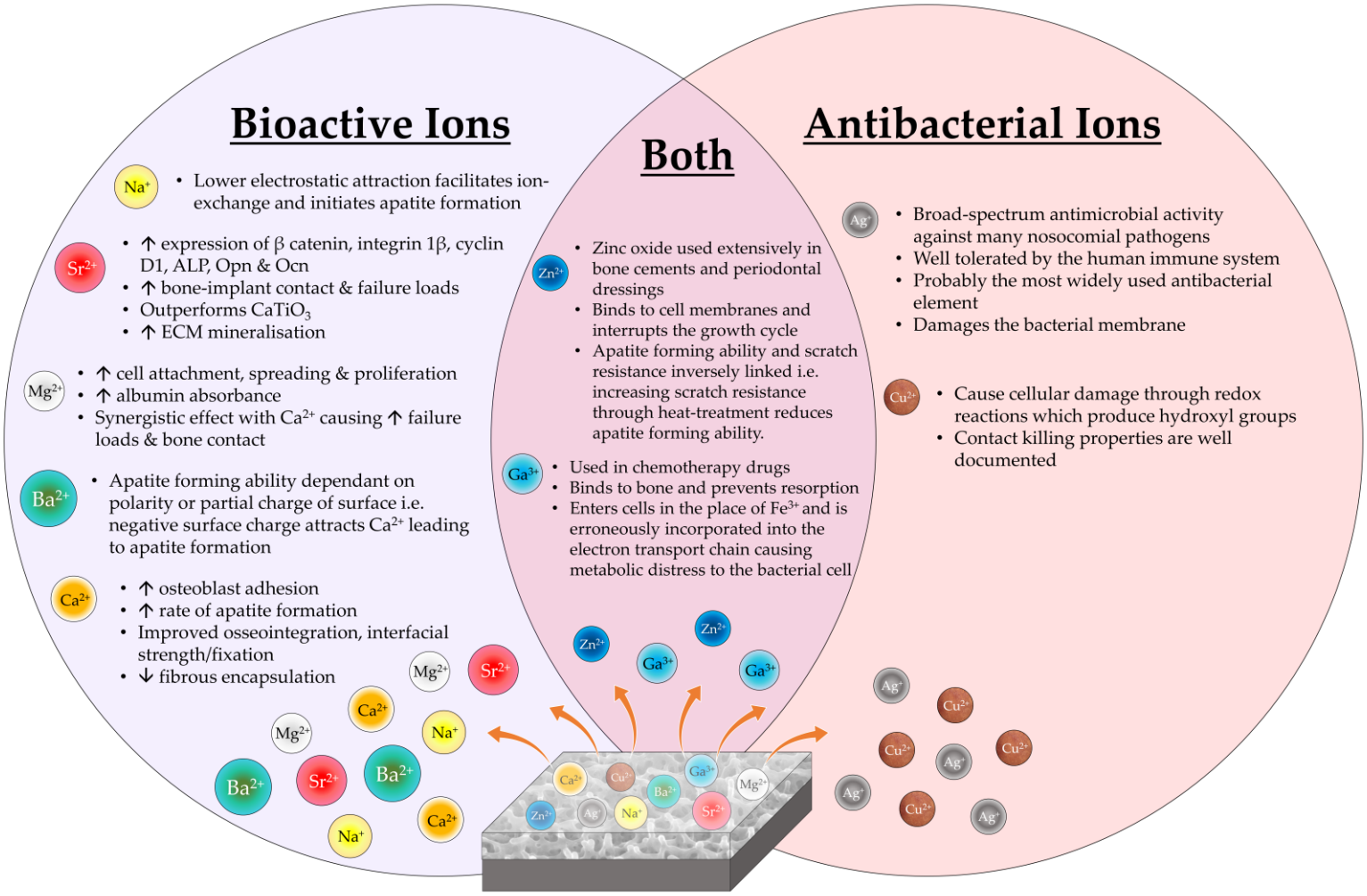

Figure 2:19. Bioactive and antibacterial effects of specific cations that have been incorporated into titanate structures for biomedical applications.

A recent paper by Janson *et al.* [248], has developed upon the idea of generating dual-functionality surfaces that incorporate titanate structures. This work, following on from previous work by Tengvall *et al.* [249], looked into the generation of a titanium-peroxy gel layer, whose composition was suggested by Tengvall *et al.*, to be:

$$[\mathrm{Ti}^{4+}(\mathrm{OH}^{-})_x\mathrm{O}_2^{2-}] - [\mathrm{Ti}^{4+}(\mathrm{OH}^{-})_y\mathrm{O}_2^{-}] - [\mathrm{Ti}^{4+}(\mathrm{OH}^{-})_4] - \mathrm{TiO}_2 \cdot n \cdot \mathrm{H}_2\mathrm{O}$$

where, through hydrogen peroxide (H_2O_2) treatment of titanium, generated bactericidal properties. By combining a hydrogen peroxide treatment, with subsequent sodium and calcium hydroxide treatments, these surfaces demonstrated bactericidal effects on *Staphylococcus epidermidis* through direct and biofilm inhibition tests, whilst ensuring bioactive and biocompatible surfaces to MC3T3 human dermal fibroblast cells [248].

Overall, although promising, these results are still preliminary, and in order to fully combat against a plethora of bacterial types (more akin to real-life scenarios), these surfaces need further systematic testing of different bacterial types and strains to confirm their 'antibacterial' status. Furthermore, *in vivo* trials would also need to be conducted to further confirm their biocompatible properties.

2.1.8 Pre-clinical animal trials and clinical applications of titanate surfaces

Prior to clinical trials, it is paramount to understand bone-bonding efficacy of such devices in animal *in vivo* models, in order to ascertain where any cytotoxic affects occur, as well as whether the initial *in vitro* assessments translate to *in vivo* scenarios. Yan *et al.* studied the effect of NaOH- and heat-treated Ti implants through implantation into rabbit tibiae, which were harvested 4, 8, and 16 weeks post-implantation [250]. At 16 weeks, the failure load of the alkali- and heat-treated implants, assessed using tensile tests of removed tibial segments, were 4.59 ± 1.76 kgf

(45.01 ± 17.3 N), compared to 1.38 ± 0.69 kgf (13.5 ± 6.77 N) for untreated-Ti, demonstrating a significant increase in bone-bonding, with no adverse tissue responses noted. Furthermore, there was no marked difference between alkali-treated samples and apatite-formed Ti samples (alkali-treated samples with subsequent 4-week submersion in SBF). Finally, there was good correlation between the *in vitro* studies conducted previously regarding apatite formation, with the *in vivo* studies conducted by Yan *et al.* [250]. A similar study by Fujibayashi *et al.* examining the effect of sodium removal on bone-bonding, exhibited corroboratory results [251].

Further studies by Nishiguchi *et al.* on alkali-treated Ti [252-255]; and Ti6Al4V, Ti-6Al-2Nb-Ta, and Ti-15Mo-5Zr-3Al alloys [254, 256], examined the implantation of such treated materials in the intramedullary canal of rabbit femora, rabbit tibiae, and dog femora. For the alkali-treated Ti metal inserted into rabbit femora and tibiae, it was clear that the tensile failure loads for alkali-treated Ti was significantly higher than that of untreated Ti (*Figure 2:20*) at 3 weeks (130.35 ± 122.75 N *vs.* 9.73 ± 11.01 N), 6 weeks (253.18 ± 141.30 N *vs.* 33.92 ± 24.26 N), and 12 weeks (411.74 ± 70.59 N *vs.* 72.17 ± 41.83 N) from rods inserted into intramedullary portion of femurs [252]; and 8 weeks (26.6 ± 14.4 *vs.* 0.20 ± 0.30 N), and 16 weeks (40.50 ± 12.30 *vs.* 4.80 ± 3.73 N) in the proximal metaphyses of tibiae [253]. It must be noted the large variation is due to the non-standard mechanical testing regime employed. Additionally, removal of the implants that had been alkali-treated resulted in detachment of bone from the surrounding area, exemplifying that the bone-implant interface exhibited stronger failure modes than the bulk bone surrounding the implant (*Figure 2:21*).

For the Ti alloys also investigated by Nishiguchi *et al.* through implantation in rabbit tibiae, similar bone-bonding properties were noted [254, 256]. Push out tests at

4 and 12 weeks confirmed that the alkali-treated Ti alloys performed significantly better than their untreated counterparts, as detailed in *Figure 2:22*.

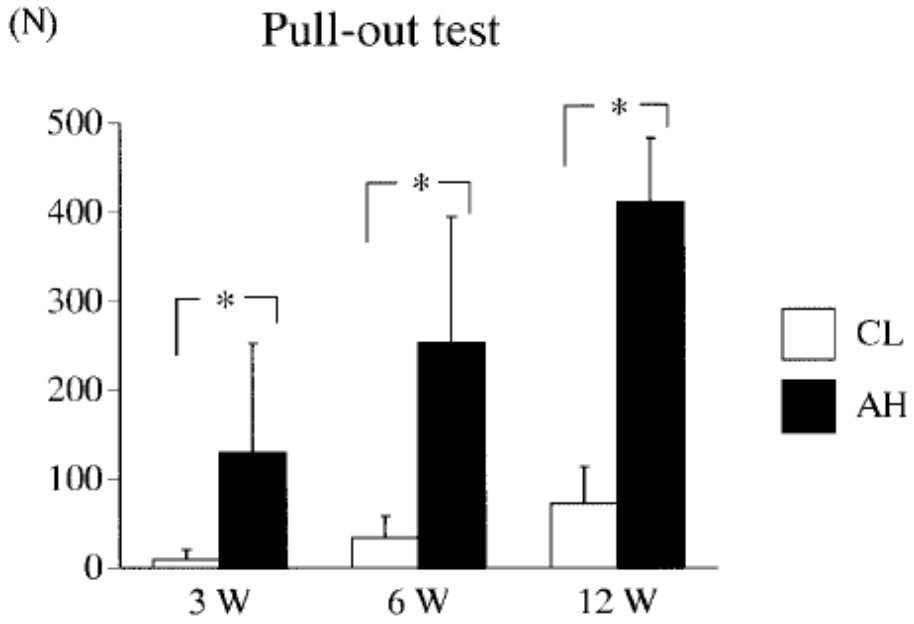

*Figure 2:20 Failure modes through pull-out tests of untreated (CL) and alkali- and heat-treated (AH) Ti rods, with the ordinate units being N. * = ($p < 0.05$). Figure taken from Nishiguchi et al.* [252].

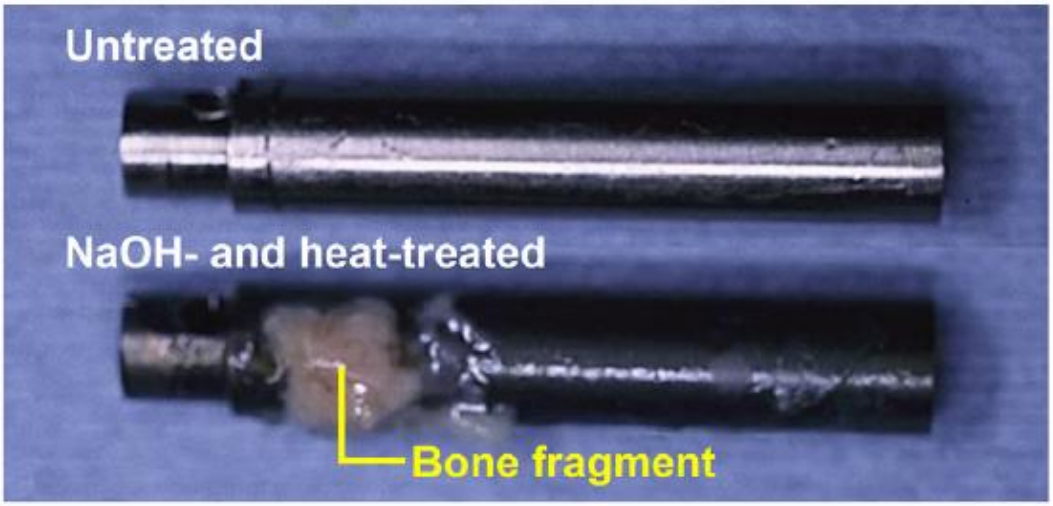

Figure 2:21 NaOH- and heat-treated and untreated Ti rods that had been implanted into the medullary canal of a rabbit femur. Explantation occurred 12 weeks following insertion, with clear bone residue left on the treated rod. Image adapted from Kokubo et al. [82, 257]

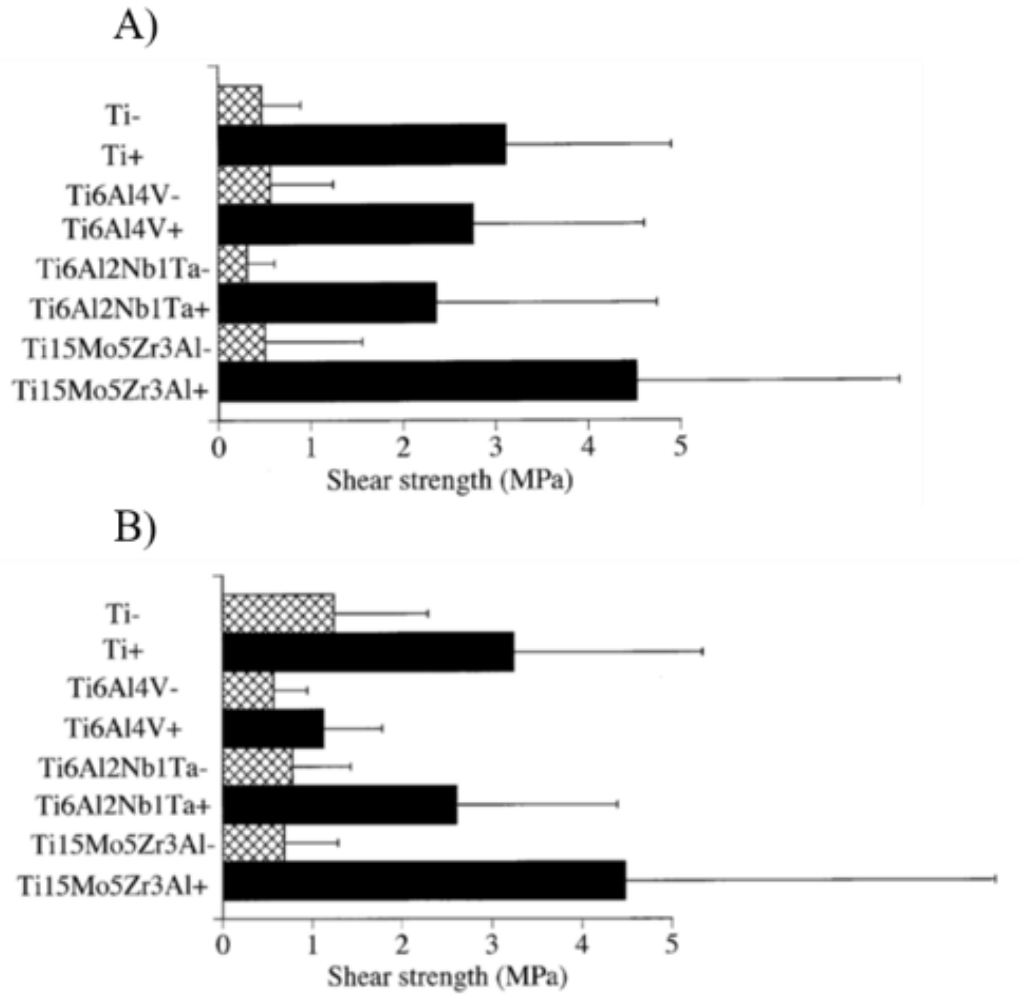

Figure 2:22 Push-out tests detailed at (A) 4 and (B) 12 weeks post-implantation. (-) = untreated. (+) = alkali- and heat-treated samples. Figure adapted from Nishiguchi et al. [254].

Again, as seen in *Figure 2:23*, the untreated samples exhibited complete spontaneous detachment within 8 and 16 weeks, with only minor failure loads noted by 24 weeks, whilst the alkali-treated samples exhibited superior failure loads due to enhanced bone-bonding. Furthermore, all alkali-treated alloys exhibited no fibrous tissue intervention at the interface between the bone and implants [256].

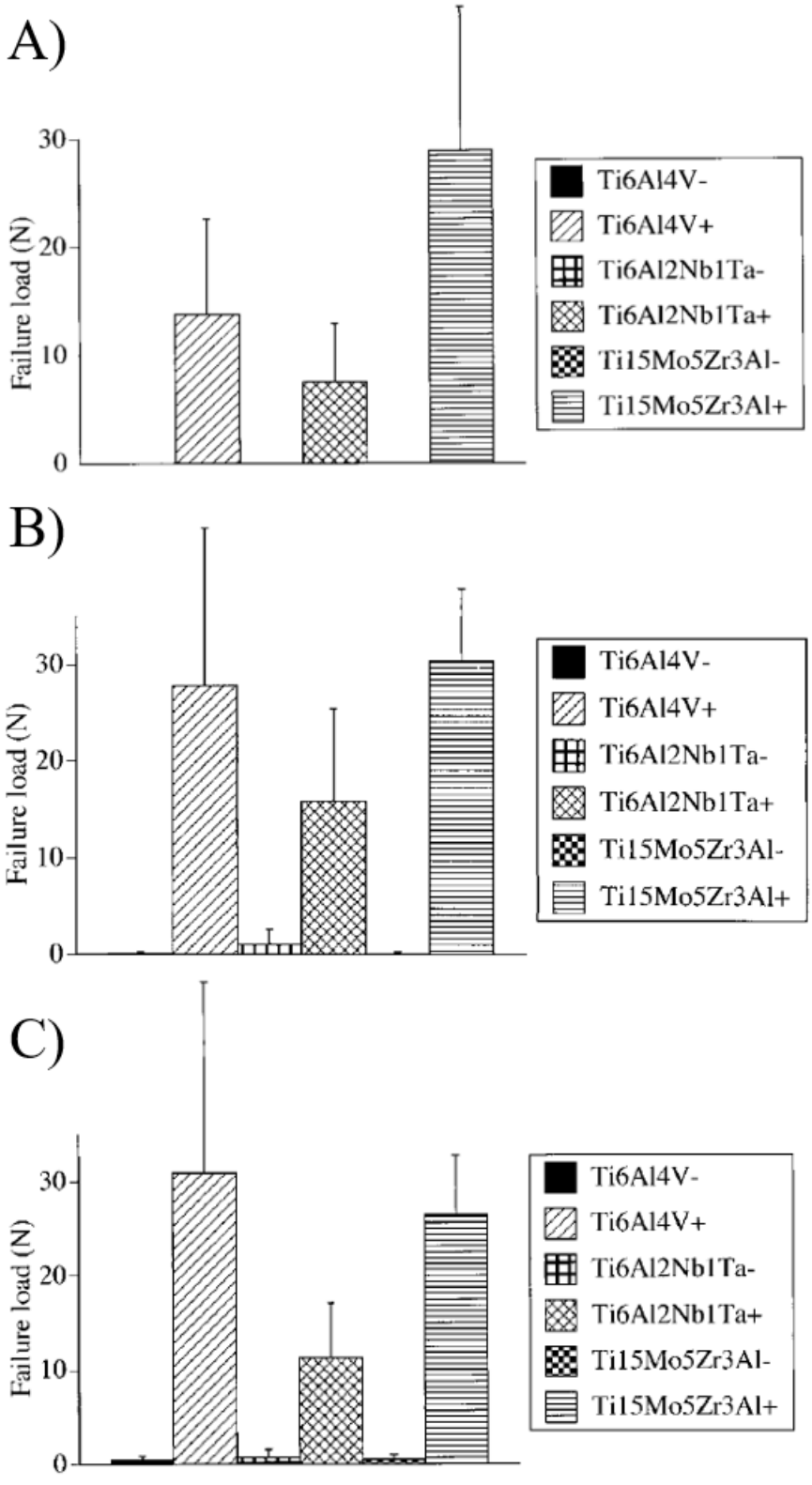

Figure 2:23 Detachment tests at A) 8, B) 16, and C) 24 weeks post-implantation for Ti6Al4V, Ti-6Al-2Nb-Ta, and Ti-15Mo-5Zr-3Al alloys. (-) = no treatment. (+) = alkali- and heat treatment. Error bars are S.D. Figures adapted from Nishiguchi et al. [256].

All studies presented confirmed the applicability for such devices through successful *in vivo* animal models, and therefore resulted in human clinical studies in Japan. To date, there have only been a small portion of studies regarding clinical deployment of alkali titanate surfaces on implant materials. Regarding total hip replacements, the alkali-treatment has been employed on a Ti-6Al-2Nb-Ta alloy, which formed part of the acetabular shell and femoral stem of a total artificial hip replacement (see *Chapter 1*, *Figure 1:6*). Implantation of 70 prostheses in 58 patients were performed at two different university hospitals between 2000 and 2002. Follow up of these uncemented hip replacements was conducted by Kawanabe *et al.*, who reported that none of the implants required revision during an average follow-up period of 57.5 months [258]. Furthermore, the average JOA score (Japanese Orthopaedic Association score: calculated from pain (/40), range of motion (/20), ability to walk (/20), ability to carry out daily activities (/20) [259]) improved from 46.9 for preoperative assessments, to 91.0 at the final follow-up; a significant increase. Furthermore, no observed osteolysis occurred in the 70 implanted hips. Unfortunately, 70% of the implants had a gap between the acetabular shell and the surrounding bone immediately after operation (*Figure 2:24*). However, no gaps were noted 6 years after operation, with all gaps closing within 12 months measured radiologically. Cumulatively, the results for Kawanabe *et al.* have demonstrated the efficacy of such a surface modification in a clinical setting, despite the short observation period [258]. The devices were made commercially available in 2007 [53].

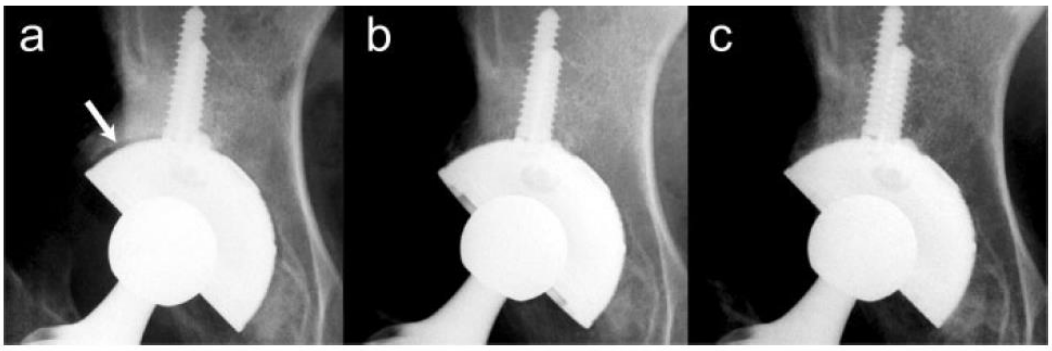

Figure 2:24 Radiographs of the acetabular cup of a 25 year old woman, located on her right hip A) 2 weeks, B) 12 months, and C) 6 years post-implantation. White arrow indicates 1.5 mm gap between acetabular component and socket. No gap evident in either B) or C). Image taken from Kawanabe et al. [258].

Corroboratory evidence of longer term survival rate (min. 8 years; average 10 years) was shown by So *et al.* [260]. In addition to similar assessments conducted by Kawanabe *et al.* [258], two retrieved implants were also investigated histologically. The overall survival rate was 98% at 10 years, with no radiographic signs of loosening. Bone was found histologically in the pores of the implant within the first 2 weeks due to retrieval of one of the implants, with deep bone bonding in the pores by 8 years from the other implant. Limitations do exist, however, as alternative studies on total hip arthroplasties have shown, as highlighted in *Table 2:7*, that the sample size and study length are inadequate to confirm alkali-treated implant superiority [260].

*Table 2:7 Review of selected articles studying the successfulness of cementless total hip arthroplasties. * indicates end point was set at revision, regardless of reason. † indicates end point was reoperation, regardless of reason. ^ indicates a Kaplan-Meier revision rate was calculated. Table adapted from So et al.* [260].

Author & Year	№ of total hips/lost hips	Average follow-up period (years; range)	Surface modifications	Survival rate (%)
Garcia-Cimbrelo *et al.* (2003) [261]	124/11	11.3 (10-13)	Grit-blasted	94.1*
Shetty *et al.* (2005) [262]	134/6	14.2 (13-15)	HA-coated	99*
de Witte *et al.* (2011) [263]	102/3	11.8 (10-17)	HA-coated	92.2*
Sariali *et al.* (2012) [264]	131/11	10 (8-11)	HA-coated	96.8*
Nourissat *et al.* (2012) [265]	90/7	9.2 (8-10.2)	HA-coated	94.2†
So *et al.* (2013) [260]	67/3	10 (8-12)	Plasma spray, alkali- and heat-treated	98*
Wittenberg *et al.* (2013) [266]	204 / 9	4.9 (2.9-7.1)	20 μm CaP coating	96.7^
Jameson *et al.* (2013) [267]	35,386 / 448	5 (no min. stated – max. 7.5)	HA-coated	97.6*
Mäkelä *et al.* (2014) [268]	Total Study (347899 / 16500) Cementless (71,454 / 3,539)	4.9 (0-17)	Large Nordic study on all hip replacement types	92.6* (10 years) 85.3* (15 years)
Noiseux *et al.* (2014) [269]	493 / 6	3.5 (2-10)	Porous tantalum acetabular components	98.8*
Hoskins *et al.* (2019) [270]	41,265 / 551	13 (N/A)	HA-coated	97.6*
National Joint Registry Annual Report (2019) [9]	410,296/38,568 (Data from Apr. 2003 and Dec. 2018)	15 (N/A)	All uncemented	90.6*

In addition to hip stems, spinal fusion cages have also been considered, however, the level of osteoinductivity from alkali-treated surfaces alone was lower than necessary for such a device; most spinal devices require an autograft (a tissue graft originating from the patient's body, and placed elsewhere on the same body) in order to induce bone growth. Therefore, a combinatory surface treatment was employed in

order to improve the osteoinduction (recruitment of immature bone cells and their stimulation [271]) and osteoconduction (growth of bone [271]) of such surfaces for spinal fusion devices. The combination of both alkali-treatments explained previously, in addition to the acid-treatments outlined in *Section 2.1.3*, was studied by various researchers. It was found previously by Uchida *et al.*, that the NaOH treatments subjected to water- and heat treatments formed a Na-free titanium oxide, which was also found to bond to living bone [272]. The premise for such a treatment is that the conversion from the sodium titanate gel into anatase should confer a more effective apatite-nucleating surface, due to compositional and structural studies conducted by Uchida *et al.* and Wei *et al.* [273-275]. Furthermore, Fujibayashi *et al.* discovered that such surfaces formed on 50% porous sintered Ti, also inherently bonded to bone *in vivo*, as well as Fujibayashi *et al.*, Takemoto *et al.*, Fukuda *et al.* and Tanaka *et al.*, confirming both osteoinductive [276-278] and osteoconductive [279] properties. Fujibayashi *et al.* initially demonstrated osteoinductivity through ectopic growth of bone after implantation into the dorsal muscle of mature beagle dogs [251, 276].

To improve the osteoinductivity further, the water-treatment was replaced with 0.5 mM HCl, as discussed by Takemoto *et al.*, since for porous structures, the water-treatments suggested could not remove all the sodium within complex 3D structures [277]. The suggested acid post-treatment effectively removed the sodium, even from deep pores in the structure. A comparison between water and acid post-treated samples was conducted through implantation into beagle dog muscles, with the new bone area fraction (bone growth in total pore area) and bone incidence (number of bone induced samples/number of implanted samples) measured [277]. It was found that at 3 months the bone area and incidence for water-treated samples was 0.5 ± 0.6% and 1/4, respectively, with acid-treated samples exhibited area and incidence values of 8.3 ±

2.5% and 4/4, respectively. The acid-treated samples exhibited significantly ($p < 0.05$) superior osteoinductivity at each time point (3, 6, and 12 months) [277].

Further studies by Pattanayak *et al.* have investigated alternate HCl concentrations to induce apatite formation, as well as differing heat treatment temperatures and acid types (HCl, H_2SO_4, or HNO_3); the optimal conditions were found to be 10-100 mM (40 ^oC, 24 h), 500-700 ^oC (1 h), irrespective of acid type [280-282]. Finally, Kokubo *et al.*, generated a titanium hydride layer (TiH_x; where $0 < x < 2$), on chemically treated Ti, which was also adsorbed with SO_4^{2-} and/or Cl^- ions. The solution used was a 1:1 ratio of HCl and H_2SO_4 [283]. The surface formed exhibited micrometre scale roughness, compared to the nanometre scale roughness exhibited by the sodium and calcium titanate surfaces (detailed in *Section 2.1.4* and *2.1.7*, respectively). Heat treatment of this surface generated rutile, with the SO_4^{2-} and/or Cl^- ions adsorbed, without morphological change. In addition, these surfaces formed apatite in SBF within 1 day.

Apatite formation occurred *via* a different mechanism to the described sodium titanate method. Initially, the adsorbed ions dissociated from the surface, generating an acidic environment, which caused the Ti—O bonds to become positively charged on the surface. This attracted the negative phosphate ions, which following their accumulation, caused the surface to become negatively charged. Subsequently, the positively charged calcium ions from solution were attracted to the surface, forming an amorphous calcium phosphate. Over time, this surface layer matured into crystalline apatite. Purely acid-treated Ti metal does not have a charge and, therefore, does not form apatite *in vitro*. Furthermore, the above-mentioned surface is not affected by humid environments; a significant issue of alkali-treated surfaces. *In vivo* studies of the Kokubo *et al.* method was conducted by Kawai *et al.*, whereby a porous

Ti metal subjected to acid- and heat treatments was implanted into a rabbit femur [284]. Significant bone ingress into the porous structure was observed within 3 weeks, in contrast to that of purely acid and purely heat-treated surfaces [284].

A canine model was set up by Takemoto *et al.* to establish the *in vivo* efficacy following the *in vitro* studies demonstrated previously [285]. Aimed as a lumbar interbody fusion device, the structure consisted of a porous titanium body, with 50% porosity and an average pore size of 300 μm. 5 devices were treated with 5 M NaOH (60 ^{o}C, 24 h), followed by 0.5 mM HCl (40 ^{o}C, 24 h), ultrapure water- (40 ^{o}C, 24 h), and heat treatments (600 ^{o}C, 1 h); 5 remained untreated. After 3 months, radiological evaluation showed all treated devices achieved interbody fusion, whilst only 3/5 of the untreated did (*Figure 2:25*). Furthermore, histomorphometric evidence demonstrated that the treated samples exhibited greater bone area ingrowth percentage: 16.7 ± 5.7 *vs.* 13.4 ± 5.9; as well as increased bone contact: 34.9 ± 7.4 *vs.* 10.5 ± 3.3. All other data which corroborated these results and are outlined in *Figure 2:26*.

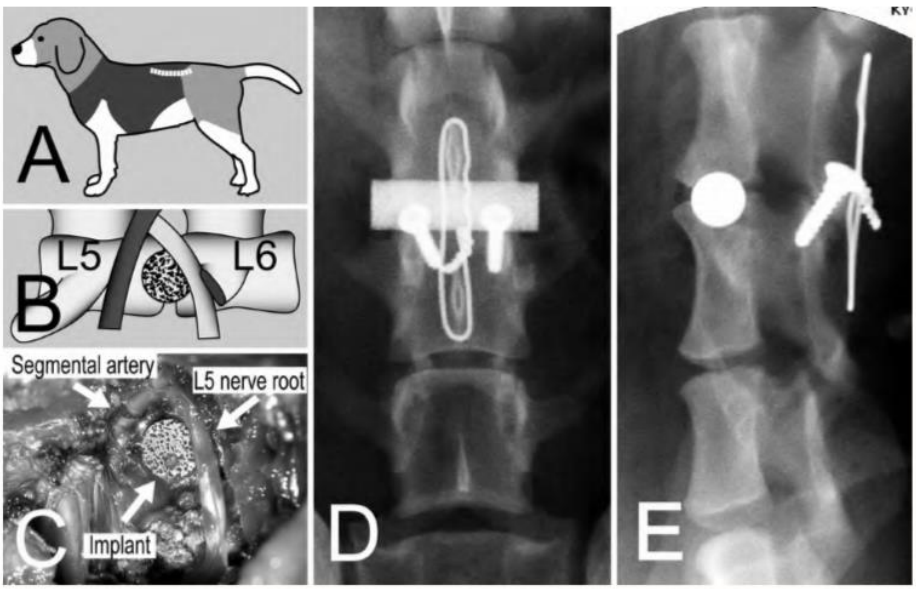

Figure 2:25 A) Location of surgical incision, B) Schematic illustration of implantation site with accompanied photograph C), D) Anteroposterior radiograph of surgical site post-implantation, and E) Lateral radiograph of same surgical area. Image taken from Takemoto et al. [285].

Following the success of the canine model, 5 spinal fusion devices were implanted into patients in Japan between 2008 and 2009 (*Figure 2:27*) [286]. Not only was bone union achieved in all of the patients, but also there was no need for autologous iliac crest bone grafting; an ideal advantage for such a device. Furthermore, all clinical results improved from pre- to post-operatively, with no adverse effects occurring during follow up. However, a further, larger, longer-term study is required to fully evaluate its efficacy [286].

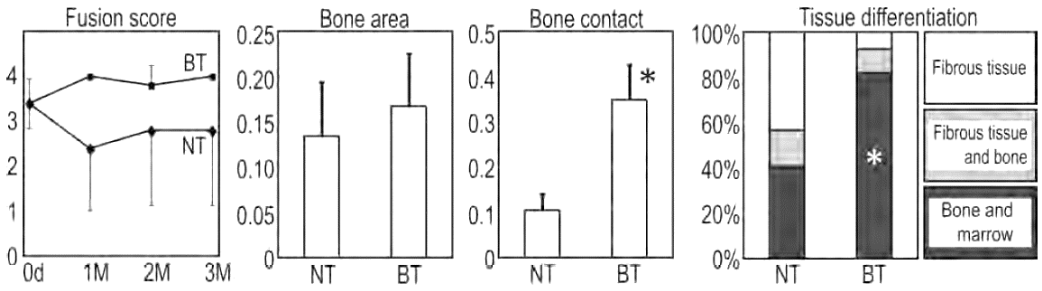

*Figure 2:26 Results of the radiological and histological evaluations. NT = Non-treated, BT = Treated. * $p<0.05$. Figure taken from Takemoto et al.* [285].

Despite their success *in vivo*, their application has been limited due to the lower shear strength (9.5 MPa [287]) exhibited through the surface layers. Therefore, such treatments cannot be conferred onto screws, since the layer can be removed during insertion [287]. Furthermore, issues regarding porous materials, such as leaching of ions in a confined volume rapidly altering the local pH, may result in adverse effects on living cell activity in small pores.

Figure 2:27 Photograph of the type of spinal fusion device used in the clinical trial. Image taken from Fujibayashi et al. [286].

Cumulatively, despite the advantageous properties of titanate structures for both bioactive and antibacterial properties, their applicability has been limited to Ti-containing substrates only. Furthermore, full elucidation of the antibacterial efficacy of such structures containing gallium need further investigation. Therefore, these research avenues will be described within this thesis.

2.2 Biodegradable metallic implants

Normally in biomedical materials, especially for metallic devices, there is a requirement for improved corrosion resistance when implanted *in vivo* [288]. However, in recent years, a special family of metallic materials are breaking this paradigm – biodegradable metals. These materials are defined by their ability to degrade *in vivo*, whilst also preventing adverse effects on cells or tissues surrounding the implant site, in addition to systemic effects [289]. Their prevalence is necessitated by the requirement for retrieval surgeries to remove fracture fixation devices, or other non-long-term devices, once their desired function has been achieved. For example, after fixation of a broken long bone with a fracture fixation plate, there is no need for the implant to remain once healed since stress shielding may offset bone remodelling. Therefore, the plate is removed, requiring additional surgical time and cost, as well as increased chance of morbidity and convalescence for the patient [71, 290].

Biodegradable metals, theoretically, can negate this issue by achieving their set function, and subsequently degrading *in vivo*, without causing adverse local or systemic effects.

Metals are preferred over degradable polymers and glasses, such as Bioglass® [67], calcium phosphate-based glasses [291], PLA [292], and PGA [293], since their mechanical properties are capable of dealing with the load bearing stresses present, whilst also combining the required bioactive properties. Another potential solution to combine the structural strength needed for load bearing applications, as well as the bioactive properties for improved integration, are biomedical composites. Through reinforcement of a matrix phase, the structural strength of the polymeric material can be improved. Also, careful choice of the reinforcement can enhance the bioactivity; inclusion of particulate HA, or other bioactive ceramic/glassy materials, is common [294]. However, issues persist with the lack of complete understanding of the behaviour of composites, particularly regarding anisotropy [295]. Furthermore, the sensitivity to sterilisation of polymeric composites, resulting in detrimental effects on mechanical properties, remains a substantial issue [295]. The above metals have significant advantages as biodegradable materials; however, improvements are still required to tailor the degradation rate, as well as improving their mechanical retention profile, making them more ideal for load-bearing applications.

2.2.1 Degradation mechanism

The main materials that have been extensively studied in this field are magnesium (Mg), iron (Fe), and their alloys, usually with additions of lithium (Li), calcium (Ca), zinc (Zn), tin (Sn) and manganese (Mn) [296]. Typically, the degradation model for biodegradable metals is a corrosion process, whereby electrochemical reactions occur within the surrounding aqueous environment, generating various degradation

products. The degradation of the metal (*M*) will occur through anodic processes, whilst reduction (cathodic) reactions occur simultaneously [289].

$$M \rightarrow M^{n+} + ne^{-} \text{ (anodic reaction)}$$

$$2H_2O + 2e^{-} \rightarrow H_2 + 2OH^{-} \text{ (cathodic reaction)}$$

$$2H_2O + 4e^{-} + O_2 \rightarrow 4OH^{-} \text{ (cathodic reaction)}$$

$$M^{n+} + nOH^{-} \rightarrow M(OH)_n \text{ (product formation)}$$

Ultimately, the metal will be converted into oxides or hydroxides depending on the environment, and the relative abundance of ions in the vicinity. Usually in physiological environments, there is an abundance of chloride (Cl^-) ions; the principal anion in extracellular fluid [297], which are aggressive against the protective oxide/hydroxide layer formed on the surface. In addition, proteins, amino acids, and lipids can attach to the metal surface altering the degradation rate. Great care and attention must be made to the material type used, and the degradation rate required, as well as the environment in which it will be situated; slight perturbations from the planned conditions may have drastic effects on the degradation rate, which is a significant issue regarding biodegradable devices.

2.2.2 Magnesium and its alloys

Mg and its alloys have been widely researched regarding automotive and aerospace applications [298], in addition to its prevalence as a biodegradable material; Witte detailed the extensive history of biomedical uses of Mg, however, such a history will not be explored in this review [299]. Pure Mg has been reported to be biologically safe, since it does not contain any known toxic alloying elements, such as Al, and rare earth elements [300, 301]. Furthermore, since it is one of the lightest metals [302], it exhibits a high stiffness-to-weight ratio (specific modulus: *ca.* $26 \times 10^6\ m^2s^{-2}$),

resulting in a Young's modulus, density, and compressive strength more akin to that of natural cortical bone (*Table 2:8*); stress shielding, therefore, would be minimised further. Additionally, regarding human metabolism, magnesium is essential, with it being the fourth most abundant cation in the body, and half of all physiological magnesium being found in bone tissue [303, 304]. Further to this, hyper-magnesium is rare due to the efficiency of excretion pathways through the urinary system [305].

Table 2:8 Mechanical properties of commonly used biomaterials in comparison to pure Mg, natural bone and synthetic HA. Data compiled from the following references [3, 18-27]. *Table adapted and improved upon from the one featured in Staiger et al.* [24]. *Majority of the data is also shown in Table 1:1.*

Properties	Natural bone	Magnesium	Ti alloy	Co-Cr alloy	Stainless steel	Synthetic HA
Density ($g.cm^{-3}$)	1.8-2.1	1.74-2.0	4.4-4.7	7.2-9.2	7.9-8.1	3.1
Elastic modulus (GPa)	3-20	41-45	105-117	200-240	189-210	73-117
Compressive yield strength (MPa)	130-180	65-100	758-1117	450-1000	170-310	600
Fracture toughness ($MPa.m^{1/2}$)	3-6	15-40	55-115	N/A	50-200	0.7

Despite its advantages regarding biomedical applications, significant drawbacks regarding Mg's degradation have necessitated additional modifications. One of the most noteworthy drawbacks is the low corrosion resistance, with it being one of the most reactive of all structural materials ($E^{\ominus}$ = -1.7 V_{nhe} in aqueous solutions [306]; NHE = Normal Hydrogen Electrode) [307], especially in physiological media (pH 7.4-7.6), whereby its mechanical integrity is lost prior to full tissue recovery. Furthermore, during the corrosion process, hydrogen gas is released [308] at a rate which is often too quick to be dealt with through normal physiological processes, hence, affecting cellular processes in the vicinity [24]. Therefore, significant modifications are needed

in order to tailor corrosion rates to that of normal wound healing for fracture fixation or other processes, such as stents for aortic aneurysms. There are two main routes by which magnesium can be improved for biomedical purposes:

1. Incorporation of alloying elements
2. Direct surface modification/coating production

Incorporation of alloying elements has been seen as an attractive solution. However, complex alloying compositions will result in excessive production costs, in addition to the difficulty in processing such alloys into the appropriate fabricated shape. Furthermore, as described previously, certain elements, which aid corrosion resistance, must be avoided since they can cause adverse effects *in vivo*. Surface modifications, however, have been considered a more efficient and effective way of controlling the degradation rate of magnesium. Wang *et al.* reviewed a significant amount of literature studies on surface modification of magnesium and its alloys, which have been presented in *Table 2:9* & *Table 2:10* [309].

The breadth of surface modifications investigated encompasses a whole variety of chemical and physical deposition methods, however, not one specific treatment is free of disadvantages. Furthermore, only a small subset of the technologies meet the requirements for *in vivo* biocompatibility and cytotoxicity, meaning a great deal of research is still needed. It was found that chemical modification demonstrated excellent bonding adhesion, however, porosity is a substantial issue, with delamination also a concern [309].

Table 2:9 Part I of a table taken from Wang et al. which details a review of surface modifications of magnesium and its alloys for biomedical applications [309]. *a = Eagle's minimum essential medium; b = Fetal bovine serum; EIS = Electrochemical Impedance Spectroscopy; PPC = Potentiodynamic Polarisation; MAO = Micro-Arc Oxidation.*

Alloy	Corrosive Media	Category	Surface modification	Pros.	Cons.	Performance indicators for corrosion resistance	Treated *vs.* untreated Mg corrosion values
AZ31	SBF	Chemical modification	90% (v/v) H_3PO_4	1. Removal of less passive films 2. Uniform compact layers + excellent adhesion 3. Simplicity	1. Porosity	1. Weight loss	9 *vs.* 22 mg/day
AZ91D	3.5% NaCl		2.5% H_2SO_4			1. EIS	10^3 *vs.* 40 Ω.cm^2
Cp-Mg	m-SBF		1 M NaOH	1. Similar composition and chemical structure with degradation products for newly formed layers 2. Simplicity	1. Porosity 2. Insufficient adhesion	1. pH	7.88 *vs.* 8.01 (ref. 7.38)
Mg-Ca	SBF		$NaHCO_3/Na_2HPO_4$ /Na_2CO_3 + HT			1. H_2 evolution 2. i_{corr} PPC	1. 0.017-0.027 *vs.* 0.111 mL/(cm^2.h) 2. 10^{-4} *vs.* 10^{-3} A/cm^2
AZ91D	3.5% NaCl		NH_4F	1. Homogeneous layer with better protection 2. Simplicity		1. EIS	8 x 10^3 *vs.* 40 Ω.cm^2
Cp-Mg	Hank's solution		HF			1. EIS 2. i_{corr} PPC	1. 5.2 x 10^3 *vs.* 0.18 x 10^3 Ω.cm^2 2. 10 *vs.* 400 μA/cm^2
Cp-Mg	SBF		Anodizing coating MAO	1. More protective outer layers 2. Controllable	1. Porosity	1. i_{corr} PPC 2. E_{corr} PPC	1. 1.73 x 10^{-7} *vs.* 1.35 x 10^{-5} A/cm^2 2. -1.69 *vs.* -1.85 V
Mg-Ca	Hank's solution		Anodizing coating MAO			1. H_2 evolution	0.007-0.108 *vs.* 1.694 mL/(cm^2.day)
Cp-Mg	E-MEM[a] + FBS[b]		Anodizing coating (electrochemical)			1. Weight loss	0.13-0.21 mg/(mm^2.day) *vs.* Null
AZ91HP	5% NaCl		e-beam treatment	1. High efficiency	1. Expensive 2. Limited corrosion improvement	1. Weight loss	0.3 *vs.* 0.75 g/(cm^2.h)
AZ91	SBF		Ion implantation (Ti)	2. Sufficient candidates with a controlled conc. 3. Little effect on the bulk alloy characteristics	1. Expensive 2. Unknown mechanisms	1. EIS	1154 *vs.* 103 Ω.cm^2

Table 2:10. Part II of a table taken from Wang et al. which details a review of surface modifications of magnesium and its alloys for biomedical applications [309]. *EIS = Electrochemical Impedance Spectroscopy; PPC = Potentiodynamic Polarisation; MAO = Micro-Arc Oxidation; DCPD = Dicyclopentadiene; TCP = Tri-Calcium Phosphate; PLLA = Polylactic Acid; PLGA = Polylactic Glycolic Acid*

Alloy	Corrosive Media	Category	Surface modification	Pros.	Cons.	Performance indicators for corrosion resistance	Treated *vs.* untreated Mg corrosion values
AZ series	3.5% NaCl	Physical modification	HA coating	1. HA akin to bone 2. Low solubility and high thermal stability	1. Low adhesion	1. i_{corr} PPC	10^{-6} *vs.* 10^{-3} A/cm^2
Mg-Zn-Ca	SBF		FHA coating				2.51 *vs.* 126.89 μA/cm^2
AZ91D	SBF		DCPD and β-TCP				3.65 x 10^{-5} *vs.* 2.97 x 10^{-4} A/cm^2
Mg-6Zn	0.9% NaCl		PLGA coating	1. Less cracks	1. Few candidates 2. Insufficient adhesion	1. Weight loss 2. i_{corr} PPC	1. (2.44-5.61) x 10^{-4} *vs.* 0.063 mg/(cm^2.h) 2. 0.085-0.097 *vs.* 26.5 μA/cm^2
AZ91	SBF		PCL coating			1. Weight loss 2. Mg corrosion conc.	1. 0.06-0.10 *vs.* 0.28 mg/(cm^2.d) 2. 238.6-433.4 *vs.* 1360 ppm
AZ31D	SBF		HA-Chitosan coating			1. i_{corr} PPC	5.097 x 10^{-5} *vs.* 3.893 x 10^{-4} A/cm^2
Mg-2Zn	SBF		TiO_2 implantation	1. Easy manufacturing	1. Insufficient adhesion 2. Non-degradable	1. E_{corr} PPC 2. H_2 evolution	1. -1.5 *vs.* -1.8 V 2. 1.95 *vs.* 4.13 mm/y
Cp-Mg	Hank's solution		CeO_2 implantation (hydrothermal)			1. i_{corr} PPC	4.0 *vs.* 430 μA/cm^2
AZ91C	3.5% NaCl		Laser surface processing	1. Homogeneous microstructure 2. Precision of dimensional control	1. Unexplained mechanism 2. Higher investment	1. Corrosion rate 2. i_{corr} PPC 3. EIS	1. 151.5 *vs.* 414.3 mpy 2. 0.1707 *vs.* 1.211 mA 3. 99.09 *vs.* 0.0931 mΩ.cm^2
AZ31	Hank's solution	Combined	90% (v/v) H_3PO_4/poly(DTH carbonate) + PLA coating	1. Above all	1. Difficult of operation	1. Corrosion rate	1. 5.6 *vs.* 31 mg/day 2. 3.5 *vs.* 31 mg/day
WE42	Hank's solution		MAO and PLLA			1. EIS	1.4 x 10^5 *vs.* 1500 Ω.cm^2
Mg-Zn-Ca	SBF		MAO and n-HA			1. i_{corr} PPC	2.4 x 10^{-7} *vs.* 3.36 x 10^{-4} A/cm^2

Physical methods, on the other hand, demonstrated coating detachment issues, as well as non-degradable products being another concern [309]. A key surface modification is the submersion in alkaline solutions; similar to that of the alkaline surface treatment mentioned in *Section 2.1.4.* This technique has been investigated extensively, due to its simplicity and effectiveness for biomaterials. Li *et al.* demonstrated that alkaline treatment for 24 h, followed by 500 ^{o}C heat treatment exhibited no mass loss in either SBF solutions containing or omitting Cl^- ions over 14 days [310]. Furthermore, the pH alterations exhibited were more gradual for the alkaline-heat-treated samples, with no inhibitory effects on marrow cell growth, or noted cellular lysis. Additionally, Al-Abdullat *et al.* detailed that pure Mg treated with $NaHCO_3$ exhibited good corrosion resistance (mass loss experiment in *Figure 2:28*) in Hank's Balanced Salt Solution (HBSS) at 25 ^{o}C up to 75 days compared to other solution treatments [311]. The ability for magnesium to exhibit such properties following very similar processing requirements to generate titanate structures necessitates investigations into whether titanate structures are possible on Ti-coated magnesium substrates.

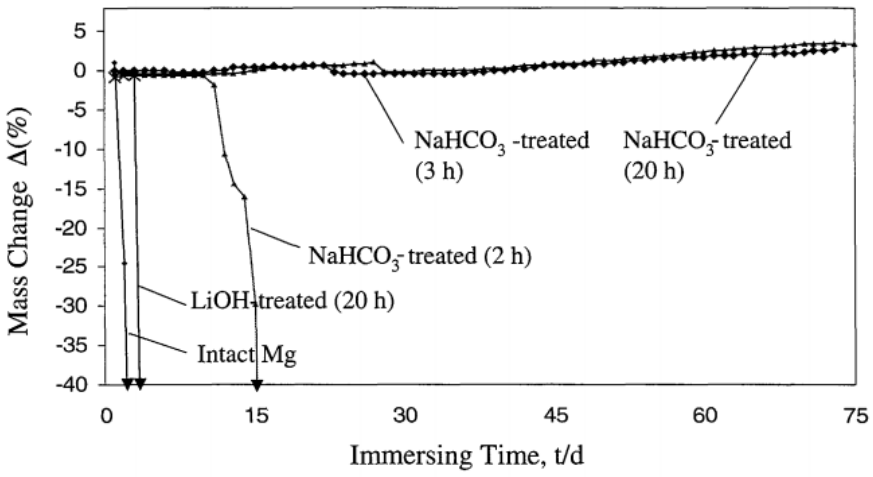

Figure 2:28 Change in mass (Δ%) of Mg in HBSS at 25 ^{o}C. Figure taken from Al-Abdullat et al. [311].

2.3 Physical vapour deposition of thin films by magnetron sputtering

As described previously (S*ection 2.1.2*), plasma spraying remains one the primary techniques for depositing orthopaedic coatings, however, their inherent disadvantages require alternative technologies to employ novel coating methodologies. One of the main alternative processes, which has gathered a large amount of interest in recent years, also reviewed by Yang *et al.* (*Table 2:3*; [118]), is magnetron sputtering (processing information found in *Section 3.2*). The process itself allows great flexibility regarding the target materials, as well as the final substrate condition. If an alloy, metallic oxide/nitride or other conformation are used as the target material, then similar films are able to be produced through choosing the appropriate target material and parameters. This is due to sputtering ionising the target constituents, and condensing them to form a film. Additionally, altering the sputtering atmosphere, and adding reactive gasses such as oxygen, will allow the formation of more exotic surface compositions, as well as blends of different surface layers.

At the target surface, the process of sputtering is not predictable at an atomic scale, since the emittance of atoms from the surface is largely dependent on multiple energy exchanges between the bombarding argon atoms and the target material. Other gases such as xenon can be used, which in turn alters momentum transfer. These occur until sufficient energy is transferred to overcome electrostatic attraction, whereby the atom is then released from the target surface [312]. Ultimately, sputtering is a very complex physical process, which is difficult to predictively model due to the number of different parameters employed, such as gas type, vacuum pressure, atomic binding energies and weights, as well as sputtering distance. The yield is simply defined as the ratio of sputtered atoms to the number of incident energetic ions [313, 314]. For mono-elemental targets, it is relatively simple to qualitatively predict the sputtering yield,

which is ideal for pure Ti used in this thesis. However, when non-elemental targets are used, the complexity increases. Theoretical work predicted preferential sputtering will occur for lighter elements within a target, which agrees with a number of actual systems [315]. Practically, the ejection of particles is somewhat disrupted due to the surface penetration of the bombarding atoms, with this process being complicated further due to multiple different atom types with varying atomic masses. For the processes outlined in this thesis, the sputtering mechanism should be relatively simple, due to the use of only pure Ti targets [312].

2.3.1 Sputtering and utilisation of pure Ti thin films

Utilisation of Ti thin films, and their chemical and structural characteristics, have been examined since the early 1990s, with Iida and Ogawa *et al.* providing initial studies in 1990 and 1991, respectively [316, 317]. Ti thin films present ideal properties, such as high strength (0.65-0.8 GPa [318]), and excellent thermal and structural stability. However, generation of such films through DC magnetron sputtering can result in a body-centred cubic (BCC) titanium phase, rather than the bulk hexagonal closed packing (HCP) phase of titanium, as concluded by Kong *et al.* [319]. Due to sputtered particles having kinetic energies on the order of 5-50 eV [320], the presence of electrostatic charges, and specific target locations reaching temperatures in excess of 850 ^{o}C despite water cooling, the propensity to form abnormal structures, such as BCC, is increased. Several studies have been conducted in order to negate formation of a BCC Ti phase during sputtering, with varying levels of success.

Table 2:11 compiles all literature references, to the best of the author's knowledge, of sputtering pure titanium thin films utilising DC magnetron sputtering. As observed, there is no consistent pattern regarding quoted sputtering variables, in addition to an

extremely broad selection of research fields encompassed in the compilation. Kong *et al.* studied the effect of crystal structure of 500 nm Ti films, through sputtering and evaporation, onto liquid nitrogen cooled copper foil substrates, and demonstrated the formation of BCC and HCP phases through sputtering and evaporation, respectively [319].

In the field of thermal insulation, low-*e* multilayers have been used broadly in architectural glass for thermal insulation properties, with Ti thin films being deposited as a sacrificial layer between dielectric and silver (Ag) layers. Godfroid *et al.* investigated these 0.5-32.5 nm sacrificial Ti layers through differing deposition rates (0.02 and 0.05 $nm.s^{-1}$) to understand the growth modes present on SnO_2 substrates. They concluded that at lower deposition rates (0.02 $nm.s^{-1}$) a Volmer-Weber mode was present, however, a pseudo Frank-van der Merwe mode manifested at higher rates (0.05 $nm.s^{-1}$) [321]. Growth modes for sputtered films include Volmer-Weber, Frank-van der Merwe, and Stransky-Krastanov. The Volmer-Weber model is where nucleation of the film occurs through formation of discrete 3D nuclei. Nuclei will then grow in size until a continuous film forms. Frank-van der Merwe exhibits monolayer island deposition, whereby the islands grow to form a continuous film. Finally, the Stansky-Krastanov model is a combination of the two previous models [312]. A pictorial representation of all models described is given in *Figure 2:29*.

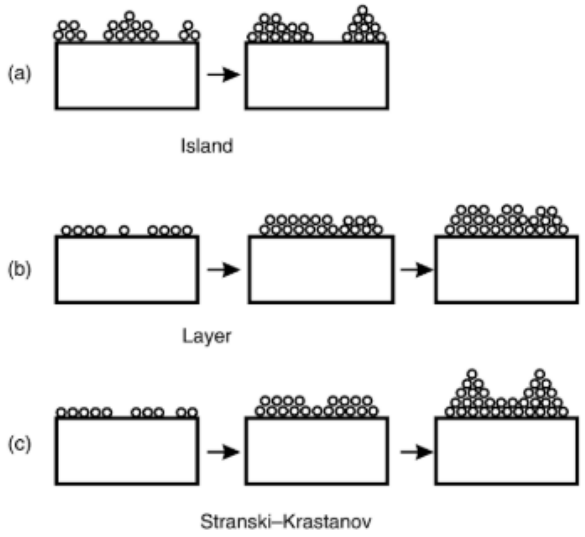

Figure 2:29 A) Volmer-Weber, B) Frank-van der Merwe, and C) Stransky-Krastanov models of thin film growth. Image taken from Sree Hashra [312].

Ti thin films have also been extensively used in Micro-Electro-Mechanical System (MEMS) devices, such as in bolometers (electrical equipment for measuring radiant energy) and low thermal conductivity electrical connectors in infrared sensors [322-324]. Tsuchiya *et al.* researched the generation of low internal stress Ti thin films, using controlled argon (Ar) gas flow and a multiple deposition process for use in MEMS devices. For 0.5 μm Ti films, the internal stress could be reduced to 0 by using 53 sccm (square cubic cm per minute) of Ar, with additional parameters outlined in *Table 2:11*. However, for 1 μm thick films, an additional cooling down (10 min) and reverse sputter process using RF power (50 W) was required, in between two 0.5 μm sputtering runs, to remove internal stresses as gas flow had become an independent quantity. These parameters allowed a low (< 35 MPa) internal stress within the 1 μm thick film, and achieved average Young's moduli, yield strains and tensile strengths of 90-100 GPa, 0.5%, and 0.65-0.8 GPa, respectively [318]. The values presented in this compilation have ultimately steered the chosen parameters for sputtering thin Ti films used in this investigation, however, it is evident that there is no strict consensus on appropriate sputtering parameters for Ti films.

*Table 2:11 Compilation of literature studies detailing conventional DC magnetron sputtering of pure Ti thin films only. All studies regarding Ti-doped films or combinatory films/multilayers have been omitted for clarity. RF denotes the plasma was generated through assistance of an RF power source. *Approximate calculated power density from voltage and current values given. ^No target size/power density given.*

Power Density / Wcm^{-2}	**Current / A**	**Voltage / V**	**Sputtering (Ar) Pressure / mTorr**	**Base Vacuum Pressure / mTorr**	**Duration / min**	**Target-Substrate Distance / mm**	**Film Thickness / nm**	**Substrate Bias? / V**	***In Situ* Heating? / ºC**	**Reference & Year**
4.7-9.7*	3-5	400-500	1.5-3.0	3.75×10^{-3}	-	-	500	✕	✕	1992 [319]
1.9-2.2	1	330-380	0.8-8.3	5×10^{-5}	20-30	80	1000	✓ (0 to -300)	✕	1993 [325]
^	-	-	20	-	-	-	60-2000	✓ (-10 to -200)	✕	1996 [326]
^	0.5	-	3.0	3×10^{-2}	-	70	1000	✕	✕	2003 [327]
2.1*	0.05	350	5.0	9.75×10^{-2}	11-27	-	0.5 - 32.5	✕	✕	2003 [321]
8.9*	2	350	6.0	-	10	48	3000-5000	✕	✓ (400)	2004 [328]
^	4	-	-	-	-	-	500-1000	✕	✕	2005 [318]
6.8	-	-	3.8	-	120	-	1000	✕	✕	2005 [329]
1.7-3.4	-	-	8.3-24.8	$(3\text{-}10) \times 10^{-3}$	-	100	72 - 138	✕	✕	2006 [330]
2.5-7.4	-	-	5-20	2×10^{-3}	Kept constant	50	3000-5000	✕	✕	2009 [331]
1.3-3.8			12.8	-	4	110	97-259	✕	✕	2009 [332]
2.2 (RF)	-	-	2.3-15	5×10^{-3}	Varied to achieve 400 nm	65	400	✕	✕	2009 [333]
4.6	-	-	0.005	-	30	-	486	✕	✕	2013 [334]
15.3	-	-	1.1-11.3	3.8×10^{-5}	90-200	220	50-400	✕	✕	2015 [335]
2.5-12.3	-	-	3.8	6.6×10^{-4}	11.4-26.9	80	1000	✕	✕	2015 [336]
10	4	375	6	-	90	120	2000	✓ (-65)	✕	2016 [337]
7.4	-	-	1.0	4.5×10^{-3}	50-60	80	450-550	✕	✕	2017 [338]
7.6	-	-	22.5	3.0×10^{-3}	20	40	450	✕	✕	2019 [339]
(150W)^	-	-	2.3	2.3×10^{-3}	100	120	550	✓ (-70)	✓ (<450)	2019 [340]

2.3.2 Key concepts for thin film sputtering and subsequent chemical conversion

In order to achieve the appropriate sputtered film, with required crystal orientation and composition, multiple parameters need to be considered. (1) Mean free path, during the sublimation of target atoms from the target surface, to impingement on the substrate, the atoms have to navigate an overabundance of free argon atoms in the space between the target and the substrate. A proportion of the ejected atoms interact with the free argon atoms, causing backscattering effects, meaning the number of atoms reaching the surface of the substrate is reduced. This phenomenon needs to be considered regarding the processing pressure used, since more argon atoms will result in higher bombardment, whilst reducing the mean free path of the ejected atoms.

(2) Temperature of the gas close (*ca.* 5 mm) to the target will also have an effect, with higher temperatures, generated from higher sputtering powers, resulting in a greater mean free path. This can be quantified using the equation below [341]:

$$\lambda = \frac{k_B \cdot T}{\sqrt{2} \cdot \pi \cdot p \cdot d^2}$$

With k_B = Boltzmann's constant (1.38×10^{-23} JK^{-1}), T = temperature (K), p = gas pressure (Pa), d = atomic diameter (m). Similar to the table detailed by Stuart [342], the mean free path of argon atoms ($d = 3.84 \times 10^{-10}$ m [343]) is compiled in *Table 2:12*.

Table 2:12 Mean free path (m) of argon atoms at various pressures and temperatures demonstrating their effect.

Temperature (ºC)	1 mTorr / 0.13 Pa	2.5 mTorr / 0.33 Pa	5 mTorr / 0.67 Pa	10 mTorr / 1.33 Pa
0	4.4×10^{-2}	1.7×10^{-2}	0.9×10^{-2}	0.4×10^{-2}
100	6.0×10^{-2}	2.4×10^{-2}	1.2×10^{-2}	0.6×10^{-2}
200	7.7×10^{-2}	3.0×10^{-2}	1.5×10^{-2}	0.7×10^{-2}
300	9.3×10^{-2}	3.7×10^{-2}	1.8×10^{-2}	0.9×10^{-2}
400	1.1×10^{-1}	4.3×10^{-2}	2.1×10^{-2}	1.1×10^{-2}
500	1.3×10^{-1}	4.9×10^{-2}	2.4×10^{-2}	1.2×10^{-2}

(3) Deposition temperature, which will affect the crystal structure and grain growth of the film deposited on the substrate, such as the effect on grain orientation described by Sonoda *et al.* (*Table 2:11*) [328]. Furthermore, it is essential that the crystal structure and grain growth formed is conducive to titanate formation following chemical treatments. If the conditions for deposition result in deposition temperatures around 0.2-0.3 T_m (melt temperature), it will normally result in columnar growth (fibre-like microstructure), whereby *"the average grain size in the plane of the film, d_i, is smaller than the average grain size perpendicular to the plane of the film, d_p"* (*Figure 2:30A*) [344]. However, if $d_i \approx d_p$, an equiaxed grain structure will be produced (*Figure 2:30B*). However, with regard to sputtering systems, an additional impact energy results, thus, the temperature can be lower than evaporation systems, whilst achieving a similar microstructure [345]. A great deal of consideration must be made regarding which type of growth is required, since it will affect the corrosion properties of such a coating. For example, columnar growth usually exhibits porosities which will allow aqueous penetration, therefore, increasing the degradation rate [346].

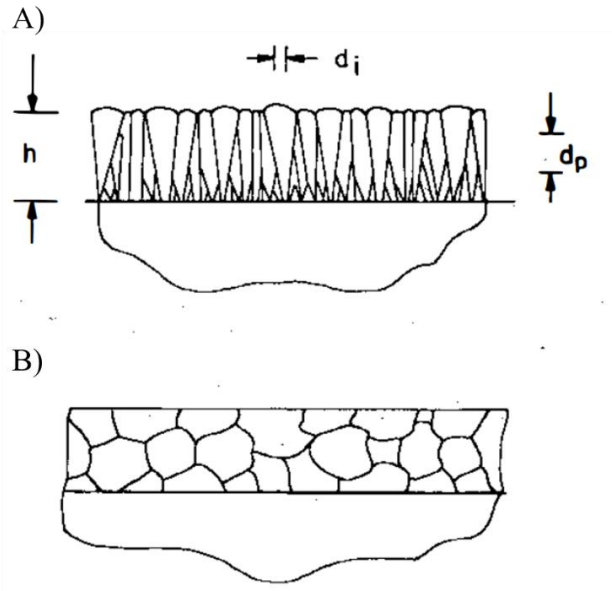

Figure 2:30 A) Columnar growth vs. B) Equiaxed growth of sputtering thin film grains, with d_i being the average grain size in the plane of the film, whilst d_p is the average grain size perpendicular to the plane of the film. Image taken from Thompson [344].

(4) Substrate biasing. The application of a substrate bias, whereby a voltage (usually around – 50 to 200 V) is applied to the substrate in order to direct some of the positive ions within the plasma toward the substrate, is a useful technique to control the structural and mechanical properties of a sputtered film; similar to the effects of deposition temperature. The process works simply through ion bombardment, similar to what is exhibited at the target surface, although to a lesser extent due to the lower voltage employed. The bombarding ions increase the surface energy of the film, enabling atomic reordering and improved properties, such as step coverage; controlled film growth; as well as the elimination of defects, such as microcracks. Despite these advantages, careful optimisation is needed, since applying an excessive bias will result in re-sputtering of the deposited layer, therefore reducing film thickness and increasing the required sputtering time [347].

2.4 Summary

This review has highlighted the importance of chemical solution treatments for titanium and titanium alloy implants in order to improve their biocompatibility and

antimicrobial properties. Many other techniques have been assessed, with chemical processing routes being regarded as the simpler, more efficient method of choice. Since 1996, titanate layers have been investigated for enhanced tailorability for medical device surfaces, which have been sufficiently researched to warrant *in vivo* human trials to have been conducted and implemented in Japan. However, to date, these structures are limited to Ti-containing materials, limiting their applicability. Furthermore, antibacterial surfaces have been investigated with silver and gallium, however, the extensiveness of such a study to warrant 'antimicrobial' properties is insufficient, and hence, additional studies are required.

Additionally, degradable metals, specifically magnesium, have been reviewed as an ideal biodegradable material, to negate retrieval of fracture fixation devices post-bone healing. However, the issues regarding its corrosion rate and local environmental effects have been outlined. Common treatments to improve the corrosion rate of magnesium, as well as improve its biocompatibility have been delineated, with chemical alkali-treatments being described as the more convenient method for such materials. Integration between titanate structures and improving magnesium corrosion and biocompatibility have yet to be tested in the literature. Finally, magnetron sputtering of thin Ti films have also been reviewed, with very broad processing parameters being noted. The sputtering parameters must be carefully chosen in order to fully control the sputtered films produced, and their applicability for titanate growth.

As detailed in the aims and objectives in *Section 1.4*, gallium titanate surfaces will be assessed to compare their efficacy against *S. aureus* on titanium surfaces. Also, the propensity for titanate structures to form onto alternative substrates, (e.g. 316L SS), through chemical conversion of sputtered Ti thin films will be studied. Furthermore, investigations into ion exchange possibilities, and alteration of the corrosion rate for

bulk magnesium for biodegradable medical applications, will be conducted. Ultimately, further understanding will be gained of the growth mechanism through thickness and oxygen content investigations.

Chapter 3. Materials and Methodology

This chapter details the materials and processing parameters used in order to generate titanate structures, and their ion exchanged counterparts, on both bulk (Cp-Ti) and Ti-coated substrates (316L SS and Mg; applied *via* magnetron sputtering), as well as Ti6Al4V and TiO_2 microspheres. *Section 3.1* outlines the preparation of both the 2D (discs) and 3D (microsphere) structures used as substrates within the studies presented. It also covers the materials parameters utilised during the DC magnetron sputtering process for generating thin Ti films onto various substrates (*Section 3.2*). Furthermore, the procedure utilised to generate titanate structures, as well as further ion exchange reactions and additional heat treatment stages are discussed in (*Section 3.3*). Finally, an in-depth section regarding the materials characterisation used within this report (*Section 3.4*), as well as the underlying principles behind each technique, are described.

3.1 2D and 3D Substrate Preparation

3.1.1 Disc preparation

3.1.1.1 Commercially Pure Titanium (Cp-Ti)

Commercially pure Ti (Grade 1) discs (10 mm diameter, 1 mm thick; >99.9% purity; Smith Metals Ltd., Nottingham), were punched out from a 200 × 200 × 1 mm sheet using a standard fly-press. Discs were ground and polished using abrasive silicon carbide (SiC; Metprep) paper, with sequentially higher grit: P240, P400, P800, P1200, P2500, & P4000, followed by colloidal silica polishing (*ca.* 0.06 μm particle size; Buehler) on MD-Chem (Struers) polishing pads. The discs were then cleaned ultrasonically in acetone (99.8% purity, Honeywell), followed by Industrial Methylated Spirit (IMS, purity 99.9%, Sigma-Aldrich) for 10 min each, and subsequently air dried (*Figure 3:1A*).

3.1.1.2 316L Stainless Steel (SS)

316L stainless steel (SS) discs (10 mm diameter; 1 mm thick; >99.9% purity; Smiths Metals Ltd., Nottingham), were punched out from a 500 × 250 × 1 mm sheet using a standard fly-press, before being polished as outlined in *Section 3.1.1.1* (*Figure 3:1B*).

Additionally, roughened samples were also generated for adhesion testing. The polished 316L SS discs outlined above were sandblasted with 120P alumina sand particles (Saftigrit White), utilising an air pressure of *ca.* 7×10^5 Pa, at a distance of *ca*. 50 mm. Discs were then ultrasonically cleaned in Acetone, IMS and deionised water (dH_2O) for 15 min apiece (as outlined previously), before drying with compressed air in order to remove any excess debris (*Figure 3:1C*).

3.1.1.3 Commercially Pure Magnesium (Cp-Mg)

A standard fly press was used to punch Mg discs (10 mm diameter; 1 mm thickness; purity: 99.9%; tempered as rolled; Advent Metals, Eynsham) from an Mg sheet. No further processing of the discs was conducted, except compressed air and bias cleaning (described in *Section 3.2.1*), due to the reactivity of the substrate (*Figure 3:1D*).

3.1.1.4 Fused Silica for SEM Cross-Sectional Observations

Polished fused silica discs (provided by Dr. Bryan Stuart; 1 mm thick; 10 mm diameter) were utilised for surface and cross-sectional SEM observations, in order to measure coating thicknesses (*Figure 3:1E*). After depositing the Ti coating (*Section 3.2.1*), the discs were scratched on the back using a diamond tipped scribe and shattered to reveal the cross-section. The shattered fragments were mounted onto a modified SEM stub using carbon tape, with the cross-section mounted orthogonal to the stubs' base. Additional Al tape (RS Components, UK) was used to secure the fragments in place, and to minimise potential charging effects. All stubs were then

carbon coated using a Quorum Q150T compact turbomolecular-pumped carbon coater, to achieve a coating thickness of *ca.* 10 nm.

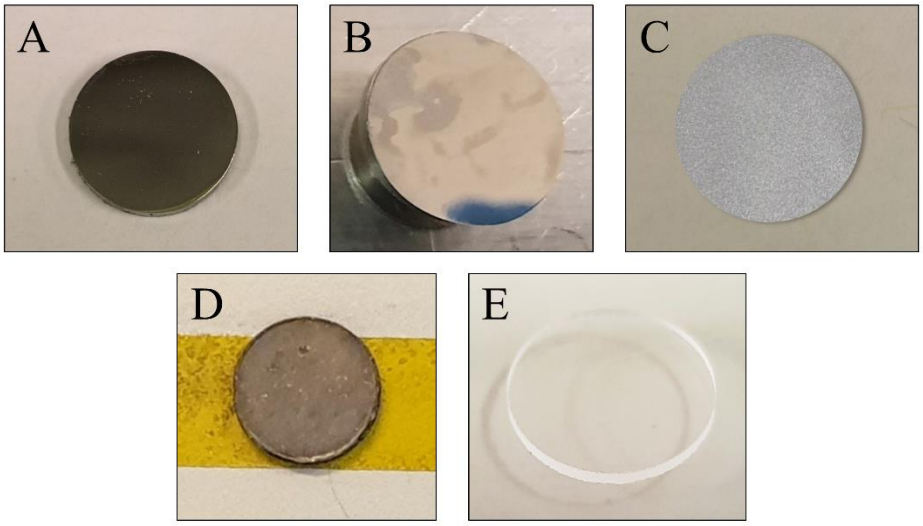

Figure 3:1. Optical images of 2D substrates used within this thesis. A) Polished commercially pure titanium (Cp-Ti); B) Polished 316L stainless steel (316L SS); C) Sandblasted 316L SS; D) Commercially Pure magnesium (Cp-Mg); E) Polished fused silica. All discs are ca. 10 mm in diameter.

3.1.2 3D Structures

3.1.2.1 Ti6Al4V and TiO_2 Microspheres

Plasma atomised Ti6Al4V Grade 23 powder (LPW Technologies, UK), was utilised for the oxygen-dependency study (*Figure 3:2A*). The powder was provided by Dr. Nesma T. Aboulkhair (Additive Manufacturing and 3D Printing Research Group, University of Nottingham), with the D_{10}, D_{50}, and D_{90} values, calculated *via* a Mastersizer 3000 (Malvern, UK) laser diffraction method, of 19.6, 31.5 and 49.1 μm, respectively [348].

The TiO_2 microspheres (both anatase and rutile counterparts) were produced by Dr. Towhidul Islam (Advanced Materials Research Group, University of Nottingham). Granular (<150 μm) particles were prepared by mixing TiO_2 (<5 μm; ≥99%, Sigma Aldrich, UK; Both Anatase and Rutile powder used separately) and 2% polyvinyl alcohol (PVA; ≥99%, Sigma Aldrich, UK) solution. The mixture was then processed utilising a flame spheroidisation process to prepare solid microspheres, which utilised

an oxy/acetylene flame spray gun (MK 74, Metallisation Ltd, UK) (*Figure 3:2B* & *C*) [349].

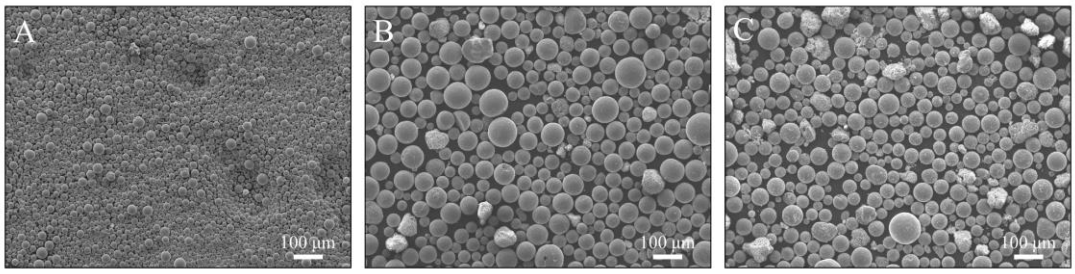

Figure 3:2. Micrographs of microspheres utilised within this thesis. A) Ti6Al4V microspheres produced via atomisation; B) TiO_2 microspheres produced from anatase powder via flame spheroidisation; C) TiO_2 microspheres produced from rutile powder via flame spheroidisation.

3.2 DC Magnetron Sputtering

In order to transfer and sputter neutral atoms from a target material, there is a requirement for ion bombardment to occur on the target surface, causing a momentum transfer process [350]. Usually, an inert gas (argon; Ar), or in the case of reactive sputtering a reactive gas (oxygen; O), is ionised whilst constrained between a potential difference from an oscillating or static electric field. This generates a plasma; the glow discharge associated with gas ionisation [347]. The ionised atoms are then propelled towards the negative cathode, which is set up to be the target material. Upon collision with the target material, atoms are ejected due to momentum transfer, with sufficient kinetic energy to negate the target-substrate separation, allowing the coating to condense. Formation of the potential difference can occur through radio frequency (RF) current, direct current (DC) or pulsed DC methods, with the type of electric potential used being dependent on target material and the requirements on the formed coating. A schematic representation the DC sputtering system utilised within this study is detailed in *Figure 3:3*.

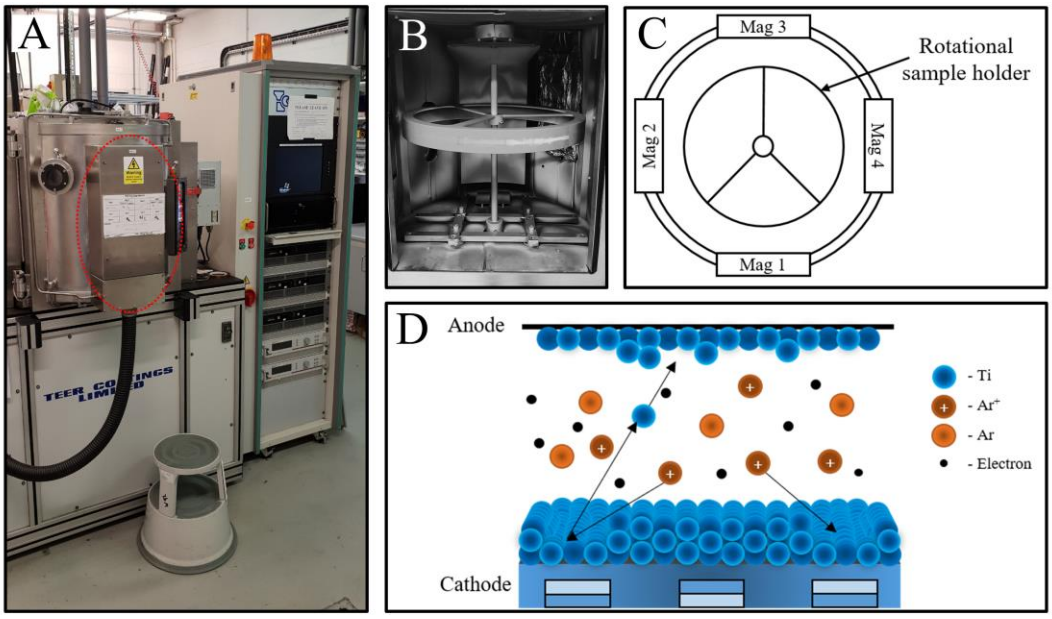

Figure 3:3 A) Image of the TEER UDP 650 Magnetron Sputtering Rig utilised within this thesis. Red circle illustrates Mag 1. B) Plane view from Mag 1 of the vacuum chamber with a rotational sample holder. C) Top-down schematic representation of the TEER rig, demonstrating the orthogonal magnetron set up. D) Representation of the sputtering process through the generation of Ar^+ and e^- within the plasma through application of a potential difference between the cathode and anode. The in situ heater is located on the chamber wall between Mag 3 and 4, and can be seen in the top right of (B).

One of the core principles in magnetron sputtering is the combination of both electric and magnetic fields to increase the ionisation efficiency. This is achieved through electrons being constrained within a set portion of the target. The constrained area is dictated by the magnetic field strength, magnet placement, electron momentum, as well as other variables. Free electrons and ions experience the Lorentz force due to the applied magnetic field (**B**) acting perpendicular to the applied electric field (**E**). The lighter electrons experience an **E**x**B** drift, as detailed in *Figure 3:4A*.

Through constraining these electrons, the deposition rate of a magnetron sputtering system can be increased by a factor of ten due to confinement of the plasma. The racetrack area where the electron density is highest means a higher density plasma is confined, and ultimately results in inhomogeneous material removal (*Figure 3:4B*). The extent of the Lorentz force (F) imparted on the electrons is given by Lorentz's law (equation below).

$$\mathbf{F} = q\big(\mathbf{E} + (\mathbf{v} \times \mathbf{B})\big) = q\mathbf{E} + q(\mathbf{v} \times \mathbf{B})$$

Where q is the charge of the electron (Coulomb: C), moving at an instantaneous velocity **v** (m/s), under the influence of an electric field **E** (N/C, or V/m), and a magnetic field **B** (Tesla: T) [351].

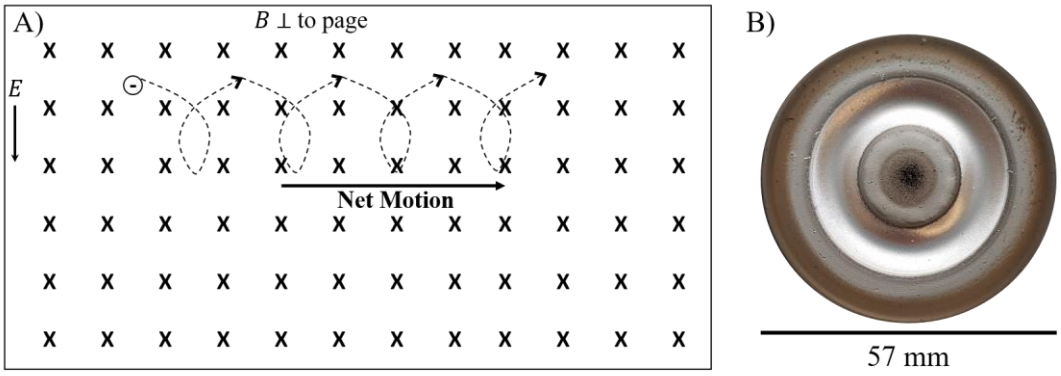

*Figure 3:4 A) **E**x**B** drift schematically shown in a combined electric and magnetic field in a perpendicular conformation. The electron path curves due to the effect of both fields. B) 'Racetrack' formed on a representative circular metallic target through routine sputtering processes.*

3.2.1 TEER UDP-650 Operation

A TEER UDP-650 type 2 unbalanced magnetron sputtering rig was used (*Figure 3:3*), which is a fully automated industrial scale rig, containing 4 orthogonal planar cathode targets, with a rotational sample holder, enabling 360º sample rotation and coverage. A commercially pure (Cp) chemical grade 1, solid Ti target (> 99.6% purity; 175 × 380 × 10 mm, Teer Coatings Ltd.) was utilised for all magnetron sputtered Ti coatings, mounted into magnetron position Nº 1 (herein labelled Mag 1; *Figure 3:3*).

All substrates were fixed to the rotating sample holder using double-sided polyimide Kapton tape, with samples mounted at a set substrate to target distance (55 ± 1 mm) and were rotated at 5 RPM. Initially, the chamber was pumped down using consecutive rotary and diffusion pumping stages to a base vacuum of $< 1 \times 10^{-5}$ Torr, before introducing Ar gas (purity 99.999%; Pureshield BOC©) at a rate of 20 standard cubic cm/min (sccm). Prior to deposition, all samples were bias cleaned using a pulsed

DC bias at a pulse width of 250 kHz, a step time of 500 ns, and a bias voltage of -100 V for 15 min. Various processing parameters were varied to induce structural difference in the Ti films produced. However, target power density was maintained at *ca.* 2.38 Wcm^{-2} (*ca.* 5 A, -300 V) to minimise sputtering times. Two parameters that were varied during the sputtering process; i) the applied bias to the substrates (either 0 or -100 V) and ii) substrate temperature, which was controlled using a mounted heater (located between Mag 3 and 4; *Figure 3:3*) within the vacuum chamber, it was either off (recorded substrate temperature <100 ^{o}C solely due to energy transfer *via* ion bombardment) or operated at a heater temperature of 150 or 300 ^{o}C; the temperatures were measured using an externally mounted controller, whilst separate substrate temperatures were measured using temperature strips (RS Components, UK) mounted to the rotational sample holder. The main processing parameters and matching sample codes, which were utilised following the initial optimisation process, are shown in *Table 3:1*.

Table 3:1. Coating parameters used for deposition of Ti films (ca. 4 µm thickness) with varying degrees of density/porosity. Sample codes are explained as follows: NB/NH = no bias and no applied heating; B/NH = -100 V bias and no applied heating; B/150 = -100 V bias and 150 ^{o}C heating; B/300= -100 V bias and 300 ^{o}C heating.

Sample Code	Target Current / A	Substrate Bias / V	Applied Substrate Heating / ^{o}C	Coating Time / min	Calculated Sputtering Rate / nm min^{-1}
NB/NH	5	0	0	263	14.8 ± 0.11
B/NH	5	-100	0	278	14.0 ± 0.12
B/150	5	-100	150	278	13.3 ± 0.15
B/300	5	-100	300	278	13.2 ± 0.08

3.2.1.1 Heater Temperature Analysis

It was noted during the preliminary trials that the heater within the rig, both through the generation of a 'recipe' (a predetermined sequence of sputtering stages to provide automated operation), as well as manual running of the rig, resulted in ramping of the

heater control rather than the actual heater temperature. This caused the heater to be turned on at the 'set' temperature, causing an overshoot of the heater temperature before reducing to the original set point value. Due to this, a simple temperature-monitoring test (described below) was conducted to ensure the overshoot was negligible in the overall coating runs, and whether further steps were needed to mitigate this.

The temperature of the rig was monitored from the external display, with the temperature recorded every second from 1 to 20 s, and subsequent temperature measurements being taken every 5 s until the temperature was stable (*ca.* 295 s). It was clear from the data (*Figure 3:5*), and from temperature strip measurements (*Section 5.2.2.1, Figure 5:11*) also conducted, that the temperature of the substrates did not exceed the set temperature of the heater, and therefore its effect was negligible on the produced films.

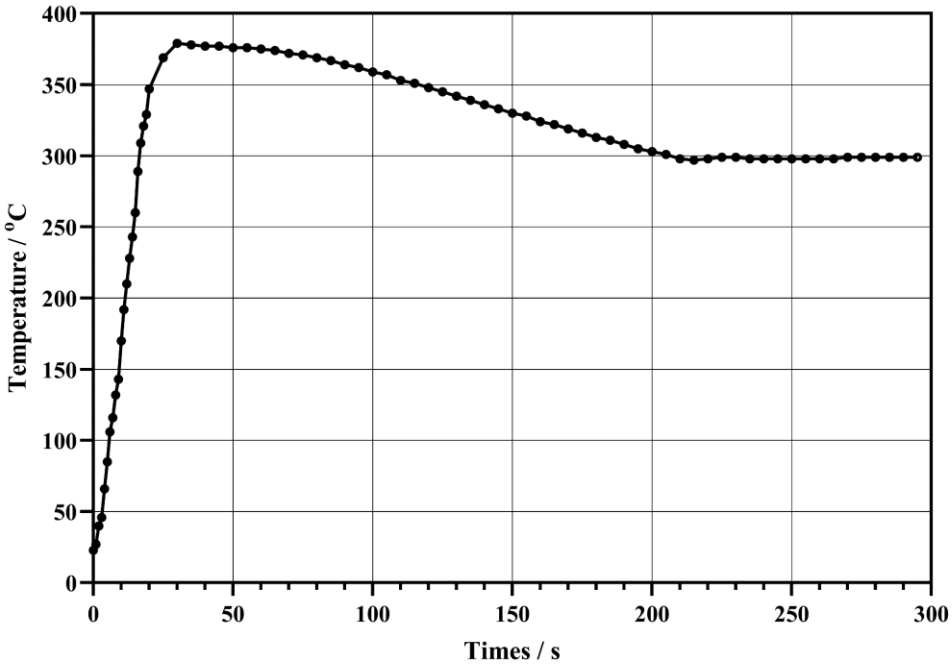

Figure 3:5. Temperature analysis of the 'overshoot' phenomenon exhibited by the internal heater utilised within the TEER UDP 650 rig.

3.3 Alkali Titanate Production

3.3.1 Sodium hydroxide treatment

A *ca.* 5 M (pH > 13.5) NaOH solution was prepared using NaOH pellets (*ca.* 19.99 g per 100 mL of distilled water; 99.9% purity; Sigma-Aldrich). 10 mL aliquots were then dispensed into polypropylene containers, with either individual discs or 5 g of microspheres immersed in each. These were then sealed and heated in a low temperature furnace at 60 ± 2 °C for 24 h (*Figure 3:6*). Upon removal (microspheres were removed *via* filtration), samples were washed in deionised water for 60 s, before compressed air drying (conventional, non-compressed, air-drying was utilised for microspheres) followed by storage within a desiccator until testing. The sodium hydroxide treatment was conducted on both Cp-Ti discs, the microsphere trial, as well as DC magnetron sputtered Ti coatings on 316L SS and Cp-Mg substrates.

3.3.2 Ion exchange treatments

3.3.2.1 Gallium

Gallium ion exchange reactions were conducted following the sodium hydroxide treatment outlined in *Section 3.3.1*, using a 4 mM (1 g/L) solution of $Ga(NO_3)_3$. The solution was prepared by dissolving 0.1 g of $Ga(NO_3)_3 \cdot xH_2O$ granules (x = 1–9) (purity: 99.9%, Sigma-Aldrich) into 100 mL of water. 10 mL aliquots in polypropylene containers were heated at 60 °C in a low temperature furnace for 24 h (*Figure 3:6*).

3.3.2.2 Calcium

Calcium ion-exhange reactions were carried out following the sodium hydroxide treatment outlined in *Section 3.3.1*. 10 mM $Ca(OH)_2$ solution was prepared by dissolving 74 mg of $Ca(OH)_2$ into 100 mL of distilled H_2O. Again 10 mL aliquots were used to submerge the now NaOH-treated substrates in polypropylene containers and heated to 60 ^oC for 24 h (*Figure 3:6*). Discs were then removed from the polypropylene containers and rinsed for 10 seconds in deionised H_2O and then dried in a desiccator.

3.3.3 Heat treatments

Both Cp-Ti and gallium titanate treated (*Section 3.3.2.1*) discs were heat-treated using a Lenton® furnace in air with a ramp rate of 5 °C min^{-1} to 700 °C. All samples were left to dwell for 1 h, followed by natural furnace cooling to room temperature (*Figure 3:6*).

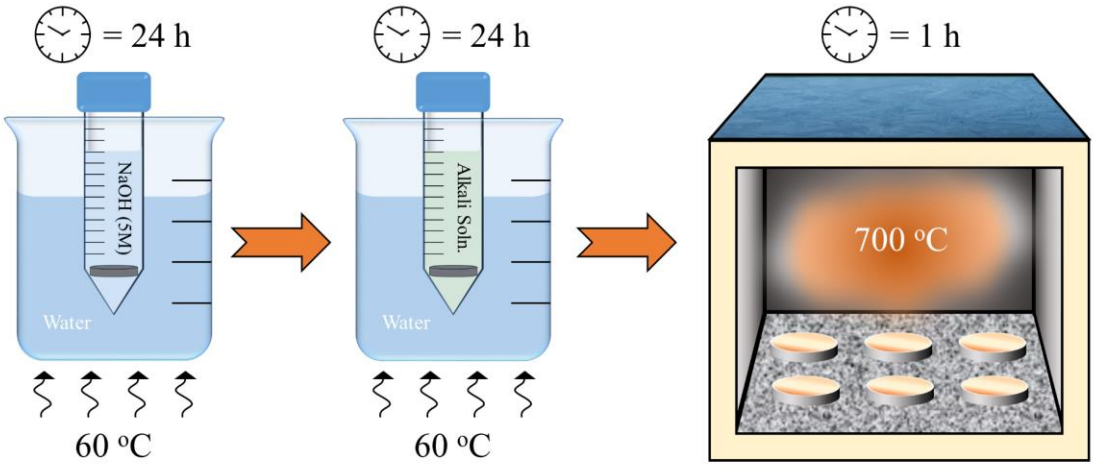

Figure 3:6. Typical titanate formation methodology onto 2D surfaces, including chronological cationic exchange and heat treatment stages. For microsphere conversion, the disc would be replaced with a suspension of the microspheres within the aqueous solutions; heat treatments were not conducted on the microspheres.

3.4 Materials characterisation

3.4.1 Ellipsometry

Theory

Ellipsometry is a spectroscopic technique that analyses discrete changes in its polarisation during the reflection on or transmission though a material. Due to this, ellipsometry has been utilised widely for thickness determination of thin transparent coatings, providing the film being measured is thin enough for appropriate transmission and subsequent detection; appropriate detection is material dependent, however, for Ti films sputtered onto specialised substrates (SiO_2-coated Si single crystals) the detection limit was *ca.* 150 nm. Plane polarised light, whereby the polarisation is perpendicular to its direction, incidents the substrate, resulting in elliptical polarisation. Elliptical polarisation is defined as the wave being polarised in directions other than perpendicular to its travel, which if viewed along its path of travel appears elliptical. The ellipsometer detects this change in polarisation, which through calculation of the refractive index, and subsequent model fitting enables film thickness calculation [352].

Sample Preparation and Working Parameters

The samples were analysed on a JA Woollam M-2000 SI spectroscopic ellipsometer using focus probes. Samples consisted of Si wafers coated with 326 nm of SiO_2, which were provided by Dr. Chris Mellor. Samples whose thickness was too large to be quantified *via* ellipsometry (*ca.* 150 nm estimated from data within this thesis) were analysed using cross-sectional SEM measurements. On each 10 × 10 mm square sample, a 3 × 3 grid of data was taken for each data point spaced from the next by 2 mm. By delineating sputtered thin film thickness, the coating thickness can be accurately predicted for better understanding of titanate formation and corrosion resistance. The model used to fit the data consisted of multiple Lorentzian oscillators. For most of the samples, the wavelength range was limited to the IR and visible spectrum, as UV had no thickness information in it. Where automated fitting was not possible due to the thickness of the film, manual fitting was employed. The term manual fit is used to describe manual adjustment of parameter values from the initial model to produce a reasonable fit 'by eye', since automated fitting, whereby algorithms adjust the parameters and calculate covariances between these parameters etc., cannot be achieved; no uncertainty values can be calculated from manually fitted models due to this.

3.4.2 Scanning electron microscopy (SEM) & energy dispersive X-Ray (EDX)

Theory

Scanning electron microscopy utilises an accelerated beam of electrons, which is focused over the sample area, impacting the surface, and causing emission of subshell (secondary) electrons; X-ray radiation; as well as backscattering of the incident electrons. These interactions, which are detected within the analysis chamber, form the basis of the images produced, as well as the elemental analysis of the sample

material [353]. Imaging resolution is largely dependent on electron acceleration. As can be seen from de Broglie's equation:

$$\lambda = \frac{h}{mv}$$

where: λ is the wavelength of light/electrons (m), h is Planck's constant (6.626×10^{-34} Js), m is the mass of electron (kg), and v is the electron's velocity (ms^{-1}). The wavelength is inversely proportional to the velocity (v) of the electron. This relation to resolution (d) is seen in Abbe's equation below:

$$\lambda = \frac{d \cdot n \cdot \sin(\alpha)}{0.612}$$

where: d is the resolution (m), n is the refractive index, and α is the angle at which the electrons enter the objective (radians). As the wavelength is decreased, which is dictated by the increase in velocity of the electrons, the imaging resolution increases (the smaller the resolution number, the higher the resolution) [353]. Alongside SEM analysis, Energy Dispersive X-ray Spectroscopy (EDX) quantification was also conducted.

Substrate Preparation and Processing Parameters

Samples for EDX and SEM surface observations were mounted onto stainless steel stubs *via* carbon tabs. The stubs were then carbon coated using an Edwards Coating System (E306A) until a *ca.* 10 nm coating was achieved.

Cross sectional observations were conducted on side-mounted discs, embedded in a carbon black resin *via* a hot mounting process. Once mounted and cooled, the samples were then polished using the same method in *Section 3.1.1*. On the contrary, cross-sectional measurements utilised fused silica discs since shattering of the discs using a diamond-tipped scribe enabled clear imaging of the cross-sectional

morphology. Thickness measurements for all samples were taken from 5 separate areas, with 3 replicate measurements taken for each area (n = 15).

Micrographs were obtained by Scanning Electron Microscopy (SEM) *via* a JEOL 6490LV SEM. A constant working distance of 10 mm was maintained, utilising a beam energy of 15 kV. Image acquisitions for higher resolution micrographs were conducted on a Field-Emission Gun Scanning Electron Microscope (JEOL 7100 FEG-SEM). Surface compositional analysis was determined *via* an Energy-Dispersive X-ray spectrometer (EDX) (Oxford Instruments) at a working distance of 10 mm, a beam voltage of 15 kV, whilst maintaining a minimum X-ray count of 150,000 counts.

3.4.3 Focus Ion Beam (FIB) SEM

Theory

In addition to the conventional *e*-beam and X-ray detection within standard SEM systems, a FIB system also incorporates an aligned ion-milling source, utilising a Ga^+ ion beam, to enable micro milling of the substrate. This process reveals coating/substrate interfacial features, as well as understanding the through-thickness morphology of the coating applied [354].

Substrate Preparation and Working Parameters

FIB-SEM was used to mill out sections of the sample for further cross-sectional analysis. An FEI Quanta 200 3D (FEI, Portland, OR) system was used, with Ga^+ ion milling performed at 30 kV, and currents ranging from 1 nA to 30 pA. Standard FEI gas injectors were used to deposit platinum (Trimethyl(methylcyclopentadienyl) platinum(IV); 25 ^oC crucible temperature), which was introduced onto the sample *via* an internal gas injector. Samples were imaged on the JEOL 7100F FEG-SEM utilising the same parameters in *Section 3.4.2*, with a 40^o stage tilt.

3.4.4 X-ray diffraction (XRD) and Texture Coefficient (T_c) Analysis

Theory

Generation of X-rays for X-ray diffraction analysis occurs through electron bombardment of a copper source, whereby emissions are directed towards the sample. Detection of diffraction peaks from a sample is due to diffraction of X-rays through crystalline planes, hence producing Bragg diffraction peaks (constructive interference) at all angles which satisfy the Bragg equation [355]:

$$n\lambda = 2dsin\theta$$

where: λ is the X-ray wavelength (m), d is the lattice spacing (m), n is an incremental integer that satisfies the Bragg equation, usually taken as unity, and θ is the angle between the incident light and lattice plane (*Figure 3:7*).

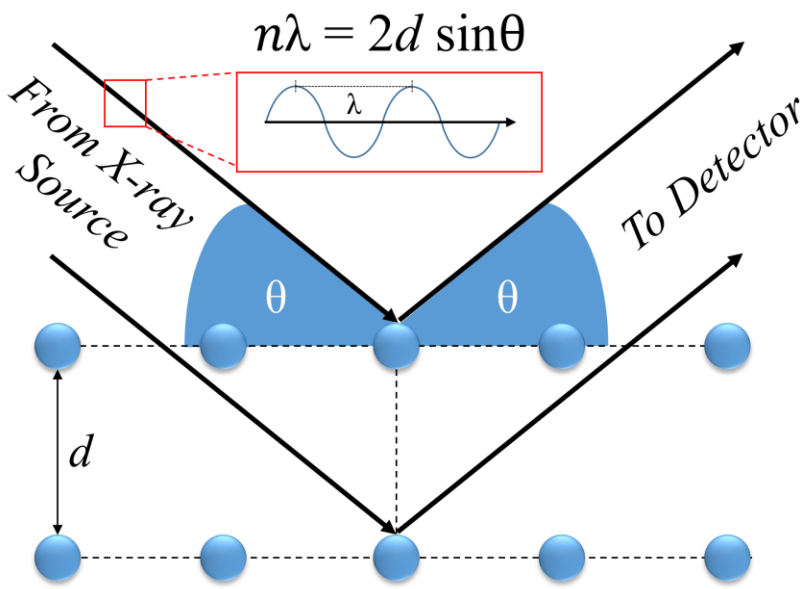

Figure 3:7 Representation of Bragg diffraction showing two incident light waves reflecting off the atoms within a crystal; one off the surface and one within the crystal. The light ray which reflects off the surface travels less distance than the light wave penetrating into the crystal structure before reflecting. The distance the light travels within the crystal before reaching the surface represents the diffraction that occurs. For the two waves to be in phase, the lattice and light parameters must satisfy the Bragg equation. Image adapted from Weidenthaler [356].

Sample Preparation and Working Parameters

All discs analysed were mounted into Perspex (polymethyl methacrylate; PMMA; Bruker) holders, ensuring the sample surface sits flush with the edge of the holder. Sample crystallinity was assessed using a Bruker D8 advanced XRD spectrometer (Cu Kα source, λ = 1.5406 Å, 40 kV, 35 mA). Measurements were taken over a 2θ range from 20 to 65°; with a step size of 0.015° (2θ); a glancing angle of 1.2°; and a dwell time of 12-16 s. The glancing angle allows the X-ray beam to graze the surface, penetrating the first few microns of material, and restricting the diffraction signal to the same depth [357].

The relative peak intensities were calculated from the raw spectral data in Bruker's DIFFRAC.EVA software, with Texture Coefficient values being obtained using the Harris equation [358]:

$$T_c(h_i k_i l_i) = \left(\frac{I_m(h_i k_i l_i)}{I_0(h_i k_i l_i)}\right)\left[\frac{1}{n}\sum_{i=1}^{n}\left(\frac{I_m(h_i k_i l_i)}{I_0(h_i k_i l_i)}\right)\right]^{-1}$$

where I_m is the measured diffraction intensity, I_0 is the diffraction database intensity value, and *n* is the number of peaks being calculated, in this case *n* = 4.

3.4.5 X-ray photoelectron spectroscopy (XPS)

Theory

XPS was conducted to understand surface composition of Ti discs. This was achieved through calculation of the binding energy of photoelectrons emitted from a few nm (depending on sample density [359]) from the sample's surface due to monochromatic X-ray photon bombardment. This energy can be calculated using the following equation:

$$E_{binding} = E_{photon} - \left(E_{kinetic} + \emptyset_f\right)$$

where: $E_{binding}$ is the electron binding energy (eV), E_{photon} is the photon energy (eV) within the X-ray source used, $E_{kinetic}$ is the electron kinetic energy (eV) detected, and $\emptyset_f$, is the work function (a correction factor for minor loss of eV due to detector absorption [360]). Each kinetic energy measured corresponds to a set binding energy unique to the shell, atom and bonding configuration it is from [361].

Sample Preparation and Working Parameters

All samples were mounted onto stainless steel stubs using carbon sticky tabs (both powder and disc samples). X-ray Photoelectron Spectroscopy (XPS) was conducted using a VG ESCALab Mark II X-ray photoelectron spectrometer with a monochromatic Al Kα X-ray source incident to the sample surface at ≈30°. Survey and high-resolution scans were conducted in addition to the measurement of adventitious C 1s for calibration: charge corrected to 284.8 eV. Parameters for acquisition were as follows: step size of 1.0; number of scans set at 5; dwell time 0.2 s for survey scans, and 0.4 s for high-resolution scans. Binding energies were measured over a range of 0–1200 eV. All spectra were analysed in Casa XPS constraining the Full Width at Half Maximum (FWHM) to the same value for all deconvoluted spectral peaks for the same element.

3.4.6 Fourier transform infrared spectroscopy (FTIR)

Theory

During bombardment of infrared radiation on elemental bonds, excitations may occur, whereby the bond may vibrate, stretch, or rock, which is characteristic to the type of bond present. Determination of such covalent compounds is quantified through determining the frequency of the excitations, which is converted to wavenumber [353, 362].

Sample Preparation and Working Parameters

All samples were placed facedown onto the spectrometer, and mounted into an adjustable clamp through pressure applied to the back of the disc by the clamp itself. Infrared absorbance was surveyed using a Bruker Tensor FTIR spectrometer with an Attenuated Total Reflectance (ATR) attachment containing a diamond crystal/ZnSe lens. Wavelengths (λ) of 2.5 to 20 μm were surveyed, corresponding to 4000 and 500 cm^{-1}, respectively.

3.4.7 Reflective high energy electron diffraction (RHEED)

Theory

RHEED is an analytical tool for surface structural analysis through the impingement, at low incident angles, of high-energy electrons produced through a finely collimated electron beam source (10-100 keV) [363]. The forward scattered diffraction pattern can then be analysed through Bragg's law, to determine *d* spacing values of the crystal structures being analysed, whereby the *d* spacing values are characteristic of a specific phase [364]. RHEED is advantageous for thin coating structures since the penetration depth (0.1-10 nm *vs.* 0.1-100 μm for RHEED and XRD, respectively) is lower, and the probing resolution is higher, than XRD [357, 364]. The conditions for diffraction are satisfied where reciprocal lattice rods (imaginary infinite points occurring perpendicular to the lattice plane) intersect with the Ewald sphere, which is defined as a sphere whose radius is equal to 2π divided by the wavelength of the incident electrons, centred around the point of incidence of the e^- beam on the surface (schematically illustrated in *Figure 3:8*) [363].

Sample Preparation and Working Parameters

Shallow angle diffraction analysis was conducted using a JEOL 2000 FX TEM with an attached RHEED stage (to which the samples were mounted) and photographic plate camera. Film acquisition was obtained using an accelerating

voltage of 200 kV, and an exposure time between 11 and 22 s to ensure visible diffraction rings were present. Diffraction ring radii were then analysed using an image processing software (ImageJ) and appropriate *d* spacing values were calculated according to Bragg's law. Calibration was conducted using a sputtered gold layer on the surface of a polished Cp-Ti substrate.

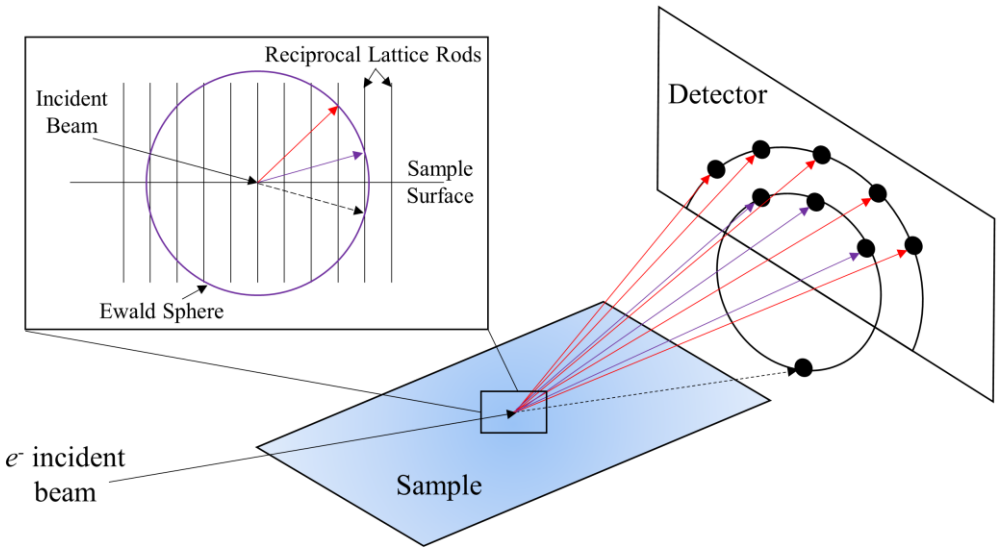

Figure 3:8. Schematic representation of RHEED, with an expanded view of the principle of RHEED diffraction conditions being satisfied.

3.4.8 Raman spectroscopy

Theory

Raman spectroscopy is a spectroscopic technique which provides information regarding sample bonding configurations through molecular vibrations. A monochromatic light source (10^2-10^4 wavenumber (cm^{-1})) is directed onto the sample, whereby most scattered light is of the same frequency as the monochromatic source, due to Rayleigh scattering. However, some scattered light is shifted in terms of its energy due to interactions between vibrational energy levels and the incident source. This shift corresponds to molecular vibrations of bonds within the sample and hence allows elucidation of the molecular structure [365].

Sample Preparation and Working Parameters

Raman spectroscopy was achieved utilising a HORIBA Jobin Yvon LabRAM HR spectrometer. Spectra were acquired using a 532 nm laser (25 mW power), 50× objective, and a 300 μm confocal pinhole. For simultaneous scanning of multiple Raman shifts, a 600 lines/mm rotatable diffraction grating along a path length of 800 mm was used. Detection of spectra was achieved through the use of a SYNAPSE CCD detector (1024 pixels) thermoelectrically cooled to −60 °C. Instrument calibration using the Rayleigh line at 0 cm^{-1} and a standard Si (100) reference band at 520.7 cm^{-1}, was employed prior to spectra acquisition. A constrained time window of 20 s was employed for each spectra recording with 20 accumulations.

3.4.9 Inductively coupled plasma (ICP)-mass spectrometry

Theory

Inductively coupled plasma relies on Mass Spectrometer analysis of an aqueous solution containing ions being injected into a plasma source. The plasma source ionises the solution, which is assessed by the mass spectrometer, and determines the number of ions contained within the solution, to understand the quantity of ions released [366].

Sample Preparation and Working Parameters

Samples were degraded in 1 mL Dulbecco's Modified Eagle Media (DMEM; MERCK, UK; contents includes amino acids, vitamins, as well as inorganic salts, which have been compiled in *Table 3:2*) and were removed after varying degradation times of 6 h, 24 h, 3 days (72 h), and 7 days (168 h). During removal, the samples were washed with 9 mL of ultrapure water, ensuring a serum dilution of 1:10, before being removed and subsequently washed in ultrapure water and air-dried. The 10 mL solutions were then analysed using inductively coupled plasma mass spectrometry (ICPMS; Thermo-Fisher Scientific iCAP-Q with CCTED). Each time point had three

replicate samples independently prepared, with calculated standard error and mean values presented. Degraded samples were also imaged using the same methodology outlined in *Section 3.4.1*.

Table 3:2. Approximate concentrations of inorganic salts within DMEM (MERCK, UK).

Inorganic Salts	Approximate Concentration / mg/L
Calcium Chloride ($CaCl_2$)	200.0
Ferric Nitrate ($Fe(NO_3)_3.9H_2O$)	0.1
Magnesium Sulfate ($MgSO_4$)	97.67
Potassium Chloride (KCl)	400.0
Sodium Bicarbonate ($NaHCO_3$)	3700.0
Sodium Chloride (NaCl)	6400.0
Sodium Phosphate Monobasic ($NaH_2PO_4.H_2O$)	125.0

3.4.10 Optical Profilometry

Theory

Optical profilometry, unlike stylus profilometry, is a non-contact surface roughness technique that utilises light interference to determine surface topography differences. Within the profilometer, a beam of light is split reflecting one beam off a reference mirror, of a known and accurate flatness, whilst the other is reflected off the test surface, any optical phase difference between the paths of light (producing interference patterns) are solely due to the roughness of the material, and therefore, its surface roughness can be calculated. Focus variation enables the combination of vertical scanning of the surface, with the small depth of focus observed with an optical system, in order to provide more accurate topographical information [367].

Sample Preparation and Working Parameters

Surface roughness quantification was conducted using focus variation microscopy performed on an Alicona Infinite Focus instrument. A 50× objective lens was used in all cases, with raw data being levelled using the least squares plane method. 3D areal

surface texture parameters were extracted using the ISO 25178-2 standard [368]. A vertical resolution of 70 nm was utilised, with a horizontal resolution of 2 μm.

3.4.11 Atomic Force Microscopy (AFM)

Theory

AFM, through either contact or non-contact operation modes, enables sub-nm morphologies to be resolved in order to understand the overall surface profile of a substrate or coating. A finely manufactured tip (*ca.* 8-12 nm radius) on a cantilever interacts with the material's surface, which does so *via* short-range attraction, as well as additional phenomena such as Coulomb repulsion, to provide morphological information. In PeakForce Tapping mode™ (Bruker), the tip contacts the surface at a constant rate, whilst maintaining a constant interaction force. This is detected *via* a laser, which is focussed onto the top of the cantilever, and is reflected to a photodetector, which monitors deflection of the cantilever due to the surface. These deflections, combined with the cantilever arm being moved over the surface, produces a 3D image of the samples' morphology [369].

Sample Preparation and Working Parameters

Roughness measurements (R_a; Arithmetic Mean Average) were taken on a Bruker Dimensions FastScan Icon AFM operated in PeakForce Tapping™ mode. The tips used were Bruker RTESPA-300 0.01 – 0.025 Ω-cm Antimony-doped Silicon tips. The scan area for all AFM micrographs was maintained at 5 x 5 μm (R_a values are mean ± standard error; $n = 3$). Nanoscope software (Bruker) was used to analyse all results, with raw data being levelled using the least squares plane method.

3.4.12 Pull Off Adhesion Strength

Theory

Pull off adhesion testing is often employed to quantify adhesion forces between sputtered coatings and their substrates [370]. Usually, an epoxy adhesive bonds a

parallel stub to the coated substrate, whereby tension is applied until detachment occurs. A caveat to such a test is that the main limitation is the adhesive strength, since adhesive failure at the glue interface does not provide any qualitative information regarding coating bonding strength [371].

Sample Preparation and Working Parameters

The adhesion strength of sputtered Ti coatings was tested using a portable adhesion testing (P.A.T handy (DFD® Instruments)) unit in accordance with ASTM-D4541-17 [372]. Stubs (2.8 mm radii) were adhesively bonded to the coated samples using DFD® E1100S epoxy, which was cured for 60 min at 140 ^{o}C, and then left to cool to room temperature. All discs were cleaned with compressed air and air bubbles formed between the stub and disc were carefully removed through pressing of the stubs. Any excess epoxy following curing was removed *via* a cylindrical cutting tool supplied with the equipment. Analysis of the failure sites were conducted using a Nikon LV100ND upright light microscope.

3.4.13 Scratch Adhesion Testing

Theory

A semi-quantitative method, scratch adhesion testing is utilised to assess the adhesion and failure modes of a wide range of coating materials, through the application of a diamond stylus under an increasing load. During the process, depending on the material type and the adhesive properties, a critical load (L_c) may be achieved, resulting in usually cracking and/or delamination of the coating. Through determination of the length of the scratch prior to specific failure, quantitative failure loads can be calculated [373, 374].

Sample Preparation and Working Parameters

Analysis of both unconverted and titanate converted coating failure was conducted in accordance to BS EN ISO 20502:2016 [375], using a CETR UMI multiple specimen

scratch testing system equipped with a Rockwell C indenter. Prior to each scratch, the indenter was cleaned with isopropyl alcohol. Modified testing regimes were utilised due to some failure modes occurring at considerably lower loads than the standard 30 N, making quantification difficult. Therefore, loads were applied over a distance of 3 mm, with pre-loading of 0.5 N and progressive loading up to a value of 15 N over a period of 180 s. The failure sites were again analysed using a Nikon LV100ND upright microscope.

3.4.14 Electrochemical Corrosion Testing

Theory

Potentiodynamic polarisation electrochemical testing is a technique that measures the dynamic changes of either the voltage or current of a system, specifically within a sample under specific conditions, in order to determine its corrosive potential. In an electrochemical system, there needs to be an anode, a cathode, as well as an electrical and ionic connection between the two systems. Usually, the potential of a system is ramped from a negative to a positive voltage through a predetermined range, whilst the current is monitored using a potentiostat. The anode (M), which is usually the sample material being tested, undergoes an oxidation reaction:

$$M \rightarrow M^{x+} + xe^{-}$$

The current measured is the rate at which the corrosion process is occurring, and is usually represented as the current density, *i.e.* the current change over the area of the electrode [376].

Sample Preparation and Working Parameters

Samples for electrochemical testing were mounted (*Figure 3:9*) using Silver Conductive Epoxy Adhesive (8331S Epoxy; MG Chemicals; 60 ^{o}C cure/2 h) into hot cured epoxy blocks (DAP Mount Blue; MetPrep, UK). A hole was drilled through the

back of the epoxy blocks, in order to insert a brass conductive rod (RS Components, UK), which was mounted in place using Red Stopping Off Lacquer (166054; MacDermid, UK). Potentiodynamic polarisation (PDP) testing was conducted in accordance with a modified version of ASTM Standard F2129-19a [377] using a Voltalab PGZ 100 (Radiometer analytical, UK) potentiostat and a three electrode electrochemical cell consisting of, one saturated calomel reference electrode (SCE), one 1 cm^2 Pt auxiliary electrode and one working electrode containing the sample being tested. Each test used 1 L of DMEM (MERCK, UK) solution balanced to a pH of 7.4 at 37 $\pm$ 1 ^oC, which was chosen due to it providing an appropriate aqueous environment akin to *in vivo* conditions. Open circuit potential (OCP) scans were conducted for 30 min, followed by PDP analysis. Anodic and cathodic scans were conducted from a potential of -2 V to 1.5 V, with a scan rate of 1 mV/s. Tafel analysis using Voltamaster software determined both E_{corr}, i_{corr}, and R_p values for each sample, with the Tafel region only shown in the figure for clarity.

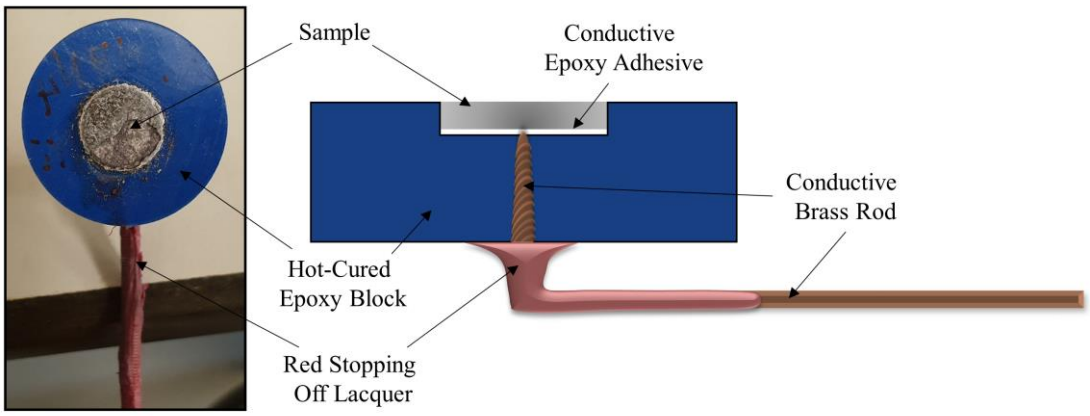

Figure 3:9. Schematic representation and phone image of a sample mounted for electrochemical corrosion evaluation.

SEM micrographs were also captured for all samples post-electrochemical degradation, and utilise the same parameters outlined in *Section 3.4.2*. Additional,

qualitative analysis on the potential corrosion rate (v_{corr}), in mm.y^{-1}, was calculated using Faraday's rate equation, according to ASTM G102:89(2015)E1:

$$CR\ (mm.y^{-1}) = K_1 \frac{i_{corr}}{\rho} EW$$

Where *CR* is the penetration rate unit (mm.y^{-1}), i_{corr} (μA.cm^{-2}) is the corrosion current density, K_1 is a constant of 3.27 x 10^{-3} (mm.g.μA^{-1}.cm^{-1}.y^{-1}), ρ is the materials density (Mg = 1.738 g.cm^{-3}), and *EW* is the 'effective weight', defined as the atomic weight divided by the number of electrons required to oxidise an atom during the corrosion process: Mg = 12.15.

3.4.15 Cell culture neutral red uptake (NRU) assay

Theory

The neutral red uptake assay is a quantitative technique for estimating the number of viable cells present within a culture. In a facile sense, the assay works through incorporation and binding of a specific dye within lysosomes. Any disruption to the surrounding cellular environment will result in a reduction in dye uptake, which is proportional to the number of viable cells present [378].

Sample Preparation and Working Parameters

The NRU assay and live/dead assay and results detailed within this report were conducted in collaboration with Kathryn G. Thomas (Ph.D. student, University of Nottingham; Cell assessments were conducted in the Wolfson Cell Culture Laboratory, whilst bacterial assessments were conducted in the Centre for Biomolecular Sciences (CBS), both at the University Of Nottingham). Samples were degraded in 1 mL DMEM containing Fetal Bovine Serum for 7 days at 37 °C, generating liquid extracts as described in ISO 10993-5:2009. The extended degradation time was used to mimic long-term contact with the body. MG-63 cells were seeded into a 24 well plate (20,000 cells.cm^{-2}) and incubated for 24 h to give a

subconfluent monolayer. The media was removed and replaced with the sample elutes. After 24 h further incubation, the media was removed, the cells washed with PBS, and 500 µL of Neutral Red medium was added. After 2 h incubation, the medium was removed, cells were washed in PBS, and 500 µL of de-stain was added per well. Plates were shaken on a plate shaker for 10 min and the NR absorption was read using an ELx800 Microplate Colorimeter (BioTek Instruments Inc.) at 540 nm.

3.4.16 Microbiological LIVE/DEAD assay

Theory

LIVE/DEAD™ staining provides direct enumeration of the amount of live and dead bacteria present within a bacterial colony. It utilises a combination of two different nucleic acid-binding stains, whereby one will bind to all bacterial membranes and fluoresces green, and the other stain only penetrates damaged (dead) bacterial membranes, with the combination of both dyes causing red fluorescence [379].

Sample Preparation and Working Parameters

All samples were sterilised *via* UVB light (Naure Class II Safety Cabinet) for 30 min per side. *S. aureus* Newman strain was cultured in Tryptone Soy Broth (TSB) overnight. Samples of each type were added in triplicate to sterile petri dishes and 15 mL pre-warmed (37 °C) TSB added. The overnight culture was washed twice in TSB, and then used to inoculate the petri dishes to 0.01 OD_{600}. The dishes were incubated (37 °C at 60 RPM) for 3 days, followed by washing in distilled water twice, then incubated at room temperature in the dark for 30 min with BacLight LIVE/DEAD stain (Invitrogen), and finally dried. The samples were imaged on a Carl Zeiss L700 Confocal Laser Scanning Microscope and biomass volume analysed *via* COMSTAT 2 plugin to ImageJ [380].

Chapter 4. Gallium Ion-Substitution for Potential Antibacterial Titanate Surfaces

4.1 Introduction

In this chapter, novel ion exchange reactions were investigated in order to confirm: the possible production of a gallium titanate structure; the chemical, structural and antibacterial properties of such a material; and the effect of such properties due to an additional heat treatment step following the ion exchange reactions. Gallium has the potential to provide dual benefits, whereby it reduces Ca release in bones, minimising osteolysis, whilst also reducing bacterial viability through a Trojan horse mechanism; the chemical similarities (charge, ionic radii, etc.) with iron (Fe) results in Ga uptake in bacteria, which cannot be reduced during metabolism, resulting in Ga-induced metabolic distress. Material characterisation in order to quantify the chemical, structural and morphological properties was conducted, with RHEED analysis of gallium titanate layers being conducted for the first time. Degradation studies in DMEM were also investigated to understand the ion exchange process occurring *in vitro*. *S. aureus* was used in this study to examine the antibacterial effect of gallium-doped titanate materials.

4.2 Results

4.2.1 SEM

Surface morphology alterations were tracked following each ion exchange reaction (both NaOH and $Ga(NO_3)_3$) and post heat treatment (700 ^oC). After the NaOH treatment at 60 ^oC (herein labelled S1: Na_2TiO_3), alteration to the morphology of Ti surfaces from S0: Cp-Ti (see *Section 3.3* in methodology for processing parameters) was exhibited (*Figure 4:1A* & *C*). Extended nanoporous networks with features on the order of a few hundred nanometres in diameter were seen, characteristic of titanate structures. Following Ga ion exchange (herein labelled S2: $Ga_2(TiO_3)_3$), micrographs

showed a similar interconnected morphology to S1: Na_2TiO_3 (*Figure 4:1E*). Post heat treatment (herein labelled S3: $Ga_2(TiO_3)_3$-HT), the interconnected morphology remained, but with the formation of flake-like features on the surface, found to be rich in Ga and O as confirmed *via* EDX analysis (*Figure 4:2*), with diameters of *ca.* 150-300 nm (*Figure 4:1G*). The inclusion of S4: Cp-Ti-HT (S0:Cp-Ti samples subjected to 700^{o}C heat treatment; *Figure 4:1I*), was to identify morphological differences between sodium titanate and characteristic rutile formation on the sample's surface. The porous angular surface of S3: $Ga_2(TiO_3)_3$-HT was significantly dissimilar to that of the relatively smooth S4: Cp-Ti-HT.

Cross-sectional FEG-SEM imaging of S1: Na_2TiO_3, S2: $Ga_2(TiO_3)_3$, and S3: $Ga_2(TiO_3)_3$-HT showed similar morphology, with a distinct porous layer on the order of *ca.* 0.5–1 μm in thickness (*Figure 4:1D. F,* & *H; Table 4:1*). This was in stark contrast to the original relatively smooth S0: Cp-Ti control sample (*Figure 4:1B*). However, the layer exhibited in S3: $Ga_2(TiO_3)_3$-HT demonstrated formation of an intermediate layer between the nanoporous surface layer and the titanium substrate (*Figure 4:1H*), comprised of relatively lower Ga and higher Ti content compared to the top layer (*Figure 4:3*). Furthermore, sample S4: Cp-Ti-HT demonstrated a different cross-sectional profile to all other samples with a thin dense titanium oxide layer (*Figure 4:1J*).

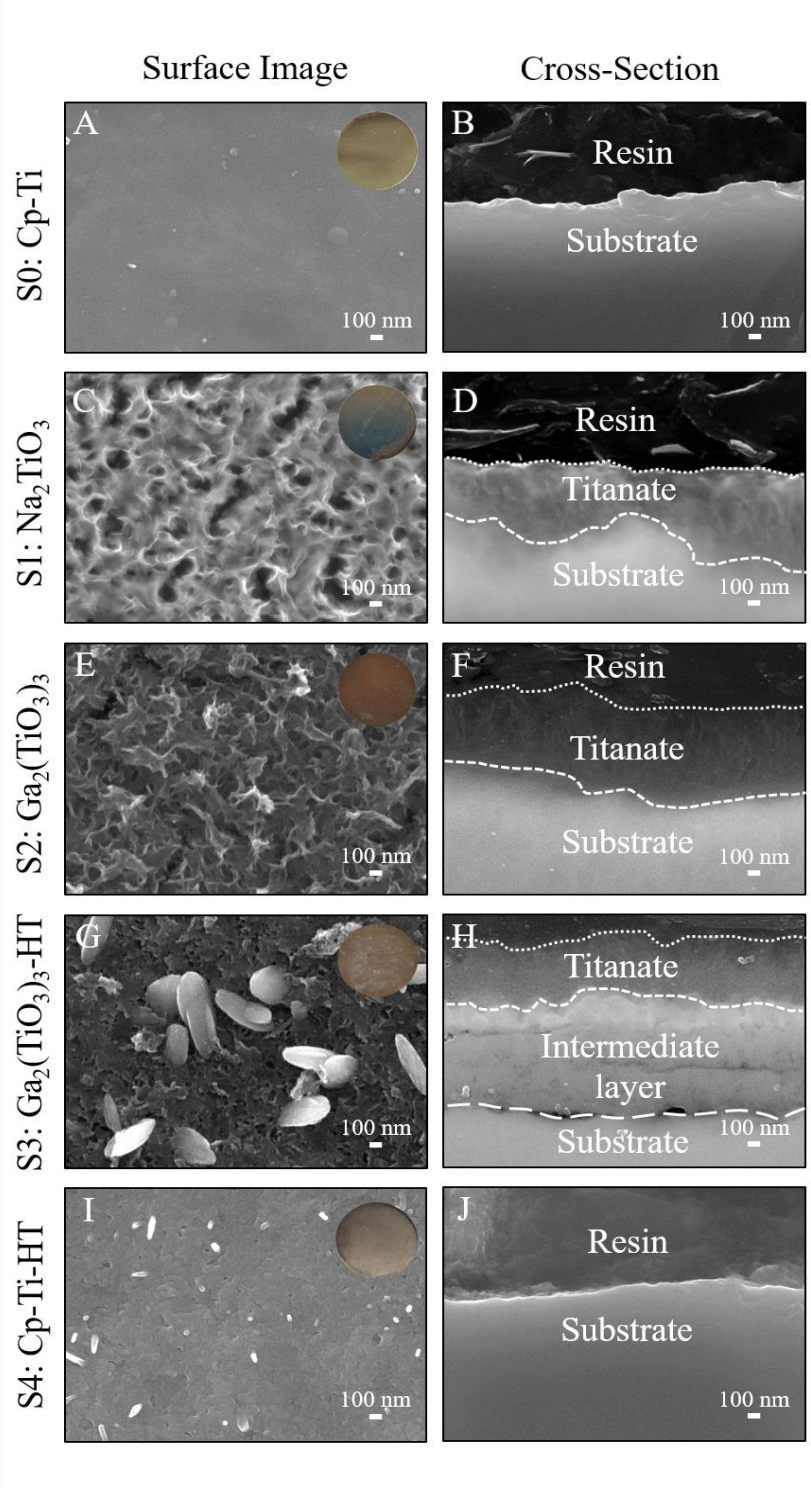

Figure 4:1. (A, C, E, G, and I) FEG-SEM surface and (B, D, F, H, and J) cross-sectional images of S0: Cp-Ti, S1: Na_2TiO_3, S2: $Ga_2(TiO_3)_3$, S3: $Ga_2(TiO_3)_3$-HT, and S4: Cp-Ti-HT samples, respectively. Inset macroscopic images are of the corresponding sample's surface.

Table 4:1. Thickness measurements of both the produced titanate thickness, as well as the intermediate layer thickness noted on solely the S3: $Ga_2(TiO_3)_3$-HT sample. All measurements, taken on one sample, are the mean ± standard error (n = 5).

Sample	Thickness Measurements	
	Titanate Thickness / nm	Intermediate Layer Thickness / nm
S0: Cp-Ti	N/A	N/A
S1: Na_2TiO_3	819 ± 77	N/A
S2: $Ga_2(TiO_3)_3$	743 ± 27	N/A
S3: $Ga_2(TiO_3)_3$-HT	544 ± 14	887 ± 39
S4: Cp-Ti-HT	N/A	N/A

4.2.2 EDX Analysis

Initially, elemental mapping analysis (*Figure 4:2* & *Table 4:2*) of S1: Na_2TiO_3 showed homogeneous distribution of Na, Ti and O, and concluded Na (*ca.* 2.7 at.%) and O (*ca.* 65.3 at.%) had been incorporated within the structure, compared to the S0: Cp-Ti control (Ti: 100 at.%). The lack of precipitates on the surface demonstrated incorporation of Na and O in the surface of the sample, rather than NaOH precipitation. Analysis of S2: $Ga_2(TiO_3)_3$ indicated complete substitution of Na (*ca.* 2.7 at.%) by Ga (9.4 at.%) within the titanate structure. Again, homogenous distribution of the Ga, Ti, and O was noted in the EDX mapping. S2: $Ga_2(TiO_3)_3$ compared to S3: $Ga_2(TiO_3)_3$-HT showed a 5.3 at.% reduction of Ga within the latter following heat treatment (*Table 4:2*), with a representative EDX cross-section measurement of S3: $Ga_2(TiO_3)_3$-HT taken to demonstrate the concentration gradient through the sample's thickness (*Figure 4:3*). Precipitates (indicated by the white circles in *Figure 4:2*), however, were noted on both the S2: $Ga_2(TiO_3)_3$ and S3: $Ga_2(TiO_3)_3$-HT samples, which were rich in Ga and O as evidenced from the EDX maps, which increased in size following the heat treatment stage.

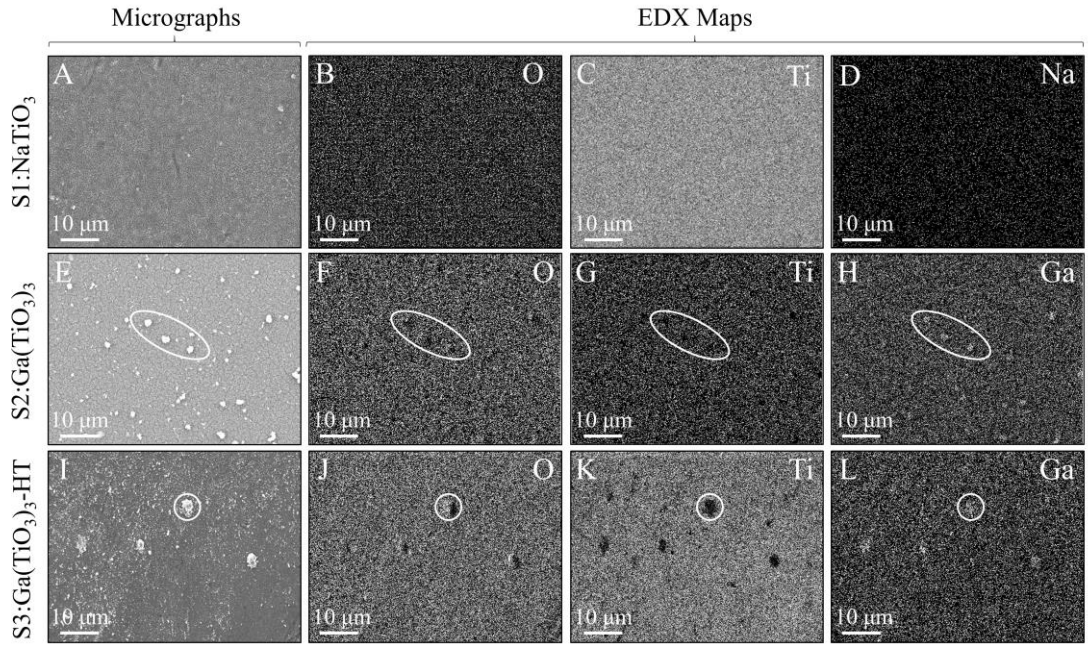

Figure 4:2. SEM micrographs and EDX maps of O, Ti, and Na/Ga elements for (A-D) S1:$NaTiO_3$, (E-H) S2:$Ga(TiO_3)_3$, and (I-L) S3:$Ga(TiO_3)_3$-HT samples. White circles identify precipitates and areas of elemental inhomogeneity, with crystals being rich in Ga and O; indicative of Ga_2O_3 or GaO(OH).

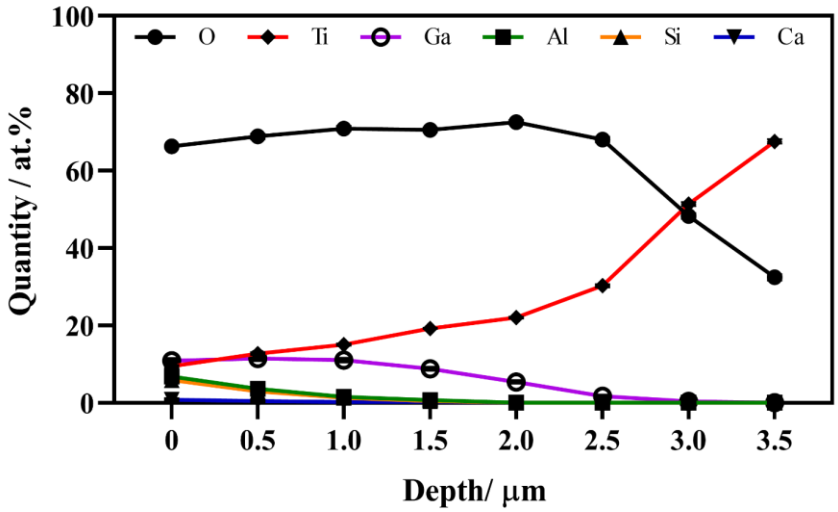

Figure 4:3. Representative cross-sectional EDX point analysis demonstrating the drop in O and Ga content through the thickness of the S3: $Ga_2(TiO_3)_3$-HT sample. Due to the large interaction volume (ca. 2 µm) accurate elemental information as a function of depth is difficult to quantify, hence this technique being used is purely in a qualitative context. 0 µm defines the top of the titanate structure from the SEM micrograph, all values are quoted means ± standard error (n = 3).

Table 4:2. EDX elemental mapping data of S0: Cp-Ti, S1: Na_2TiO_3, S2: $Ga_2(TiO_3)_3$, S3: $Ga_2(TiO_3)_3$-HT, and S4: Cp-Ti-HT samples over a 400 μm^2 area of the sample surface. Mean atomic percent (at.%) are shown with standard error (n = 3).

Sample	Elemental Composition / at.%			
	Ti	O	Na	Ga
S0: Cp-Ti	100	0	0	0
S1: Na_2TiO_3	31.9 ± 0.1	65.3 ± 0.1	2.7 ± 0.2	0
S2: $Ga_2(TiO_3)_3$	20.1 ± 0.2	70.5 ± 0.3	0	9.4 ± 0.1
S3: $Ga_2(TiO_3)_3$-HT	22.6 ± 0.4	73.3 ± 0.4	0	4.1 ± 0.2
S4: Cp-Ti-HT	30.2 ± 0.1	69.8 ± 0.1	0	0

4.2.3 XRD Analysis

As seen in *Figure 4:4E*, the only diffraction peaks present for S1: Na_2TiO_3 and S2: $Ga_2(TiO_3)_3$ were that of the Ti substrate (S0: Cp-Ti), which produced peaks associated with titanium (α-Ti: ICDD PDF 00-44-1294). Following heat treatment (S3: $Ga_2(TiO_3)_3$-HT), further diffraction peaks emerged located at *ca.* 26, 37, 40, and 55° 2θ, which were attributed to gallium titanate (Ga_2TiO_5: ICDD PDF 00-020-0447). The peak at *ca.* 57° 2θ correlated to rutile (TiO_2: ICDD PDF 00-021-1276), and peaks at *ca.* 37, 40, and 53° 2θ were related to the sub-stoichiometric titanium oxide (Ti_6O: ICDD PDF-01-072-1471) phase. However, the lack of high quality diffraction data for gallium titanate, the lower intensity, as well as the overlap of gallium titanate with rutile ruled the XRD data alone meant RHEED analysis was conducted. This technique offers greater spatial resolution and shallower probing depth (0.1-10 nm) as compared to XRD (0.1-100 μm), necessary to elucidate the structural information of the upper titanate surface [357, 364].

4.2.4 RHEED

RHEED analysis of S4: Cp-Ti-HT (*Figure 4:4D*) demonstrated clear and distinct diffraction rings, as well as matching *d* spacing values with rutile (TiO_2: ICDD PDF-

00-021-1276: *Table 4:3*) consistent with the SEM-EDX results. The diffraction patterns present in S1: Na_2TiO_3, S2: $Ga_2(TiO_3)_3$, and S3: $Ga_2(TiO_3)_3$-HT (*Figure 4:4A*, *B*, and *C*, respectively) demonstrated a significant change from that of S4: Cp-Ti-HT, indicating an alternative layer than rutile (*Figure 4:4D*). The *d* spacing values for S1: Na_2TiO_3 were ascribed to sodium titanate ($Na_{0.23}TiO_2$: ICDD PDF 00-022-1404, and Na_4TiO_4: ICDD PDF 00-042-0513) and titanium (Ti: ICDD PDF 00-044-1294). Furthermore, S2: $Ga_2(TiO_3)_3$ *d* spacing values were akin to calcium and sodium titanate variants ($CaTi_2O_5$: ICDD PDF 00-025-1450, and Na_2TiO_3: ICDD PDF 00-037-0346), as well as S3: $Ga_2(TiO_3)_3$-HT being similar to gallium and calcium titanate variants (Ga_2TiO_5: ICDD PDF 01-070-1993, and $CaTi_2O_5$: ICDD PDF 00-025-1450).

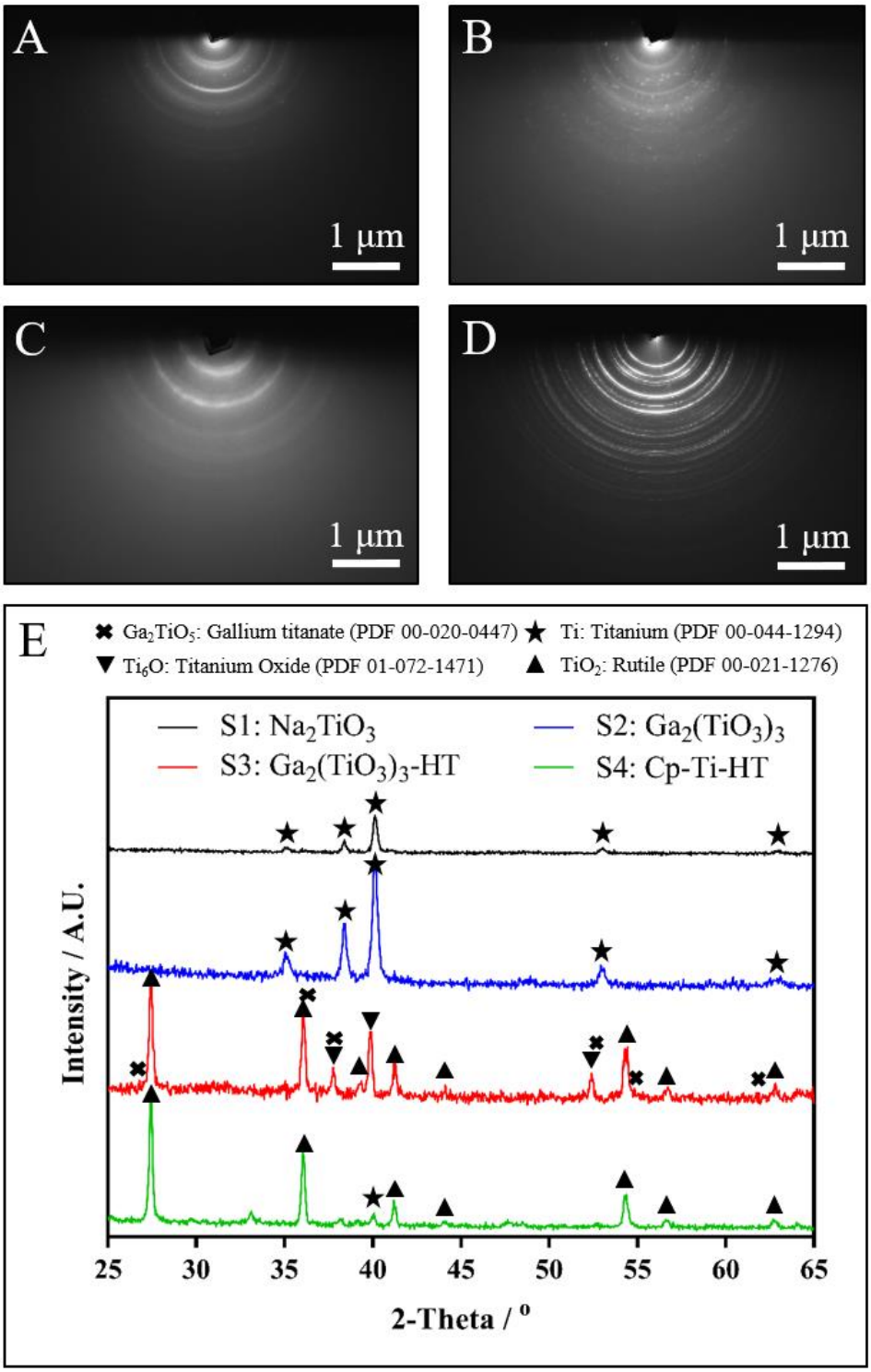

Figure 4:4. (A, B, C and D) RHEED diffraction patterns for S1: Na_2TiO_3, S2: $Ga_2(TiO_3)_3$, S3: $Ga_2(TiO_3)_3$-HT, and S4: Cp-Ti-HT, respectively. (E) XRD data of aforementioned samples. Deconvolution of the peaks are as follows: ▲ - rutile (TiO_2: ICDD PDF 00-021-1276); ▼ - titanium oxide (Ti_6O: ICDD PDF 01-072-1471); ✖ – gallium titanate (Ga_2TiO_5: ICDD PDF 00-020-0447); ★ - titanium (Ti: ICDD PDF 00-044-1294).

Table 4:3. Quantitative RHEED analysis data for calculated d spacing (using principles from Bragg's law) figures compared to database values. Calculated d spacing values all have standard errors <0.01. Ring radii and d spacing data has been rounded to 3 s.f.

Sample	Database file	Calculated *d* spacing / Å	Database *d* spacing / Å
S1: Na_2TiO_3	Sodium Titanate ($Na_{0.23}TiO_2$) (ICDD PDF 00-022-1404)	3.70	3.65
		1.87	1.92
	Titanium (Ti) (ICDD PDF 00-044-1294)	2.28	2.24
	Sodium Titanate (Na_4TiO_4) (ICDD PDF 00-042-0513)	3.22	3.23
		2.28	2.21
		1.87	1.87
S2: $Ga_2(TiO_3)_3$	Calcium Titanate ($CaTi_2O_5$) (ICDD PDF 00-025-1450)	3.50	3.50
		1.83	1.87
	Sodium Titanate (Na_2TiO_3) (ICDD PDF 00-037-0346)	3.27	3.23
		1.83	1.87
S3: $Ga_2(TiO_3)_3$-HT	Gallium Titanate (Ga_2TiO_5) (ICDD PDF 01-070-1993)	3.50	3.38
		2.88	2.75
	Calcium Titanate ($CaTi_2O_5$) (ICDD PDF 00-025-1450)	3.50	3.50
		2.88	2.92
		1.82	1.87
S4: Cp-Ti-HT	Rutile (TiO_2) (ICDD PDF 00-021-1276)	3.23	3.25
		2.45	2.49
		2.28	2.30
		2.19	2.19
		2.05	2.05

4.2.5 Raman Spectroscopy

Raman spectral analysis (*Figure 4:5A*) of S3: $Ga_2(TiO_3)_3$-HT and S4: Cp-Ti-HT revealed bands located at *ca.* 247, 445, and 611 cm^{-1}, which were attributed to rutile, Ti—O bonding [381-383]. Conversely, alternate peaks were found in the S2: $Ga_2(TiO_3)_3$ sample at *ca.* 273, 425, 700, and 811 cm^{-1}, as well as *ca.* 400 and 662 cm^{-1} in S1: Na_2TiO_3, which were found to be attributable to titanate structures, such as sodium titanate ($Na_2Ti_3O_7$; Na—O bonding) [384]. A shoulder was present in S3: $Ga_2(TiO_3)_3$-HT at *ca.* 700 cm^{-1}, which is present as an identifiable peak in S2: $Ga_2(TiO_3)_3$ and

corresponds to GaO(OH) [385, 386]. No discernible peaks were noted on the S0: Cp-Ti sample and, therefore, have not been shown.

4.2.6 FTIR Analysis

IR absorption showed peaks detailed from 500 to 900 cm^{-1}, matching TiO_6 vibrations, Ti—O bending and Ti—OH non-bridging bonds, which are prevalent across all samples (*Figure 4:5B*) [381-383]. Additionally, a peak around 1100 cm^{-1} and a broad peak from 3000 to 3500 cm^{-1}, which appear in S1: Na_2TiO_3 and S2: $Ga_2(TiO_3)_3$ samples, correspond to Ti—O—C vibrations and H—O—H stretching, respectively [387, 388]. Three peaks at *ca.* 1130, 1300 and 2350 cm^{-1} are seen in the S4: Cp-Ti-HT control, which were consistent with rutile Ti—O, Ti—O—Ti stretching, and CO_2 contamination, respectively [389, 390]. The peak at *ca.* 2050 cm^{-1} remains unmatched. Doublet peaks around 2880 cm^{-1} in S3: $Ga_2(TiO_3)_3$-HT, match C—H furnace contamination [389]. Finally, all spectra except S4: Cp-Ti-HT exhibited a peak at *ca.* 1610 to 1630 cm^{-1}, consistent with O—H bonds [391]. Again, no bonds were noted on the S0: Cp-Ti sample and, therefore, have not been shown for clarity.

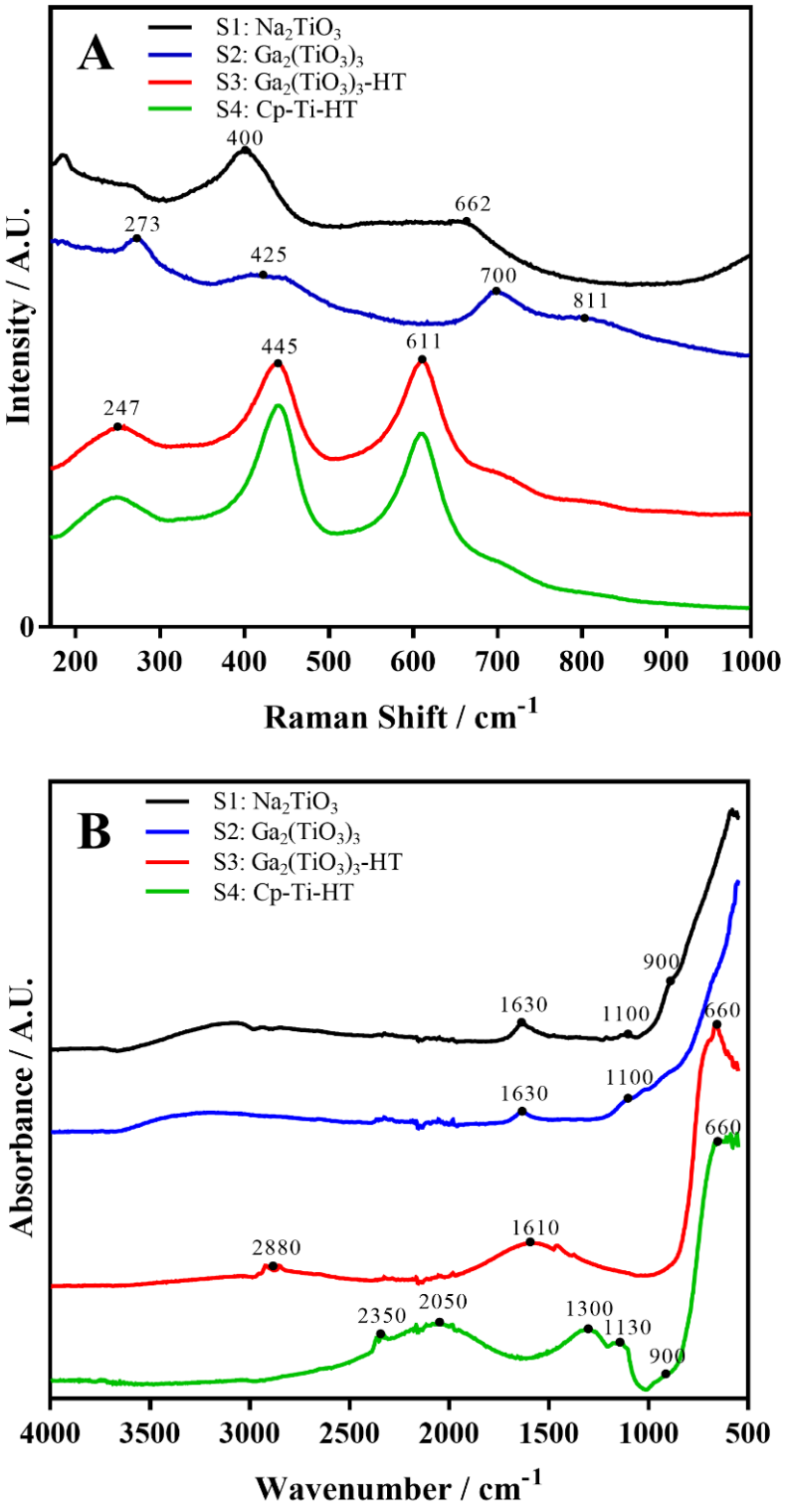

Figure 4:5. (A) Raman infrared spectrometry analysis, and (B) FTIR analysis of S1: Na_2TiO_3, S2: $Ga_2(TiO_3)_3$, S3: $Ga_2(TiO_3)_3$-HT, and S4: Cp-Ti-HT samples.

4.2.7 XPS Analysis

XPS analysis of S1: Na_2TiO_3, S2: $Ga_2(TiO_3)_3$, and S3: $Ga_2(TiO_3)_3$-HT samples was conducted (*Figure 4:6*); note the control samples are not shown for clarity of the titanate data, but are detailed in *Table 4:5*. The S0: Cp-Ti and S4: Cp-Ti-HT samples exhibited similar spectra and elemental ratios with Ti and O being present in both samples, with the relative O content being higher in the S4: Cp-Ti-HT sample (*ca.* 74.5 *vs*. 71.6 at.%; *Table 4:4*). Additionally, the S0: Cp-Ti sample exhibited two Ti doublet peak deconvolutions, for both the metallic (Ti^0; *ca.* 22.1 at.%) and oxide (Ti^{4+}; *ca.* 77.9 at.%) states, with the Ti^0 deconvolution diminishing in the S4: Cp-Ti-HT sample. Furthermore, there were two O peak deconvolutions for the S0: Cp-Ti sample at 530.2 and 531.9 eV, corresponding to O^{2-} and –OH, respectively; whilst the S4: Cp-Ti-HT sample demonstrated 3 peaks: 530.2, 531.6, and 532.9, corresponding to O^{2-}, –OH/Non-lattice O, and H_2O, respectively.

The initial O 1s peak (*Figure 4:6A*) at 529.6 eV in the S1: Na_2TiO_3 sample exhibited a shift to 531.6 eV and 530.7 eV in S2: $Ga_2(TiO_3)_3$ and S3: $Ga_2(TiO_3)_3$-HT, respectively. Deconvolution of O 1s for S1: Na_2TiO_3 demonstrated three peaks at 530.2, 531.6, and 532.9 eV, with area ratios of 75.0, 15.3, and 9.7%, respectively. Each peak matched O—Ti^{4+}, Ti—OH/Non-lattice O, and –OH (H_2O), respectively. This reduced to two peaks at 530.3 (49.3%) and 531.9 (50.7%) eV in the S2: $Ga_2(TiO_3)_3$ sample, eliminating –OH (H_2O). Moreover, S3: $Ga_2(TiO_3)_3$-HT demonstrated two peaks, with shifts to 530.7 (82.4%) and 532.4 (17.6%) eV.

A perceptible shift was noted in the Ti 2p doublet peak (*Figure 4:6B*) for S3: $Ga_2(TiO_3)_3$-HT. Initial positions at 458.6 and 464.3 eV, corresponded to Ti 2p 3/2 and Ti 2p 1/2 in the S1: Na_2TiO_3 sample. These shifted to 458.5 and 464.2 eV in S2: $Ga_2(TiO_3)_3$. However, a further shift to 459.0 and 464.7 eV was observed in

S3: $Ga_2(TiO_3)_3$-HT, which corresponded to Ti^{4+}. The Ti content of the S1: Na_2TiO_3, S2: $Ga_2(TiO_3)_3$ and S3: $Ga_2(TiO_3)_3$-HT samples exhibited a large reduction in comparison to the S0: Cp-Ti control (*ca.* 28.4 at.%), with values of *ca.* 23.4, 4.9 and 8.6 at.%, respectively.

The Na 1s peak at 1071.9 eV (*Figure 4:6C*), matching Na—O, in the S1: Na_2TiO_3 sample (Ti LMM Auger peaks located at 1067.3 and 1075.1 eV), diminished after Ga ion exchange in both S2: $Ga_2(TiO_3)_3$ and S3: $Ga_2(TiO_3)_3$-HT. The elemental quantity of Na was 10.7 at.% (*Table 4:4*), with the Ga content of S2: $Ga_2(TiO_3)_3$ and S3: $Ga_2(TiO_3)_3$-HT being *ca.* 31.3 and 38.1 at.%, respectively; all much higher than found in EDX (*Table 4:2*). Furthermore, the Ga 2p doublet peak (*Figure 4:6D*) showed distinct peaks at 1118.3 and 1145.2 eV (Δ = *ca.* 26.9 eV), corresponding to Ga 2p 3/2 and Ga 2p 1/2 for Ga^{4+}—O and/or Ga^{3+}—O, respectively, in S2: $Ga_2(TiO_3)_3$ and 1118.4 and 1145.3 eV, respectively in S3: $Ga_2(TiO_3)_3$-HT.

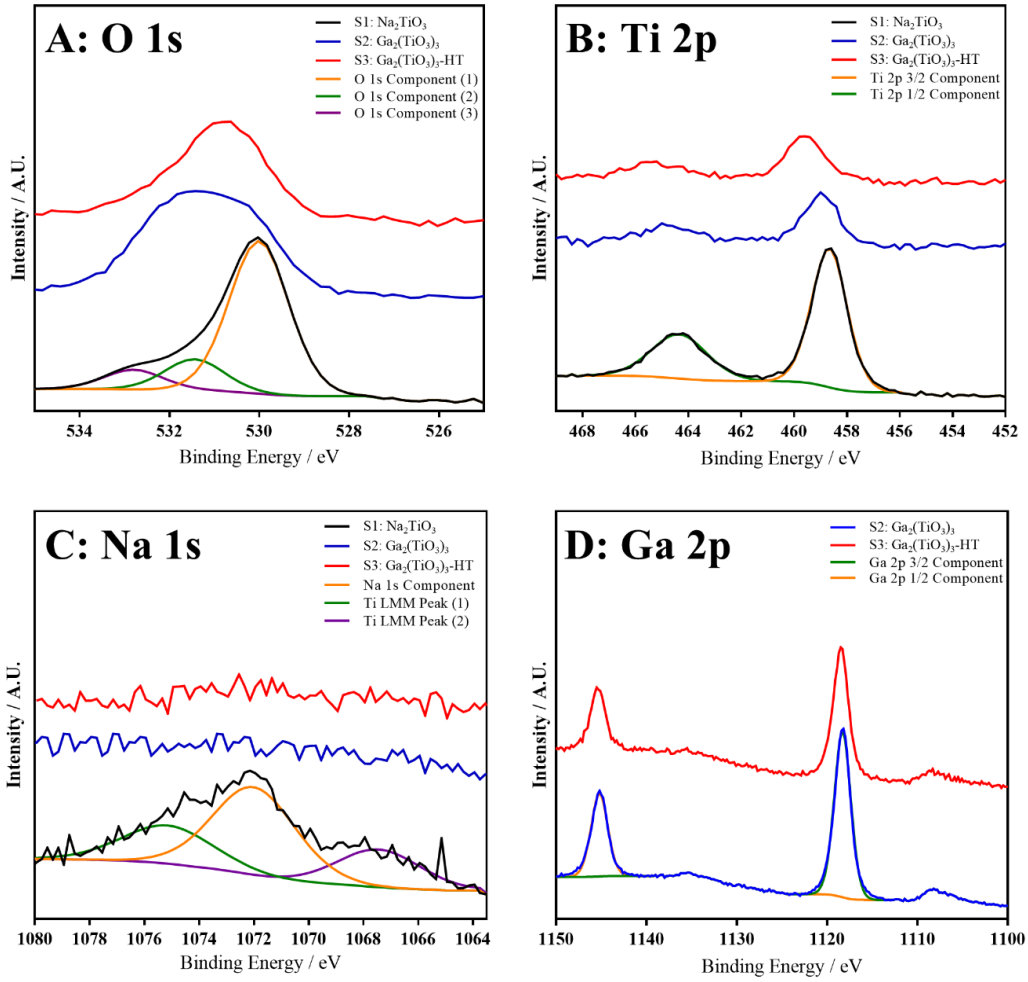

Figure 4:6. XPS analysis of S1: Na_2TiO_3, S2: $Ga_2(TiO_3)_3$, and S3: $Ga_2(TiO_3)_3$-HT. (A) High resolution O 1s spectra, (B) High resolution Ti 2p spectra, (C) High resolution Na 1s spectra, and (D) High resolution Ga 2p spectra.

Table 4:4. XPS elemental data of S0: Cp-Ti, S1: Na_2TiO_3, S2: $Ga_2(TiO_3)_3$, S3: $Ga_2(TiO_3)_3$-HT, and S4: Cp-Ti-HT samples. Mean atomic percent (at.%) are shown with standard error (n = 3).

Sample	Elemental Composition / at.%			
	Ti	O	Na	Ga
S0: Cp-Ti	28.4 ± 0.5	71.6 ± 0.5	0	0
S1: Na_2TiO_3	23.4 ± 0.6	65.9 ± 1.0	10.7 ± 1.1	0
S2: $Ga_2(TiO_3)_3$	4.9 ± 0.5	63.7 ± 1.0	0	31.3 ± 1.0
S3: $Ga_2(TiO_3)_3$-HT	8.6 ± 1.0	53.3 ± 1.4	0	38.1 ± 1.4
S4: Cp-Ti-HT	25.5 ± 0.5	74.5 ± 0.5	0	0

Table 4:5. XPS peak deconvolutions and their corresponding bond and area information for the S0: Cp-Ti, S1: $NaTiO_3$, S2: $Ga(TiO_3)_3$, S3: $Ga(TiO_3)_3$-HT, and S4: Cp-Ti-HT samples.

Sample Code	Elements	Binding Energy / eV	Corresponding Bonds (Area / %)	Refs.
S0: Cp-Ti	O 1s	530.2 (O^{2-}) 531.9 (OH^-)	Ti^{4+}—O (83.8) Ti—OH/Non-lattice O (16.2)	[392, 393]
	Ti 2p 3/2	458.6 (Ti^{4+}) 454.1 (Ti^0)	O—Ti^{4+} (77.9) Ti—Ti (22.1)	[215, 392, 394]
S1: $NaTiO_3$	O 1s	530.2 (O^{2-}) 531.6 (OH^-) 532.9 (H_2O)	Ti^{4+}—O (75.0) Ti—OH/Non-lattice O (15.3) O—H (9.7)	[215, 393-395]
	Ti 2p 3/2	458.6 (Ti^{4+})	O—Ti^{4+} (100)	[215, 394]
	Na 1s	1071.9	O—Na (55.2)	[215]
S2: $Ga(TiO_3)_3$	O 1s	530.3 (O^{2-}) 531.9 (OH^-)	Ti^{4+}—O (49.3) Ti—OH/Non-lattice O (50.7)	[83, 215, 393-395]
	Ti 2p 3/2	458.6 (Ti^{4+})	O—Ti^{4+} (100)	[83, 215, 394]
	Ga 2p 3/2	1118.3 (Ga^{3+}/Ga^{4+})	$Ga^{3+/4+}$—O (100)	[83, 396, 397]
S3: $Ga(TiO_3)_3$-HT	O 1s	530.7 (O^{2-}) 532.4 (H_2O)	Ti^{4+}—O (82.4) O—H (17.6)	[83, 215, 394, 395]
	Ti 2p 3/2	459.0 (Ti^{4+})	O—Ti^{4+} (100)	[83, 215, 394]
	Ga 2p 3/2	1118.4 (Ga^{3+}/Ga^{4+})	$Ga^{3+/4+}$—O (100)	[83, 396, 397]
S4: Cp-Ti-HT	O 1s	529.6 (O^{2-}) 531.3 (OH^-) 532.6 (H_2O)	Ti^{4+}—O (79.17) Ti—OH/Non-lattice O (14.9) O—H (5.9)	[392, 393]
	Ti 2p 3/2	458.2 (Ti^{4+})	O—Ti^{4+} (100)	[392]

4.2.8 Degradation and ion leaching

Figure 4:7(*A-F*) demonstrated the surface alteration of S2: $Ga_2(TiO_3)_3$ and S3: $Ga_2(TiO_3)_3$-HT samples after degradation in 1 mL DMEM over 168 h. Compared

to surfaces illustrated in *Figure 4:1*, the surface deposition/growth occurred during degradation. Spherical deposits were seen on both S2: $Ga_2(TiO_3)_3$ and S3: $Ga_2(TiO_3)_3$-HT at 24 and 72 h. EDX analysis of the deposits demonstrated their composition to be rich in Ca and P. The Ca:P ratios were then obtained, as demonstrated in *Figure 4:7G*, with S3: $Ga_2(TiO_3)_3$-HT resulting in a surface Ca:P ratio close to 1.34, whereas S2: $Ga_2(TiO_3)_3$ reached 1.71 by 168 h; close to stoichiometric hydroxyapatite (Ca:P = *ca.* 1.67 [398]). Furthermore, rod-like deposits were also seen on both samples at 24 and 72 h. Their composition, as confirmed by EDX, consisted mainly of Ga and O, chemically and morphologically suggesting Ga_2O_3 or similar (GaO(OH)) had deposited [385, 399]. By 168 h, the surface morphology (*Figure 4:7E & F*) showed an absence of both spherical and rod-like surface growths in S2: $Ga_2(TiO_3)_3$, and larger clusters of rod-like deposits had formed on S3: $Ga_2(TiO_3)_3$-HT.

A combination of EDX and ICP (*Figure 4:8*) was used to identify the alteration of both surface and solution ion concentrations during DMEM degradation. Over 168 h, aqueous Ga ion concentrations gradually increased for S3: $Ga_2(TiO_3)_3$-HT (*Figure 4:8D*), as expected. However, the Ga concentrations increased at a slower rate than S2: $Ga_2(TiO_3)_3$ (*Figure 4:8B*), with a peak Ga ion concentration of 2.76 and 0.68 ppm, for S2: $Ga_2(TiO_3)_3$ and S3: $Ga_2(TiO_3)_3$-HT, respectively. The size of the error bars at 168 h in S2: $Ga_2(TiO_3)_3$ meant quantification here was difficult. Additionally, S2: $Ga_2(TiO_3)_3$ surface Ga concentration (*Figure 4:8A*) decreased over the course of 168 h, whereas the S3: $Ga_2(TiO_3)_3$-HT sample (*Figure 4:8C*) demonstrated a re-deposition of Ga during the later time points (72+ h). For both S2: $Ga_2(TiO_3)_3$ and S3: $Ga_2(TiO_3)_3$-HT, Ca and P aqueous ion concentrations decreased between 0 and 168 h (*Figure 4:8B & D*). Surface Ca and P ion concentrations increased for

S2: $Ga_2(TiO_3)_3$, (*Figure 4:8A*), however S3: $Ga_2(TiO_3)_3$-HT exhibited deposition and subsequent release during the 168 h period (*Figure 4:8C*).

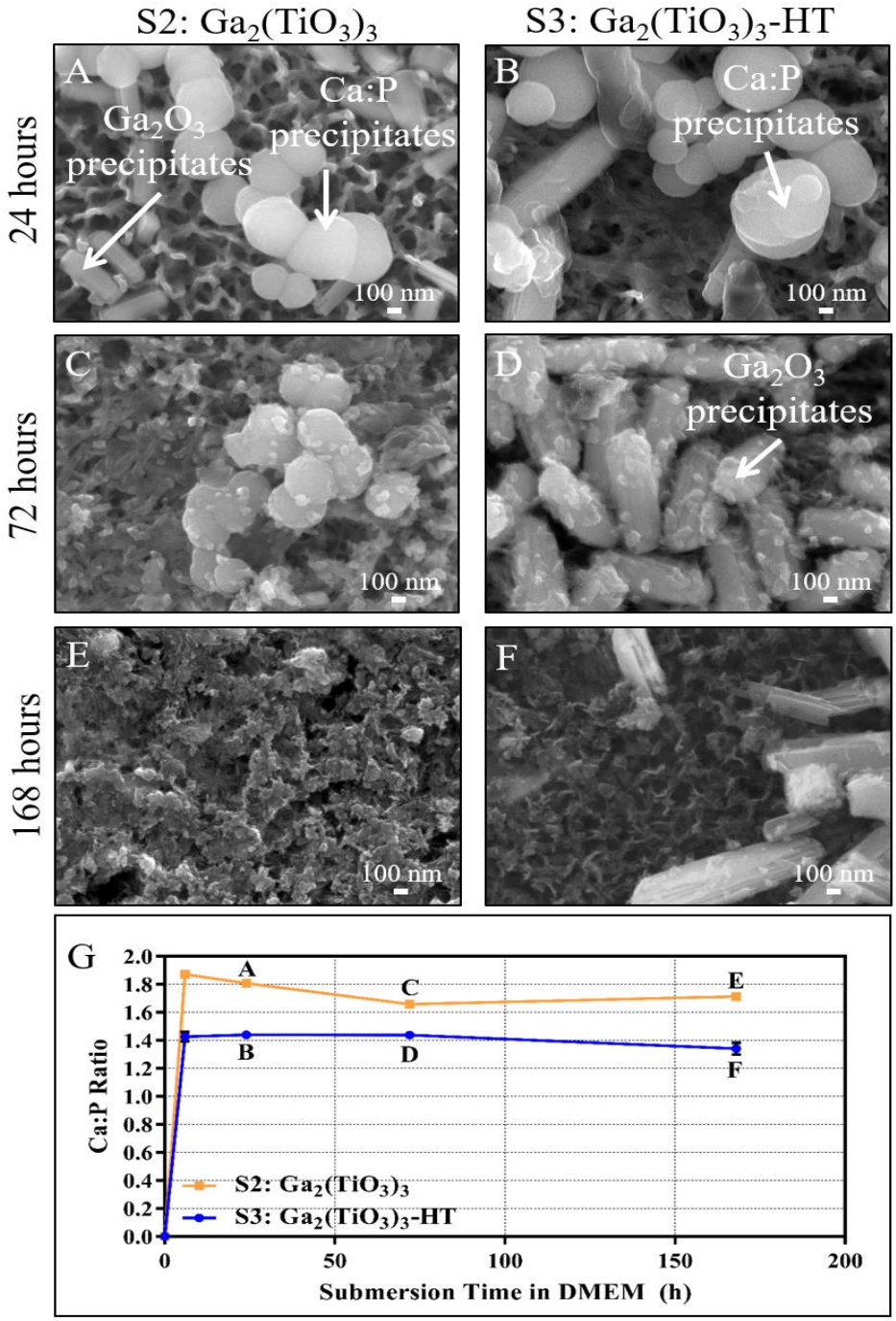

Figure 4:7. (A, C, and E) FEG-SEM images of the surface of degraded S2: $Ga_2(TiO_3)_3$ samples in 1 mL DMEM (diluted with 1:10 ratio of ultrapure water) at time points 24, 72, and 168 h, respectively. (B, D, and F) FEG-SEM images of the surface of degraded S3: $Ga_2(TiO_3)_3$-HT samples at 24, 72, and 168 h, respectively. (G) Graph showing the alteration in Ca:P ratio on the surface of S2: $Ga_2(TiO_3)_3$ and S3: $Ga_2(TiO_3)_3$-HT during the degradation study. Ca:P rich nodules and Ga_2O_3 precipitates were observed.

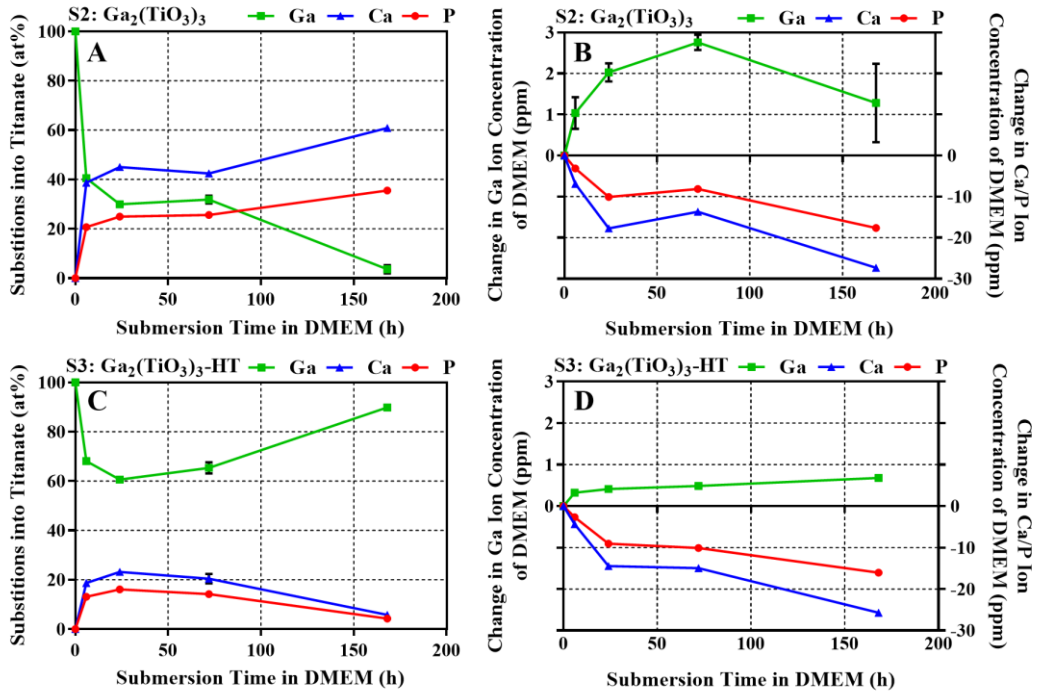

Figure 4:8. (A & C) EDX analysis of the substitution of Ca, P, and Ga ions on the surface of S2: $Ga_2(TiO_3)_3$ and S3: $Ga_2(TiO_3)_3$-HT during 168 h of degradation, respectively. (B & D) ICP Ca, P, and Ga ion alterations of S2: $Ga_2(TiO_3)_3$ and S3: $Ga_2(TiO_3)_3$-HT in DMEM solution during degradation over 168 h, respectively. Error bars of S.E.M (n = 3), with EDX taken over a 3600 μm^2 area.

4.2.9 Neutral Red Cell Viability Assay

From ISO 10993-5:2009, the definition of a cytotoxic effect demonstrated by NRU assay is a >30% reduction in cell viability from the non-treated cells (TCP control). The dotted line in *Figure 4:9* shows this threshold at 70% signal intensity. The untreated S0: Cp-Ti sample demonstrated an average signal of *ca.* 94.2%, with S2: $Ga_2(TiO_3)_3$ and S3: $Ga_2(TiO_3)_3$-HT showing average signals of *ca.* 24.2% and 81.4%, respectively. Therefore, both S0: Cp-Ti and S3: $Ga_2(TiO_3)_3$-HT samples are above the viability threshold, with a clear reduction in cell viability noted for the S2: $Ga_2(TiO_3)_3$ sample. It was shown through a One-way ANOVA, followed by the Bonferroni post-test that the S2: $Ga_2(TiO_3)_3$ sample, was the only sample that exhibited a significant difference ($p < 0.0001$; ****) from the TCP control.

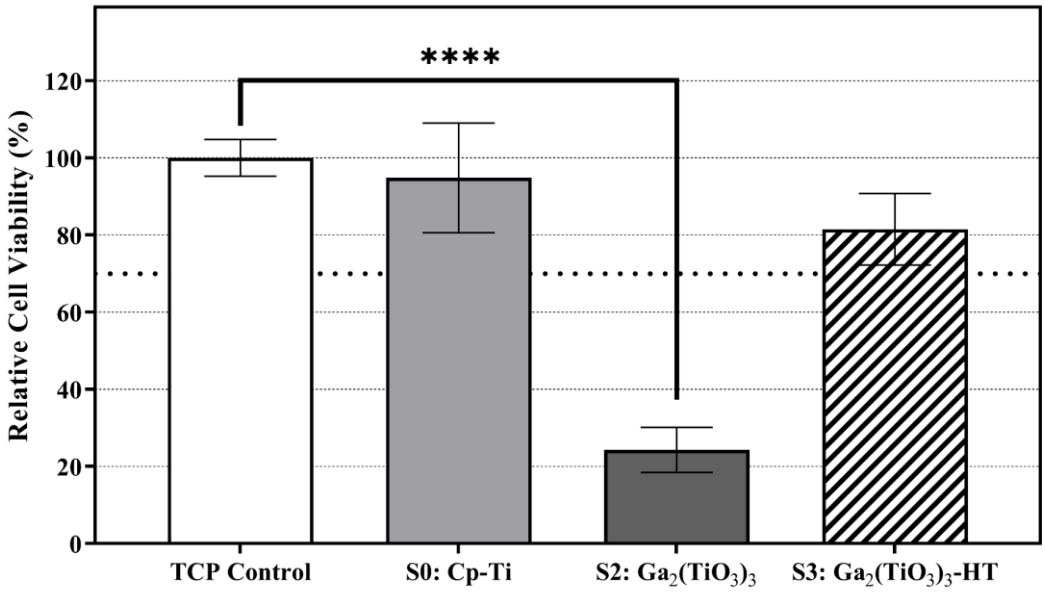

Figure 4:9. Effect of elution products of S0: Cp-Ti, S2: $Ga_2(TiO_3)_3$ and S3: $Ga_2(TiO_3)_3$-HT samples compared TCP control on the viability of MG-63 cells measured by NRU assay. All values are mean values ± SEM (n = 6). Dotted line represents 70% threshold for cytotoxic effects (ISO 10993-5:2009).

4.2.10 Microbiological LIVE/DEAD Assay

Biofilm development assay results are shown in *Figure 4:10* & *Figure 4:11*, with no significant difference being noted between the live or dead biomass on any of the samples. The presence of dead bacteria on the Ti control sample was expected due to the length of the incubation period (3 days). An antimicrobial effect would be shown either by a significantly reduced total signal (both live and dead) from either titanate structures compared to the S0: Cp-Ti control, or by a significant decrease in live (green) signal and subsequent increase in dead (red) signal. Neither of these effects were prevalent in the data shown.

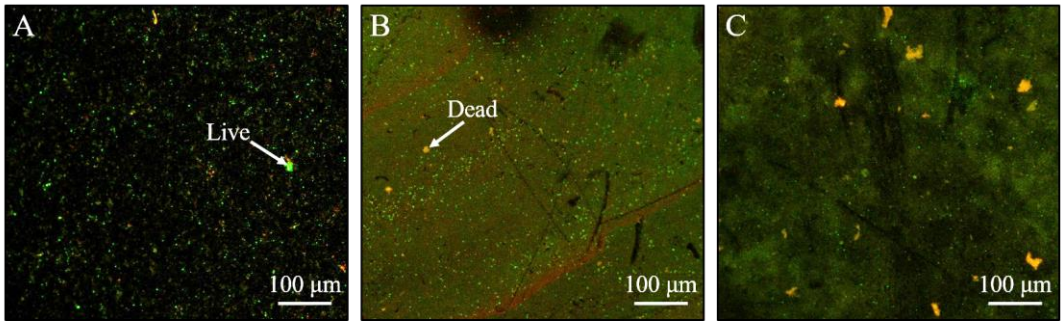

Figure 4:10. (A, B, & C) Representative LIVE/DEAD staining maps for S0: Cp-Ti, S2: $Ga_2(TiO_3)_3$, and S3: $Ga_2(TiO_3)_3$-HT, respectively. Live bacteria are stained green, with dead bacteria stained red, as indicated.

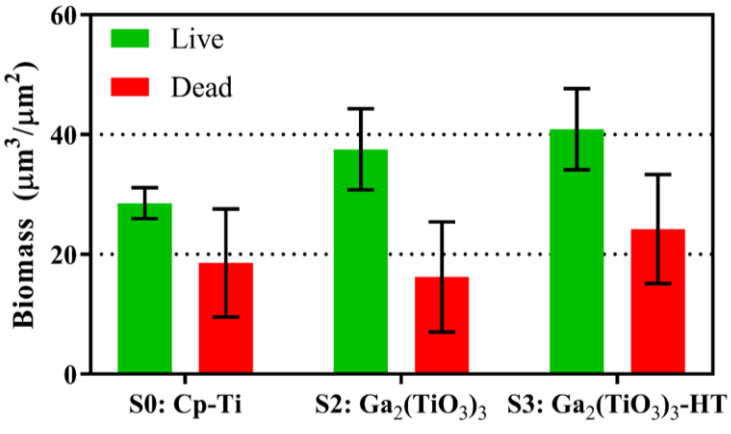

Figure 4:11. Live and dead biomass from a 3-day culture of S. aureus analysed via COMSTAT. There is no significant difference between the Live or Dead values between the samples (2-way ANOVA). The experiment was repeated, and the same trends observed (n = 3; error bars in S.E.M).

4.3 Discussion

4.3.1 Composition and topographical analysis.

The ion exchange reactions were a key development in the production of tailored titanate surfaces. This was due to the initial, layered sodium (hydrogen) titanate formed from the NaOH treatment, allowing ion incorporation and substitution with Na^+ ions already present. Not only were these surfaces able to release ions into the surrounding media, but they could also facilitate further ion exchange reactions *in vivo*, allowing the generation of calcium phosphate layers that are a precursor phase to HA [400], or release of therapeutic or antimicrobial ions [59, 401].

The nanoporous surface morphology exhibited by S1: Na_2TiO_3 and S2: $Ga_2(TiO_3)_3$ was consistent with the only other gallium titanate study published [83] (which occurred concurrently with the work presented) and the higher resolution presented in this work (*see Figure 4:1 vs. Figure 4:12*) clearly showed interesting differences from the S0: Cp-Ti control, where no significant features were present. Initially, the sodium hydrogen titanate and the isomorphic gallium hydrogen titanate formed after ion exchange, exhibited an open, nanoporous morphology. Upon heat treatment, the surface layers increased in thickness, as well as becoming denser, upon conversion to gallium titanate. Furthermore, flake-like features (Ø ≈ 100-150 nm), formed of Ga and O from EDX analysis (*Figure 4:1G* & *Table 4:2*), suggested gallium oxide/hydroxide formation. However, morphologically these features were significantly different to the gallium oxide precipitates noted on the degraded surfaces (*Figure 4:7*). A study by Dulda *et al.* demonstrated GaO(OH) precipitates formed through alkali precipitation, which morphologically were similar to the flake-like precipitates on S3: $Ga_2(TiO_3)_3$-HT [385] and correlated with the GaO(OH) peak noted in FTIR (*Figure 4:5B*), suggesting these are GaO(OH) flakes.

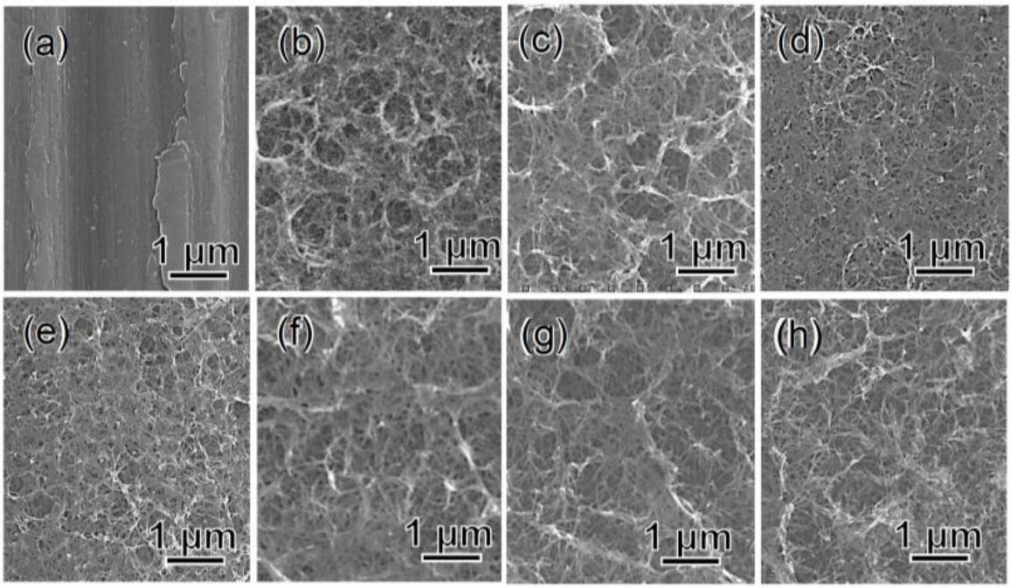

Figure 4:12. Titanate surfaces generated by Yamaguchi et al. [83]. *FEG-SEM photographs of surfaces of Ti (a) untreated or subjected to (b) 5 M NaOH treatment, and subsequent (c) 100 mM Ca + 0.05 mM Ga and (d) heat treatment (600 °C), and finally (e) water treatment (80 °C/24 h), or (f) 100 mM Ga after the NaOH treatment, and subsequent (g) heat and finally (h) water treatment.*

EDX analysis demonstrated no sodium was detectable on either gallium-treated samples, matching the lack of a Na 1s peak in XPS, indicating gallium ions readily ion exchange with sodium in the titanate structure, supporting the postulated ion exchangeability. The atomic percent of Ga exhibited in S2: $Ga_2(TiO_3)_3$ was 9.4 at.%; much greater than sodium (2.7 at.%) in S1: Na_2TiO_3. However, from the XPS analysis (*Table 4:4*), much higher concentrations of Na and Ga were found in the surface of the S1: Na_2TiO_3 (Na; 10.7 at.%), S2: $Ga_2(TiO_3)_3$ (Ga; 31.3 at.%), and S3: $Ga_2(TiO_3)_3$-HT (Ga; 38.1 at.%) samples compared to EDX. This was expected due to the diffusion gradient present within wet-chemical converted titanate samples [201, 402]. The higher Ga content, as well as the increase following heat treatment, is partially due to either the precipitation of Ga_2O_3/GaO(OH) species on the surface (exemplified through the large reduction in relative Ti content from 23.4 in S1: Na_2TiO_3 to 4.9 and 8.6 at.% in S2: $Ga_2(TiO_3)_3$ and S3: $Ga_2(TiO_3)_3$-HT, respectively), as well as potential further crystal growth following the heat treatment stage, although the probability was

low due to the excessive temperatures needed (> 1000 ºC) [403]. Furthermore, the higher Ga content compared to the Na could be due to a number of factors, including high Ga doping in the titanate structure (at either Ti^{4+} or Na^{+} sites), higher concentration of Ga in the surface compared to the sample through thickness, or additional factors such as growth mechanism variances or differences in cationic radii [404]. The surface features formed on S3: $Ga_2(TiO_3)_3$-HT were significantly different to the S4: Cp-Ti-HT sample (*Figure 4:1*), showing clear structural differences between the nanoporous titanate layers and the dense smooth rutile formed during heat treatment. The formation of an intermediate layer within the S3: $Ga_2(TiO_3)_3$-HT sample was indicative of the additional diffusion that occurs due to the heat treatment stage conducted, as described by Kim *et al.* and Kokubo *et al.* [201, 402].

The XRD results suggested the initial hydrothermally produced (S1:Na_2TiO_3), and ion exchanged layers (S2: $Ga_2(TiO_3)_3$) were amorphous in nature, since no additional crystalline peaks further to the S0: Cp-Ti control were present, correlating with the diffuse ring patterns noted in RHEED (*Figure 4:4*). This was expected as no heat treatment had been conducted, therefore, the surface layer produced should be amorphous; crystallisation temperature >500 ºC [405]. Smaller, less intense, peaks were noted in XRD, with the lower intensities potentially attributed to lower quantities of surface crystals, due to the temperature being below the stated crystallisation temperature of gallium titanate (*ca.* 1100 ºC [406]). However, this evidence alone was not conclusive, due to significant overlap with rutile, to identify the formation of titanate layers, and hence RHEED analysis was also conducted. This enabled shallower beam penetration, of the order of a few tens of nanometres, as well as higher spatial resolution (0.01-0.001 nm) [364].

Upon heat treatment (S3: $Ga_2(TiO_3)_3$-HT), the sample yielded new Bragg peaks corresponding to rutile: a characteristic phase transformation of titanium at > 600 ^oC in oxygen, as anticipated [407]. Formation of rutile was also seen in the S4: Cp-Ti-HT sample, in the RHEED *d* spacing analysis, as well as two characteristic peaks detailed in FTIR (*Figure 4:5B*), and three in Raman spectroscopy (*Figure 4:5A*). Furthermore, smaller Bragg peaks at *ca.* 26, 37, 40 and 55^o 2θ from the XRD patterns, were deconvoluted as gallium titanate derivatives, partially confirming its formation. RHEED was employed to avoid characterising just the rutile produced in S3: $Ga_2(TiO_3)_3$, as well as the Ti substrate in S1: Na_2TiO_3 and S2: $Ga_2(TiO_3)_3$, and allowed characterisation of the top surface layers alone. The similar probing depth of RHEED and XPS used in this study, therefore, provided an ideal technique to compare and corroborate results. As seen in *Figure 4:4D*, RHEED demonstrated a clear diffraction pattern for rutile on S4: Cp-Ti-HT, and matched *d* spacing values from the database, as well as confirming the results from XPS (*Figure 4:6*). Rutile diffraction rings were not observed in samples S2: $Ga_2(TiO_3)_3$ and S3: $Ga_2(TiO_3)_3$-HT. However, even with RHEED, it was noted that the S1: Na_2TiO_3, S2: $Ga_2(TiO_3)_3$, and S3: $Ga_2(TiO_3)_3$-HT samples exhibited a more diffuse pattern than S4: Cp-Ti-HT, which caused overlap and complicated the quantification. This diffuseness could be attributed to the amorphous sodium or gallium hydrogen titanate layers present. Despite the diffuse rings, quantification of *d* spacing values was possible for S1: Na_2TiO_3, S2: $Ga_2(TiO_3)_3$, and S3: $Ga_2(TiO_3)_3$-HT, which matched sodium titanate derivatives ($Na_{0.23}TiO_2$ and Na_4TiO_4) and titanium; calcium and sodium titanate variants ($CaTi_2O_5$ and Na_2TiO_3); and gallium and calcium titanate derivatives (Ga_2TiO_5 and $CaTi_2O_5$), respectively. The gallium titanate phases noted here agreed well with the study by Yamaguchi *et al.* [83].

The evidence demonstrated through XRD and RHEED, was supported by IR absorption spectrometry, (*Figure 4:5*), which demonstrated characteristic TiO_6 octahedron vibrations, Ti—O bond stretching and Ti—OH non-bridging bonds of titanate structures. Edge-sharing TiO_6 octahedra and Ti—O—Ti stretching were also present in the Raman analysis [381-383]. Additionally, XPS also supported titanate formation, through the presence of Ti^{4+}—O bonding [408], which was ubiquitous across all samples, in both the Ti 2p and O 1s deconvolution, and is characteristic of titanate structures, as discussed by Takadama *et al.* [215].

Specifically, for S1: Na_2TiO_3, there were no other FTIR absorption bonds corresponding to sodium titanate formation, however, this may be attributed to limitations on the FTIR spectrometer used, which made analysis lower than 600 cm^{-1} difficult [409]. Nevertheless, FTIR ruled out formation of re-precipitated NaOH, due to the lack of characteristic O—H tension peaks around 3600 cm^{-1} [384]. Despite this, Raman (*Figure 4:5*) and XPS analysis confirmed the presence of Na—O bonds, which were readily seen in sodium titanate structures [410]. The additional presence of O—H bending modes in Raman (as described by Oleksak *et al.* [391]), and –OH bonds in XPS, before and after heat treatment, suggested amorphous sodium and gallium hydrogen titanate may also be present on the surface.

The shoulder exhibited between 800-900 cm^{-1}, shown in FTIR for S2: $Ga_2(TiO_3)_3$, may have corresponded to GaO(OH) vibrations and Ga—OH bending modes, which could be attributed to gallium hydrogen titanate formation prior to heat treatment, as well as the GaO(OH) flakes noted in *Figure 4:1G* [385, 399]. Furthermore, peaks demonstrated by Raman spectroscopy may correspond to gallium oxide, as shown by Zhao *et al.* [386], Rao *et al.* [411], and Gao *et al.* [412], or derivatives of gallium titanate. The Raman peak at 700 cm^{-1} remains as a shoulder in S3: $Ga_2(TiO_3)_3$-HT,

and correlates with the GaO(OH) flakes seen in *Figure 4:1G*. Gallium titanate formation is also confirmed by XPS analysis, with the Ga 2p 3/2 peak position at *ca.* 1118.5 eV relating to Ga—O in its Ga^{4+} state, which may be doped at various Ti^{4+} sites, as detailed by Deng *et al.* [396]. On the contrary, a study by Surpi *et al.* observed modifications of TiO_2 thin films through the influence of a Ga focused ion beam, and demonstrated that a Ga 2p 3/2 position of *ca.* 1118.6 eV may also correspond to Ga^{3+}, characteristic of Ga_2O_3 [397]. Both 3+ and 4+ Ga states are suggested by Yamaguchi *et al.* following co-doping of Ga and Ca into the titanate structure [83]. Despite the discrepancy, the presence of $Ga^{3/4+}$, Ti^{4+} and O bonding *via* XPS, as well as the presence of Ti—O Raman bonds in S2: $Ga_2(TiO_3)_3$, suggested gallium titanate formation, irrespective of the valence state of Ga, since the cationic doping was ionic in form, similar to Na^+, Ca^{2+} etc. [78]. A significant alteration, which correlates well with the EDX results previously mentioned, was the reduction in the Na 1s peak in XPS for both S2: $Ga_2(TiO_3)_3$ and S3: $Ga_2(TiO_3)_3$-HT, demonstrating complete Na replacement, and the subsequent formation of gallium titanate.

In addition to titanate formation, broad absorption peaks from 3000-3500 cm^{-1}, seen in both S1: Na_2TiO_3 and S2: $Ga_2(TiO_3)_3$, could be ascribed to H—O—H stretch bonds of any remaining surface, or chemisorbed/interlamellar, water since this stage was prior to the heat treatment step [387]. The removal of these peaks in both heat-treated samples: S3: $Ga_2(TiO_3)_3$-HT and S4: Cp-Ti-HT, support this postulation and is further backed up by Shiropur *et al.,* who showed peak elimination during dehydration [381]. Interestingly, FTIR demonstrated a peak at 1100 cm^{-1} in both S1: Na_2TiO_3 and S2: $Ga_2(TiO_3)_3$, potentially matching Ti—O—C vibrations, which is unexpected, as the carbon location would be in place of either gallium or sodium in the titanate structure [388]. It was evident from the heat treatment stage, through the

generation of doublet peaks at 2880 cm^{-1} (S3: $Ga_2(TiO_3)_3$-HT) and the shoulder at 2350 cm^{-1} in FTIR, matching C—H bonds and atmospheric CO_2, respectively, that carbon contamination on the surface of the samples was present and unavoidable [389].

4.3.2 Surface degradation and ion release

During submersion in DMEM spherical and rod-like deposits, which through EDX analysis were found to be formed of Ca:P, and Ga:O, respectively, were noted (*Figure 4:7*). Morphologically, the rod-like Ga:O deposits look similar to those generated by Zhao *et al.* and Shah *et al.* [413, 414]. Deposition may have occurred due to over-saturation of the surrounding solution. However, further studies would be needed to confirm this postulation. Additional EDX analysis was conducted on the Ca and P deposits to understand the Ca:P ratio, and whether these deposits were similar to HA. For S2: $Ga_2(TiO_3)_3$, the Ca:P ratio increased significantly above 1.8 within 6 h and gradually plateaued at 1.71 by day 7. This was in stark contrast to the heat-treated sample (S3: $Ga_2(TiO_3)_3$-HT), which had a Ca:P ratio of *ca.* 1.42 at 6 h and reached a final ratio of 1.34 by 7 days. Stoichiometric HA contains a Ca:P = 1.67, with calcium deficient and calcium rich HA having ratios of < 1.67 and > 1.67, respectively [415]. Correlating this with the Ca:P generated on both samples, S2: $Ga_2(TiO_3)_3$ and S3: $Ga_2(TiO_3)_3$-HT were calcium rich and calcium deficient, respectively. Studies conducted by Kizuki *et al.* demonstrated the relative propensity for ion inclusion into the titanate layer for Ca^{2+} and Na^{+} [218]. The studies concluded that, even with a calcium contamination of 0.0005% in the sodium containing solution, divalent Ca^{2+} ions would preferentially enter the structure, as it had a more potent electrostatic attraction to negative TiO_6 [387]. It was hypothesised that the calcium contained within the solution, preferentially ion exchanged into the surface layer due to its

relatively higher propensity, as demonstrated through literature studies investigating Ca^{2+} ions preferentially exchanging into the titanate structure [52, 77, 82]. As S2: $Ga_2(TiO_3)_3$ has a less stable layer compared to S3: $Ga_2(TiO_3)_3$-HT, due to the increased release rate of Ga ions, this explained why there was a higher Ca content on S2: $Ga_2(TiO_3)_3$.

The opening of the porous network, as well as the deposition of Ca:P and Ga_2O_3 exhibited in the micrograph images (*Figure 4:7*), correlated with the ICP and EDX analysed ionic alterations on the sample's surface and in solution. As shown in *Figure 4:8*, S3: $Ga_2(TiO_3)_3$-HT released gallium at a much slower rate than S2: $Ga_2(TiO_3)_3$, suggesting the heat treatment had a significant effect on the stability of the titanate surface generated. Moreover, the peak Ga solution concentration was much greater for S2: $Ga_2(TiO_3)_3$ (2.76 ppm; day 3) compared to S3: $Ga_2(TiO_3)_3$-HT (0.68 ppm; day 7). Additionally, the trend in surface concentration of Ga in *Figure 4:8* agreed well with the micrographs presented in *Figure 4:7*. The S2: $Ga_2(TiO_3)_3$ sample exhibited an overall decrease in Ga ions with no deposition occurring, whereas S3: $Ga_2(TiO_3)_3$-HT demonstrated a deposition of Ga back onto the surface after 24 h, with a large proportion of Ga:O deposits. Furthermore, the decrease in solution ionic concentrations of Ca and P, as well as the overall increase of these ions on S2: $Ga_2(TiO_3)_3$, related to the deposition of Ca:P deposits seen in *Figure 4:7*. The anomalous re-release of Ca and P from the surface of S3: $Ga_2(TiO_3)_3$-HT, which did not match the solution concentration, could be due to detachment of Ca:P precipitates, which were not detectable *via* ICP; no suspended precipitates were seen in the aqueous solution however. Distinction between Ca ions penetrating into the titanate layer and deposition on the surface was not possible with the techniques used, hence further studies would be needed.

The mechanism for calcium phosphate formation, and subsequent apatite maturation, has been explained previously by [52, 416]. The surface titanate layers, containing positive metallic ions, with this case being Ga^{3+}, facilitate ionic exchange between H_3O^+ (hydronium) ions and Ga^{3+}. This exchange generates Ti—OH bonds upon the top surface of the titanate layers, generating an overall negative surface charge. This negative charge allows Ca^{2+} ions to preferentially ion exchange into the surface. High concentration of Ca^{2+} ions on the surface generates an overall positive surface charge, allowing phosphate ions present within the DMEM solution to be attracted to the surface generating calcium phosphate precipitates (*Figure 4:7*). Since S3: $Ga_2(TiO_3)_3$-HT contained a heat treatment stage and, therefore, had a more stable surface layer, Ga release was much lower than S2: $Ga_2(TiO_3)_3$ (*Figure 4:8*), which evidently resulted in lower consumption of Ca ions from the DMEM onto the surface (*Figure 4:7* & *Figure 4:8*). This was evident in the calcium-deficient Ca:P precipitates present on S3: $Ga_2(TiO_3)_3$-HT, as well as the smaller quantity of precipitates present on the surface (*Figure 4:7*).

Although the relationship between heat treatment temperatures and Ga release was not investigated here, the conversion of a sodium titanate hydrogel following heat treatments was the subject of a previous study by Kim *et al.* Their findings showed that the progressive increase in heat treatment temperatures converted the gel into an amorphous and crystalline sodium titanate at 400 and 700 °C, respectively, reducing its reactivity and propensity to form apatite in simulated body fluid [77]. It is postulated that Ga ion release would decline with increases in heat treatment temperatures in a similar manner.

4.3.3 Cytotoxicity and antimicrobial assessment

Initial evaluation on the effect of titanate surfaces on human cells was performed *via* a Neutral Red Uptake assay. Upon exposure to media, which had been in contact with the samples for 7 days, significant reduction in cell viability was only shown for S2: $Ga_2(TiO_3)_3$, with the performance of the control S0: Cp-Ti, S3: $Ga_2(TiO_3)_3$-HT and cells exposed to untreated media showing no significant differences (*Figure 4:9*). From the ICP analysis, the maximum Ga^{3+} release for the S2: $Ga_2(TiO_3)_3$ and S3: $Ga_2(TiO_3)_3$-HT samples were 2.76 and 0.68 ppm (39.6 and 18.6 µM), respectively. Although these concentrations were lower than those commonly seen in the literature for Ga^{3+} toxicity to human cells, the hypothesis that the heat treatment stabilised the rate of gallium release was supported by these results [417, 418]. The toxicity of Ga^{3+} can also be affected by local Fe^{3+} concentrations and any binding molecules, which can promote Ga^{3+} uptake into the cells. It was also possible that a toxic pH was caused by the elutant of the S2: $Ga_2(TiO_3)_3$ samples during ion exchange within the structure; an effect which was lost after heat treatment.

In the pilot microbiology study *S. aureus* was used, as it was a clinically relevant pathogen commonly associated with nosocomial infection and orthopaedic biofilm infections, occurring in as many as 75% of joint infections [419-421]. Although Ga^{3+} has been demonstrated to be antimicrobial against a wide variety of pathogens, its efficacy varies over a wide range of inhibitory concentrations (µM-mM) specific to each bacterial strain. An antimicrobial effect of gallium titanate structures against *A. baumannii* has been recently demonstrated by Yamaguchi *et al.* [83]. *A. baumannii* has been found to be particularly susceptible to Ga^{3+} (2-100 µM), whereas *S. aureus* is relatively more resistant compared to other species (0.32-5.12 mM) [241, 247]. Although the concentration of gallium used to produce these structures was far higher than in the *Yamaguchi* study, these results suggested that it still fell short of the

minimum inhibitory concentration required to prevent a *S. aureus* infection. In DMEM, the Ga^{3+} release after 6 h was 1.04 and 0.32 ppm for S2: $Ga_2(TiO_3)_3$ and S3: $Ga_2(TiO_3)_3$-HT, respectively (15 and 4.6 μM in 1 mL solution), which fell well below the toxic concentrations for *S. aureus*, in addition to being considerably lower than concentrations clinically used [422]. However, upon reflection, further, more comprehensive, microbiological studies should be conducted to fully elucidate the antimicrobial status of gallium titanate surfaces against *S. aureus* and other common nosocomial pathogens.

4.3.4 Summary

This chapter aimed to generate gallium titanate structures through the use of wet chemical ion exchange reactions of sodium titanate surfaces, in order to confer antibacterial properties. As evidenced from the results, this chapter has highlighted both positive and negative aspects regarding the production and characterisation of these surfaces. The successful production of gallium titanate surfaces, and their subsequent heat treatment, was achieved for the first time, concurrently with the study by Yamaguchi *et al.* To date, the Yamaguchi *et al.* study remains as the only known investigation, aside from the study presented within this thesis, into the production of gallium titanate surfaces for antibacterial applications [83]. The similar chemical and structural properties between the studies exemplified the reproducibility of such structures. Furthermore, this work demonstrated that the cytotoxicity of the surface can be controlled through the heat treatment stage, which is certainly beneficial for biomedical applications. However, despite the inability to demonstrate appropriate antibacterial properties, this result was not wholly negative, since subsequent tailoring of the structures, as well as broad testing against a wide variety of bacterial types, would glean a more comprehensive analysis of the applicability of these structures.

Ultimately, this preliminary study has highlighted the potential of these structures as a multifunctional orthopaedic surface.

The potential of nanoporous titanate structures to be produced onto non-Ti containing surfaces, therefore broadening the applicability of these structures, has been explored in the subsequent chapter (*Chapter 5*).

Chapter 5. Understanding the Titanate Mechanism & the Translation onto Non-Ti Substrates

5.1 Introduction

Nanoporous titanate surfaces have been previously limited to Ti and its alloys, due to the nature of the chemical conversion employed. To address this, this chapter highlights a novel method for generating nanoporous titanate structures on alternative biomaterial surfaces, such as other metals/alloys, ceramics or even polymers, to provide bioactive and/or antibacterial properties in a simple yet effective way. In this chapter, optimisation of sputtering parameters (*Section 5.2.1*), such as substrate biasing (*Section 5.2.1.3*) and substrate heating (*Section 5.2.2.1*) was conducted, ensuring batch-to-batch and sample-to-sample consistency of Ti thin films, which were generated on polished and sandblasted 316L stainless steel (SS) substrates, to confirm titanate formation through wet chemical conversion.

Initially, calibration assessments were conducted to establish optimum processing conditions, with the focus being on the appropriate target current density, as well as understanding the sputtering rates through SEM and ellipsometry calibration measurements (*Section 5.2.1.1*). Wet chemical (NaOH; 5M; 60^{o}C; 24 h) conversion of DC magnetron sputtered Ti surfaces on 316L stainless steel were investigated to explore the effects of microstructure, specifically the comparison between columnar and equiaxed microstructures, on sodium titanate conversion (*Section 5.2.2*). Additionally, further insights into the growth mechanism of titanate structures as a function of the sputtered Ti coating thickness (*Section 5.2.4*), and oxygen content (using Ti6Al4V *vs.* TiO_2 microspheres; *Section 5.2.5*) is presented. Prior to this study, no research had been conducted on the production of titanate layers on Ti-containing

microspheres. The study presented investigated the effect of oxygen (O) content in Ti based microspheres (comparing Ti6Al4V and TiO_2 microspheres due to the relative ease of producing Ti6Al4V and TiO_2 microspheres of similar size) to ascertain whether the presence of oxygen was limiting the titanate mechanism and whether titanate structures could be produced on 3D surfaces. Similarly, the study conducted on titanate growth as a function of initial Ti thickness was the first of its kind, with incremental thicknesses (50, 100, 200 and 500 nm) measured to understand the morphological, structural and chemical properties of the converted surfaces. These results are then discussed in detail in *Section 5.3*.

5.2 Results

5.2.1 Optimisation of Sputtering Rate, Viability and Variability of Ti Thin Films

In order to determine appropriate sputtering conditions, and to calculate the appropriate sputtering rates for each of the chosen sputtering parameters, calibration and optimisation experiments were first conducted. Initially, the target current for the sputtered Ti films was varied, with the sputtering rate variations, as well as the chemical and structural differences in the films produced, being measured. Comparisons were made between shorter and longer time point sputtering runs in order to determine the accuracy of SEM thickness measurements, through a combination of ellipsometric (shorter time point) and SEM thickness (longer time point) measurements. Sample and batch-to-batch reproducibility was also conducted to demonstrate efficacy of the sputtering processes.

5.2.1.1 Effect of Target Current Variation on Coating Thickness

Three nominal target current values (1, 3, and 5 A, in line with typical literature values and the maximum safe target current for the rig used. Samples are denoted NB/NH for no substrate bias/no *in situ* heating) were utilised to compare the chemical, morphological and structural differences, as well as thickness variation, in the

produced Ti films. Both short (5, 10 and 15 min) and long (1 h) time points were investigated, utilising ellipsometry and SEM analysis to measure film thickness, respectively. Ellipsometry measurements are shown in *Table 5*:*1*, and demonstrate that the 1 A samples achieved a thickness of *ca*. 40.8 nm after 15 min. The samples produced at 3 A achieved a thickness of *ca.* 90 nm, whilst the 5 A samples revealed *ca.* 146 nm thick film after the same sputtering period requiring manual fitting of the data. Both 3 and 5 A samples after 15 min could not be measured due to the thickness being greater than the machine tolerance.

Table 5:1. Ellipsometry film thickness measurements of NB/NH samples at 1, 3 and 5 A target currents. Where possible, standard model fitting was employed, unless otherwise stated. Value omissions are due to thicknesses exceeding the method's capability: > ca. 150 nm from the data presented in this thesis.

Current / A	Time / min	Thickness / nm	Uniqueness / nm	Std. Dev. (*n* = 9)	Refractive Index (*n* at 632.8 nm)
1	5	14.6	1.5	0.2	2.047
	10	27.8	1.2	0.2	2.495
	15	40.8	3.0	0.2	2.218
3	5	49.6	6.0	0.4	2.384
	10	90	Manual fit	Manual fit	-
	15	-	-	-	-
5	5	87	9	0.3	2.197
	10	146	Manual fit	Manual fit	2.149
	15	-	-	-	-

The ellipsometry outputs obtained are also plotted in *Figure 5*:*1.* It must be noted that uniqueness and standard deviation values are presented, which have different statistical meanings. Uniqueness is a measure of how unique the model is, which is estimated by changing the thickness and then refitting all other parameters, with its value corresponding to an *ca.* 10% change in the mean square error (MSE). Standard deviation values are the standard deviation of the best fits taken at 9 data points, demonstrating how uniform the film is and how reproducibly the model fits the data.

Refractive index was calculated as an additional check for the accuracy of the model, with the JA Woollam Library refractive index of polycrystalline Ti = 2.16.

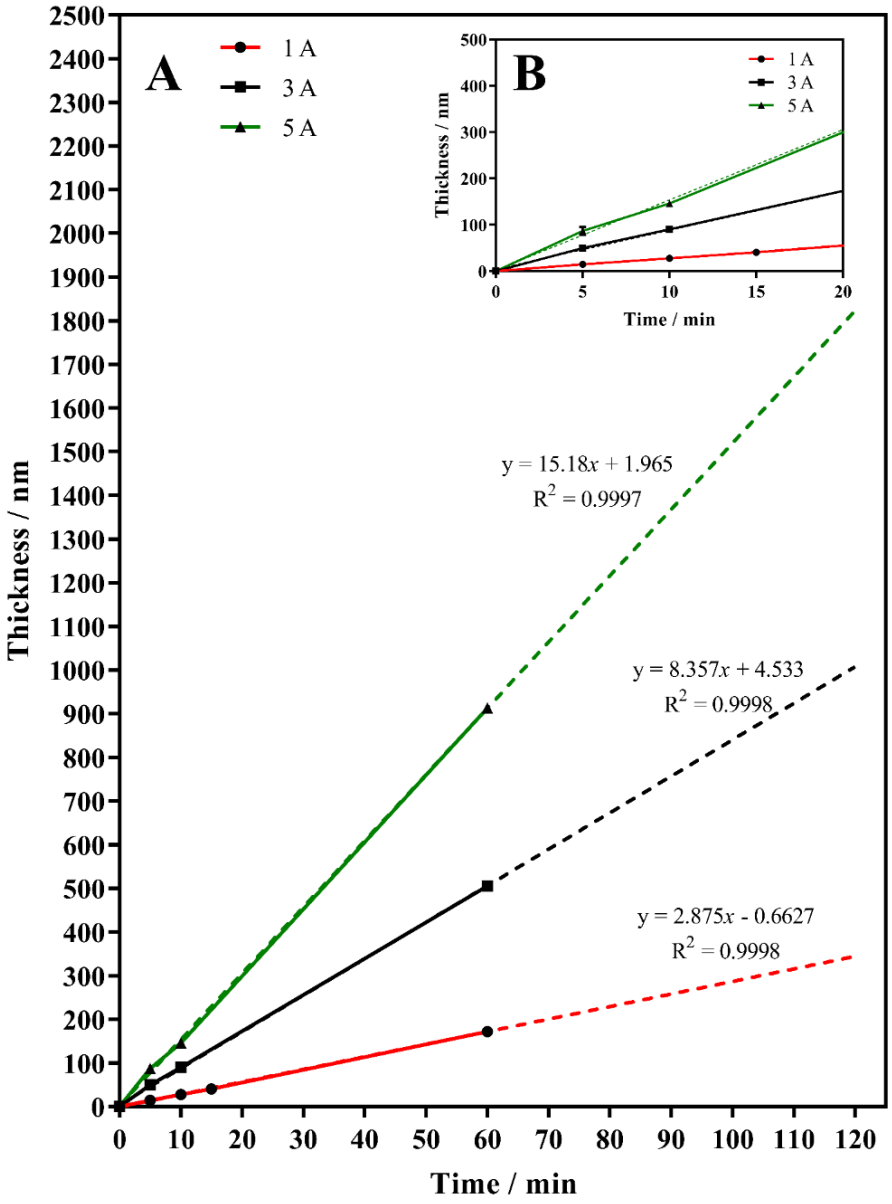

Figure 5:1. Combined ellipsometry and SEM cross-sectional thickness measurements of the non-biased/non-heater (NB/NH) samples using 1, 3 and 5 A target currents at varying time intervals. A) Combined thickness measurements, with calculated linear regressions using GraphPad Prism; line equations and respective R^2 values are given. B) Ellipsometry thickness measurements only of the aforementioned samples demonstrating linearity even at short time points. Raw data = solid lines, linear regression = dashed.

To further confirm the linearity of sputtering thickness with time, a longer time point of 1 h was used, and assessed using cross-sectional SEM (*Figure 5*:*2*). Through the application of higher target current, and in extension a higher power density (target area remains constant), the coatings increased in thickness from *ca.* 172 nm in the 1 A (NB/NH) sample to *ca.* 505 and 913 nm in the 3 A and 5 A samples (both NB/NH), respectively, confirming their linearity despite the same sputtering time. The size and presence of the Ti grains and voids, respectively, also increased with increasing target current, as shown *via* SEM analysis (see *Figure 5*:*2*), further demonstrating the columnar grown film morphology.

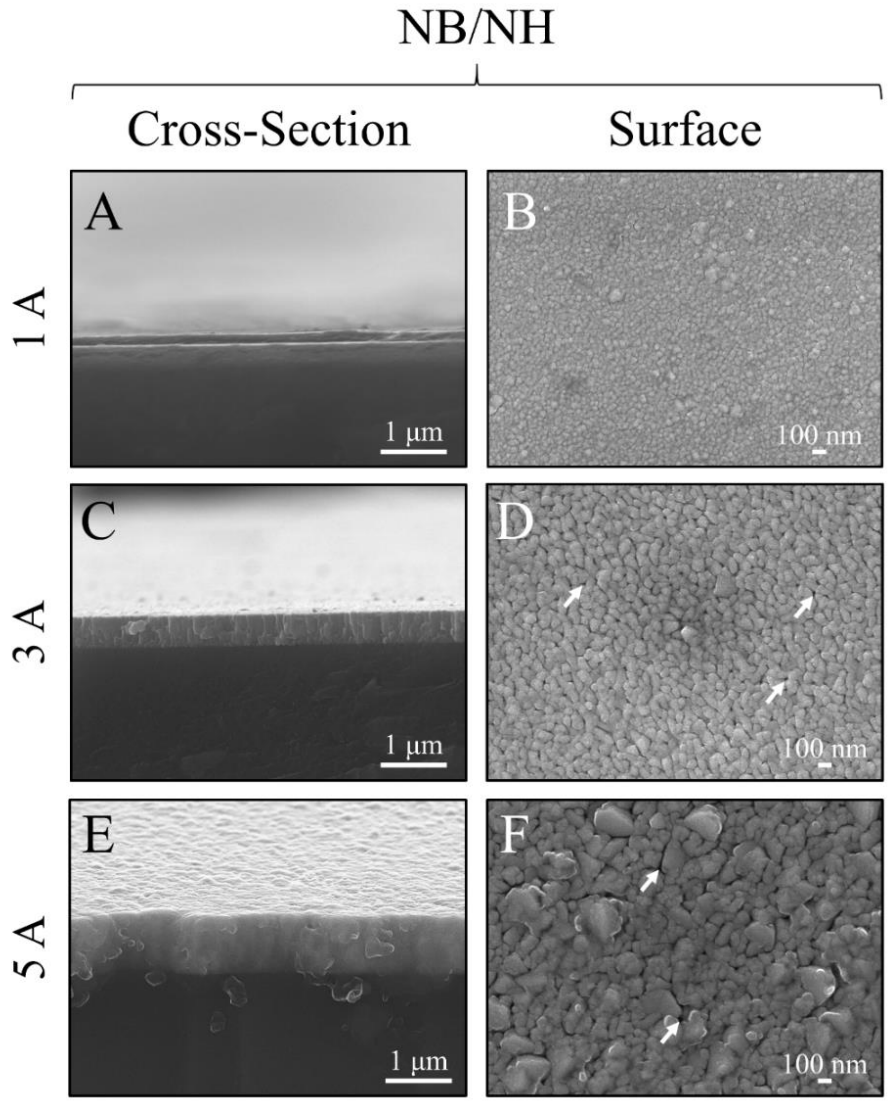

Figure 5:2. Cross-sectional and surface SEM micrographs demonstrating the surface morphology, as well as the thickness of the produced coatings. A, C, & E) Cross-sectional micrographs of the 1, 3, and 5 A NB/NH samples, respectively. B, D, & F) Surface micrographs of the 1, 3, and 5 A NB/NH samples, respectively. White arrows demonstrate the presence of voids between the grown Ti grains.

5.2.1.2 Reproducibility (Sample and Batch-to-Batch)

To quantify homogeneity of the film thicknesses produced, as well as the batch-to-batch reproducibility of such coating regimes, both 2 and 4 μm thick Ti coatings were produced using 5 A target currents. Additionally, the sputtering rates (*Figure 5:3*) for the sputtering parameters used were also calculated. Individual samples had 15 measurements (5 different measurements taken at 3 separate coating locations) in

order to assess the variance in coating homogeneity. Batch-to-batch reproducibility was assessed using a random sample from 3 separate batches, with 15 measurements taken per sample (Batch n = 3, total n = 45). All measurements were conducted using cross-sectional SEM (*Figure 5*:*4*).

The coating thickness homogeneity (*Figure 5*:*3* & *Figure 5*:*4A*) for the randomly selected 2 μm sample demonstrated a mean coating thickness of *ca.* 1996 nm (± 8 nm), with batch-to-batch thicknesses of *ca.* 1999 nm (± 6 nm), signifying good reproducibility (*Figure 5*:*3*). For the 4 μm run, the coating thickness homogeneity (*Figure 5*:*4C*) decreased as compared to the intended coating thickness (predicted based on the fitting equation in *Figure 5*:*1*), at *ca.* 3892 nm (± 36 nm), which was within an agreeable tolerance (± 5%). The batch-to-batch reproducibility also demonstrated agreement within the aforementioned tolerance, at 3853 nm (± 31 nm) (*Figure 5*:*3*). Due to chronology of the batches produced (all 2 μm runs were conducted first, followed by all 4 μm runs), a reduction in desired thickness was expected due to erosion of the target *vs.* sputtering time, localised higher target cooling, and increased substrate-target distance affecting the mean free path. Clear uniformity was seen in both the surface and cross-sectional SEM micrographs, demonstrating appropriate reproducibility for the optimised sputtering runs. A further observation, which was in good agreement with the optimisation experiments conducted previously, was the growth in grain size from the surface SEM micrographs (*Figure 5*:*4B & D*) as the film thickness increased.

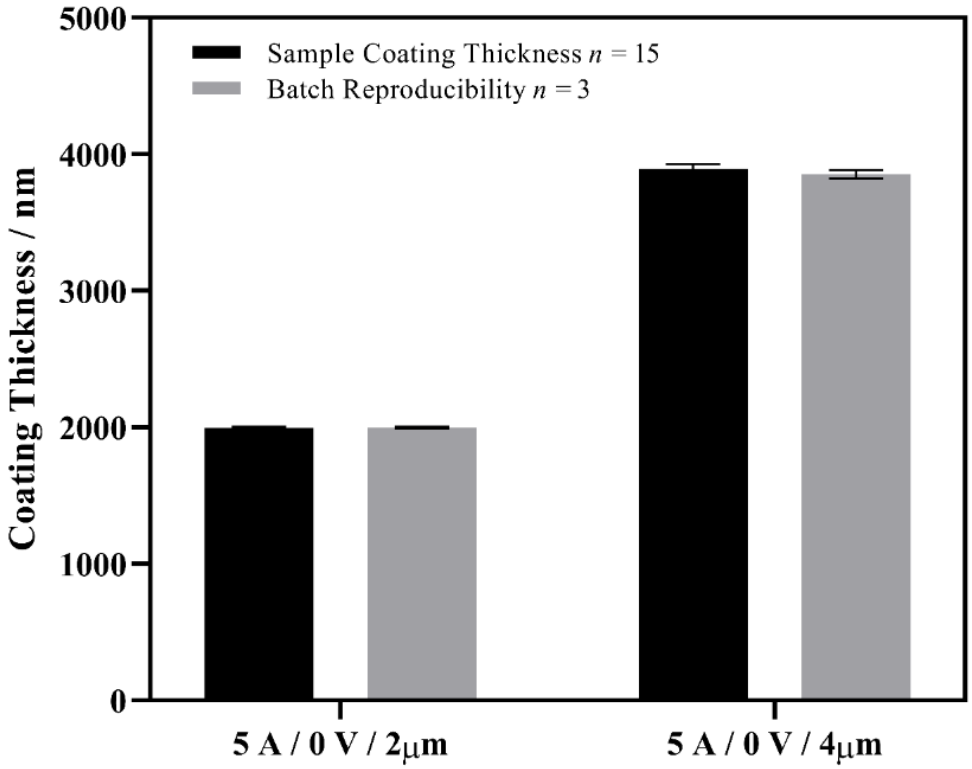

Figure 5:3. Thickness measurements of 2 and 4 μm reproducibility runs. Sample homogeneity and batch-to-batch variability are detailed, with clear reproducibility shown due to the low error shown. All values are calculated values with standard error (n = 15 & 3 for samples and batch-to-batch measurements, respectively)

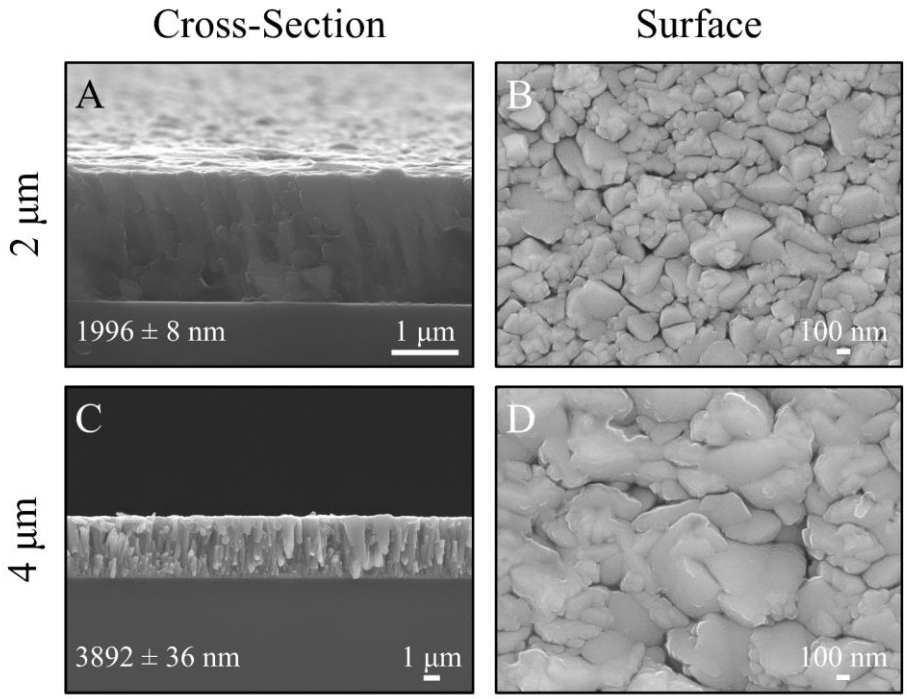

Figure 5:4. Surface and Cross-sectional SEM measurements of 2 and 4 µm reproducibility runs. A & B) Representative SEM micrographs of the film cross-section and surface for the 2 µm reproducibility run, respectively. C & D) Representative SEM micrographs of the film cross-section and surface for the 4 µm reproducibility run, respectively. Thicknesses given are average as the average of n = 15 measurements with standard error.

5.2.1.3 Effect of Substrate Bias on Sputtering Rate

To further understand how varying sputtering parameters affect the sputtered films produced, a -100 V bias (as indicated by TEER Coatings Ltd., the manufacturer of the industrial rig used, to be optimal between increasing the surface energy given to the film, whilst minimising the effect of re-sputtering of the coating due to ion-bombardment) was applied to the substrates during sputtering (herein labelled B/NH). This was conducted to direct some of the Ar^+ within the plasma towards the substrates, resulting in energy transfer to the film produced, potentially generating a more equiaxed coating through atomic reordering.

SEM analysis of the cross-sectional and surface morphologies of the films produced are described in *Figure 5*:*5*. In comparison to the thicknesses described in

Figure 5:*2*, the biased film thicknesses exhibited a reduction, which was more apparent in *Figure 5*:*6*. The 1 A B/NH sample exhibited a film thickness of 167 nm (± 5 nm), which reduced from 172 nm (± 3 nm) in comparison to the NB/NH counterpart. Both the 3 and 5 A B/NH samples demonstrated film thicknesses of 457 (± 6 nm) and 807 nm (± 13 nm), respectively; the thickness reductions were *ca.* 48 and 106 nm, respectively. All B/NH samples exhibited a relatively smoother morphology (lower appearance of surface voids and smaller Ti grains) in comparison to the NB/NH samples.

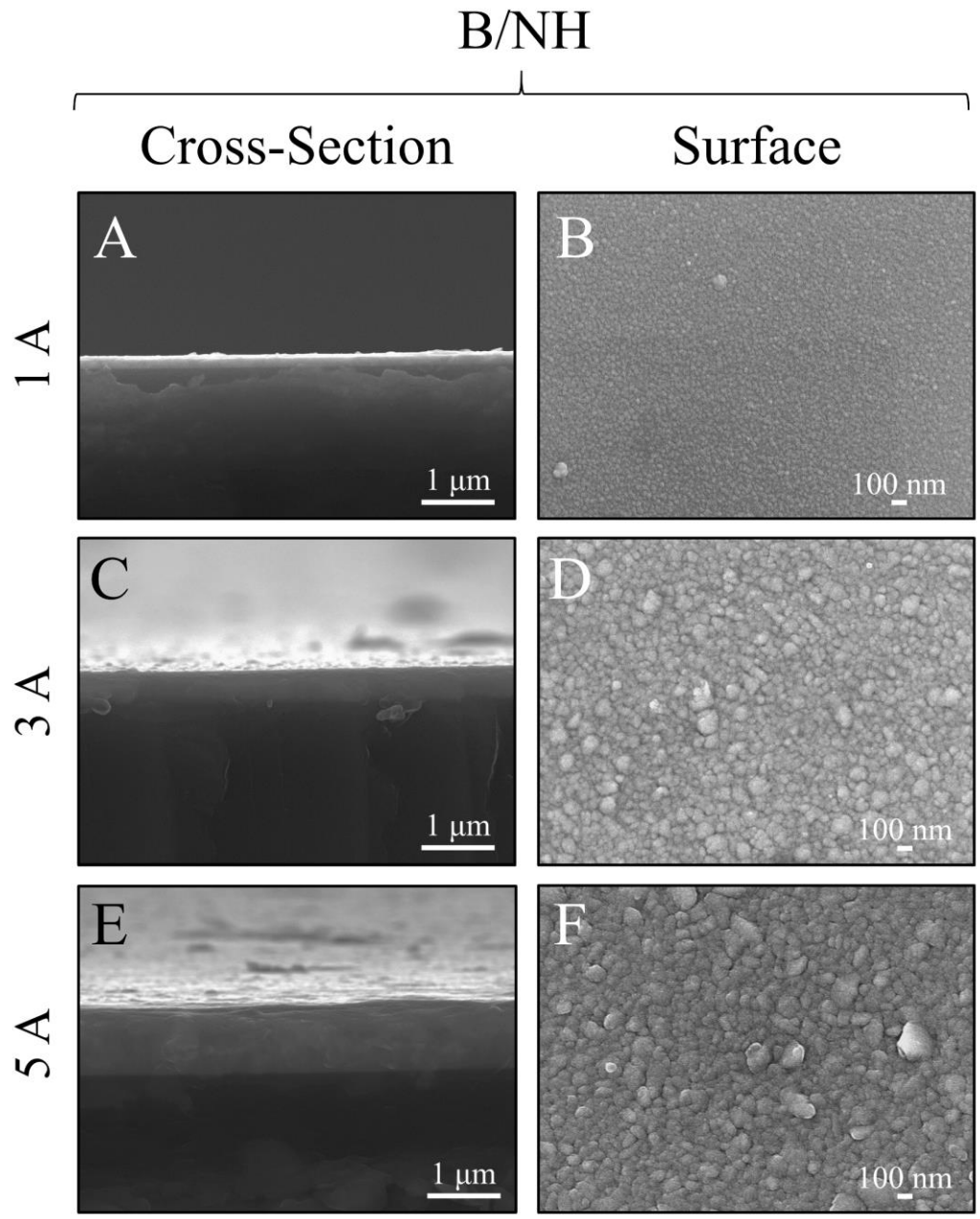

Figure 5:5. Comparison of SEM surface morphologies and cross-sectional thin film thickness due to varying target currents of 1 h sputtering runs, of the B/NH samples. A, C & E) Cross-sectional thickness of NB/NH samples using 1, 3, and 5 A target currents, respectively; B, D, & F) Surface morphology of NB/NH samples using 1, 3, and 5 A target currents, respectively.

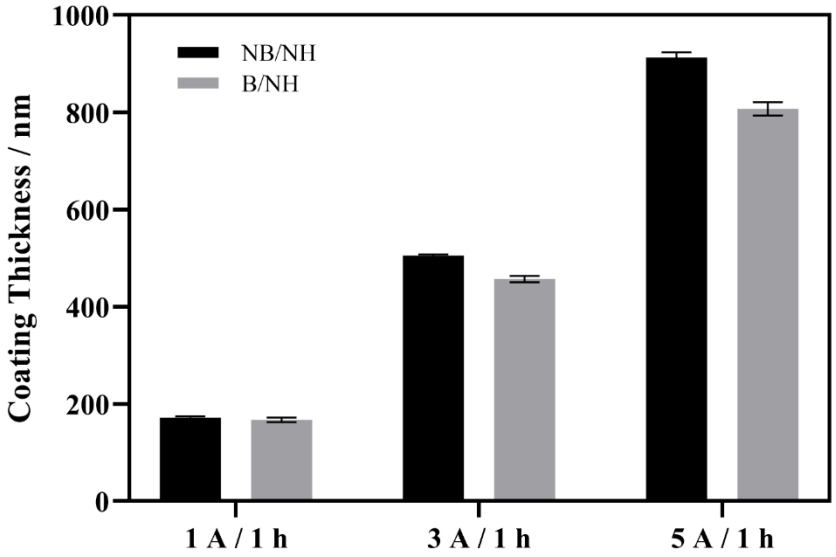

Figure 5:6. Thickness comparison between un-biased (NB/NH) and biased (B/NH) sputtering runs after 1 h of sputtering at different target currents. The data is presented as mean ± standard error (n = 15).

5.2.1.4 X-Ray Diffraction Analysis of Un-biased and Biased Sputtering Runs

In addition to morphological analysis of the NB/NH and B/NH samples, crystallographic analysis was also conducted to investigate structural properties of the films generated. As seen in *Figure 5:7*, the NB/NH samples exhibited an increase in the intensity of the produced hexagonal close packed (HCP) α-Ti (PDF 00-044-1294) due to the increased sputtering time, resulting in a thicker film. The influence of coating thickness and peak intensity was noted, since the XRD was limited to the thickness of the coating being analysed and the incident angle chosen. There was a subtle difference between the 3 and 5 A 1 h samples, whereby the intensity ratio between the (002) and (101) planes (*ca.* 38.4 and 40.2^{o} 2θ, respectively) increased, as the relative intensity of the (101) plane decreased for the 3 A sample. All samples exhibited no peaks in the 5 and 10 min sputtering times. Interestingly, the 3 A 15 min sample exhibited peaks corresponding to (002) and (101) Ti planes, however, the 5 A sample with the same sputtering time did not.

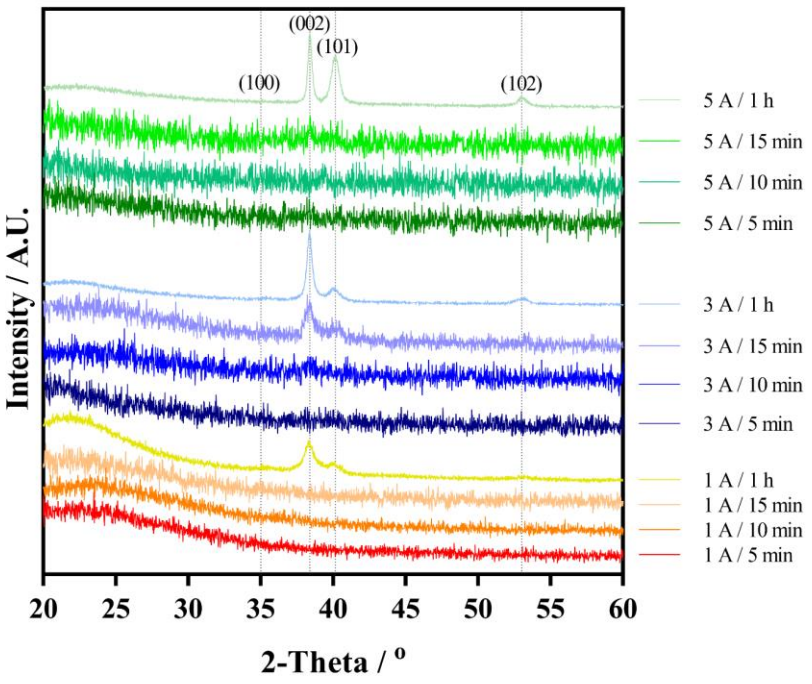

Figure 5:7. X-ray diffraction patterns for the 1, 3 and 5 A NBNH samples at varying sputtering times (5, 10, 15 and 60 min). All peaks were attributed to HCP Ti (PDF 00-044-1294). The amorphous nature of the measured spectra for the thinner Ti coatings is due to the underlying glass substrate.

Figure 5:8 compares the films produced, whilst keeping sputtering time constant for the 1, 3, and 5 A target currents. The amorphous region present (20-30°) was from the underlying glass substrate used [423]. The NB/NH samples both exhibited peaks at *ca.* 38.4, 40.2, and 53° 2θ corresponding to (002), (101), and (102) crystalline HCP α-Ti (PDF 00-044-1294) planes, respectively. After biasing, an additional peak at 35° was noted corresponding to the (100) α-Ti plane, as well as a shoulder on the α-Ti (002) peak at *ca.* 38.8° and a further peak at *ca.* 56.1° corresponding to the (110) and (200) planes for body-centred cubic (BCC) β-Ti (PDF 01-077-3482), respectively (indicated with * in *Figure 5:8*). The differences between the B/NH samples at 3 and 5 A, were negligible, since both exhibited similar relative peak intensities for the sample crystallographic planes; as further confirmed in the texture coefficient analysis in *Figure 5*:*9*. The 1 A sample exhibited a subtle difference between the NB/NH and B/NH sample types, with a reduction in the (101) peak (40.2°) following substrate

biasing. Hence the 1 A samples were discounted as a viable sputtering condition due to the low sputtering rate and previously described morphological and structural data.

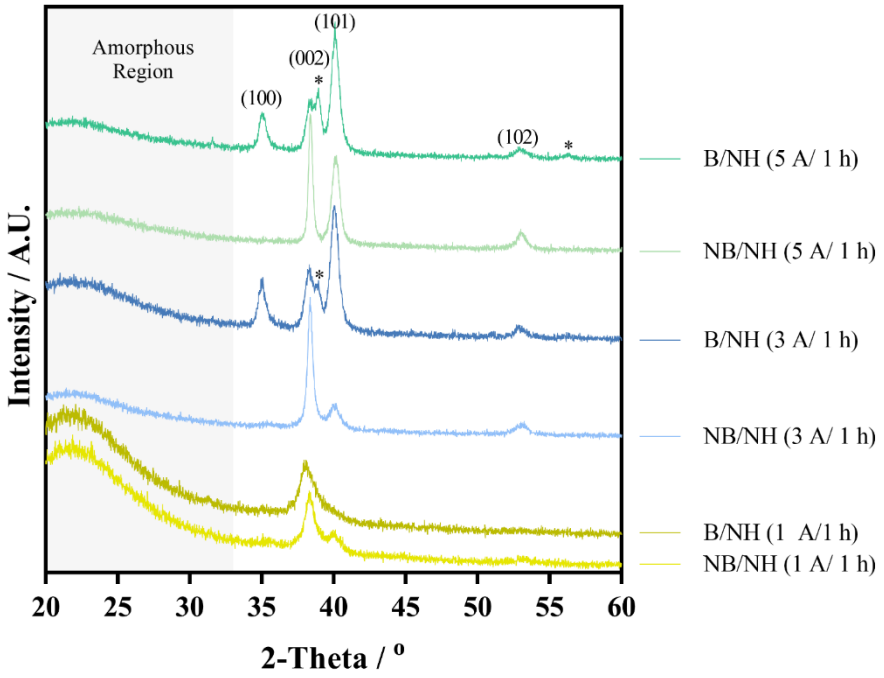

Figure 5:8. Comparison between the NB/NH and B/NH samples at different target currents (1, 3, and 5 A) whilst maintaining the same sputtering time (1 h). The distinct and numbered peaks were attributed to the HCP α-Ti database file (PDF 00-044-1294), with an additional phase quantified as BCC β-Ti (PDF 01-077-3482).

Texture coefficient (T_c) analysis (*Figure 5:9 & Table 5:2*) was conducted to further quantify the effect of a substrate bias on the structural properties of the coatings produced (see *Section 3.4.4*). For the 1 A samples, no significant changes were noted between the NB/NH and B/NH samples, with a small reduction in the preferentially orientated (002) plane, T_c from 2.25 to 2.11, with all other planes noting similar changes. When the 3 A target current was applied to the NB/NH sample, a significant increase in T_c of the preferred (002) plane was noted, increasing from 2.25 in the 1 A NB/NH sample to 2.92, with all other planes exhibiting a reduction in their T_c. Following application of the -100 V bias (B/NH) the T_c in the (002) reduced significantly to 1.33, with the highest T_c being 1.38 for the (100) plane. Despite the (101) plane exhibiting the highest relative intensity, when compared to the database

values for HCP α-Ti, there was preferential alignment in the (100) plane, since its intensity is higher than the database value. For the 5 A sample (NB/NH), there was a reduction in the T_c (from 2.92 to 2.45) noted for the (002) plane compared to the 3 A NB/NH sample, whilst still exhibiting preferential orientation within this plane. Again, biasing (B/NH) resulted in significant alteration to the crystal orientation of the film, with a reduction from 2.45 to 1.31 for the T_c of the (002) plane, which remained the most preferentially aligned.

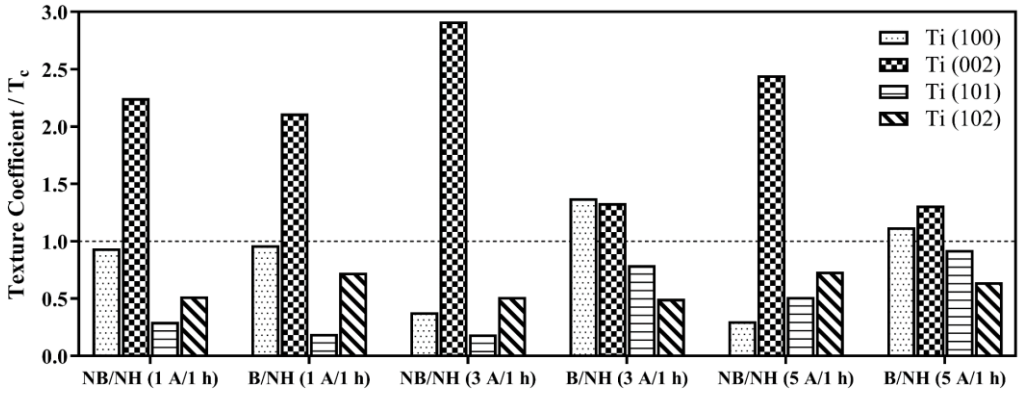

Figure 5:9. Texture coefficient analysis, calculated via the Harris equation, of the NB/NH and B/NH samples using 1, 3, and 5 A target currents and 1 h sputtering times. The dotted line indicates a T_c = 1, which represents and purely equiaxed sample, akin to that of bulk materials.

Table 5:2. Raw texture coefficient data for the NB/NH and B/NH samples using 1, 3, and 5 A target currents at 1 h sputtering times.

Sample		Texture Coefficient (T_c)			
		(100)	(002)	(101)	(102)
1 A	NB/NH	0.94	2.25	0.30	0.52
	B/NH	0.97	2.11	0.19	0.73
3 A	NB/NH	0.38	2.92	0.19	0.51
	B/NH	1.38	1.33	0.79	0.50
5 A	NB/NH	0.30	2.45	0.52	0.74
	B/NH	1.12	1.31	0.92	0.64

5.2.1.5 Raman Spectroscopy

As seen in *Figure 5:10*, all peaks exhibited the same Raman spectral bands located at *ca.* 142 (E_g), 415 (B_{1g}), and 600 cm^{-1}, which corresponded to anatase modes [424].

Additional bands at 142 (B_{1g}), 255 (which does not coincide with theoretically calculated fundamental modes, although is postulated in the literature to be due to second-order or disorder induced scattering [424]) and 600 cm^{-1}, corresponded to rutile. 142 and 600 cm^{-1} are a combination of multiple modes of rutile and anatase; 600 cm^{-1} being an example of a broad peak containing shoulders that correspond to rutile (A_{1g}; *ca.* 610 cm^{-1}) and anatase (A_{1g}, B_{1g}; *ca.* 520 cm^{-1})(E_{1g}; *ca.* 630 cm^{-1}) [424]. This confirmed that the films are chemically consistent despite changes in sputtering parameters.

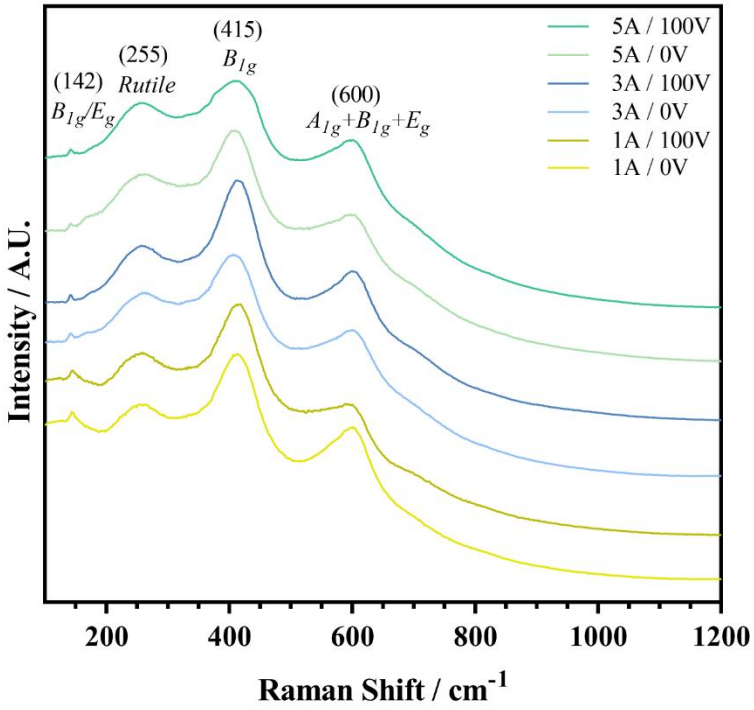

Figure 5:10. Raman spectra comparison of deposited Ti thin films using: 1, 3, and 5 A target currents; with (B/NH) or without (NB/NH) a -100 V substrate bias; and 1 h sputtering time.

5.2.2 Alkali Titanate Conversion of Optimised Ti Thin Films

From the previous findings (*Section 5.2.1*), the 5 A target current was chosen for all further samples, due to the faster deposition rate, and the controlled differences in preferential orientation and grain morphology through combination with the other parameters. Hence, the 4 main sample types chosen for the remainder of the project were the NB/NH (no bias/no substrate heating), B/NH (- 100 V bias/no substrate

heating), B/150 (- 100 V bias/150 ^{o}C substrate heating) and the B/300 (- 100 V bias/300 ^{o}C substrate heating); all using a 5 A target current. It was predicted, based on common sputtering principles [425], that additional thermal energy should result in more equiaxed coatings being produced due to atomic reordering; hence, two additional heating temperatures (150 and 300 ^{o}C) were employed. These films were then investigated to explore the potential for titanate conversion and the effect of structural and chemical properties of the films on subsequent titanate formation.

5.2.2.1 Substrate Temperature Analysis

Applied substrate heating was employed to impart additional energy to the condensed Ti atoms on the substrate surface to induce atomic reordering into equiaxed (random) crystallographic orientations, as opposed to the characteristic columnar (preferred orientation) structures commonly seen in magnetron sputtered coatings. Temperature measurements (*Figure 5*:*11*) were conducted to understand the temperature seen by the substrates in a rotational run without heating (NB/NH), with a bias (B/NH) and at half (150 ^{o}C) and maximum (300 ^{o}C) temperature runs, both with the application of a bias (B/150 and B/300, respectively). As expected, the application of a bias and increasing substrate heating increased the substrate temperature. Temperatures of *ca.* 74, 119, 124, and 135 ^{o}C were recorded for the NB/NH, B/NH, B/150 and B/300 samples, respectively after *ca.* 5 h runs (*ca.* 4 μm coating thickness). The inset graph in *Figure 5*:*11* for the NB/NH run illustrates an equilibrium temperature is reached after 5 minutes of the run time.

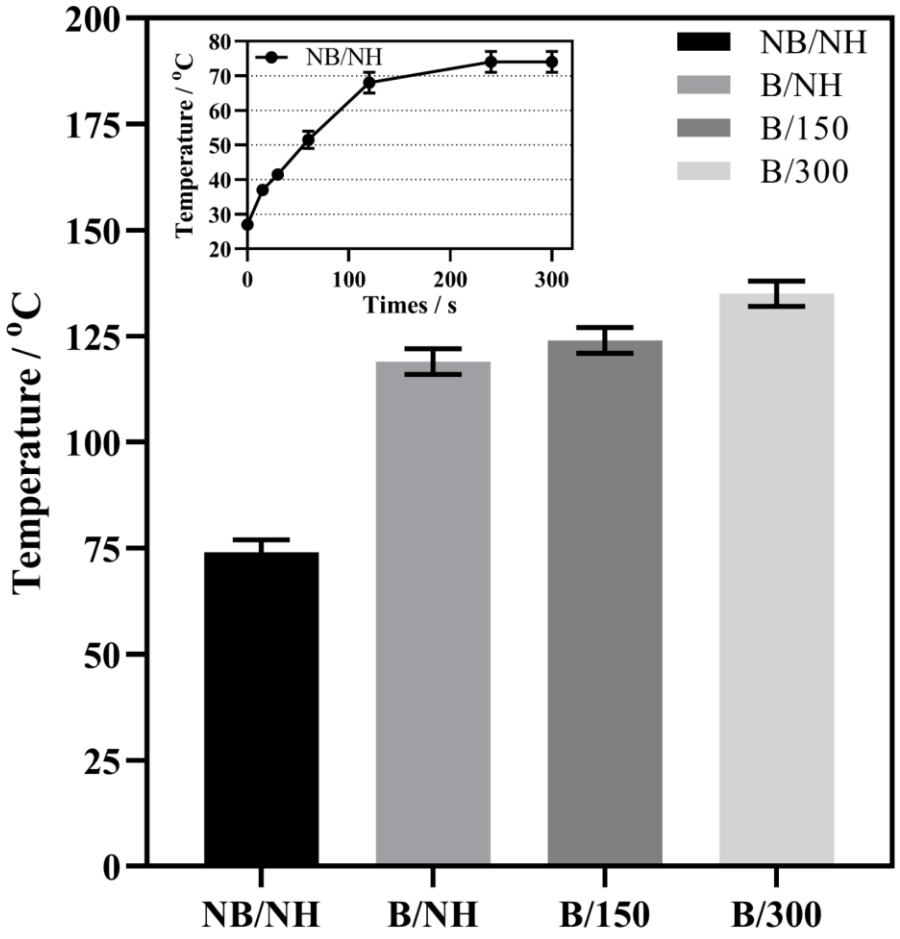

Figure 5:11. Substrate temperature measurements for the 4 μm runs (ca. 5 h) showing median temperature of the range noted on the temperature strips, with S.D. being the range of the strip measurements. Inset graph showing incremental measurements for the NB/NH sample only, demonstrating the time taken to reach equilibrium during the run.

5.2.2.2 SEM Morphological and EDX & XPS Compositional Analysis

As observed in the SEM micrographs (*Figure 5:12A & B; Figure 5:13A & B*) the frequency (*ca.* 4.1, 3.0, 1.8, and 0.6 μm^{-2}, for NB/NH, B/NH, B/150 and B/300 samples, respectively) and area (*ca.* 3714, 2541, 1437, and 1029 nm^2, for NB/NH, B/NH, B/150 and B/300 samples, respectively) of surface voids appeared to diminish from the NB/NH sample to the B/300 sample (for further information see *Section 5.2.2.4, Figure 5:15*). The sputtering time was increased from 263 min for the NB/NH sample (*Figure 5:12C*) to 278 min for the B/NH sample (*Figure 5:12D*) to maintain the same coating thickness (*ca.* 3.9 μm). The application of substrate heating at 150

and 300 ^{o}C, clearly demonstrated the thickness of the films produced at the same sputtering time decreased to *ca.* 3.7 μm for the B/150 and B/300 samples (*Figure 5:13C & D*) with further densification observed by SEM; *Figure 5:12* & *Figure 5:13*.

Following titanate conversion, all samples showed nanoporous morphologies consistent with sodium titanate surfaces (*Figure 5:12E & F; Figure 5:13E & F*). It was also noted that the pore size (defined as the area enclosed by the larger strutted structures, as indicated by the diagonal red arrows) increased with increasing density of the produced Ti coating. In addition to the titanium coating, the thickness of the titanate converted (_TC suffix) films was also assessed. When observing the thickness of the titanate converted portion of the Ti coating, it was evident that this region increased in depth through the application of a bias (from the NB/NH_TC sample (*ca.* 1.12 μm) to the B/NH_TC sample (*ca.* 1.20 μm); *Figure 5:12G* & *H*), as well as the increase in substrate temperature (from the B/150_TC sample (*ca.* 1.20 μm) to the B/300_TC sample (*ca.* 1.63 μm); *Figure 5:13G* & *H*). The increase in depth from all titanate converted samples to the B/300_TC sample were statistically significant ($p < 0.0001$; ****). However, the increase from the NB/NH_TC, to both the B/NH_TC and B/150_TC samples exhibited no statistical significance ($p > 0.05$).

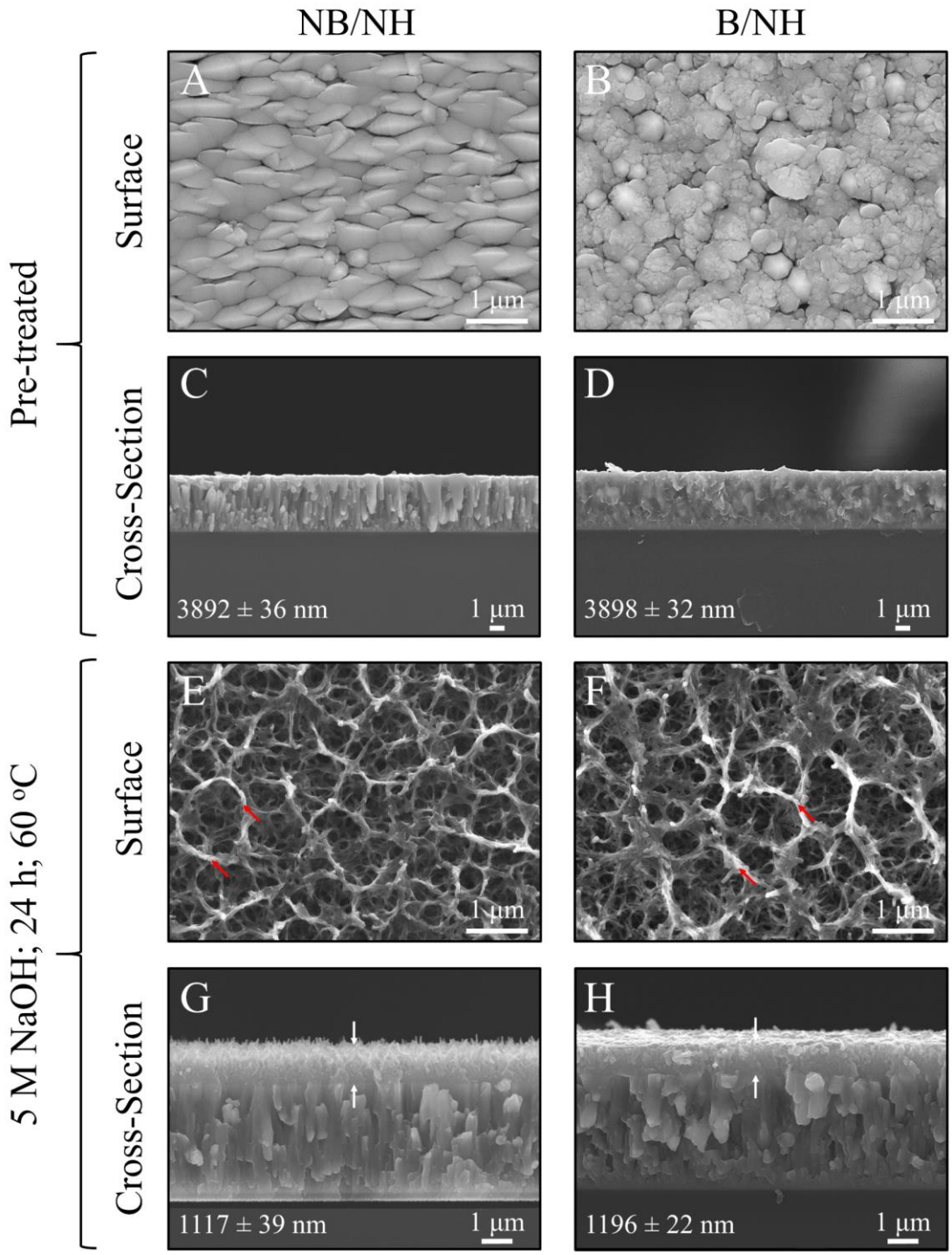

Figure 5:12. SEM surface and cross-sectional micrographs for unconverted and converted DC magnetron sputtered films of the non-biased (NB/NH) and biased (B/NH) samples. A & B) Surface micrographs of unconverted Ti samples. C & D) Cross-sectional images of unconverted Ti samples. E & F) Surface micrographs of converted titanate samples, with red arrows indicating larger strutted regions. G & H) Cross-sectional images of converted samples, with white arrows indicating titanate portion. Coating thickness with standard error is written in each image.

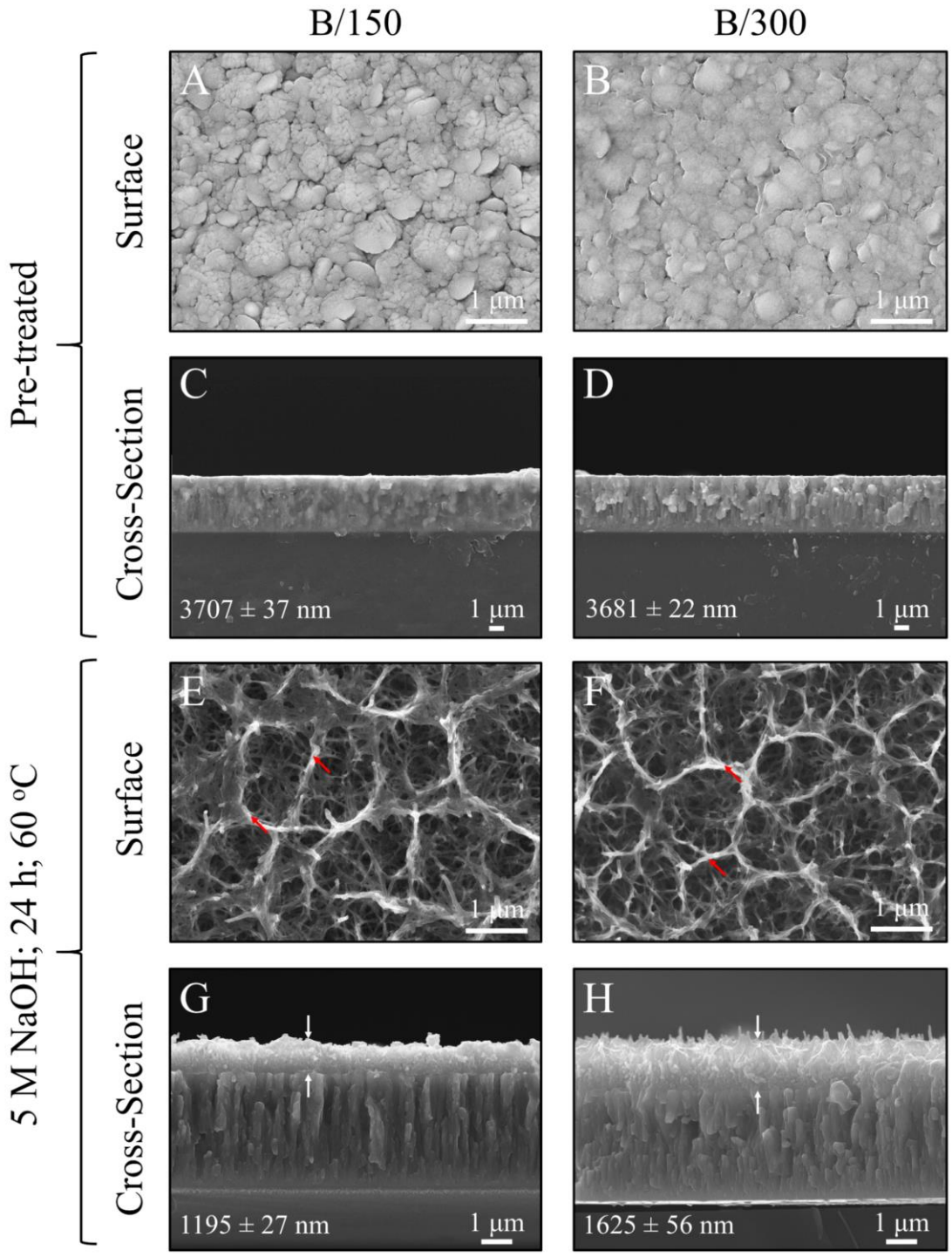

Figure 5:13. SEM surface and cross-sectional micrographs for unconverted and converted DC magnetron sputtered films of the biased and substrate heated samples (B/150 and B/300). A & B) Surface micrographs of unconverted Ti samples. C & D) Cross-sectional images of unconverted Ti samples. E & F) Surface micrographs of converted titanate samples, with red arrows indicating larger strutted regions. G & H) Cross-sectional images of converted samples, with white arrows indicating titanate portion. Coating thickness with standard error is written in each image

Elemental analysis *via* EDX (*Table 5*:*3*) demonstrated similar sodium (Na) inclusion of *ca.* 7.6, 8.9, 5.6 and 7.6 at.% for the NB/NH_TC, B/NH_TC, B/150_TC,

and B/300_TC samples, respectively. Both Ti and O content remained constant, with trace inclusions (< 1 at.%) of Ca. In comparison, elemental analysis determined *via* XPS showed a large increase in Na for all samples, with 25.6, 26.8, 16.1, and 17.8 at.% for NB/NH_TC, B/NH_TC, B/150_TC and B/300_TC, respectively. The surface composition examined by XPS showed that Ti and O content remained similar for the NB/NH_TC, B/NH_TC samples, which was higher for the B/150_TC and B/300_TC samples.

Table 5:3. EDX and XPS data of titanate converted DC magnetron sputtered Ti films. Values given with standard error values (n = 3). All unconverted samples contained 100% Ti.

Sample	EDX			XPS		
	Na / at.% (EDX)	**O / at.% (EDX)**	**Ti / at.% (EDX)**	**Na / at.% (XPS)**	**O / at.% (XPS)**	**Ti / at.% (XPS)**
NB/NH_TC	7.6 ± 0.1	61.0 ± 0.1	30.8 ± 0.1	25.6 ± 0.6	56.9 ± 0.6	17.5 ± 0.3
B/NH_TC	8.9 ± 0.1	57.3 ± 0.5	33.2 ± 0.6	26.8 ± 0.7	55.4 ± 0.6	17.8 ± 0.3
B/150_TC	5.6 ± 0.1	57.6 ± 0.2	36.9 ± 0.2	16.1 ± 0.4	62.4 ± 0.5	21.5 ± 0.3
B/300_TC	7.6 ± 0.1	60.1 ± 0.2	32.2 ± 0.1	17.8 ± 0.4	62.4 ± 0.5	19.9 ± 0.3

5.2.2.3 Ti Thickness Changes due to Titanate Conversion

Figure 5:14 demonstrated the variation in titanate thickness and the change in Ti thickness due to the conversion into titanate, herein labelled ΔTi (difference from the original Ti thickness to the Ti thickness post-titanate conversion). The more columnar structures (NB/NH and B/NH samples) exhibited large values of ΔTi than more equiaxed samples (B/150 and B/300) with values of *ca.* 296, 365, 25, and 81 nm for NB/NH_TC, B/NH_TC, B/150_TC and B/300_TC samples, respectively; indicating larger titanate penetration. Correlating this with the titanate thicknesses produced, the more equiaxed surfaces exhibited thicker titanate structures, as described previously in *Section 5.2.2.2*.

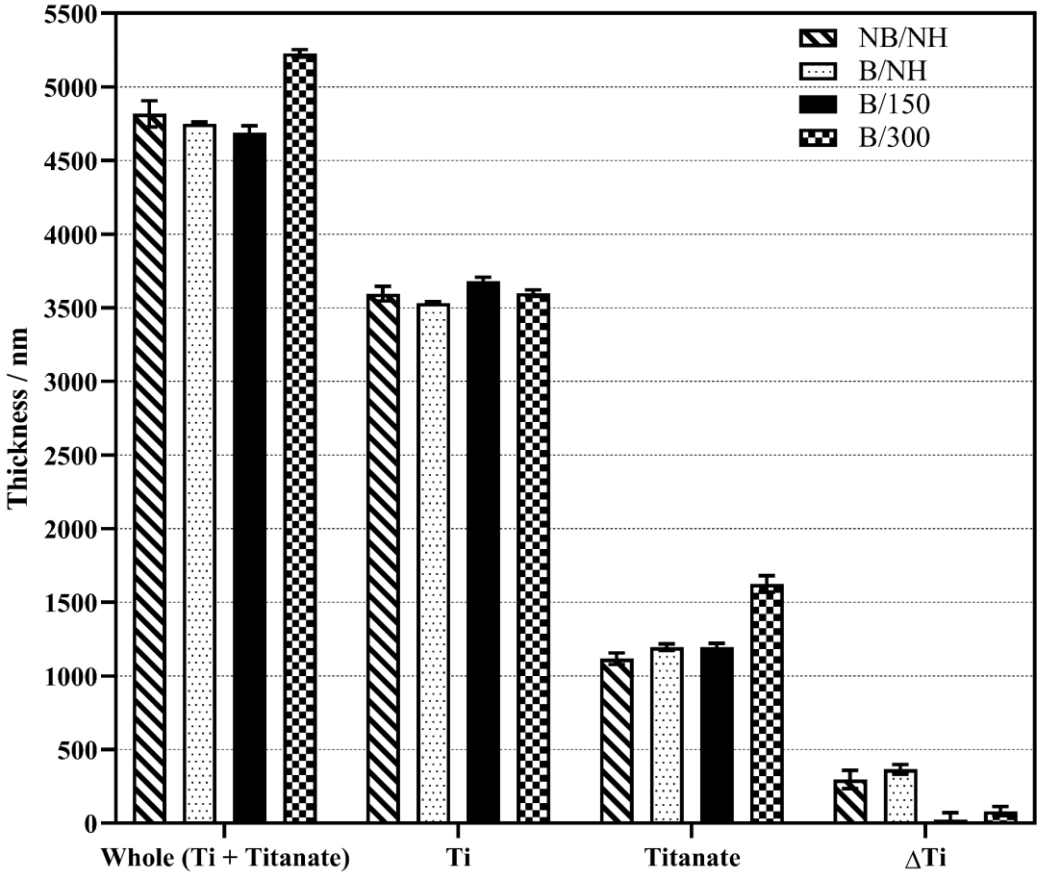

Figure 5:14. Thickness and depth penetration quantification of the Ti coating and the portion of the titanate structure present, as well as the reduction in the Ti coating to produce the titanate structures, and the whole thickness (Ti + titanate) of the coating produced. All values are mean ± standard error (n = 15).

5.2.2.4 Void and Pore Analysis: ImageJ

The quantification of void frequency and area of unconverted Ti coatings, as well as the pore area of the titanate-converted samples, was examined using ImageJ analysis through optimised thresholding of SEM micrographs. *Figure 5:15* shows the void frequency and average void area decreased from *ca.* 3713.7 nm^2 and 4.1 μm^{-2} in the NB/NH sample, to 1029 nm^2 and 0.6 μm^{-2} in the B/300 sample, respectively, correlating with the increase in the energy imparted on the coatings (*via* substrate biasing and *in situ* substrate heating).

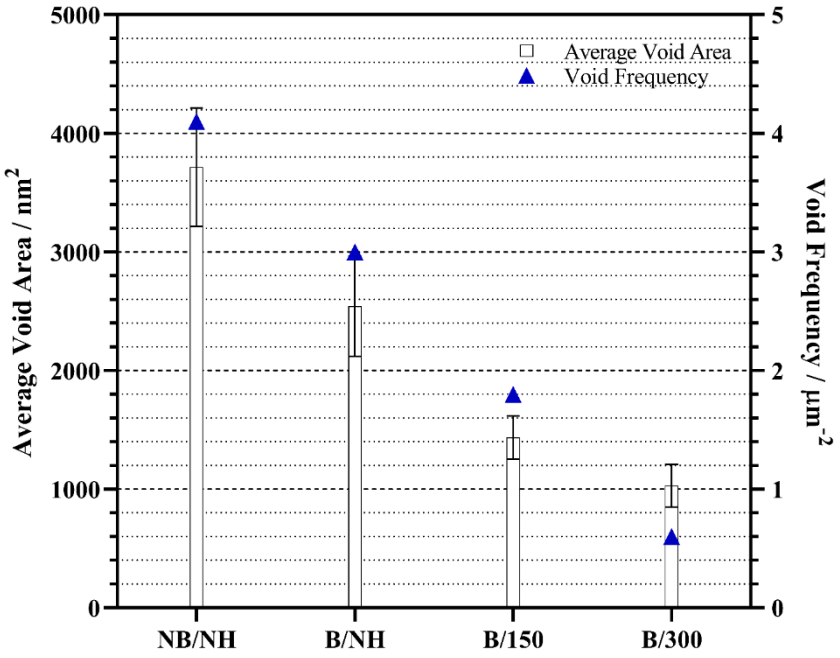

Figure 5:15. Average void area and void density/frequency for unconverted samples as calculated via ImageJ analysis, indicating the increase in coating density from NB/NH to B/300 samples. All values are mean ± standard error (n = 5). Acquisitions were taken over an area of ca. 29 µm² (x20,000 magnification JEOL 7100F FEG-SEM)

Further pore size analysis (*Figure 5:16*) was conducted on the titanate converted samples, to assess whether any quantifiable morphological changes were exhibited on the titanate structure as a result of the sputtering parameters used. There was a subtle trend noted, with the pore size appearing to increase with the application of a substrate bias and heating. However, due to the growth mechanism present, reproducible pore sizes were not possible, hence, the large statistical error associated with the data.

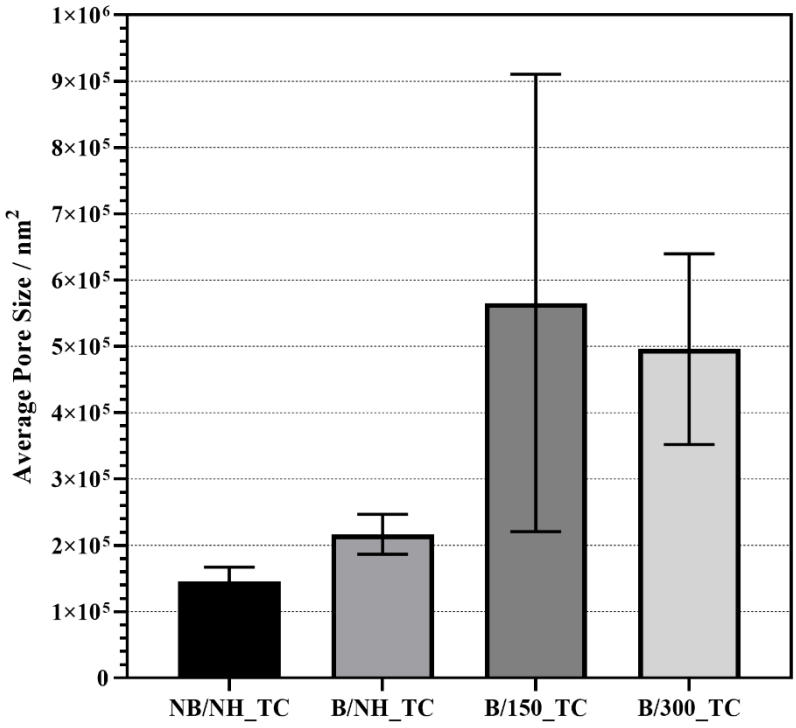

Figure 5:16. Average pore area of titanate converted samples. All values are mean ± standard error (n = 5). Acquisitions were taken over an area of ca. 29 μm² (x20,000 magnification JEOL 7100F FEG-SEM).

5.2.2.5 Focused Ion Beam Scanning Electron Microscopy (FIB-SEM)

Additional cross-sectional information of the samples was determined *via* FEG-SEM of a FIB-milled titanate converted sample. However, the FIB milling process caused significant alteration to the titanate structure, as well as bending of any extracted lamella. The representative micrograph (*Figure 5:17A*), which was the only useable FIB-milled sample, demonstrated clear interconnected nanoporosity, with homogenous distribution of sodium (*Figure 5:17C*) across the surface of the sample, and homogeneous distribution of titanium within the coating (*Figure 5:17F*). Sodium and oxygen (*Figure 5:17C & D*) diffusion appeared to decrease through the thickness of the coating, demonstrating a clear diffusion gradient. Vertical growth of the titanate struts were clear on the insert micrographs.

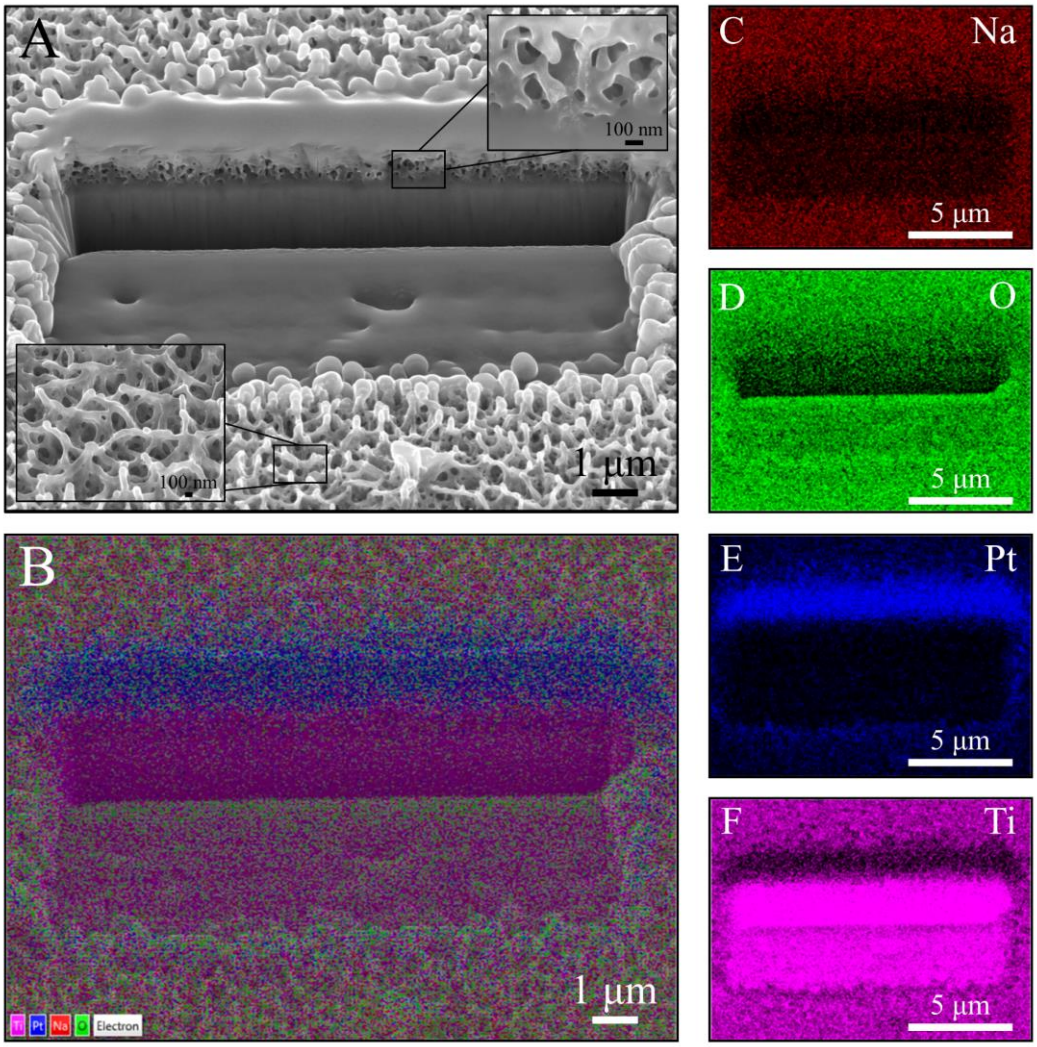

Figure 5:17. A) Representative FEG-SEM micrograph of a FIB-milled, titanate converted sample tilted at 40° to demonstrate the interconnected porosity and interface between the Ti thin film and the converted titanate portion (insert images show higher resolution micrographs of aforementioned features). B) Composite EDX maps of all elements present with individual elemental maps of C) sodium, D) oxygen, E) platinum (introduced from the FIB milling process), and F) titanium.

5.2.2.6 X-Ray Diffraction and Texture Coefficient Analysis

XRD spectral data (*Figure 5:18A*) for the NB/NH sample demonstrated preferred orientation in the (002) plane of HCP α-Ti (PDF 00-044-1294) at 38.4° 2θ, with additional smaller peaks at 40.2° and 53.0° 2θ corresponding to the (101) and (102) planes, respectively; no other peaks were observed. However, through the application of a bias in the B/NH sample, the relative intensities of the peaks, and number of peaks, increased with a new peak at 35.2° 2θ corresponding to the (100) plane. The peak corresponding to the (101) plane increased in intensity. Continuing the trend, through

application of substrate heating in both the B/150 and B/300 samples, peaks corresponding to the (100) and (101) planes saw an increase in their relative intensities, with the (101) peak having the highest relative intensity for both samples. Following titanate conversion (*Figure 5:18B*), three additional broader peaks (indicative of sub-micron crystallites [426]) were detected on all samples at *ca.* 24.2, 28.4 and 48.2° 2θ, assigned to isomorphic titanate species (PDF 00-022-1404 and PDF 00-025-1450). However, direct assignment was difficult due to the amorphous nature of the peaks.

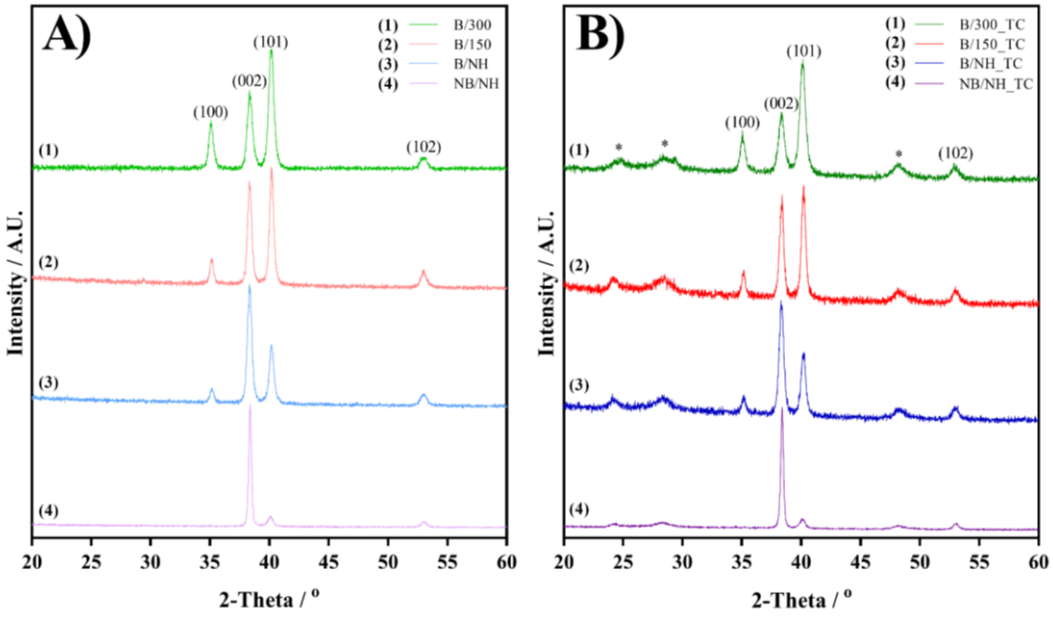

*Figure 5:18. XRD spectral analysis of unconverted Ti (A) and titanate converted (B) samples. Deconvolution of Ti peaks corresponded to HCP Ti (PDF 00-044-1294), with * indicating additional peaks, attributed to isomorphic titanate species (PDF 00-022-1404 and PDF 00-025-1450), which were not found in the unconverted samples.*

Further analysis of the change in preferred orientation was conducted through calculation of texture coefficients (T_c; *Figure 5:19*). Using Harris' equation (described in *Section 3.4.4*), the degree of preferred orientation was numerically calculated through ratios between measured peak intensities and database intensities for the same material. A T_c of 1 would indicate an equiaxed, bulk sample equating to the material's database structure, whilst a texture coefficient of *n* (*n* being the number of peaks

calculated; in this case n = 4) would indicate complete preferred orientation in that plane. For the NB/NH sample, as seen with the XRD data, the crystalline structure was preferentially orientated in the (002) plane, with a $T_{c(002)}$ = 3.39. This value reduced to 2.67 in the B/NH sample, showing a subtle shift from the more columnar structure exhibited in the NB/NH sample. Further reductions of $T_{c(002)}$, to *ca.* 2.04 and 1.54 occurred for the B/150 and B/300 samples, respectively, demonstrating further shifts from preferred orientation in the columnar grown NB/NH sample, to more equiaxed structures as $T_c \rightarrow 1$.

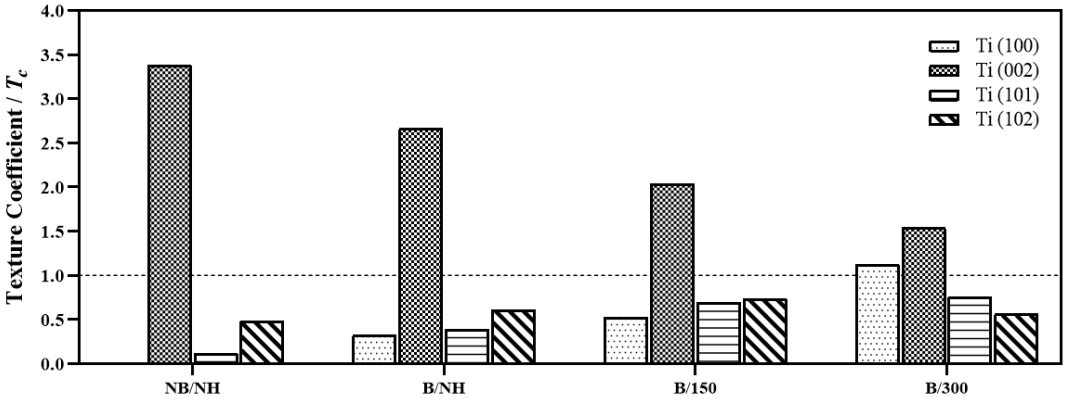

Figure 5:19. Texture coefficient analysis of all unconverted Ti samples calculated from relative intensity values and X-ray diffraction peak data.

Table 5:4. Raw texture coefficient data for NB/NH, B/NH, B/150 and B/300 4 µm runs.

Sample	Texture Coefficient (T_c)			
	(100)	(002)	(101)	(102)
NB/NH	0.00	3.39	0.12	0.49
B/NH	0.33	2.67	0.39	0.61
B/150	0.53	2.04	0.70	0.74
B/300	1.13	1.54	0.76	0.57

5.2.2.7 X-ray Photoelectron Spectroscopy (XPS)

XPS quantification (*Figure 5:20*, *Table 5:5* & *Table 5:6*) showed significant differences in the high-resolution Ti 2p, O 1s, and Na 1s spectra, as well as subtle alterations in peak intensity/presence, and elemental quantities. In the survey spectra

(*Figure 5:20A*), noticeable differences from the control to all Ti coated samples were noted, with consistent peak positions and peak intensities of all Ti and O photoelectron emissions. Following NaOH treatment, peaks corresponding to Na were detected (most notable being the Na 1s at *ca.* 1071 eV and Na KLL Auger peak at *ca.* 498 eV), with significant increase relative to the intensity of the Ti LMM peaks, which overlap with Na 1s spectra.

Concerning the high-resolution spectra, noticeable differences in the O 1s peak (*Figure 5:20B*) deconvolutions and subsequent positions were identified. The peak for the 316L SS control contained three constituent peaks located at 530.1 (39.0%), 531.6 (48.9%), and 533.1 (12.1%) eV, corresponding to O^{2-} ($M^{x+}O_x$; M = Cr, Fe, etc.), OH^- ($M^{x+}(OH)_x$; M = Cr, Fe, etc.), and H_2O chemical states. For the Ti coated samples, the three constituent peaks remained with similar peak positions, however, their relative proportions differed; O^{2-} (79.1 ± 0.7%; Ti^{4+}—O), OH^-/defective oxides (15.6 ± 0.5%; hydroxides/Ti^{3+}—O/Ti^{2+}—O), and H_2O (5.3 ± 0.5%). Following titanate conversion, an additional constituent peak appeared at *ca.* 535.2 eV, which matched the Na KLL Auger peak. Again, all other peaks remained in their position at 530.0, 531.7, and 533.1 eV corresponding to O^{2-} (75.2 ± 0.4%; Ti^{4+}—O), OH^- (11.6 ± 0.4%; hydroxides), and H_2O (5.3 ± 0.6%; experiencing a subtle shift). Variations in the relative intensities were noted as above for the Ti coated samples, with lower proportions of the OH^- photoelectron peak.

For the Ti 2p doublet deconvolutions (*Figure 5:20C*), there was a clear alteration in the number of constituent peaks following titanate conversion of the produced Ti films. Initially, the Ti coated samples contained Ti in 4 different valence states; Ti^{4+} (69.9 ± 1.5%; 2p 3/2 = *ca.* 458.6 eV), Ti^{3+} (9.9 ± 0.5%; 2p 3/2 = *ca.* 457.1 eV), Ti^{2+} (4.5 ± 0.2%; 2p 3/2 = *ca.* 455.3 eV), and Ti^0 (15.7 ± 1.1%; 2p 3/2 = *ca.* 453.4 eV),

representing different titanium oxide and hydroxide states (TiO, Ti_2O_3, TiO_2, etc.), as well as metallic titanium. Post-titanate conversion, the number of constituent peaks dropped to only contain Ti in its 4^+ valence state (2p 3/2 = *ca.* 458.4 eV).

In the high-resolution spectra of the range for Na 1s (*Figure 5*:*20D*), a peak was present in both the pre- and post-titanate converted samples, however, this was due to the overlapping of the Ti LMM Auger peaks with the Na 1s spectrum. The intensity of the peak increased for the titanate converted samples, demonstrating a peak at *ca.* 1071.4 eV, quantified as Na 1s (Na—O; 56.6 ± 6.9%).

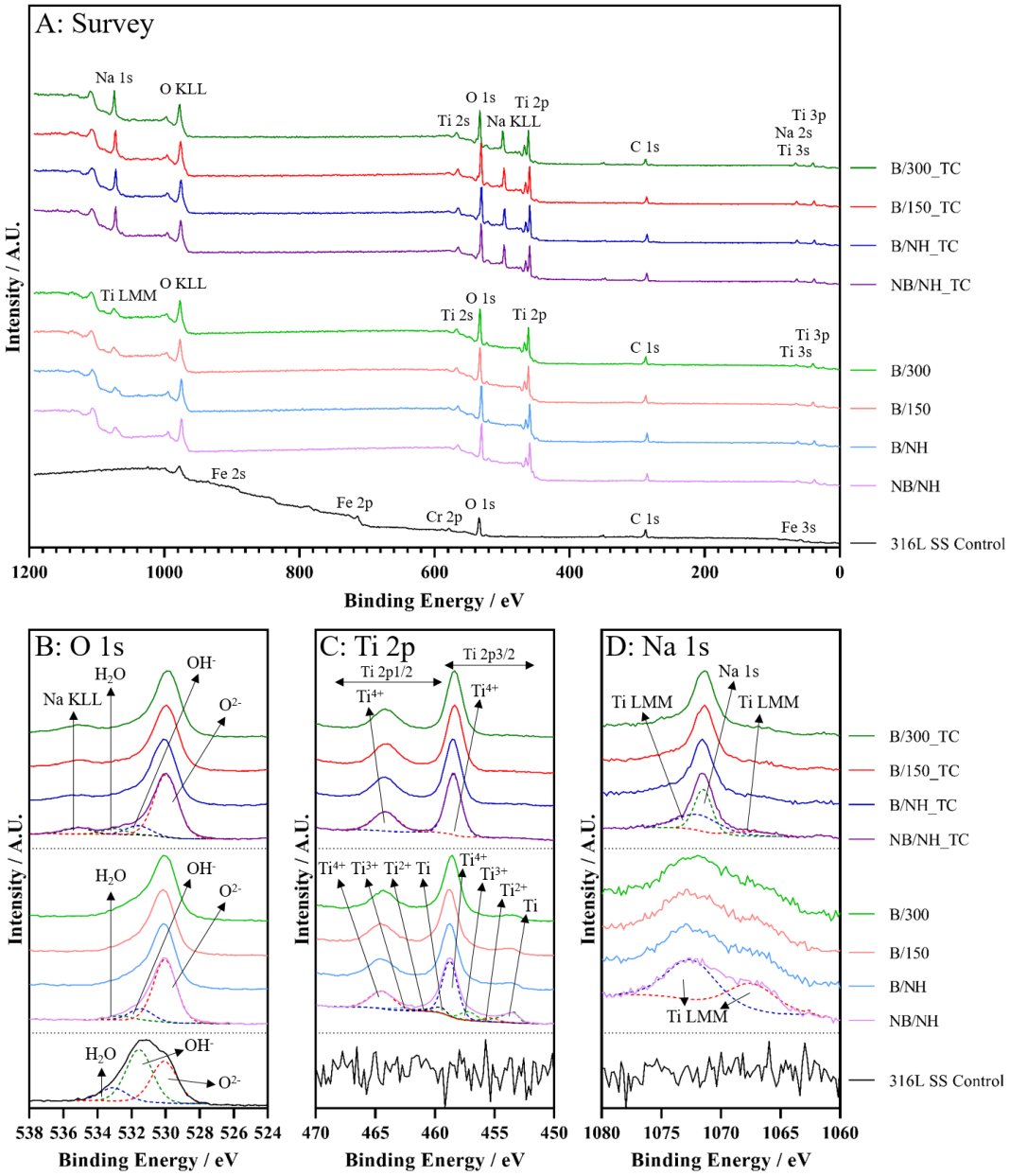

Figure 5:20. X-ray photoelectron spectral analysis for control, Ti coated, and titanate converted samples. A) Survey spectra identifying all elemental photoelectron emissions, B) High-resolution spectra of O 1s peaks with overlapping Na KLL Auger emission, C) High-resolution spectra of Ti 2p doublet splitting peaks, and D) High resolution spectra of Na 1s, with overlapping Ti LMM Auger emissions.

Table 5:5. XPS binding energy data for all deconvoluted peaks for 316L S.S. Control, NB/NH, B/NH, B150, and B/300 samples.

Sample Treatment	Sample Code	Elements	Binding Energy / eV	Corresponding Bonds (Area / %)	Ref.
Control	316L S.S. Control	O 1s	530.1 (O^{2-}) 531.6 (OH^{-}) 533.1 (H_2O)	M^{x+}—O (38.95) M^{x+}—OH (48.85) O—H (12.20)	[427-430]
Ti Coated	NB/NH	O 1s	530.0 (O^{2-}) 531.5 (OH^{-}) 532.7 (H_2O)	Ti^{4+}—O (77.51) Ti—OH, $Ti^{2+/3+}$—O (16.02) O—H (6.47)	[394, 431-433]
		Ti 2p 3/2	458.7 (Ti^{4+}) 457.2 (Ti^{3+}) 455.4 (Ti^{2+}) 453.4 (Ti^{0})	O—Ti^{4+} (66.39) O—Ti^{3+} (11.17) O—Ti^{2+} (4.87) Ti—Ti (17.58)	[394, 432, 433]
	B/NH	O 1s	530.0 (O^{2-}) 531.6 (OH^{-}) 532.9 (H_2O)	Ti^{4+}—O (78.59) Ti—OH, $Ti^{2+/3+}$—O (16.81) O—H (4.60)	[394, 431-433]
		Ti 2p 3/2	458.7 (Ti^{4+}) 457.2 (Ti^{3+}) 455.4 (Ti^{2+}) 453.5 (Ti^{0})	O—Ti^{4+} (72.80) O—Ti^{3+} (9.44) O—Ti^{2+} (4.17) Ti—Ti (13.58)	[394, 432, 433]
	B/150	O 1s	530.1 (O^{2-}) 531.5 (OH^{-}) 532.7 (H_2O)	Ti^{4+}—O (79.70) Ti—OH, $Ti^{2+/3+}$—O (14.81) O—H (5.48)	[394, 431-433]
		Ti 2p 3/2	458.5 (Ti^{4+}) 457.0 (Ti^{3+}) 455.2 (Ti^{2+}) 453.3 (Ti^{0})	O—Ti^{4+} (71.61) O—Ti^{3+} (10.14) O—Ti^{2+} (4.17) Ti—Ti (14.07)	[394, 432, 433]
	B/300	O 1s	530.2 (O^{2-}) 531.7 (OH^{-}) 533.0 (H_2O)	Ti^{4+}—O (80.72) Ti—OH, $Ti^{2+/3+}$—O (14.84) O—H (4.44)	[394, 431-433]
		Ti 2p 3/2	458.6 (Ti^{4+}) 457.1 (Ti^{3+}) 455.3 (Ti^{2+}) 453.4 (Ti^{0})	O—Ti^{4+} (68.68) O—Ti^{3+} (9.02) O—Ti^{2+} (4.58) Ti—Ti (17.72)	[394, 432, 433]

Table 5:6. XPS binding energy data for all deconvoluted peaks for NB/NH_TC, B/NH_TC, B/150_TC, and B/300_TC samples.

Sample Treatment	Sample Code	Elements	Binding Energy / eV	Corresponding Bonds (Area / %)	Ref.
NaOH Treatment (5 M; 60 °C; 24 h)	NB/NH_TC	O 1s	530.0 (O^{2-}) 531.6 (OH^-) 532.9 (H_2O) 535.1 (Na KLL)	Ti^{4+}—O (74.15) Na^+—O—Ti (11.05) O—H (6.71) - (8.10)	[215, 394, 395]
		Ti 2p 3/2	458.4 (Ti^{4+})	O—Ti^{4+} (100)	[215, 394]
		Na 1s	1071.4	O—Na (46.07)	[215]
	B/NH_TC	O 1s	530.0 (O^{2-}) 531.8 (OH^-) 533.3 (H_2O) 535.3 (Na KLL)	Ti^{4+}—O (76.17) Na^+—O—Ti (12.73) O—H (4.72) - (6.37)	[215, 394, 395]
		Ti 2p 3/2	458.4 (Ti^{4+})	O—Ti^{4+} (100)	[215, 394]
		Na 1s	1071.4	O—Na (46.75)	[215]
	B/150_TC	O 1s	530.0 (O^{2-}) 531.6 (OH^-) 533.1 (H_2O) 535.2 (Na KLL)	Ti^{4+}—O (75.62) Na—O—Ti (10.98) O—H (5.51) - (7.90)	[215, 394, 395]
		Ti 2p 3/2	458.4 (Ti^{4+})	O—Ti^{4+} (100)	[215, 394]
		Na 1s	1071.4	O—Na (58.09)	[215]
	B/300_TC	O 1s	530.0 (O^{2-}) 531.6 (OH^-) 533.2 (H_2O) 535.2 (Na KLL)	Ti^{4+}—O (74.82) Na^+—O—Ti (11.78) O—H (4.07) - (9.32)	[215, 394, 395]
		Ti 2p 3/2	458.2 (Ti^{4+})	O—Ti^{4+} (100)	[215, 394]
		Na 1s	1071.3	O—Na (75.64)	[215]

5.2.2.8 Raman Spectroscopy

As seen in *Figure 5:21A*, there were clear differences in peak positions from the pre-treated samples, compared to the titanate converted films. For all pre-treated samples, the peaks presented were all attributed to TiO_2 with anatase phases in the lower Raman shifts (< 300 cm^{-1}), similar to that seen in *Section 5.2.1.5* [434, 435]. Following NaOH treatment, alternate peaks at 285, 440, and 900 cm^{-1}, with broad

peaks around 630-690 cm^{-1} were delineated as a form of sodium hydrogen titanate ($Na_xH_{2-x}Ti_3O_7$) [209].

5.2.2.9 Fourier Transform Infrared Spectroscopy (FTIR)

The FTIR spectrum for all converted titanate samples is detailed in *Figure 5:21B.* The unconverted Ti films did not present any discernible peak from the background measurements and, therefore, have not been shown. The broad band between 3000 and 3500 cm^{-1} is attributable to fundamental O—H stretching groups of chemisorbed water. Additionally, there were potential peaks consistent with Ti interaction with –OH groups contained within this broad peak. The peak at 1650 cm^{-1} was also related to O—H bonding. The doublet peak located at 1410 and 1440 cm^{-1} was characteristic of C—H deformations of adventitious carbon and the peaks detailed between 850 and 900 cm^{-1} were attributable to Ti—O and Ti—O—Ti bonding.

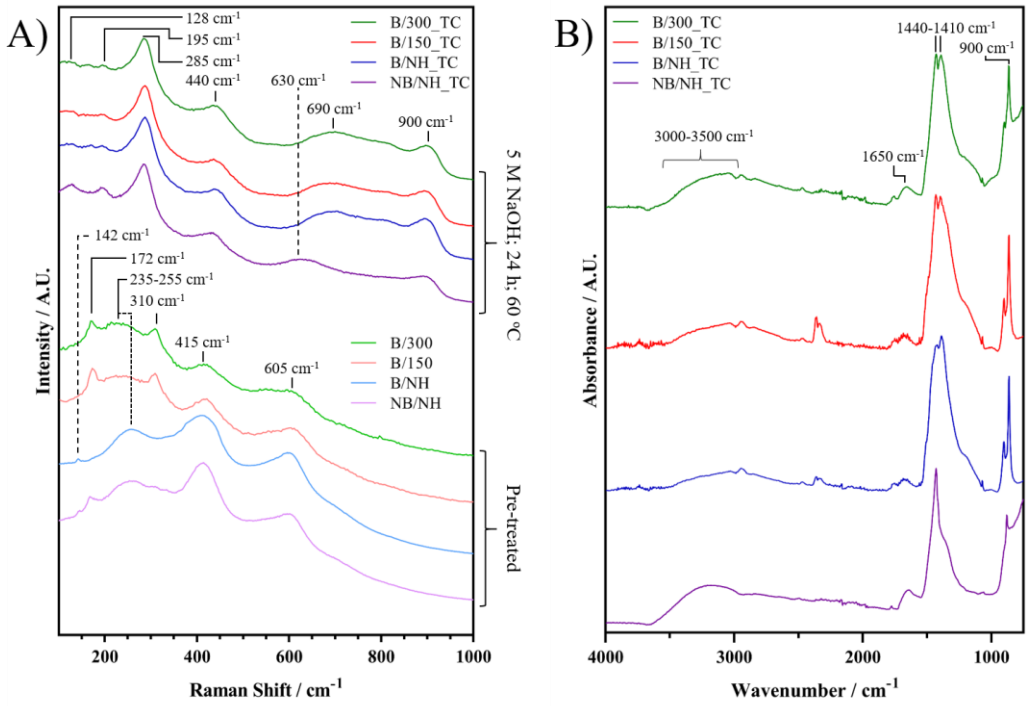

Figure 5:21. A) Raman spectral data for both unconverted and converted Ti films. B) FTIR data of converted Ti films; all unconverted produced no discernible peaks and, therefore, are not shown.

5.2.2.10 Optical Profilometry

To determine sample topography and roughness, optical profilometry was utilised, as detailed in *Figure 5:22.* It was clear that the polished 316L SS substrate exhibited a reduction in surface roughness (S_a = *ca.* 130 nm for the Control (316L SS), which reduced to < 40 nm) following sputtering of the Ti films. The roughness of the samples increased significantly from *ca.* 24, 40, 28, and 36 nm to 141, 94, 90, and 53 nm, for the NB/NH, B/NH, B/150, B/300, and NB/NH_TC, B/NH_TC, B/150_TC, and B/300_TC samples, respectively, with the exception of B/300 (whose S_a only subtly increased), following titanate conversion (B/300_TC).

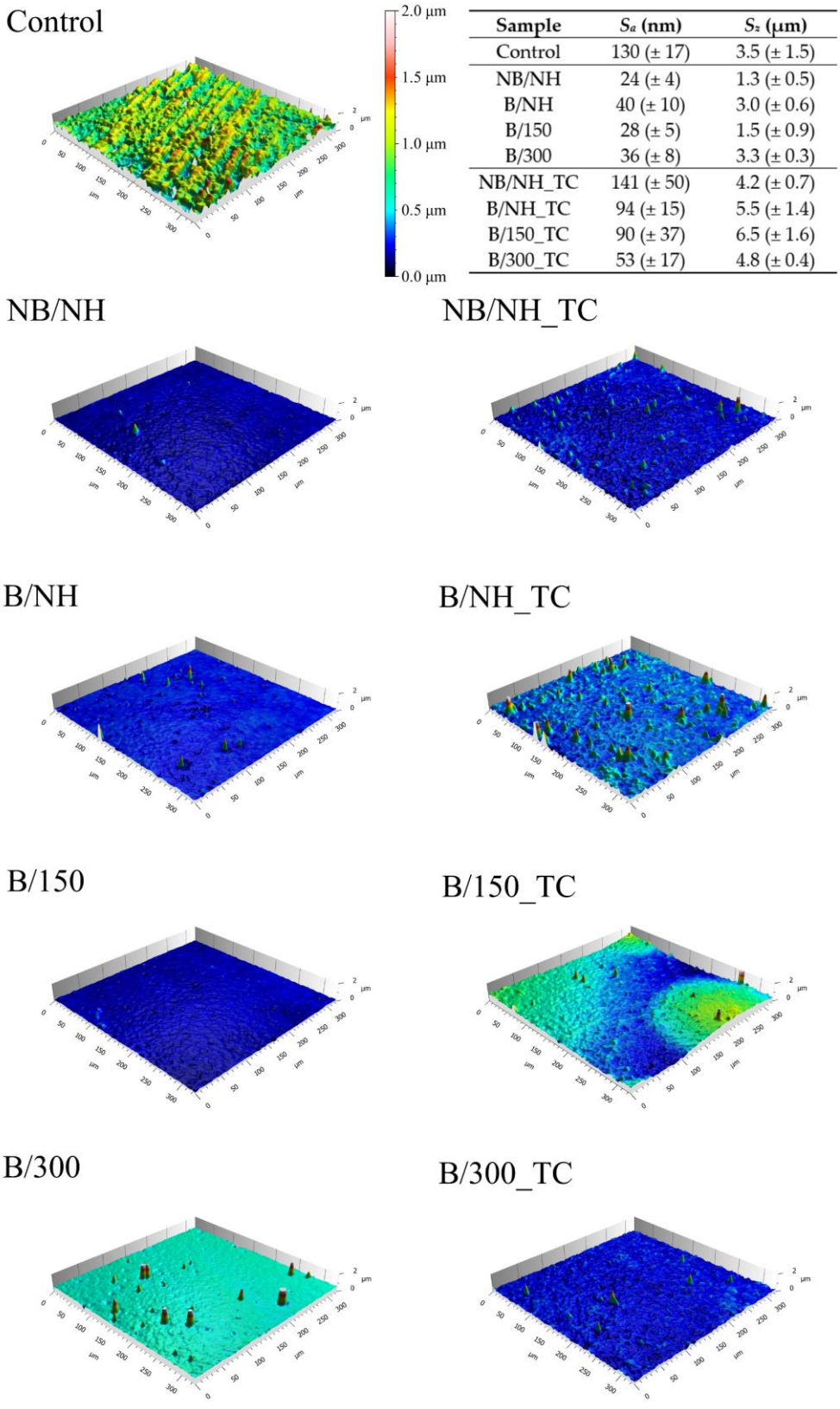

Sample	S_a (nm)	S_z (µm)
Control	130 (± 17)	3.5 (± 1.5)
NB/NH	24 (± 4)	1.3 (± 0.5)
B/NH	40 (± 10)	3.0 (± 0.6)
B/150	28 (± 5)	1.5 (± 0.9)
B/300	36 (± 8)	3.3 (± 0.3)
NB/NH_TC	141 (± 50)	4.2 (± 0.7)
B/NH_TC	94 (± 15)	5.5 (± 1.4)
B/150_TC	90 (± 37)	6.5 (± 1.6)
B/300_TC	53 (± 17)	4.8 (± 0.4)

Figure 5:22. 3D visualisation and table of optical profilometry roughness values of surface topography for control, unconverted and titanate converted samples. S_a and S_z values represent arithmetic mean height and maximum height of surface features, respectively; n = 3.

Table 5:7. Additional raw optical profilometry values, with S_q = root mean square height, S_p = maximum peak height, and S_v = maximum pit height. All values are mean ± standard error; n = 3.

Sample	**S_q (nm)**	**S_p (µm)**	**S_v (µm)**
Control	169 (± 19)	2.4 (± 1.2)	1.2 (± 0.2)
NB/NH	43 (± 14)	0.7 (± 0.2)	0.6 (± 0.5)
B/NH	100 (± 35)	2.0 (± 0.2)	1.0 (± 0.4)
B/150	48 (± 14)	1.2 (± 0.8)	0.3 (± 0.1)
B/300	95 (± 13)	2.3 (± 0.7)	1.1 (± 0.6)
NB/NH_TC	222 (± 69)	3.2 (± 0.6)	1.1 (± 0.7)
B/NH_TC	227 (± 67)	3.1 (± 0.9)	2.3 (± 1.0)
B/150_TC	165 (± 38)	5.6 (± 1.6)	0.7 (± 0.3)
B/300_TC	149 (± 17)	4.5 (± 0.4)	0.3 (± 0.0)

5.2.2.11 Atomic Force Microscopy

As a complimentary technique to optical profilometry, AFM was also conducted to investigate the nano- and microscale roughness of the Ti sputtered and titanate-converted samples (*Figure 5:23* & *Figure 5:24*). Overall, the AFM measurements demonstrated an increase in the surface roughness following sputtering of the Ti films (*Figure 5*:*23*, *Figure 5*:*24*, & *Table 5*:*8*), with decreasing roughness noted for the more equiaxed samples (*ca.* 32.6 *vs.* 26 nm for the NB/NH and B/300 samples, respectively). Furthermore, following titanate conversion, the roughness further increased for the samples, with values of *ca.* 134 to 187 nm, compared to *ca.* 26 to 33 nm for the titanate converted and Ti sputtered films, respectively.

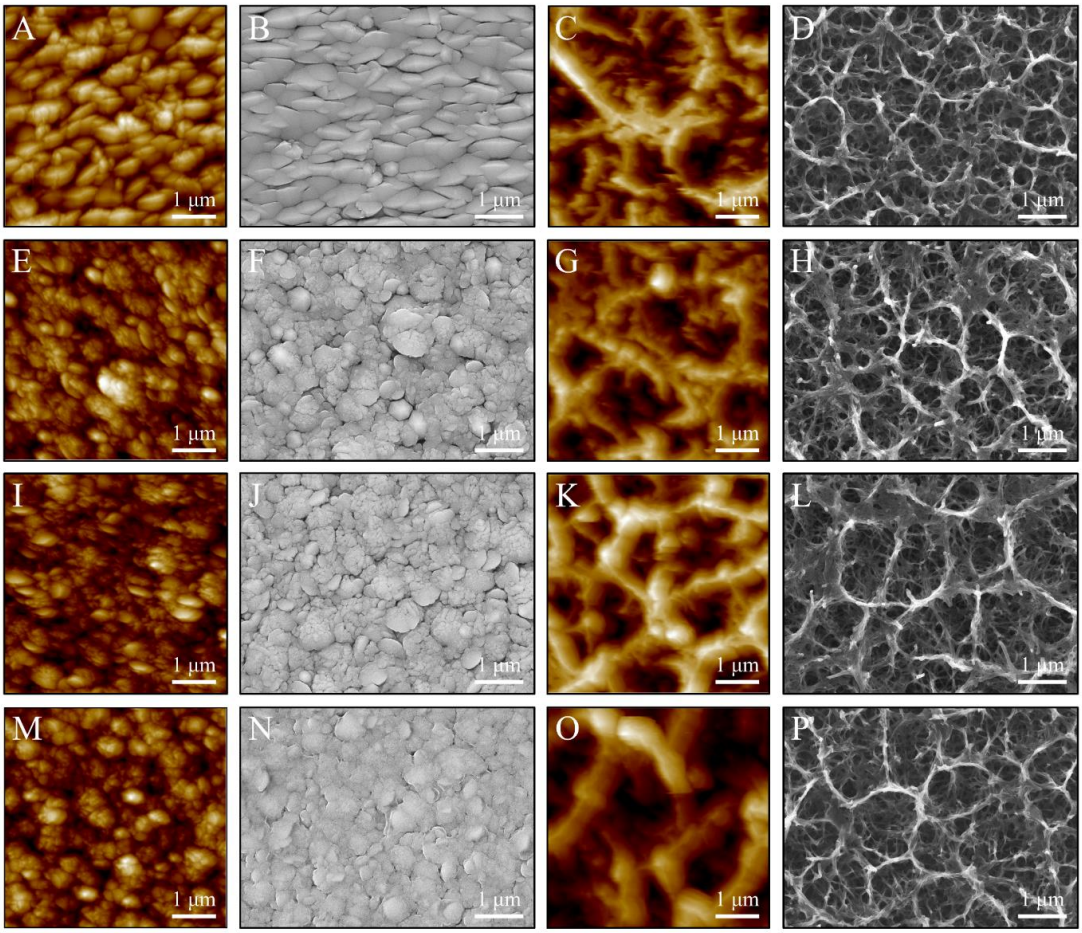

Figure 5:23 AFM and SEM micrographs for A & B) NB/NH, C & D) NB/NH_TC, E & F) B/NH, G & H) B/NH_TC, I & J) B/150, K & L) B/150_TC, M & N) B/300, O & P) B/300_TC, respectively.

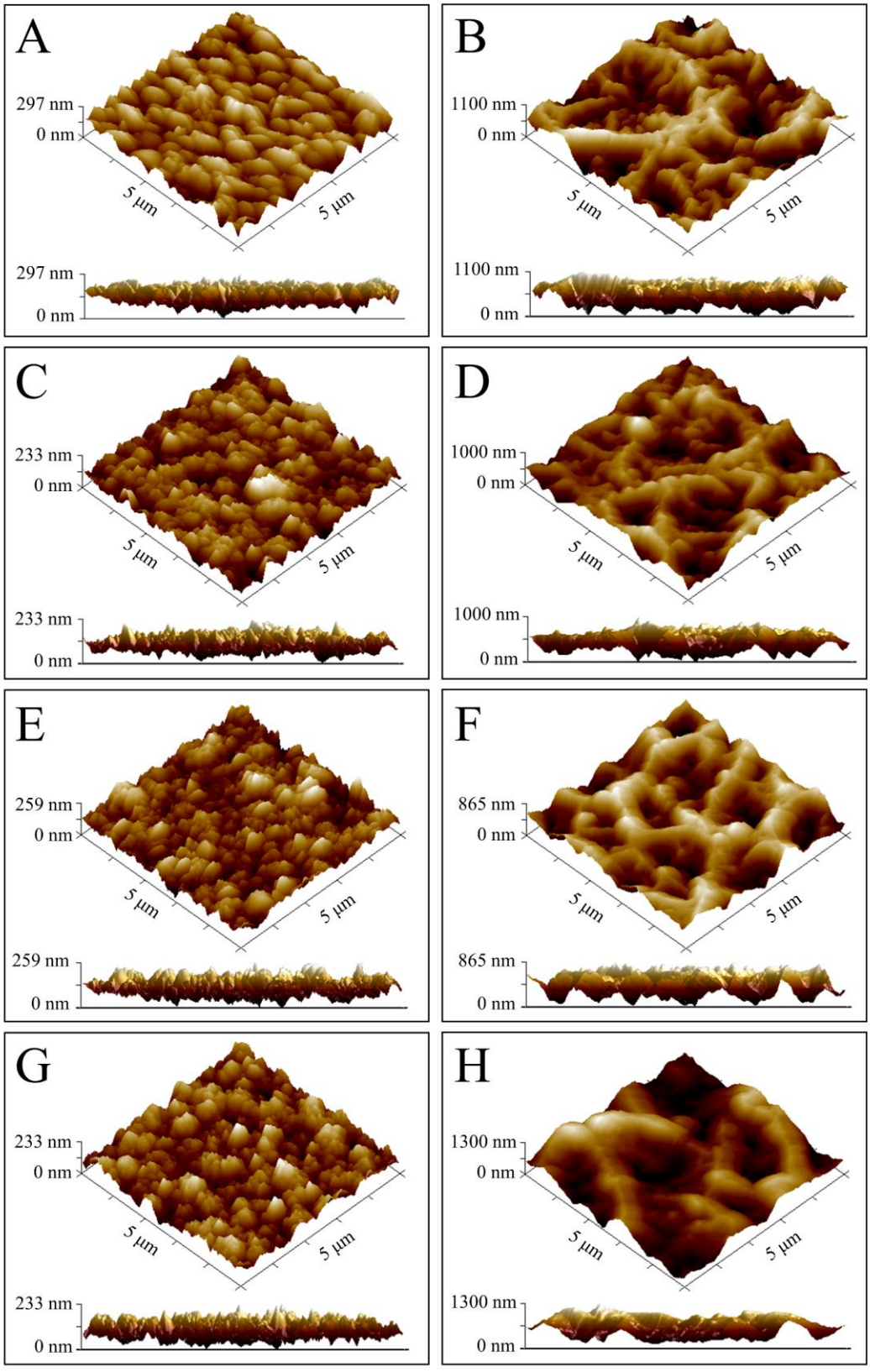

Figure 5:24. Representative AFM micrographs of A) NB/NH; B) NB/NH_TC; C) B/NH; D) B/NH_TC; E) B/150; F) B/150_TC; G) B/300; H) B/300_TC samples.

Table 5:8. Raw roughness (R_a) values calculated from the AFM micrographs. All values are mean ± standard error; n = 3.

Sample	R_a (nm) ± Standard Error (*n* = 3)
Control	2.1 ± 0.3
NB/NH	32.6 ± 1.1
B/NH	28.8 ± 2.3
B/150	26.0 ± 1.6
B/300	26.0 ± 0.5
NB/NH_TC	136.2 ± 8.5
B/NH_TC	134.4 ± 3.4
B/150_TC	141.2 ± 5.5
B/300_TC	187.4 ± 8.9

5.2.3 Mechanical Testing of Pre- and Post Titanate-Converted Ti Thin Films

5.2.3.1 Pull Off Adhesion Strength

Coating adhesion strength on polished and sandblasted substrates was determined using pull off adhesion testing. For the polished substrates, it was noted that through the application of a substrate bias (from NB/NH to B/NH), as well as the introduction of substrate heating (B/150 and B/300), the coating adhesion strength on the polished substrates decreased, with strengths of 42.2, 30.5, 14.5, and 5.7 MPa for the NB/NH, B/NH, B/150, and B/300 samples, respectively. Additionally, the incidence of full and partial coating failure increased with bias and substrate heating (*Table 5:9* & *Figure 5:25*). After subsequent titanate conversion, the coating adhesion strength significantly decreased compared to the unconverted samples, revealing a reduction from *ca.* 42 to 14 MPa for the NB/NH and NB/NH_TC samples, respectively. Similar trends were observed for all other titanate samples, with a clear reduction from the unconverted Ti samples to the titanate-converted samples, for the same parameter type (*Table 5:9*).

For the sandblasted samples, the pull off failure loads were significantly higher than the polished substrate counterparts. However, failure of all sample types, as

observed using microscopic evaluation, occurred through epoxy cohesive failure. Due to this, comparative analysis could not be made since the failure load of the coating exceeded that of the adhesive. However, the data below has been included for clarity (*Table 5:10*).

Table 5:9. Pull off adhesion data on polished 316L S.S. substrates, demonstrating average failure strength of both unconverted and converted Ti films (n = 8). Additionally, the frequency of each failure mechanism has been detailed.

Sample	Failure Strength / MPa	Full Interfacial Failure	Partial Interfacial Failure	Adhesive Failure in the Epoxy
NB/NH	42.2 ± 3.5	0	5	3
B/NH	30.5 ± 3.7	2	3	3
B/150	14.5 ± 4.8	8	0	0
B/300	5.7 ± 0.6	1	6	1
NB/NH_TC	13.7 ± 2.0	4	4	0
B/NH_TC	10.8 ± 3.5	2	3	3
B/150_TC	8.1 ± 2.2	5	3	0
B/300_TC	3.0 ± 0.9	7	0	1

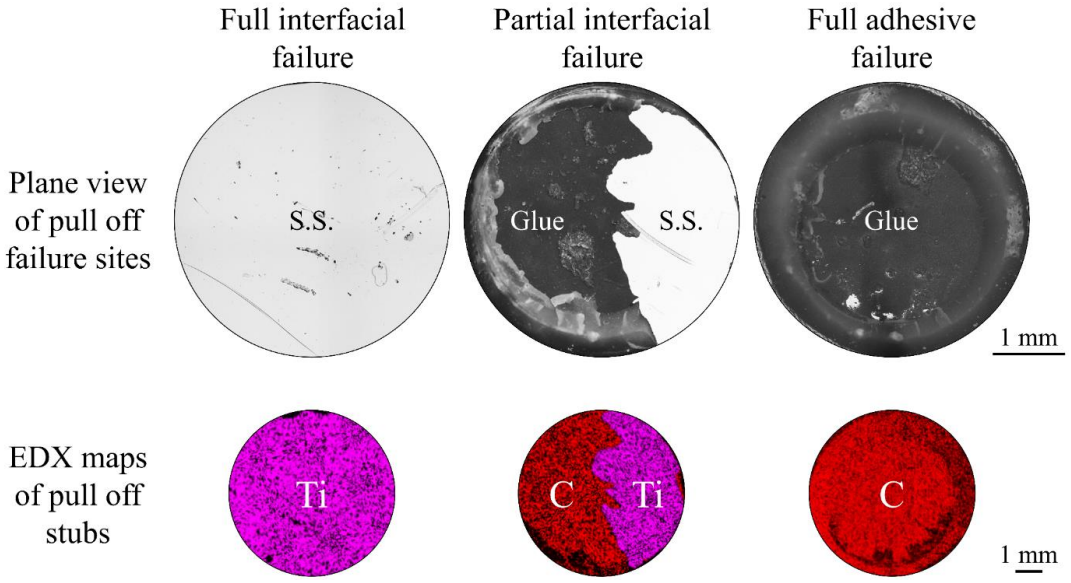

Figure 5:25. Optical microscope images and EDX elemental maps of sample surfaces and pull off stubs, respectively. Typical failure modes of full interfacial, partial interfacial and full adhesive failure shown. C elemental maps are attributed to the epoxy adhesive, whilst Ti indicates the failed coating.

Table 5:10. Pull off adhesion data on sandblasted 316L S.S. substrates, demonstrating average failure strength of both unconverted and converted Ti films (n = 8). Additionally, the frequency of each failure mechanism has been detailed. Due to all samples exhibiting epoxy failure, direct comparisons cannot be made, however, the data is presented for clarity.

Sample	Failure Strength / MPa	Full Interfacial Failure	Partial Interfacial Failure	Adhesive Failure in the Epoxy
NB/NH	51.3 ± 7.9	0	0	8
B/NH	51.5 ± 3.5	0	0	8
B/150	52.3 ± 4.1	0	0	8
B/300	37.2 ± 5.6	0	0	8
NB/NH_TC	41.4 ± 3.5	0	0	8
B/NH_TC	34.4 ± 5.0	0	0	8
B/150_TC	42.4 ± 4.5	0	0	8
B/300_TC	35.7 ± 4.7	0	0	8

5.2.3.2 Scratch Adhesion Testing

Scratch adhesion analysis was conducted as a complimentary technique to assess the relative failure loads and the associated failure modes of the films produced. Due to unexpected failure of the scratch testing equipment, and the closure of laboratories due to the COVID-19 pandemic meaning alternative testing arrangements could not be made, only polished substrates were analysed and presented in this thesis. In *Figure 5:26* and *Table 5:11*, there was a clear reduction in the required applied load to cause coating cracking and hence spallation during the transition from the NB/NH sample to the B/300 sample, as well as following titanate conversion for all sample types. Both the NB/NH and B/NH samples exhibited no spallation (L_{c3}) up to the applied 15 N load. However, the B/150 and B/300 samples exhibited spallation at *ca.* 2.9 and 1.6 N, respectively. Tensile cracking (L_{c1}) was observed for all sample types with loads of *ca.* 2.6, 2.2, 1.6, and 1.3 N for the NB/NH, B/NH, B/150, and B/300 samples, respectively, agreeing with the above trend (*Table 5:11* & *Figure 5:26*). Following titanate conversion, the samples were limited to ductile perforation leading to interfacial delamination. The trend between the samples was the same as that of the unconverted samples, with the NB/NH_TC sample demonstrating the highest load for

spallation (L_{c3}; *ca.* 4.3 N) and the B/300_TC sample exhibiting the lowest (L_{c3}; *ca.* 1.0 N).

Table 5:11. Failure loads calculated from failure initiation of scratch testing track profiles. Error calculated from 5 samples, in accordance with ISO 20502:2016.

Sample	Tensile Cracking (L_{c1}) / N	Buckling/Chevron Cracking (L_{c2}) / N	Spallation (L_{c3}) / N
NB/NH	2.6 ± 0.1	9.9 ± 0.5	-
B/NH	2.2 ± 0.2	6.5 ± 0.7	-
B/150	1.6 ± 2.9	-	2.9 ± 0.4
B/300	1.3 ± 0.3	-	1.6 ± 0.5
NB/NH_TC	-	-	4.3 ± 0.4
B/NH_TC	-	-	2.3 ± 0.4
B/150_TC	-	-	1.4 ± 0.7
B/300_TC	-	-	1.0 ± 0.3

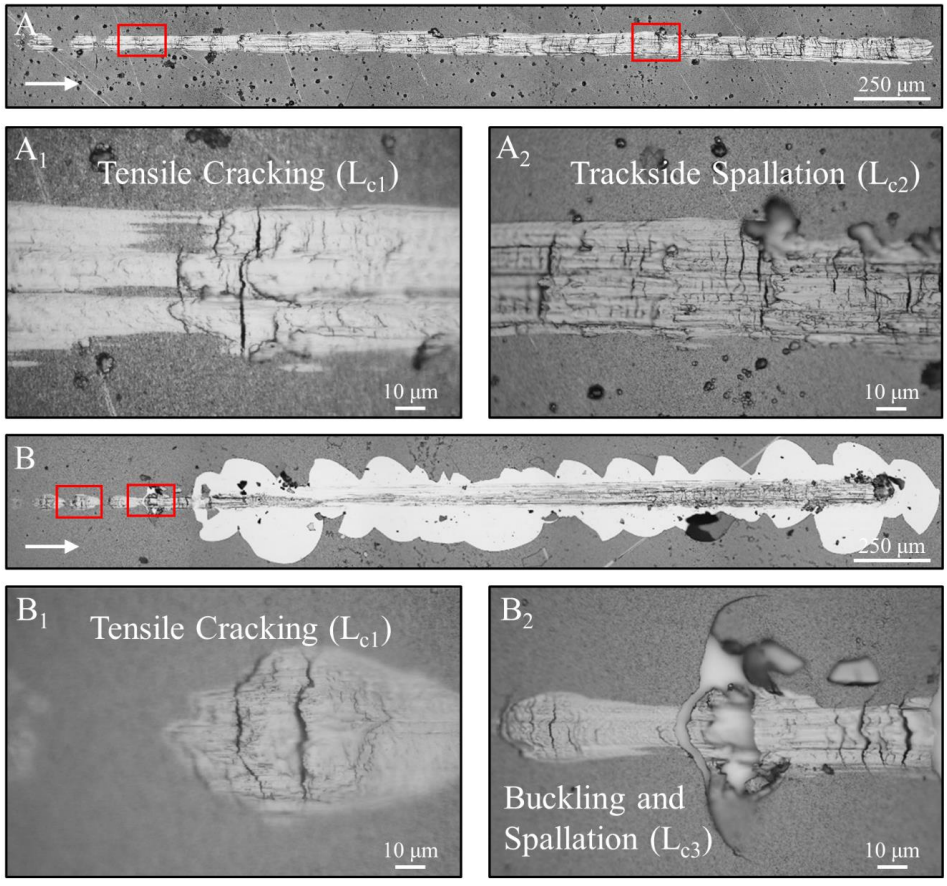

Figure 5:26. Optical microscope images of typical scratch testing tracks showing the characteristic failure modes, such as tensile cracking (L_{c1}), chevron cracking (L_{c2}), and buckling/spallation (L_{c3}) denoted. A) Non-titanate converted sample; B) Titanate converted counterpart.

5.2.4 The Effect of Titanium Film Thickness on Titanate Formation

As detailed in *Section 5.2.2.3*, it was found that only a maximum of 9.4% of the 4 μm Ti films converted into titanate structures, indicating the film thickness utilised was excessive and, therefore, not optimal. Hence, a further thickness optimisation study was conducted on 316L SS, utilising nominal coating thickness of 50, 100, 200 and 500 nm, which were chosen due to the ΔTi measurements in *Figure 5:14*, in order to ascertain whether there is a minimum Ti thickness below which nanoporous titanate conversion does not occur.

5.2.4.1 SEM analysis

From the SEM micrographs (*Figure 5:27*), the Ti coatings exhibited good step coverage of the roughened SS substrates (sandblasted using methodology in *Section 3.1.1.2*), used due to the increased adhesion (*Section 5.2.3.1*), as expected from magnetron sputtered films. Following the wet chemical treatment, it was clear titanate conversion had occurred even on the 50 nm thick coatings. The titanate structures formed were relatively smaller on the thinner titanium coatings with a clear critical thickness point occurring between the 100 and 200 nm coatings. For both the 200 and 500 nm coatings, larger struts were noted with ‘webbing’ observed between the struts in the 500 nm_Ti sample.

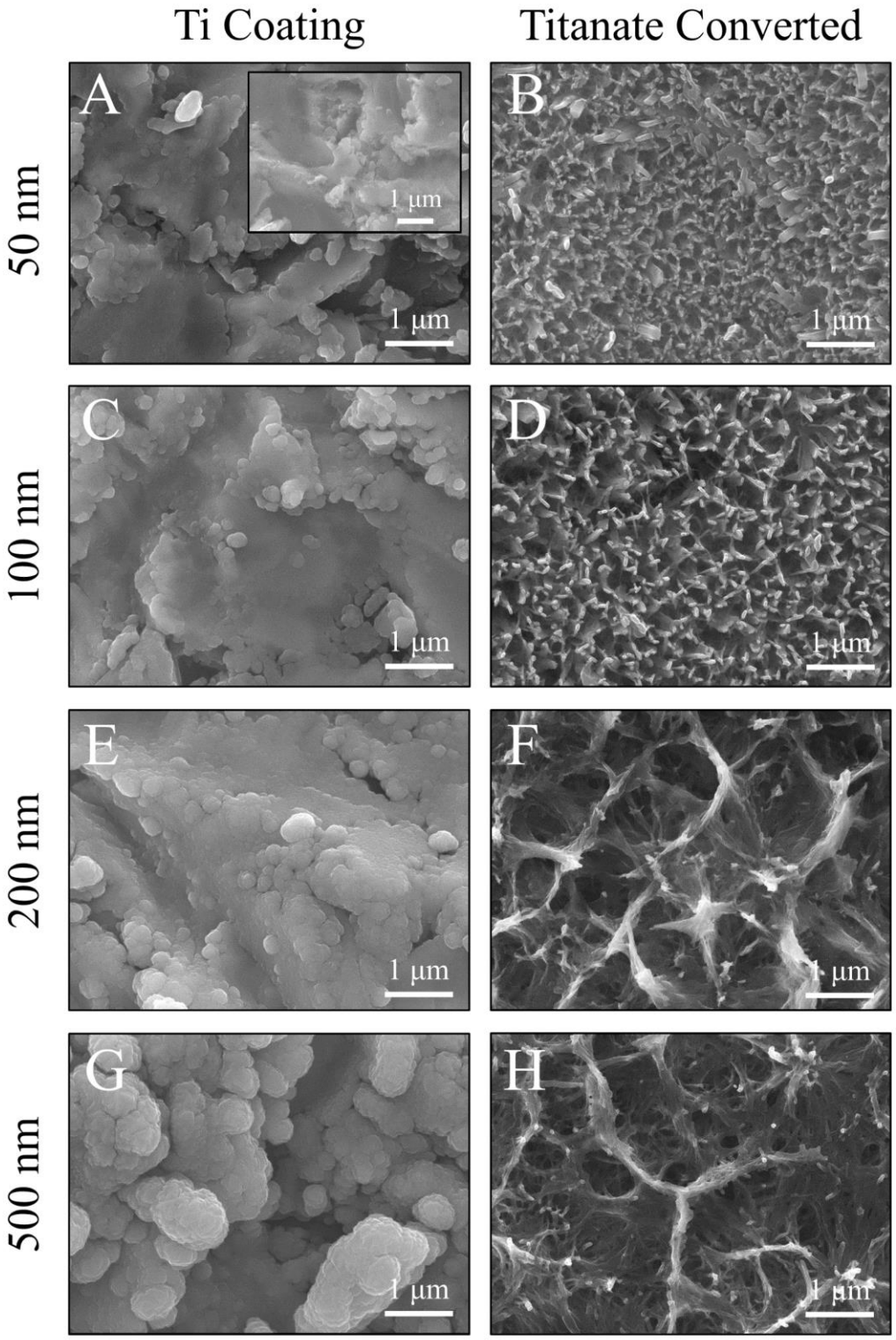

Figure 5:27. SEM micrographs showing the surface of unconverted and titanate converted Ti thin films, on 316L SS, of various thicknesses. A, C, E, and G) Ti coated samples with thicknesses of 50, 100, 200 and 500 nm, respectively. Insert image in A is the SS control substrate. B, D, F, and H) Titanate converted samples with initial Ti thickness of 50, 100, 200 and 500 nm, respectively.

5.2.4.2 XRD analysis

Crystallographic analysis demonstrated subtle differences between the 50, 100 and 200 nm samples, with peaks noted at *ca.* 43.7, 44.5, and 50.7^{o} 2θ for austenite (111), ferrite (110) and austenite (200), respectively, from the underlying SS substrate. Increasing intensities were noted for the (002) plane of HCP Ti (PDF 00-044-1294) located at 38.4^{o} 2θ from the sputtered Ti coating. Austenite and ferrite phases were quantified from PDF 00-033-0397 and 00-054-0331, respectively. Additional peaks from the Ti coating were present in the 500 nm sample, with peaks corresponding to the (100), (101) and (102) planes located at *ca.* 35.2, 40.1, and 53.0 ^{o} 2θ, respectively.

Following titanate conversion additional low intensity peaks were noted at 24.2, 28.4 and 48.2^{o} (PDF 00-022-1404 and PDF 00-025-1450), which correspond to isomorphic titanate species, which were also noted previously (*Section 5.2.2.6*). The complete loss of the (002) peak in the 50, 100 and 200 nm samples, with reduced intensity noted also in the 500 nm sample, indicated that conversion of the Ti coating into titanate resulted in a thickness of Ti, which was smaller than was discernible *via* XRD. From the Ti coatings alone, a 100 nm thick layer was needed to observe this *via* XRD and, therefore, gave an estimate of the reduced thickness of the Ti coating.

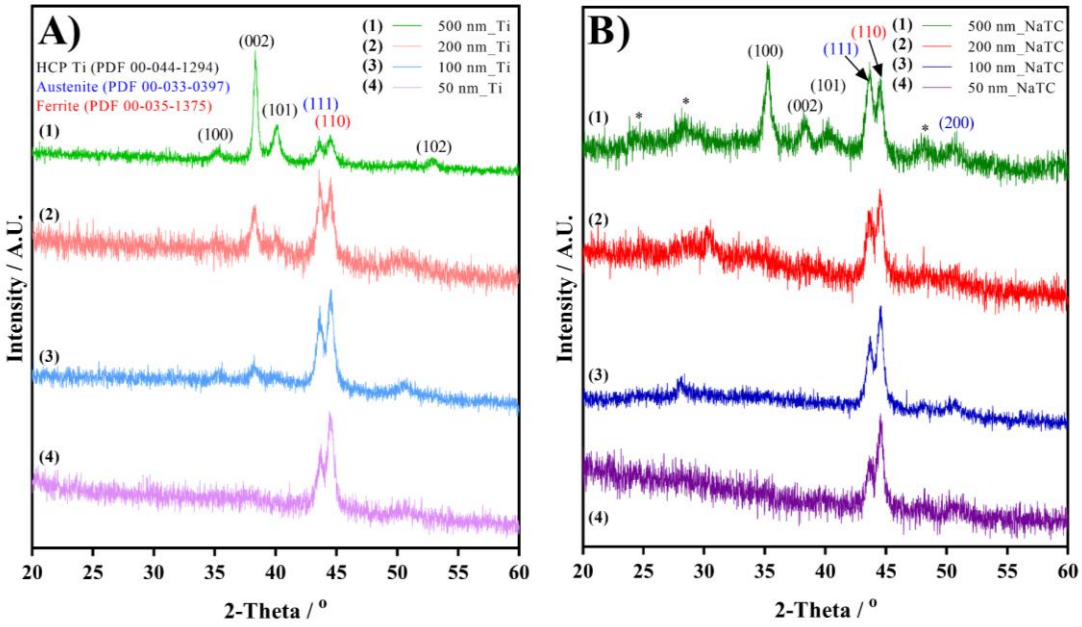

Figure 5:28. A) XRD spectra of unconverted samples with varying Ti thicknesses (50, 100, 200, 500 nm), with three different phases noted from the SS substrate (PDF 00-033-0397 and PDF 00-054-0331 for Austenite and Ferrite, respectively) and the Ti coating (PDF 00-044-1294). B) Titanate converted samples with varying aforementioned Ti thicknesses, with additional phases noted corresponding to titanate species (PDF 00-022-1404 and PDF 00-025-1450).

5.2.4.3 XPS analysis

From the XPS analysis conducted (*Figure 5:29, Table 5:12, Table 5:13,* & *Table 5:14*) clear deconvolution and binding energy differences were noted for Na 1s, O 1s and Ti 2p spectra for pre- and post-titanate converted samples. For the Ti coatings of different thicknesses (50, 100, 200 and 500 nm) the peak deconvolutions noted remained the same, however, subtle binding energy shifts were noted for the O 1s and Ti 2p peak deconvolutions.

For the O 1s peaks, three deconvolutions were noted in all Ti sample types, located at *ca.* 529.6, 531.0, and 532.2 eV, corresponding to O^{2-}/Lattice O, OH^{-}/Surface O, and H_2O, respectively. Overall, all peaks recorded decreases in binding energy values (*ca.* 0.5 eV) as thickness of the Ti coating increased, whilst the overall area percentages

for each deconvolution remained constant irrespective of coating thickness (*Table 5:12*). For the Ti 2p doublet peaks, four deconvoluted states were found for all Ti coatings, corresponding to the four valence states of Ti (Ti^{4+}, Ti^{3+}, Ti^{2+} and metallic Ti). Again, the peak deconvolutions shifted to lower binding energy states as the thickness of the coatings increased, aside from the 200 nm_Ti sample which demonstrated a subtle increase (*ca.* 0.1-0.3 eV) for all deconvolutions. All peak positions and deconvolution data is outlined in *Table 5:12.*

Following titanate conversion (NaTC), various changes were noted in the number of peak deconvolutions and binding energy positions. O 1s for all NaTC sample types demonstrated an increase in the number of peak deconvolutions from three to four with the addition of the Na KLL Auger peak at *ca.* 535.2 eV. All other peak deconvolutions remained constant, with a shift to higher binding energy values due to an increase in Ti coating thickness (*ca.* 0.3-0.6 eV). The Ti 2p doublet peaks reduced from four peak deconvolutions, to just one corresponding to Ti^{4+}, which remained constant irrespective of coating thickness at *ca.* 458.3 eV. An additional peak for all NaTC samples was also noted at 1071.5 eV corresponding to Na—O. Detailed deconvolution and binding energy analysis for NaTC samples is described in *Table 5:13*.

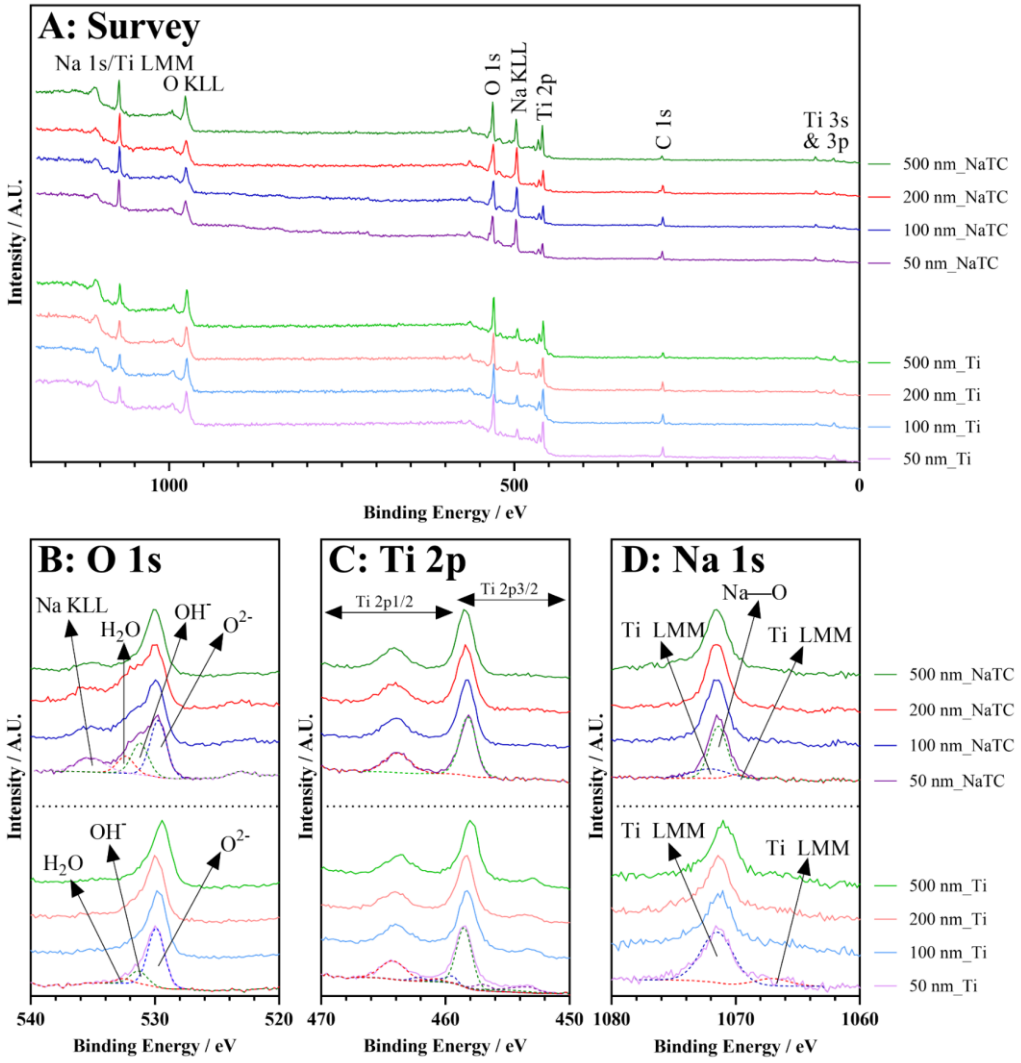

Figure 5:29. XPS spectra of graded Ti film thicknesses and there subsequent conversion into titanate structures. A) Survey spectra; B) O 1s high-resolution spectra; C) Ti 2p high-resolution spectra; and D) Na 1s high-resolutioin spectra.

Table 5:12. High-resolution raw data of Ti coated 316L SS discs with varying thicknesses (ca. 50, 100, 200, and 500 nm) of sputtered films.

Sample	Elements	Binding Energy / eV	Corresponding Bonds (Area / %)	Ref.
50 nm_Ti	O 1s	529.9 (O^{2-}) 531.3 (OH^{-}) 532.5 (H_2O)	Ti^{4+}—O (76.64) Ti—OH, $Ti^{2+/3+}$—O (17.20) O—H (6.16)	[394, 431-433]
	Ti 2p 3/2	458.5 (Ti^{4+}) 457.0 (Ti^{3+}) 455.2 (Ti^{2+}) 453.3 (Ti^{0})	O—Ti^{4+} (67.45) O—Ti^{3+} (8.31) O—Ti^{2+} (6.35) Ti—Ti (17.89)	[394, 432, 433]
100 nm_Ti	O 1s	529.7 (O^{2-}) 531.2 (OH^{-}) 532.5 (H_2O)	Ti^{4+}—O (76.90) Ti—OH, $Ti^{2+/3+}$—O (17.55) O—H (5.55)	[394, 431-433]
	Ti 2p 3/2	458.2 (Ti^{4+}) 456.7 (Ti^{3+}) 455.0 (Ti^{2+}) 453.0 (Ti^{0})	O—Ti^{4+} (66.63) O—Ti^{3+} (10.99) O—Ti^{2+} (5.71) Ti—Ti (16.68)	[394, 432, 433]
200 nm_Ti	O 1s	529.9 (O^{2-}) 531.2 (OH^{-}) 532.2 (H_2O)	Ti^{4+}—O (75.62) Ti—OH, $Ti^{2+/3+}$—O (16.86) O—H (7.52)	[394, 431-433]
	Ti 2p 3/2	458.3 (Ti^{4+}) 456.8 (Ti^{3+}) 455.0 (Ti^{2+}) 453.3 (Ti^{0})	O—Ti^{4+} (70.20) O—Ti^{3+} (7.90) O—Ti^{2+} (3.60) Ti—Ti (18.29)	[394, 432, 433]
500 nm_Ti	O 1s	529.4 (O^{2-}) 530.7 (OH^{-}) 532.0 (H_2O)	Ti^{4+}—O (77.44) Ti—OH, $Ti^{2+/3+}$—O (19.25) O—H (3.31)	[394, 431-433]
	Ti 2p 3/2	458.0 (Ti^{4+}) 456.5 (Ti^{3+}) 454.7 (Ti^{2+}) 452.7 (Ti^{0})	O—Ti^{4+} (66.76) O—Ti^{3+} (15.59) O—Ti^{2+} (9.51) Ti—Ti (8.15)	[394, 432, 433]

Table 5:13. Continuation of previous XPS table: Table 5:12.

Sample	Elements	Binding Energy / eV	Corresponding Bonds (Area / %)	Ref.
50 nm_NaTC	O 1s	529.7 (O^{2-}/Lattice O) 531.2 (OH^-/Surface O) 532.4 (H_2O) 535.1 (Na KLL)	Ti^{4+}—O (43.73) Na^+—O—Ti (24.45) O—H (13.19) - (18.63)	[215, 394, 395, 436]
	Ti 2p 3/2	458.2 (Ti^{4+})	O—Ti^{4+} (100)	[215, 394]
	Na 1s	1071.4	O—Na (69.41)	[215]
100 nm_NaTC	O 1s	529.9 (O^{2-}/Lattice O) 531.6 (OH^-/Surface O) 532.8 (H_2O) 535.2 (Na KLL)	Ti^{4+}—O (52.50) Na^+—O—Ti (22.36) O—H (8.83) - (16.30)	[215, 394, 395, 436]
	Ti 2p 3/2	458.3 (Ti^{4+})	O—Ti^{4+} (100)	[215, 394]
	Na 1s	1071.5	O—Na (64.86)	[215]
200 nm_NaTC	O 1s	529.9 (O^{2-}/Lattice O) 531.6 (OH^-/Surface O) 533.0 (H_2O) 535.4 (Na KLL)	Ti^{4+}—O (48.73) Na—O—Ti (24.92) O—H (10.52) - (15.83)	[215, 394, 395, 436]
	Ti 2p 3/2	458.4 (Ti^{4+})	O—Ti^{4+} (100)	[215, 394]
	Na 1s	1071.5	O—Na (62.10)	[215]
500 nm_NaTC	O 1s	530.0 (O^{2-}/Lattice O) 531.7 (OH^-/Surface O) 532.9 (H_2O) 535.2 (Na KLL)	Ti^{4+}—O (71.25) Na^+—O—Ti (12.09) O—H (4.18) - (12.48)	[215, 394, 395, 436]
	Ti 2p 3/2	458.2 (Ti^{4+})	O—Ti^{4+} (100)	[215, 394]
	Na 1s	1071.5	O—Na (48.99)	[215]

Elemental composition analysis was also calculated *via* XPS, as detailed in *Table 5:14.* The Ti and O content remained constant (*ca.* 71 and 29 at.% for O and Ti, respectively) for all Ti coatings, irrespective of coating thickness. A reduction was observed in the at.% of O following titanate conversion, due to the increase in Ti thickness of the original coating, from *ca.* 71.3 at.% in the 50 nm_NaTC sample to *ca.* 64.7 at.% in the 500 nm_NaTC sample. Ti content also appeared to increase as the Ti thickness increased (from *ca.* 12 at.% to 19 at.%; 50 to 500 nm). Na demonstrated elemental composition values of *ca.* 17 at.%, with no trend noted due to Ti thickness.

Table 5:14. Elemental composition of pre- and post-titanate converted samples of varying Ti thickness as determined via XPS. All values are mean ± standard deviation calculated via CasaXPS.

Sample	Elemental Composition (XPS)		
	Na / at.%	O / at.%	Ti / at.%
50 nm_Ti	0	71.7 ± 1.0	28.3 ± 1.0
100 nm_Ti	0	70.7 ± 1.0	29.3 ± 0.9
200 nm_Ti	0	71.6 ± 0.9	28.4 ± 1.0
500 nm_Ti	0	71.5 ± 1.0	28.5 ± 1.1
50 nm_NaTC	16.7 ± 0.6	71.3 ± 0.8	12.0 ± 0.5
100 nm_NaTC	15.6 ± 0.7	69.4 ± 0.9	15.0 ± 0.6
200 nm_NaTC	18.0 ± 0.8	67.9 ± 0.8	14.2 ± 0.6
500 nm_NaTC	16.3 ± 0.6	64.7 ± 0.8	19.0 ± 0.6

5.2.5 Effect of Oxygen Content on Titanate Production

In addition to understanding the effect of Ti film thickness on the alkali titanate formation mechanism, further analysis on the effect of oxygen content of the unconverted substrates were investigated; such a study has yet to be conducted in the literature. Ti6Al4V and TiO_2 microspheres were subjected to NaOH wet chemical treatments, with the effect of oxygen on the titanate mechanism detailed.

5.2.5.1 SEM/EDX Analysis

As observed in *Figure 5:30A-C*, the Ti6Al4V microspheres (Ti6Al4V_MS) exhibited a relatively smooth morphology (size range *ca.* 0.2-15 μm) produced *via* the atomisation process. However, following wet-chemical conversion in NaOH (Ti6Al4V_MS NaTC), a nanoporous morphology characteristic of titanate structures was present, with clear morphological differences (*Figure 5:30C* & *F*) noted between pre- (_MS) and post-titanate (_MS NaTC) converted samples. In some cases, cross growth and bonding between titanate structures of neighbouring microspheres was exhibited, with examples of bonded (*Figure 5:31A & B*) and fractured structures (*Figure 5:31C & D*); fracturing occurred due to removal of the spheres from their container (*Figure 5:32*). During conversion, this bonding between microspheres was

also indicated at the macroscopic level, with the spheres agglomerating or 'self-assembling' together, which remained stationary even with agitation of the solution (see *Figure 5:32*).

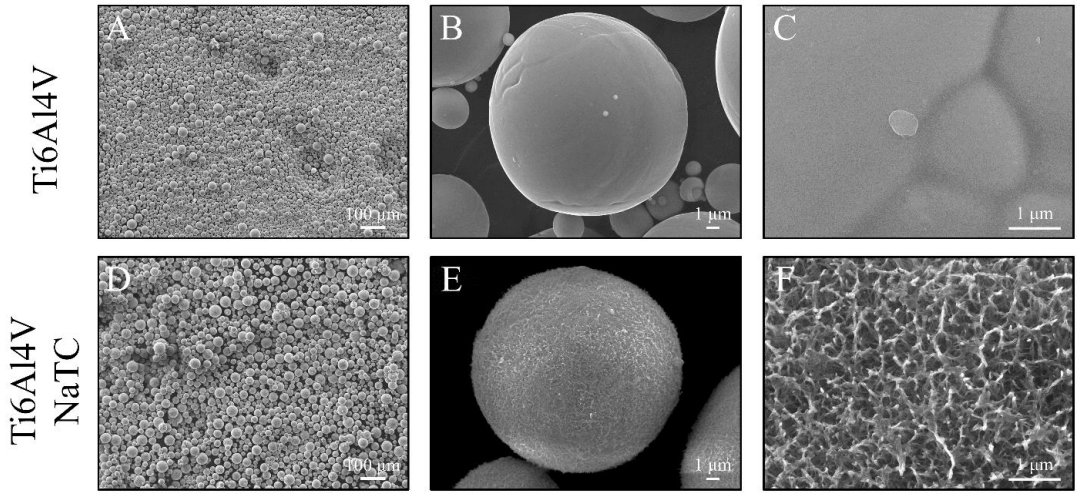

Figure 5:30. SEM micrographs showing unconverted (Ti6Al4V_MS) and converted (Ti6Al4V_MS NaTC) Ti6Al4V microspheres demonstrating the ability to convert the surface into nanoporous titanate structures. A, B & C) Ti6Al4V_MS samples at varying magnifications, and D, E & F Ti6Al4V_MS NaTC samples also at varying magnifications.

Delamination of the fracture structures occurred predominantly at the interface of the Ti substrate and the titanate formed layer, which are clearly exhibited in *Figure 5:31C* & *D*, as both fracture ends revealed a smooth morphology; matching the underlying microsphere surface texture. Interestingly, when the same chemical conversion was applied to titania (TiO_2) microspheres, the morphology of the microspheres (size range *ca.* 10-100 μm) did not produce any discernible change in structure of the produced microspheres, aside from removal of surface particulates (*Figure 5:33*). However, small levels of Na were seen on the surface from EDX analysis (*Table 5:15*); it was hypothesized that the level of oxygen content in the surface had a marked influence of the growth mechanism seen. In comparison, the Na levels were significantly lower, with *ca.* 4.7, 0.5 and 0.2 at.%, for the Ti6Al4V_MS NaTC, Anatase_MS NaTC, and Rutile_MS NaTC samples, respectively; the latter two

results are below the threshold for accurate assessment *via* EDX (*ca.* 1 at.%). A significant reduction in Ti (*ca.* 87 to 31 at.%) and increase in O (*ca.* 0 to 61 at.%) content was noted for the Ti6Al4V_MS, compared to the Ti6Al4V_MS NaTC samples. Both the anatase and rutile samples maintained constant Ti (*ca*. 30-32 at.%) and O (*ca*. 68-70 at.%) levels.

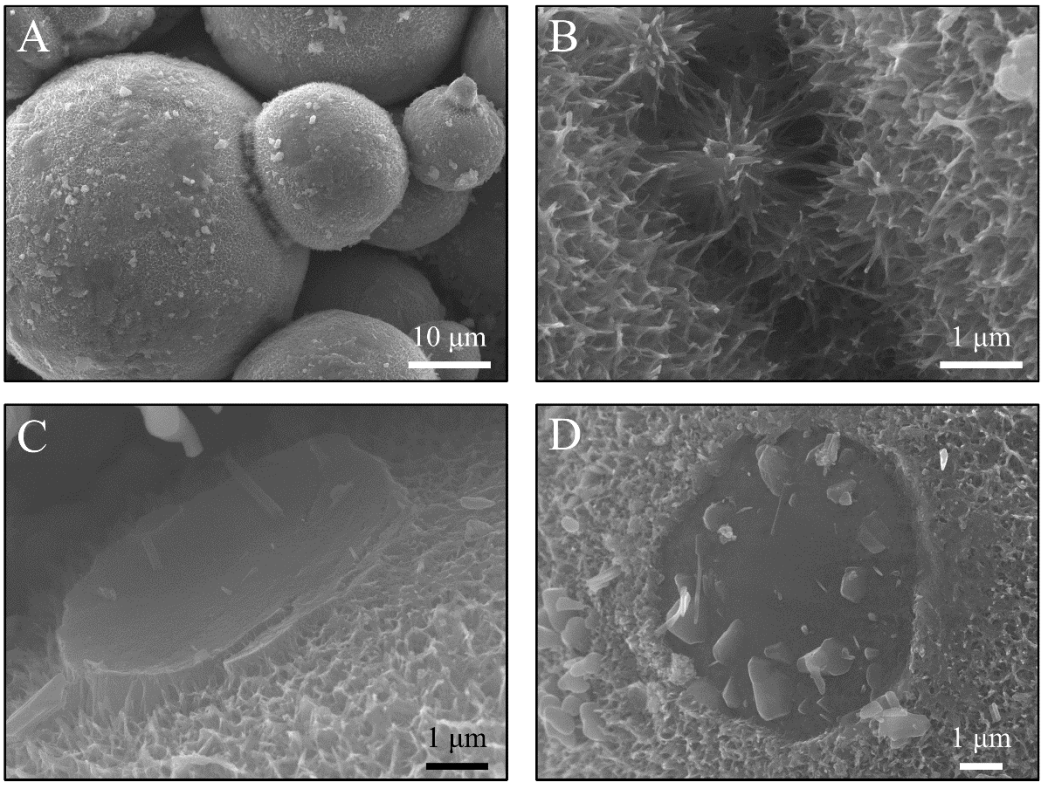

Figure 5:31. Example SEM micrograph features noted on the titanate converted Ti6Al4V microspheres (Ti6Al4V_MS NaTC). A) & B) Demonstrate at varying magnifications of the same area, the cross-linking of two individual microspheres through the growth and bonding of the produced titanate nanostructures. C) & D) Demonstrate the morphology of these surfaces at the failure of this bonded interface at both ends of the failure.

Figure 5:32. Titanate converted Ti microspheres within a polypropylene Falcon tube, exhibiting agglomeration and 'self-assembly' despite agitation of the solution.

The EDX mapping presented in *Figure 5:34* shows that Ti, O and Na (present in the NaTC samples only) were homogeneously distributed across the spheres. Higher relative quantities of Na (in relation to Ti and O) in the Ti6Al4V_MS NaTC sample were observed compared to both the Anatase_MS NaTC and Rutile_MS NaTC samples (*Table 5:15*).

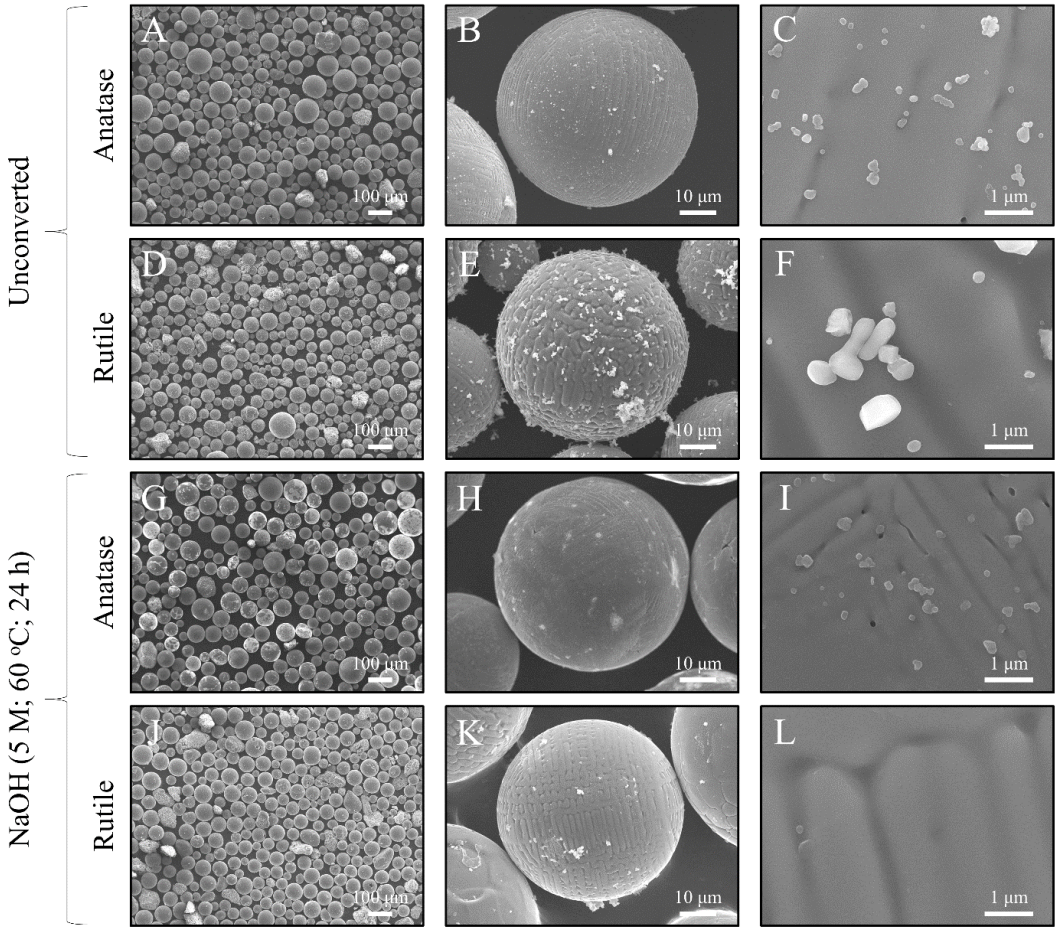

Figure 5:33. TiO_2 microspheres produced via a flame spheroidisation process using rutile or anatase starting powder, with subsequent titanate (NaTC) conversion. A-C) Anatase_MS; D-F) Rutile_MS; G-I) Anatase_MS NaTC; J-L) Rutile_MS NaTC.

Table 5:15. EDX elemental composition of Ti6Al4V, Anatase and Rutile microspheres (Ti6Al4V_MS, Anatase_MS, and Rutile_MS, respectively), as well as sodium titanate conversion of all three types, herein labelled with NaTC suffix. All values are mean ± standard error (n = 3).

Sample ID	Elemental Composition / at.%				
	Na	Ti	O	Al	V
Ti6Al4V_MS	0	86.7 ± 0.1	0	9.4 ± 0.1	3.9 ± 0.1
Ti6Al4V_MS NaTC	4.7 ± 0.3	30.9 ± 0.7	60.5 ± 0.5	2.6 ± 0.1	1.4 ± 0.1
Anatase_MS	0	30.0 ± 3.6	70.0 ± 3.6	0	0
Anatase_MS NaTC	0.5 ± 0.1	31.0 ± 1.9	68.4 ± 1.9	0	0
Rutile_MS	0	31.3 ± 3.3	68.7 ± 3.3	0	0
Rutile_MS NaTC	0.2 ± 0.0	30.0 ± 3.3	69.8 ± 3.2	0	0

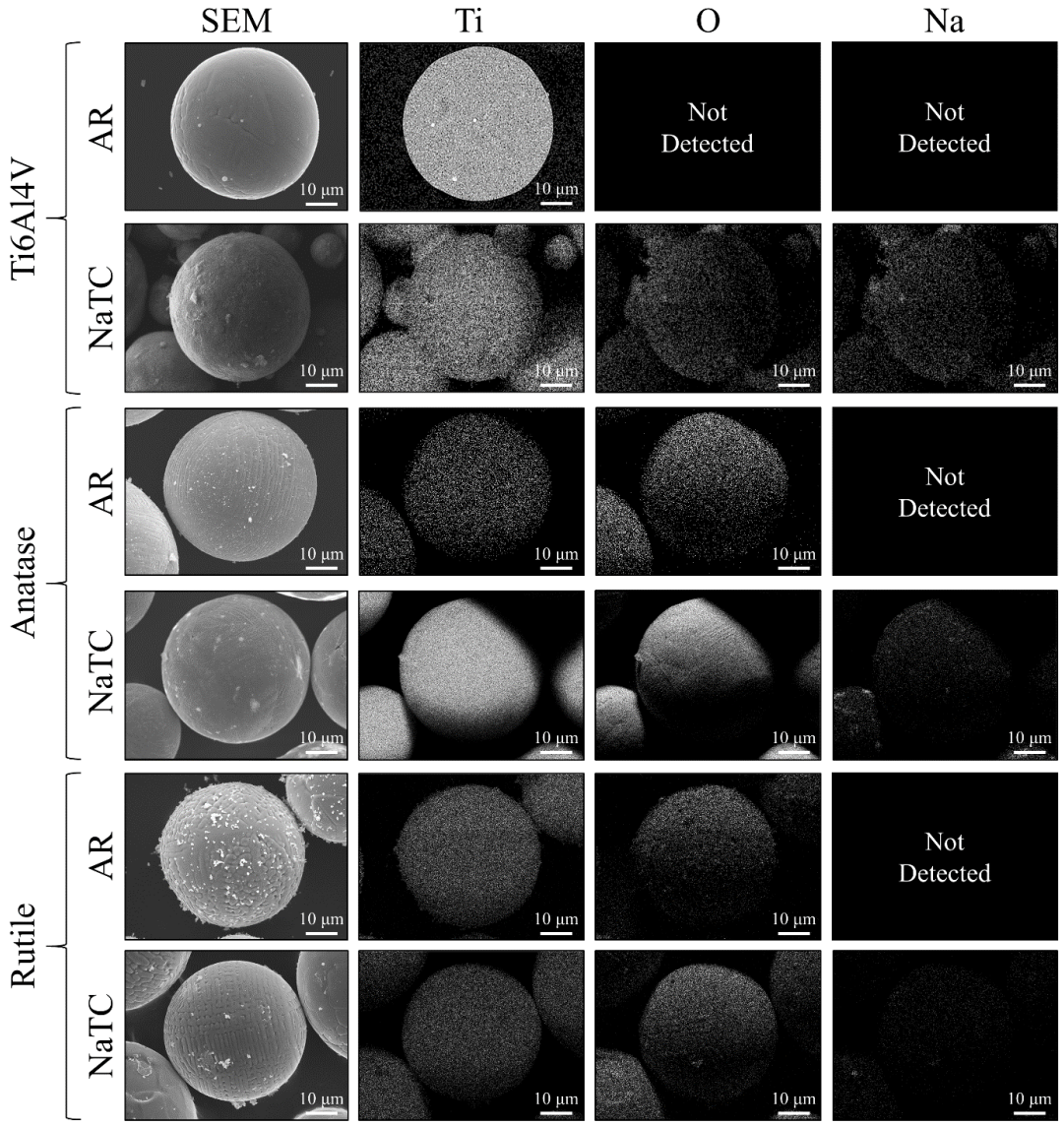

Figure 5:34. EDX mapping of Ti6Al4V_MS, Anatase_MS, and Rutile_MS samples, with their NaTC counterparts, demonstrating homogeneous distribution of Ti, O and Na, where applicable, with relative elemental ratios due to count intensities. AR = as received prior to titanate conversion; NaTC = titanate converted.

5.2.5.2 XPS Analysis

XPS analysis of both the titanate converted and non-titanate converted Ti6Al4V and TiO_2 (anatase and rutile) microspheres are detailed in *Figure 5:35*, *Table 5:16* & *Table 5:17*. For the Ti6Al4V_MS samples, the Ti was found to be in its 4^+ valence state (2p 3/2 = *ca.* 458.7 eV), characteristic of the passivated TiO_2 layer that forms due to exposure to air. O had 2 peak deconvolutions located at *ca.* 530.3 (60.5%) and 532.3 (39.5%) eV corresponding to metallic oxide and hydroxide bonding, respectively.

Upon conversion to sodium titanate (Ti6Al4V_MS NaTC), there was a shift (*ca.* 0.7 eV) to lower binding energies in the Ti peak position (*ca.* 458.0 eV), which was characteristic of Ti^{4+} within titanate structures. There was an increase in the number of O peak deconvolutions, with 4 peaks located at *ca.* 529.6, 531.3, 532.5 and 534.9 eV corresponding to O^{2-} (*ca.* 54.7%; Ti^{4+}—O), bridging OH^-_{br}/defective oxides/Non-lattice O (*ca.* 24.0%), terminal OH^-_t/H_2O (*ca.* 9.4%), and Na KLL Auger e^- (*ca.* 11.8%). A peak was also formed at 1071.1 eV corresponding the Na—O bonding of titanate structures, with two Ti LMM Auger peaks that were also present in the Ti6Al4V_MS sample.

For the Anatase_MS and Rutile_MS samples, similar peak deconvolutions to the Ti6Al4V_MS sample were noted. Ti was found in its 4^+ valence state (*ca.* 458.4 – 458.6 eV), and the O deconvolutions revealed two peaks at *ca.* 529.9 (73.6 – 78.2%) and 532.2 (21.8 – 26.4%) eV, again corresponding to the aforementioned bonding. Following titanate conversion, both the Anatase_MS NaTC and Rutile_MS NaTC samples again exhibited similar deconvolutions to the Ti6Al4V_MS NaTC counterpart, with notable shifts in binding energies for both Ti and O to lower eV values. The peak deconvolutions for the O spectral range exhibited 4 peaks located at *ca.* 529.4 (*ca.* 28.1%), 531.2 (*ca.* 38.3%), 532.8 (*ca.* 17.1%), and 535.5 (*ca.* 16.5%) eV for the Anatase_MS NaTC samples, whilst the Rutile_MS NaTC sample exhibited peaks at *ca.* 529.6 (*ca.* 16.8%), 531.6 (*ca.* 31.2%), 533.0 (*ca.* 45.0%), and 535.6 (*ca.* 7.0%) eV, corresponding to O^{2-} (Ti^{4+}—O), bridging OH^-_{br}/defective oxides, terminal OH^-_t/H_2O, and Na KLL Auger e^-, respectively. The relative percentages of each type of bonding, specifically the reduction in Ti^{4+}—O bonding characteristic of titanate structures, demonstrated that the quantity of surface titanate that formed was

considerably less for the Anatase_MS NaTC and Rutile_MS NaTC, and may only be present in the top few nanometres of the surface.

It was clear from the relative elemental compositions (*Table 5:17*) that the Ti6Al4V_MS NaTC samples exhibited higher Na content compared to both converted anatase and rutile samples, however, there was no significant difference between the Anatase_MS NaTC and Ti6Al4V_MS NaTC samples. Furthermore, the Ti and O content for the Ti6Al4V_MS and Ti6Al4V_MS NaTC samples remained constant; however, the anatase and rutile counterparts exhibited a reduction in Ti and increase in O content.

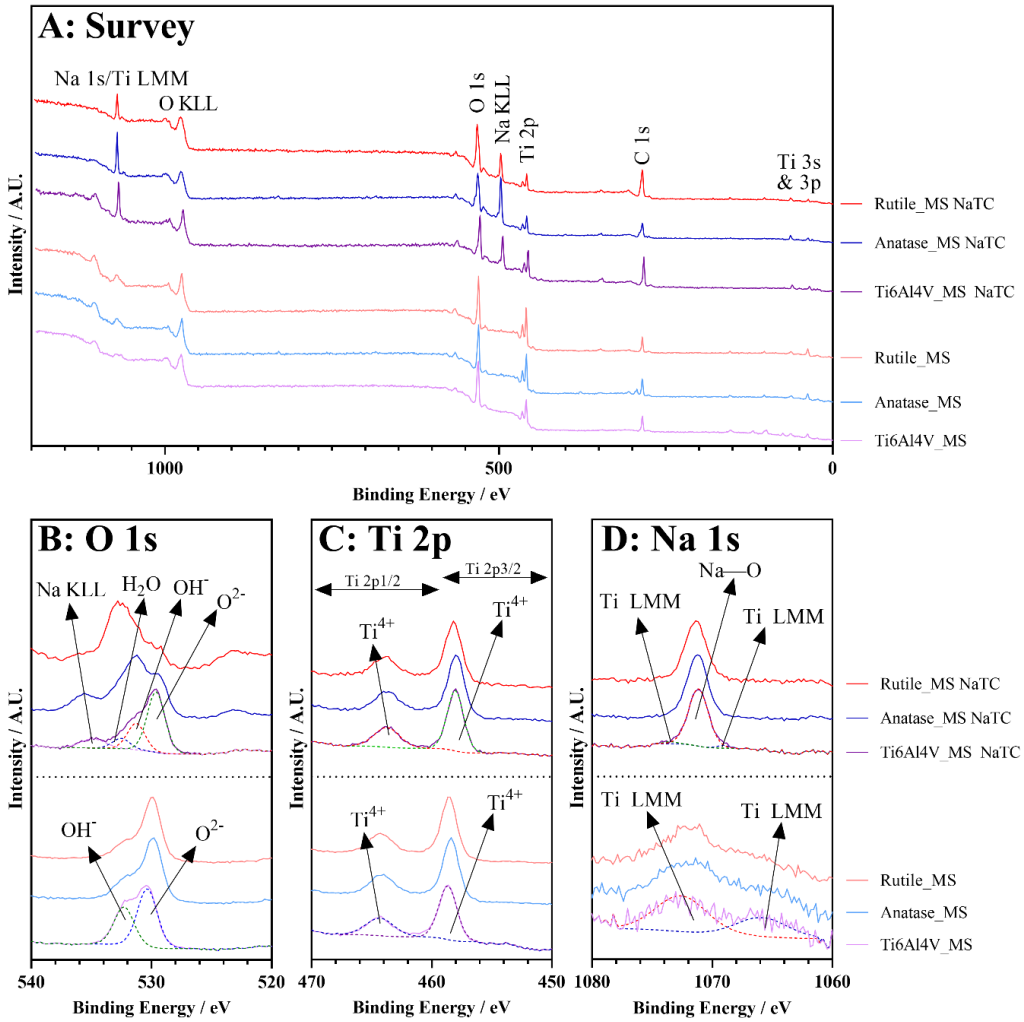

Figure 5:35. X-ray photoelectron spectral analysis for as-prepared (Ti6Al4V_MS; Anatase_MS; Rutile_MS), and titanate converted Ti6Al4V (Ti6Al4V_MS NaTC) and TiO_2 (anatase – Anatase_MS NaTC; rutile – Rutile_MS NaTC) microspheres. (A) Survey spectra identifying all elemental photoelectron emissions, (B) High-resolution spectra of O 1s peaks with overlapping Na KLL Auger emission, (C) High-resolution spectra of Ti 2p doublet splitting peaks, and (D) High resolution spectra of Na 1s, with overlapping Ti LMM Auger emissions.

Table 5:16. XPS analysis of titanate converted (_MS NaTC) and non-titanate (_MS) converted Ti6Al4V and TiO_2 microspheres.

Sample Code	Elements	Binding Energy / eV	Corresponding Bonds (Area / %)	Ref.
Ti6Al4V_MS	O 1s	530.3 (O^{2-}) 532.3 (OH^-_t)	M^{x+}—O (60.54) M^{x+}—OH (39.46)	[437, 438]
	Ti 2p 3/2	458.7 (Ti^{4+})	O—Ti^{4+} (100)	[437]
Ti6Al4V_MS NaTC	O 1s	529.6 (O^{2-}) 531.3 (OH^-_{br}) 532.5 (OH^-_t/H_2O) 534.9 (Na KLL)	Ti^{4+}—O (54.70) Ti^{4+}—OH (24.04) O—H (9.44) - (11.82)	[438]
	Ti 2p 3/2	458.0 (Ti^{4+})	O—Ti^{4+} (100)	[77, 78, 189, 201, 394]
	Na 1s	1071.1	O—Na (95.2)	[77, 78, 189, 201, 394, 439]
Anatase_MS	O 1s	529.9 (O^{2-}) 532.2 (OH^-_t)	Ti^{4+}—O (73.56) Ti—OH (26.44)	[437, 438]
	Ti 2p 3/2	458.4 (Ti^{4+})	O—Ti^{4+} (100)	[437]
Anatase_MS NaTC	O 1s	529.4 (O^{2-}) 531.2 (OH^-_{br}) 532.8 (OH^-_t/H_2O) 535.5 (Na KLL)	Ti^{4+}—O (28.12) Ti^{4+}—OH (38.31) O—H (17.12) - (16.45)	[438]
	Ti 2p 3/2	458.0 (Ti^{4+})	O—Ti^{4+} (100)	[77, 78, 189, 201, 394]
	Na 1s	1071.2	O—Na (81.4)	[77, 78, 189, 201, 394, 439]
Rutile_MS	O 1s	529.9 (O^{2-}) 532.2 (OH^-_t)	Ti^{4+}—O (78.19) Ti—OH, $Ti^{2+/3+}$—O (21.81)	[437, 438]
	Ti 2p 3/2	458.6 (Ti^{4+})	O—Ti^{4+} (100)	[437]
Rutile_MS NaTC	O 1s	529.6 (O^{2-}) 531.6 (OH^-_{br}) 533.0 (OH^-_t/H_2O) 535.6 (Na KLL)	Ti^{4+}—O (16.84) Ti^{4+}—OH (31.22) O—H (44.95) - (7.00)	[438]
	Ti 2p 3/2	458.2 (Ti^{4+})	O—Ti^{4+} (100)	[77, 78, 189, 201, 394]
	Na 1s	1071.2	O—Na (83.2)	[77, 78, 189, 201, 394, 439]

Table 5:17. Elemental composition analysis (at.%) as confirmed via XPS analysis of survey spectra. Data presented is the software calculated mean and standard deviation from CasaXPS

Sample ID	Elemental Composition / at.%		
	Na	O	Ti
Ti6Al4V_MS	0	84.4 ± 0.4	15.6 ± 0.4
Ti6Al4V_MS NaTC	17.6 ± 0.8	66.8 ± 0.9	15.6 ± 0.6
Anatase_MS	0	77.6 ± 0.5	22.4 ± 0.5
Anatase_MS NaTC	16.5 ± 0.4	73.4 ± 0.4	10.2 ± 0.3
Rutile_MS	0	75.5 ± 0.4	24.5 ± 0.4
Rutile_MS NaTC	9.5 ± 0.4	83.9 ± 0.5	6.7 ± 0.3

5.3 Discussion

5.3.1 Optimisation and Conversion

5.3.1.1 Bias and Heating Effects on Optimising Sputtering Parameters and Produced Films

DC magnetron sputtering of metallic films has been widely investigated within the literature for a variety of applications ranging from electrical to biomedical fields. Furthermore, the investigation of Ti films for biomedical applications have also been considered. Magnetron sputtering is a versatile processing technique to produce chemically, morphologically, and structurally dissimilar films, through the variance of sputtering parameters, such as the substrate bias, target current, and processing gas flow-rate. Herein the aim was to produce pure Ti thin films, with varying structural properties from columnar (characteristic of metallic and ceramic magnetron sputtered films, such as those studied by Wang *et al.* [440], Konstantinidis *et al.* [441], and Dirks *et al.* [442]) to more equiaxed films akin to bulk metallic structures. Due to the sputtering system employed in this study, there were inherent effects that required optimisation in order to produce films with varying structure factor. For example, applying a substrate bias to increase film density and enable a higher rate of atomic reordering within the film [443], has its limitations, since increasing the bias too much will result in re-sputtering of the coating, drastically reducing the film thickness produced [444]. Furthermore, limitations on the power density that could be applied to the target, and the temperature of the heater, meant that despite applying the maximum possible parameters, a purely equiaxed film could not be achieved. Hence, the term ‘equiaxed’ in this study refers to the most extreme parameters possible within the technique chosen, *i.e.* the most equiaxed/least columnar film generated.

Prior to the addition of substrate bias and substrate heating, the initial optimisation of the Ti films through variation in power densities of the Ti target was achieved

through variation in target current (1, 3, and 5 A). These variations demonstrated a clear increase in the deposition rate (*Figure 5:1*), as well as the grain size of the sputtered films (*Figure 5:2*) as expected [350]. Furthermore, the sputtering parameters used resulted in both batch-to-batch, as well as sample homogeneity and reproducibility for both the 2 and 4 μm coatings. An acceptable reduction was noted in the deposited thickness compared to the intended thickness, which was likely due to excessive, non-uniform target erosion due to the enclosed magnetic field, as illustrated in *Figure 5:36*. This erosion ($\Delta d_0(t)$) resulted in localised cooling of the target and hence reducing the energy imparted to the Ti atoms during the ion-bombardment process. Furthermore, the increased target-substrate distance ($d_0(s\text{-}t)$) resulted in fewer atoms reaching the substrate surface. Finally, localised re-deposition due to oblique angle sputtered could also occur.

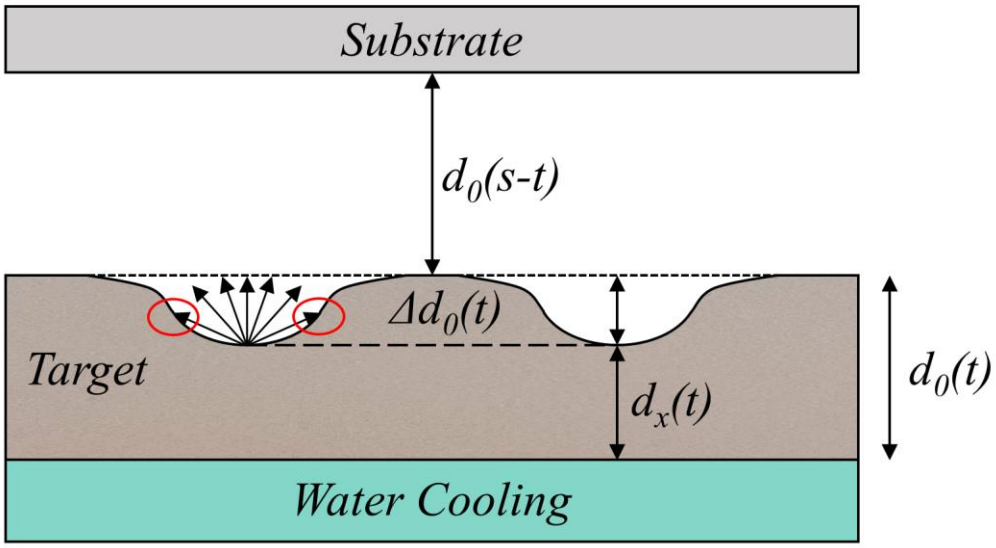

Figure 5:36. Schematic demonstrating various phenomena that can occur due to the localised erosion of magnetron sputtered targets. Red circles illustrate re-deposition due to oblique angle sputtering.

Application of a substrate bias and external heating has been investigated previously within the literature for Ti and Ti-containing compound films, in order to modify the structural properties of the sputtered film. Regarding substrate biasing

alone, studies by Wang *et al.* [440], Petrov *et al.* [445], and Martin *et al.* [446], have all demonstrated similar film and sputtering characteristics despite differences in material type and sputtering parameters. Wang *et al.*, on the effect of substrate bias on TiC deposition, noted that optimal mechanical properties arose at -100 V. As the bias was increased (from -20 to -200 V), increased preferred orientation was seen in the (111) TiC crystalline plane, since higher atomic motility was noted. Furthermore, as the substrate bias was increased, grain sizes decreased (from *ca.* 27 to 14 nm), whilst film hardness (13.9 to 28.8 GPa) and Young's modulus (208.6 to 302.5 GPa) increased [440]. Similar phenomena were noted by Petrov *et al.* during reactive, biased sputtering of TiN polycrystalline films. Grain size significantly reduced (from *ca.* 54 nm at < 30 V to *ca.* 20 nm at 800 V) as the substrate bias value increased, whilst re-sputtering of the sputtered film increased (from *ca.* 0 at < 30 V to *ca.* 0.3 at 1800 V; measured as a ratio of ejected Ti atoms per incident ion) [445]. Similarly, Martin *et al.* found a decrease in deposition rates (from *ca.* 54.2 nm/min to *ca.* 36.7 nm/min) of sputtered Ti and (from *ca.* 3.42 nm/min to *ca.* 2.83 nm/min) TiO_2 films as a result of increasing the substrate bias power from 0 to 600 W. Additionally, the energy per deposited atom increased due to increased substrate biasing (from *ca.* 0 to 322 $eV.atom^{-1}$ for Ti and *ca.* 0 to 1274 $eV\ atom^{-1}$ for Ti and TiO_2 films, respectively) [446].

In the optimisation study presented, the application of a substrate bias demonstrated a clear qualitative reduction in the number of voids present when comparing the 5 A NB/NH (*Figure 5*:*2*) and 5 A B/NH (*Figure 5*:*5*) samples, which is more perceptible at higher target currents. A visible reduction in the size of the grains presented in the SEM micrographs was also observed through the application of a -100 V bias. Furthermore, from the XRD analysis (*Figure 5*:*7*) comparing the

NB/NH and B/NH samples, clear preferential orientation differences were noted due to the increase in target current and the application of a substrate bias. Due to the insufficient deposition rate, only broad, low intensity peaks were noted on the 1 A (NB/NH and B/NH) samples, hence, the reason for discounting this sputtering condition during the later assessments. The 3 A and 5 A NB/NH samples exhibited similar XRD spectra, however, higher relative intensity was noted for the 3 A (002) plane (*ca.* 38.4^{o}), however, this preferential alignment was also noted in the 5 A sample, to a lesser extent. The application of a bias for both the 3 A and 5 A B/NH samples, resulted in preferential alignment in the (101) plane (*ca.* 40.2^{o}), with similar relative intensities noted for both 3 and 5 A B/NH samples. This shift in preferential alignment was due to the increased atomic energy, and in extension, enhanced atomic motility, due to ion-bombardment on the substrate surface [440, 445, 446]. As delineated in the objectives, the influence of the structural properties of the film in order to produce titanate structures were to be investigated, with the evidence above outlining how the structural properties can be easily varied *via* application of a substrate bias.

An additional method for increasing the energy *in situ* during sputtering deposition is the use of a heater directly onto the substrates. From the literature, studies by Thornton [447] and others [448-450] (reviewed by Kelly and Arnell [350]) have demonstrated the increase of atomic motility and atomic energy for sputtering systems in order to produce more equiaxed, dense coatings, akin to bulk. This has been achieved through the generation of Structure Zone Models (SZMs; *Figure 5*:*37*), with a novel three dimensional model produced by Kelly and Arnell [350, 425]; it is worth mentioning that there are still discussions within the literature as to the credibility of such models, due to significant differences between studies, the theory and the actual

results presented. The three conditions, which can be manipulated in order to achieve different coating structures, are the bias voltage (described previously), the ion-to-atom ratio $\left(\frac{J_i}{J_a}\right)$ (not discussed here), and finally the homologous temperature. The homologous temperature is the ratio between the substrate temperature (T) and the melt temperature (T_m) of the coating material (in Kelvin). The 3D SZM demonstrated that in order to switch to more equiaxed (coined Zone 3 or 'fully dense') coatings, an increase in one or more of these parameters simultaneously must be achieved. Hence, in this study both substrate biases and substrate heating were employed, due to their relative ease of modifying.

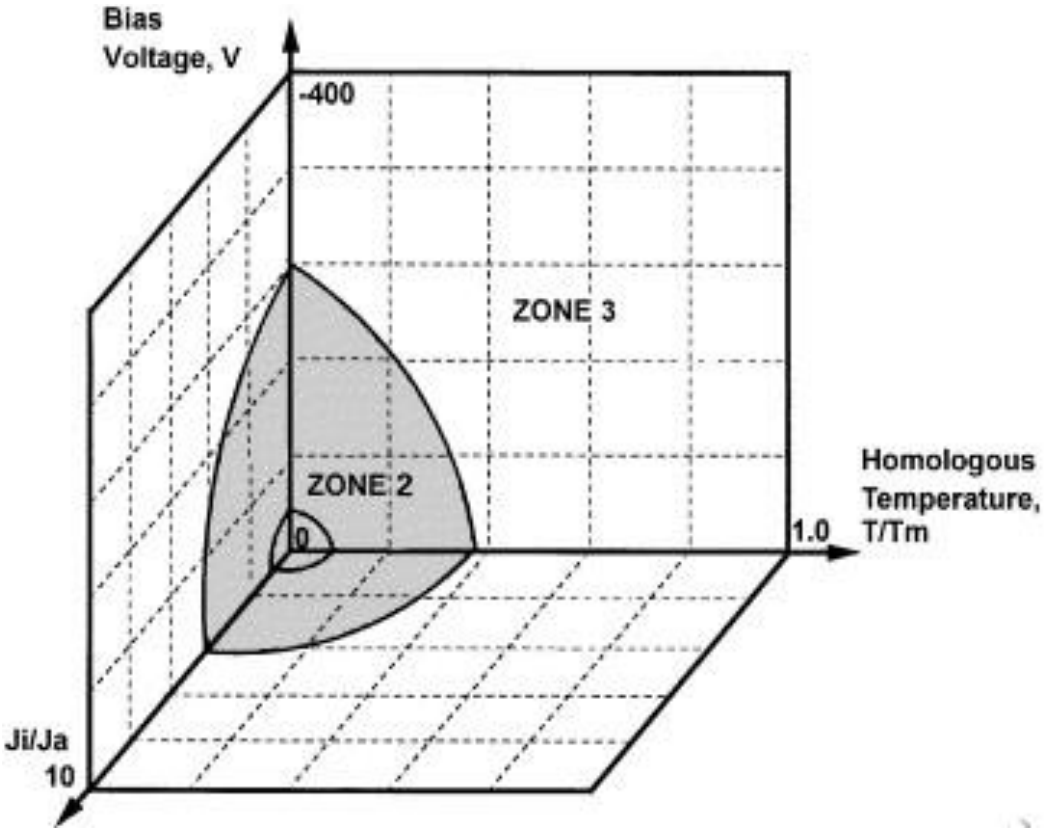

Figure 5:37. 3D Structure Zone Model (SZM) demonstrating the 3 parameters (ion-to-atom ratio, substrate bias, and homologous temperature), which strongly influence the formation of different coating structures. Zone 1 coatings, termed 'porous columnar', consist of tapered columnar grains separated by voids. Zone 2, termed 'dense columnar', are still columnar in appearance, however, there are a lack of voids. Zone 3, termed 'fully dense' coatings, exhibit a more equiaxed grain structure. Image taken from Kelly and Arnell [350, 425].

For this study, the heater utilised had a maximum safe operating temperature of 300 ^{o}C and, therefore, for optimisation two nominal temperatures (150 and 300 ^{o}C) were used and assessed, in addition to substrate biasing prior to the titanate conversion study. It was found that both the 150 ^{o}C (B/150 ^{o}C) and 300 ^{o}C (B/300) samples exhibited substrate temperatures which were higher (*ca.* 124 and 135 ^{o}C for B/150 and B/300, respectively) than the non-biased (NB/NH; *ca.* 74 ^{o}C) and biased (B/NH; *ca.* 119 ^{o}C) samples. This demonstrated that the sample parameters being tested were suitably dissimilar for further testing (*i.e.* the energy provided to the samples were sufficiently different to generate different surface temperatures; the majority of energy imparted to the substrate surface is through energetic particle bombardment [451]),

and hence the NB/NH, B/NH, B/150 and B/300 samples were chosen for the remaining conversion studies.

5.3.1.2 Topographical, Structural and Compositional Analysis of Titanate-Converted Optimised Ti Films

The ability to produce nanoporous titanate surfaces on alternative materials through chemical conversion of Ti sputtered films, allows improved surface properties of bioinert materials, whilst also broadening the applicability of these surfaces. To date, no study has been able to produce such structures on alternative substrate materials. If appropriate bonding and optimisation of the produced films is met, these surfaces would potentially be utilised in a wide variety of applications, from hip stems, to fracture fixation devices based on metallic and non-metallic implant materials. Specifically, the broadening of this process to incorporate polymeric materials makes this technique advantageous for future biomedical applications.

By varying processing parameters, with the ultimate aim of producing denser, equiaxed Ti films, the effects of oxygen penetration, coating microstructure and relative ingress of the NaOH solution on the formation mechanism of titanate was explored. The application of a substrate bias from the NB/NH sample (5 A target current; 0 V substrate bias), to the B/NH sample (5 A target current, -100 V substrate bias), enabled bombardment of the substrate by Ar^+, with sufficient energy to transfer into the produced coating. This then allowed reordering of the atoms into more equiaxed structures; akin to those of bulk metallic materials. However, such a process can also cause re-sputtering of the produced coating and, therefore, an optimised bias was selected based on experience by TEER for the rig set-up used, as well as an investigation by Priyadashini *et al*, with -100 V showing significant grain refinement [452].

The application of additional surface heating in the B/150 and B/300 samples (150 and 300 ^{o}C, respectively) aided in energy transfer, atomic re-ordering, and, hence, its crystalline structure [451, 453]. The approach here was confirmed in the average void area/frequency (*Figure 5*:*15*), XRD (*Figure 5*:*18*) and subsequent texture coefficient analyses (*Figure 5*:*19*), with the NB/NH sample exhibiting preferred orientation in the (002) plane of HCP α-Ti (PDF 00-044-1294), with a T_c of 3.39, as well as the highest measured average void area (3.71 (± 0.5) × 10^{-3} μm^2), and void frequency (4.1 μm^{-2}) (*Figure 5*:*15*); as would be expected for more columnar structures. The Ti (002) crystal plane is preferred during sputter deposition of titanium due to it being the most stable configuration for HCP structures, and exhibits the lowest surface energy, as described by Wu *et al.* [454]. Both T_c and void area/frequency values decreased through the application of a bias and subsequent heating at different temperatures, with the B/300 sample exhibiting the lowest T_c (1.54; → 1), void area (1.03 (± 0.2) × 10^{-3} μm^2), and void frequency (0.6 μm^{-2}) values (*Figure 5*:*15*). These values approached that of bulk equiaxed Ti.

It was hypothesised that the more porous, columnar grown coating (NB/NH) would enable greater penetration of NaOH solution, and in turn, would cause greater conversion of the produced Ti coating, resulting in deeper titanate structure growth than the more equiaxed films (B/300). However, this was not observed in the results presented, and SEM observations (*Figure 5*:*12*) determined that the thicker titanate structures were consistent with that of the more dense, equiaxed films (B/300_TC; 1.63 μm) *vs.* the more porous, columnar structures (NB/NH_TC; 1.12 μm). However, all coating types successfully produced titanate structures similar to those already in the literature for bulk Ti, and as was seen in *Chapter 4* [209, 455]. In terms of Na inclusion in the produced titanate films, the at.% quantity remained between *ca.* 5.5

and 8.9 at.%. for the EDX measurements (*Table 5*:*3;* higher than was seen in *Chapter 4*), which was the average quantity over the whole e^- interaction volume; *ca.* 1-2 μm penetration depth is common for most material types [359]. Approximate penetration depths can be calculated from the Kanaya-Okayama equation [456]:

$$r\ (\mu\text{m}) = \frac{0.0276 \cdot A \cdot E_0^{1.67}}{\rho \cdot Z^{0.89}}$$

where *A* is the atomic mass, *Z* is the atomic number, E_0 is the electron gun voltage, and ρ is the material density, r = *ca.* 1.72 μm for Ti at 15 kV).

From the XPS quantity measurements (also *Table 5*:*3*), the more columnar structures retained more Na (25.6 and 26.8 at.% for NB/NH_TC and B/NH_TC, respectively) in the top portion of the coating (X-ray penetration for XPS on the order of a few nm; slightly higher for nanoporous titanate [359]) compared to the *in situ* heated samples (16.1 and 17.8 at.% for B/150_TC and B/300_TC, respectively); the diffusion gradient was also evident in the FIB milled sample (*Figure 5:17*). As discussed by Zaraté *et al.*, due to the relative ratios of contained elements quantified from the XPS analysis, the titanate composition can be correlated with values obtained from EDX. In this study, exact correlation to commonly seen titanate phases ($Na_2Ti_3O_7$ = 25 at.% Ti, 58 at.% O, 17 at.% Na; $Na_2Ti_2O_5.H_2O$ = 17 at.% Ti, 50 at.% O, 16 at.% Na) was not seen. However, as reported by Zaraté *et al.*, the produced titanate structure may be a mixture of closely related phases ($Na_2Ti_3O_7$; $Na_2Ti_3O_7.nH_2O$; $Na_2Ti_2O_5.nH_2O$). This was confirmed *via* FTIR (Devi *et al.* [457]; *Figure 5*:*21B*), XPS (Zaraté *et al.*, Takadama *et al.* and others described in Takadama's paper [215, 395]; *Figure 5*:*20*), XRD (Devi *et al.* [457]; *Figure 5*:*18*), and Raman (Zhang *et al.* & Kasuga *et al.* [458, 459]; *Figure 5*:*21A*). XRD (*Figure 5*:*18*) of the titanate converted samples exhibited 3 broad peaks at *ca.* 24.2, 28.4 and 48.2° 2θ, which agreed with Devi *et al.*, for $Na_2Ti_3O_7$. Despite this, there were a lack of clear

peaks at *ca.* 33 and 36^{o} 2θ, which may have been be due to either the size of the nanocrystals/amorphous phases present, or the masking of the latter peak in the (100) Ti diffraction peak [457].

A key feature also noted with respect to the growth of the coatings, was that the portion of the Ti coating left on all samples following conversion was less than the original coating height (*ca.* 3.5-4 μm) produced. Furthermore, the final whole (Ti + titanate) film thickness was always greater than the original Ti film thickness (*Figure 5:14*), suggesting a two directional growth of titanate with the outwards growth being dominant; the conversion of titanium to titanate *via* diffusion results in expansion of the gel layer outwards. Contrary to the original hypothesis that a columnar structure would produce a thicker titanate structure *via* increased ingress of the NaOH solution, an alternative hypothesis was proposed. As the Ti coating transitions from a columnar to a more equiaxed structure, the fraction of voids present between the crystals reduces (*Figure 5:15*). As stated above, the growth of these titanate structures, produced through chemical routes, occurs perpendicular to the surface. However, in the columnar films, perpendicular growth to the crystal surface can cause growth at more oblique angles due to the presence of voids, resulting in a thinner titanate film. The B/300 sample, being the most equiaxed and therefore containing the lowest void fraction of the films tested, produced a thicker titanate structure. The proposed phenomenon above correlates well to the observed trends of decreasing void fraction (*Figure 5*:*15*) and increased titanate thickness (*Figure 5*:*12*) as the Ti coating shifts from columnar (NB/NH) to more equiaxed films (B/300). A schematic representation is presented in *Figure 5*:*38*.

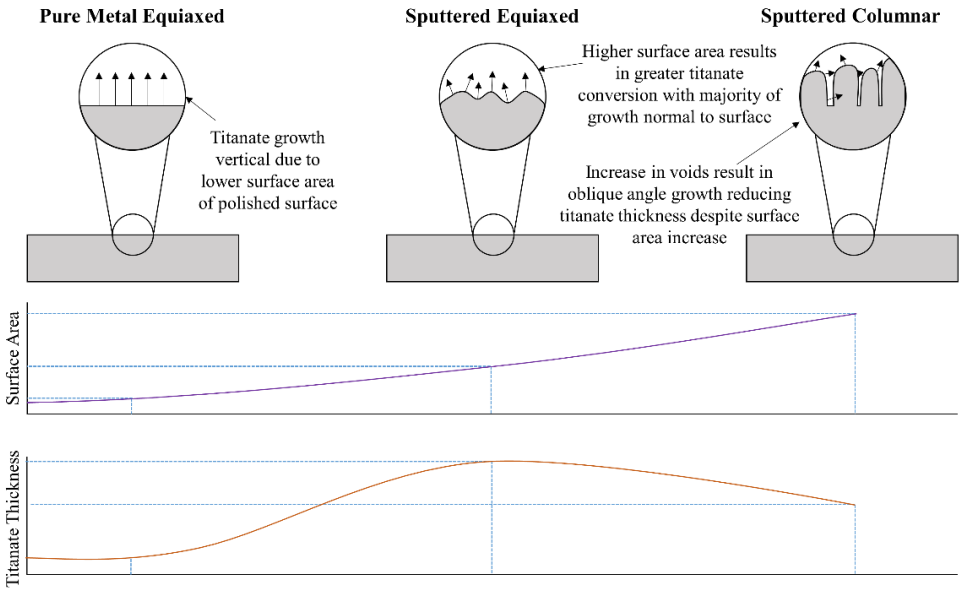

Figure 5:38. Schematic representation of different substrate/coating structures and their effect on subsequent titanate film thickness.

The presence of TiO_2 peaks in the Raman (*Figure 5*:*21A*) spectra were to be expected since the Raman spectrometer was utilised in reflectance, hence, the thin passivated TiO_2 layer (from *ca.* 20 Å to a few nm [460-462]) would have the highest intensity. Hanaor *et al.* described the formation of varying phases of TiO_2, particularly noting anatase occurs in pressures less than 20 kbar and below 600 ^{o}C [463], as observed here from the Raman results. The broad peaks around 415 and 605 cm^{-1} were also in agreement with studies presented by Ocana *et al.* [464], Hsu *et al.* [465], and Exarhos [466]. It is worth noting that the location of these peaks were similar to that of A_{1g} and E_g rutile modes, whereby Exarhos delineated that both have the same localised structural groups, however, with the additional absence of long-range order [466].

XPS analysis (*Figure 5*:*20*) demonstrated that the produced surface layers contained multiple Ti valence states, corresponding to different titanium oxide forms (TiO_2, Ti_2O_3, and TiO). TiO_2 is the most abundant compared to Ti_2O_3 and TiO states, with the TiO being the least abundant due to thermodynamic favourability, as

described by Hanawa *et al.* [467]. These oxides were not detected by any of the other characterisation techniques used, which is likely due to the shallower penetration depth of XPS.

Once treated in the NaOH solution, conversion into sodium titanate was observed, with Raman peaks being detected at *ca.* 285, 440, 630-690, and 900 cm^{-1} [218, 280, 468]. The peaks at 285 and 900 cm^{-1} are in good agreement with intrinsic hydrogen titanate ($H_2Ti_3O_7$) bands found in a study conducted by Rodriguez *et al.* [469]. This may alternatively correspond to $Na_2Ti_3O_7$, as detailed by Bamberger *et al.*, which revealed good agreement with the XPS and XRD analyses detailed above [470]. Furthermore, both Ma *et al.* and Kim *et al.* quantified the formation of a peak at 440 cm^{-1}, which was indicative of Ti—O bending vibrations, whereby the Ti atoms are 6-coordinated in the perovskite structure [78, 383]. The broad peak in all TC samples ranging from 630-690 cm^{-1}, was characteristic of [TiO_6] octahedral Ti—O—Ti vibrations found in titanate structures, as characterised by Kasuga *et al.* and Zhang *et al.* [458, 459]. These results are further confirmed from the complimentary FTIR measurements (see *Figure 5*:*21B*), where Ti—O and Ti—O—Ti bonds were detected at *ca.* 850 and 900 cm^{-1}, respectively.

There were also clear morphological and roughness differences noted from correlating the SEM (*Figure 5*:*12*), optical profilometry (*Figure 5*:*22*) and AFM measurements (*Table 5*:*8*, *Figure 5*:*23* & *Figure 5*:*24*). Despite the clear limitations in both techniques (such as limitations in sample size/spatial resolution and probe contact for AFM; and the inability to accurately measure highly angled surfaces by optical profilometry; discussed by Murthy *et al.* [471]), similarities were noted in the observed trends in the samples between the two measurement methods. Both the optical profilometry and AFM measurements demonstrated increases in surface roughness

when comparing the pre- and post-titanate converted samples. Furthermore, the AFM micrographs translated across to what were seen morphologically in the SEM micrographs, illustrating the characteristic nanoporous titanate structure (*Figure 5*:*23*); similar micrographs were demonstrated by Fawzy and Amer (*Figure 5*:*39*) on titanate converted dental Ti implants, however the lower resolution presented meant titanate delineation was difficult [472].

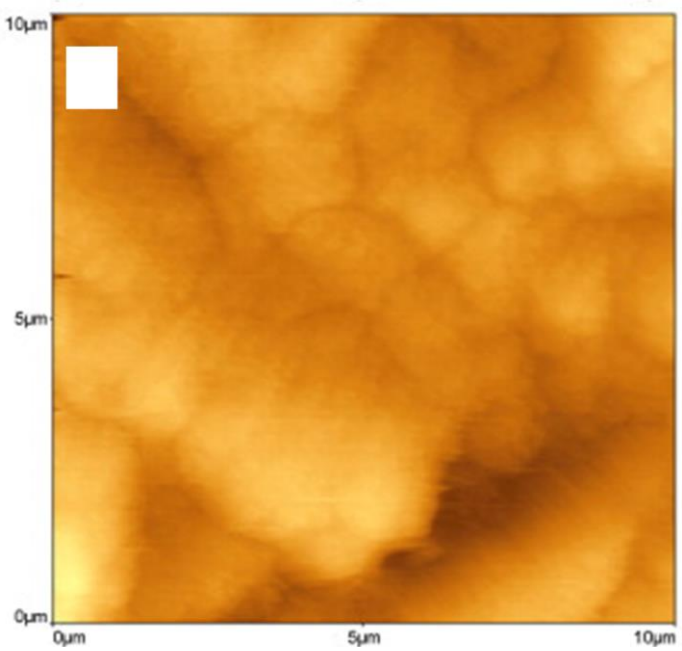

Figure 5:39. AFM micrograph of NaOH treated (10 M; 60 °C; 24 h) Cp-Ti substrate, with subsequent heat treatment (600 °C) from Fawzy and Amer's study [472].

The advantage of AFM is that it was able to observe the titanate struts, despite some 'broadening' being observed. The accuracy of this measurement is influenced by many factors, such as the size of the feature in relation to the tip size, the 'sharpness' or depth of a protrusion/void, tip contamination, *etc.*, which can lead to differences in the perceived roughness compared to the actual roughness. An example of this is demonstrated in *Figure 5*:*40*, where interaction higher up the tip's leading edge, rather than interacting with the actual tip, can lead to broadening of the measured features [473].

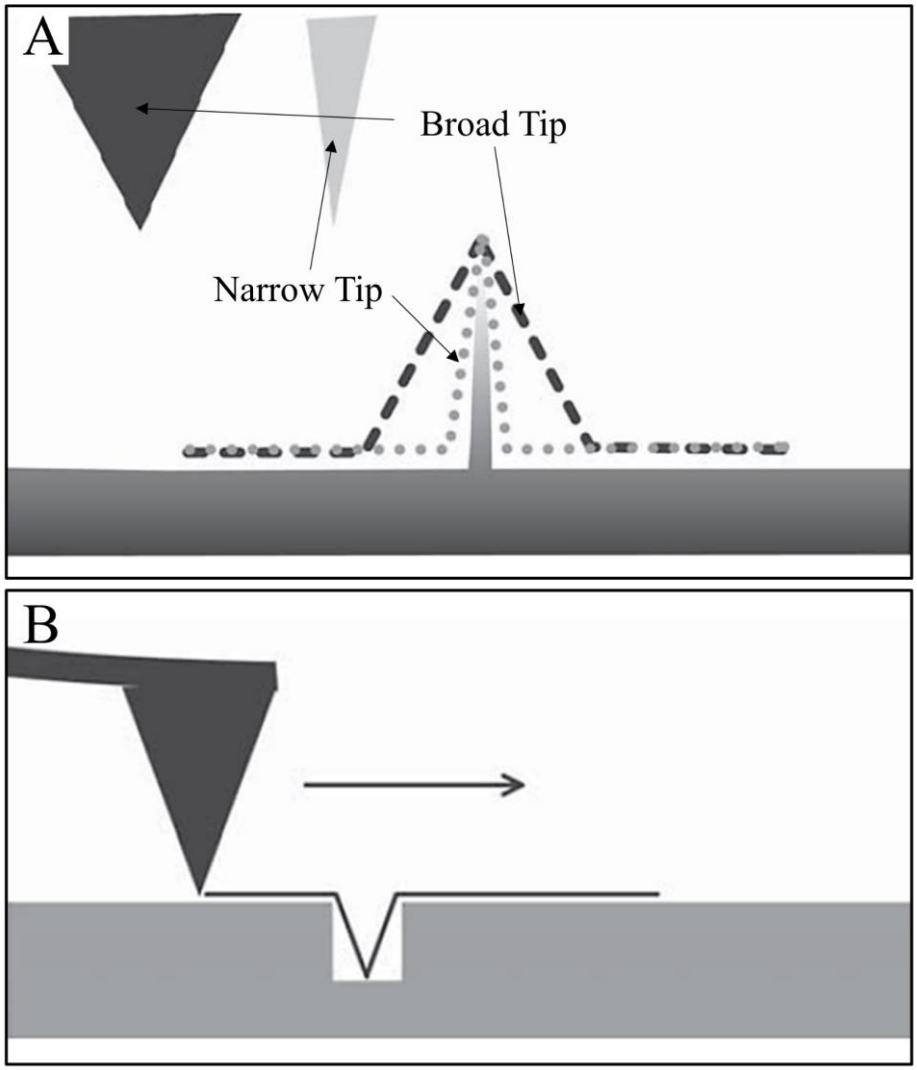

Figure 5:40. A) Feature broadening observed in a sharp protrusion due to interaction of the feature with the leading edge of a broader tip. B) Due to the width of the tip and 'steepness' of the void, accurate reproducible features has not been achieved in this instance. Adapted from Ricci and Braga [473].

Cumulatively, the compositional and morphological analysis confirmed the titanate conversion of all Ti films, irrespective of the structure factor present, with the more equiaxed structure (B/300_TC) producing the thickest titanate (*ca.* 1.6 μm), demonstrating the distinct effect of the crystalline structure on the depth of titanate penetration.

5.3.1.3 Mechanical testing

A key consideration for any biomaterial, which has been coated for improved surface properties, is the adherence of the produced coating since application-

dependent environments may cause fretting, micro-motion, and delamination. As determined *via* pull-off adhesion testing (*Figure 5*:*25*, *Table 5*:*9* & *Table 5*:*10*), as well as coating scratch testing (*Figure 5*:*26* & *Table 5*:*11*), the more columnar NB/NH samples exhibited the greatest adhesion strength on the polished 316L SS samples (*ca.* 42.2 MPa, comparable to the FDA's minimum requirement of 50.8 MPa [111]), and despite cracking, did not spall during the scratch testing analysis (*Figure 5*:*26* & *Table 5*:*11*), proving good adhesion even on polished substrates. However, following the application of a substrate bias and substrate heating, the failure strength and spallation forces greatly reduced. As discussed by Shen *et al.* (in relation to tungsten (W) coatings), ion-bombardment plays a significant role in the stress and microstructure of the produced coating [474]. The production of residual stresses within the coating, occurring *via* an 'atomic shot peening' effect, are higher in the denser, less columnar films, with more columnar films being unable to support large internal stresses [474].

Following titanate conversion, the respective films experienced a reduction in the adhesion strength and failure loads, which is possibly due to ingress of NaOH solution under the Ti films, converting the bottom portion of the coating, which is exacerbated by the smooth nature of the substrate to which the coating is applied. Furthermore, the conversion from a ductile metal to a ceramic material, and the mismatch in specific properties, such as thermal expansion coefficient, residual stresses, and chemical differences, may also explain the perceived reduction in adhesion strength [475].

Despite the mechanical properties presented, the coating adhesion should increase if applied to roughened surfaces, more akin to those found on orthopaedic implants, due to the mechanical interlock present [476]. This is partially seen in the roughened samples tested within this study (*Table 5*:*10*), however, comparison between the

different parameters on the roughened surface were unable to be compared, since all of the failures occurred in the adhesive as opposed to the coating-substrate interface. Furthermore, excessively thick coatings would not be used in practical purposes, since (as determined by Vega-Morón *et al.* [477]) the thicker the films used the weaker the adhesion strength of the produce sputtered coating. Hence, it was clear further studies into the optimisation of these surfaces in terms of structure and thickness were needed (which have been presented in *Section 5.3.2*), as well as future work detailing an in-depth view on cellular proliferation/adherence and integration into surrounding tissue in *in vitro* and *in vivo* tests, respectively.

5.3.2 Titanate Mechanism Dependence on Ti Thickness

Despite extensive research in the literature focussing on the development, and eventual deployment of titanate structures for biomedical applications [82, 224, 478], no current work has focussed on understanding the effects of both oxygen content and Ti thickness on the mechanism of titanate formation. The effect of oxygen has been studied and is described in *Sections 5.2.5* & *5.3.3*, through different microsphere compositions. However, to fully understand thickness dependence, further investigations have also been conducted within this thesis. The limited studies regarding this were likely due to the fact that conversion of Ti coatings, the foundation of which has been investigated in this thesis through their novel generation, as opposed to Ti substrates, has only recently been described.

Following on from the initial optimisation studies in *Sections 5.2.1-5.2.3*, only the NB/NH sputtering parameters were used, since the adhesion was superior and, hence, would enable better quantification and conversion. Furthermore, as described in *Section 5.2.3.1*, the sandblasted substrates also demonstrated superior adhesion properties and since the application of such coatings would be for the biomedical

sector, improved adhesion was advantageous, hence, their utilisation in this study. It was also hypothesised that there would be a limit below which titanate formation would not proceed, and following from the data in *Section 5.2.2*, this was estimated to be less than 500 nm, based on the ΔTi values. Hence, nominal thicknesses of 50, 100, 200 and 500 nm were investigated.

From the SEM micrographs (*Figure 5*:*27*), it was evident that even through the use of 50 nm Ti coatings, it was possible to generate characteristic titanate structures, however, the conventional 'webbing' that occurred between the nanocrystalline struts was not present; this effect can be seen in the study by Pattanayak *et al.*, whereby different solution treatments (NaOH, HCl etc.) were trialled to generate bioactive TiO_2 layers on Ti metal [282]. This was likely due to the limited free Ti available to react, form, and interlink the titanate structures. The nano-needle-like morphology was also present on the 100 nm_NaTC sample, however, the characteristic 'webbing' only formed on the 200 nm_NaTC and 500 nm_NaTC samples; this was further exemplified in a study by Guo *et al.* which generated titanate structures onto Ti metal flakes [479]. This indicated that a critical Ti thickness, occurring between 100 and 200 nm, was required in order to enable interlinked growth between the titanate nanocrystals, which resulted in the 'webbing' seen. The confirmation of such a critical thickness is partially demonstrated in *Section 5.2.2*, whereby the ΔTi thickness falls between *ca.* 25 and 365 nm, depending on the sputtering parameters utilised; for the NB/NH sputtering parameters, used in this study, the ΔTi value was *ca.* 296 nm. This indicated that if the original Ti coating thickness > ΔTi (post-conversion), then the reaction mechanism, outlined by Kim *et al.* [77] & Kokubo *et al.* [480, 481], should reach equilibrium, resulting in titanate thicknesses in excess of 1 μm, due to the reaction being diffusion limited. However, if the Ti thickness is < ΔTi (post-

conversion), the system will reach a steady state, however, such a system will be limited due to the quantity of free Ti, not the ability for Na and O to diffuse into the system. Cross-sectional observations were not possible in this study, since the conventional method of using a glass substrate resulted in disintegration of the coating during titanate conversion. Furthermore, additional methods, such as cross-sectional polishing resulted in a 'smearing' effect, as detailed in [482]. The disintegration was likely due to a combination of residual stresses in the coating, thermal mismatch between the glass and Ti coating, as well as the potential full conversion of the Ti coating into titanate [331].

Despite differences in the morphology of the produced structures, chemical analyses (XRD: *Figure 5*:*28*, and XPS: *Figure 5*:*29*) confirmed the formation of titanate structures on all of the Ti samples with different Ti thicknesses. From the XRD measurements, there was good agreement with the hypothesis that the Ti coatings had converted into titanate for the 200 nm and thinner samples, as the presence of α-Ti peaks (PDF 00-044-1294; 35.2, 38.4, 40.1 and 53.0^{o}; mainly the (002) peak located at 38.4^{o} being the most prevalent) in the spectra had completely reduced in intensity, despite being visible in the unconverted samples. Due to the probing depth, limitations on quantifying coatings of *ca.* 50 nm or less have been reported [483]. Furthermore, the increase in relative intensity of the ferrite and austenite peaks, the increased noise of the background (indicative of increased quantity of amorphous phases), as well as formation of broad, low intensity titanate species (similar to peaks detailed by Devi *et al.* [457]), confirmed titanate formation.

XPS quantification gave greater precision regarding the top surface conversion into titanate structures, due to the shallow probing depth (*ca.* 5-10 nm [359]) of the technique. Similar to the previous analysis and discussion in *Section 5.2.2.7 & 5.3.1.2*,

characteristic binding energy and deconvolutions for both the magnetron sputtered Ti coatings and titanate structures were seen. The clear reduction in the Ti valence states to just Ti^{4+} found in TiO_6 octahedral perovskite compounds post-titanate conversion, as well as the formation of Na—O bonds as detailed by Zarate *et al.* [395] & Takadama *et al.* [215], were also in good agreement with data presented in *Section 5.2.2*, demonstrating the characteristic formation of titanate structures.

Significant peak shifts were noted for the Ti and O peak deconvolutions, which appeared to have a potential dependency on thickness of the Ti coating. On average in the titanate converted samples (_NaTC) both the O 1s and Ti 2p deconvolutions exhibited shifts (the largest being *ca.* 0.5 eV) to higher binding energies. As described by Zomorrodian *et al.* there is a relationship noted between the interatomic distance within the perovskite structure and the subsequent binding energy value for the Ti 2p 3/2 e^-, with an *ca.* 0.8 eV shift as a result of just *ca.* 0.6 Å shift in interatomic distance. This was plausible given the possible interaction/vacancies of Ti/Na cations in the perovskite titanate structure, and the variation seen in Na and Ti content in this study depending on Ti thickness [484]. Similarly, as described by Atuchin *et al.* there were large variances noted in XPS (both Ti 2p and O 1s core levels) binding energy shifts for titanium-bearing oxides, including titanate perovskite structures, and their relation to mean chemical bond lengths. The TiO_6 octahedra in titanate structures examined in the literature (Pb, Ba, Ca, Mg, etc.), are highly distorted, which is due to the very inhomogeneous electron density distribution along the Ti—O bonds in these structures [485].

Ultimately, further analysis would be required to establish whether there was any significant trend in composition as a result of thickness of the original Ti coating.

However, the significance of the presented results has provided further understanding of the titanate formation mechanism presented within the literature.

5.3.3 Effect of Oxygen Content on Titanate Production

Within the literature presently, there have been limited investigations into varying the chemical makeup of the Ti-containing material being converted into titanate, aside from varying the alloys being utilised [57, 77, 224, 481]. Kokubo *et al.* studied the mechanism of titanate formation on Cp-Ti substrates and demonstrated that the process was diffusion dependent, with movement of Na and O into the substrate to allow subsequent formation. This was achieved on both pure Ti, as well as many alloy types, including Gum metal (Ti-36Nb-2Ta-3Zr-0.3O) [224, 227]. The most notable paper by Xie *et al*., details the formation mechanism of titanate nanotubes using TiO_2 precursor materials, however, their formation occurred through hydrothermal methods at much higher temperatures (200 ^oC) than the present lower temperature (60 ^oC) methodology [486].

As outlined previously in the literature review chapter (*Chapter 2*), and adapted from seminal papers by Kim *et al.* [77] and Kokubo [480], initially, the TiO_2 passivated layer on the surface is partially dissolved due to corrosive attack of hydroxyl groups.

$$TiO_2 + OH^- \rightarrow HTiO_3^-$$

Simultaneously, hydration of the underlying Ti metal due to diffusion processes occurs, enabling the foundation for subsequent titanate formation:

$$Ti + 3OH^- \rightarrow Ti(OH)_3^+ + 4e^-$$

$$Ti(OH)_3^+ + e^- \rightarrow TiO_2 \cdot H_2O + \left(\frac{1}{2}H_2\right)\uparrow$$

$$Ti(OH)_3^+ + OH^- \leftrightarrow Ti(OH)_4$$

Consequently, the hydrated TiO_2 formed from the aforementioned reactions generates negatively charged titanium oxide hydrates.

$$TiO_2 \cdot nH_2O + OH^- \leftrightarrow HTiO_3^- \cdot nH_2O$$

Since these structures are negatively charged, combination with alkali ions in solution occurs, which in the case of NaOH is Na^+ to form sodium (hydrogen) titanate structures. However, to what extent this dependence on O has on the formation of titanate has yet to be quantified fully. This study outlined insights into this part of the titanate mechanism, through the production of Ti6Al4V microspheres (Ti6Al4V_MS), as well as those comprised of TiO_2 (anatase and rutile starting powders; Anatase_MS and Rutile_MS, respectively). Comparison of the morphological, structural and chemical properties of these materials pre- and post-titanate conversion has enabled further insights into the role of O in the titanate mechanism to be gleaned.

From the data collected in this study, it was evident that O played a significant role in the conversion of titanate, with excessive quantities, or in other words the lack of free Ti metal, resulting in minimal titanate conversion (see SEM; *Figure 5*:*30* & *Figure 5*:*33*). From the Kim *et al.* mechanism [77], titanate formation was reliant on a thin passivated TiO_2 layer forming on the top of the Ti-containing substrate, in which this layer facilitated the initial growth of the titanate structure through corrosive attack and diffusion of Na. Once the growth began to occur, this TiO_2 layer, and hydrate derivatives thereof, converted into sodium titanate (*Figure 5*:*41*). The nanoporosity of this layer enhances diffusion of O and Na into the underlying Ti material, as well as facilitating additional corrosive attack, forming further TiO_2 derivatives, which subsequently convert into sodium titanate. There is a limitation on the thickness of the titanate produced since this mechanism is reliant on diffusion of Na and O, which

ultimately is thickness dependent; Fick's law of diffusion states that the rate of diffusion for a substance is proportional to both the surface area and concentration gradient and is inversely proportional to the thickness of the membrane/substrate which the diffusing substance is diffusing into [487]. Although O can penetrate further (*ca.* 2 μm [201, 402]) into the Ti surface through heat treatments, the process is limited by the initial O and Na diffusion, which reaches equilibrium at *ca.* 1 μm, hence the titanate thickness is limited to this [481].

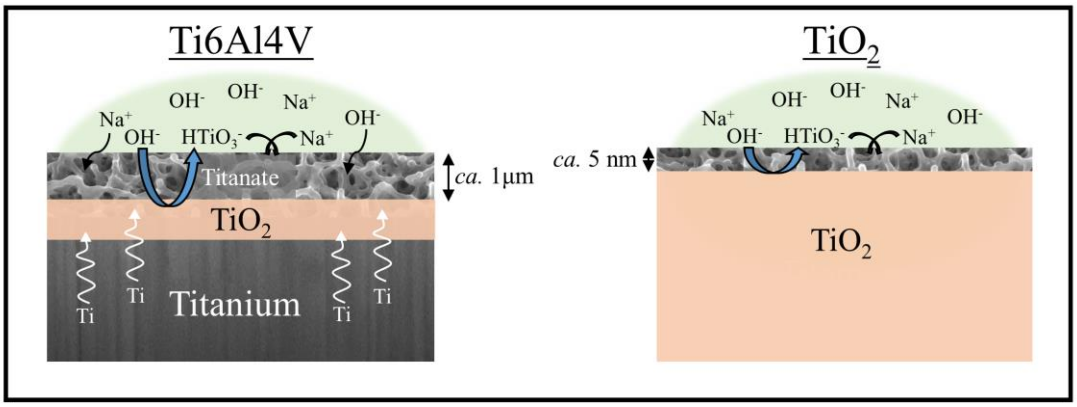

Figure 5:41. Schematic diagram demonstrating titanate conversion as a result of substrate used; Ti6Al4V vs. TiO_2.

By producing a purely TiO_2 surface, the middle aforementioned reactions (2-4) cannot occur since there is no free Ti available to generate such species, although conversion can still occur *via* the first equation at the top surface as there is TiO_2 available to convert. Further growth and conversion of the titanate structure can, therefore, not be facilitated, and hence, is not seen in the TiO_2 microspheres (aside from the XPS analysis (*Figure 5*:*35*), which investigated the top *ca.* 5 nm of the surface). Furthermore, diffusivity of O was hindered due to the formation of TiO_2, since this layer can act as a barrier to O, since the lattice vacancy sites now occupied by O are regarded as immobile blocking sites [488, 489]. From Ouyang *et al.*, the diffusivity of oxygen in α-Ti, β-Ti and TiO_2 was examined [490]. Diffusivity, being the rate of diffusion of one substance through another [491], as defined by:

$$D_A = Ae^{-\left(\frac{E}{RT}\right)}$$

where: D_A is the rate of species A diffusing through the reaction interface, A is the pre-exponential factor derived empirically, E is the activation energy of oxidation ($J \cdot mol^{-1}$), T is the temperature (K) and R is the molar gas constant (8.314 $J \cdot K^{-1} \cdot mol^{-1}$) [490]. Ouyang *et al.*'s study derived expressions for O diffusion (pure O_2 atmosphere) in α-Ti (HCP), β-Ti (BCC) and TiO_2, which were:

$D_\alpha(m^2 \cdot s^{-1}) = 7.78 \times 10^{-5}\, e\left(-\frac{203400}{RT}\right)$, $D_\beta(m^2 \cdot s^{-1}) = 3.3 \times 10^{-2}\, e\left(-\frac{246000}{RT}\right)$ and $D_{TiO_2}(m^2 \cdot s^{-1}) = 1.7 \times 10^{-6}\, e\left(-\frac{276000}{RT}\right)$, respectively. Assuming the diffusion mechanism obeys Arrhenius kinetics, the diffusivity of O^{2-} and O_2 in α-Ti and TiO_2 at the temperature used in this study (333 K) for titanate synthesis is 9.65×10^{-37} and 8.62×10^{-50} $m^2 \cdot s^{-1}$, respectively. This substantial reduction in O diffusion through TiO_2 relative to α–Ti demonstrates that one of the significant pathways for this mechanism is impeded, and therefore will inhibit titanate formation significantly compared to pure Ti or Ti alloys; this is exemplified in the SEM (*Figure 5*:*30*, *Figure 5*:*31* & *Figure 5*:*33*), EDX (*Figure 5*:*34*) and XPS (*Figure 5*:*35*) results gleaned.

Although significant, the diffusion of O is not the only limiting portion of the reaction presented. Once the TiO_2 surface has reacted with the NaOH solution to form the $HTiO_3^-$ ions, there is a requirement for hydration of the underlying Ti metal. This process must occur in theTi6Al4V spheres, which are assumed to behave like bulk Ti due to the size of the spheres (> 20 μm) compared to the titanate thickness (*ca.* 1-1.6 μm), such as the bulk Ti seen in *Chapter 4* and the Ti coatings in this chapter. However, this process must be inhibited in the TiO_2 materials described. A postulate for this is presented in Xie *et al.'s* study [486], whereby different Ti-containing precursors were assessed on the formation of titanate nanowires through hydrothermal

(200 ^{o}C) methods. They proposed that the mechanism occurs through a dissolution-crystallisation mechanism. The Ti contained within the substrate dissolves into the basic solution (NaOH), causing formation of $[Ti(OH)_4(OH_2)_2]^0$; similar species to those outlined in the mechanism above by Kim *et al.* [77]. Saturation occurs, which results in combination and formation of titanate structures, which nucleate on the surface. Subsequent diffusion, dissolution and formation occurs until a steady state is reached. This process occurred on Ti and TiO_2, however, this was due to the differences in processing temperatures (200 *vs.* 60 ^{o}C). It is likely this process is impeded in TiO_2 due to the lower temperature employed in this thesis, hence reducing the potential diffusion and dissolution of free-Ti.

Additionally, from the EDX and XPS analysis, it was clear that trends in the oxygen, sodium and titanium content of the samples tested varied depending on the original composition, as well as the subsequent titanate conversion. From the Ti6Al4V samples, the data gathered agreed well with the hypothesis outlined above for the conversion of Ti6Al4V microspheres, compared to TiO_2. For the oxygen content following titanate conversion, the amount increased from *ca.* 0 to 61 at.% in EDX, whilst observing a reduction from *ca.* 88 to 67 at.% in XPS. The increase in O from EDX indicated there was a diffusion gradient occurring in the microspheres, akin to bulk Ti in *Chapter 4*. A reduction in XPS is indicative of the relative ratio between the Ti, O and Na, since there is an increase in Na due to the titanate conversion. The Na content also increases for both EDX (*ca.* 0 to 5 at.%) and XPS (*ca.* 0 to 18 at.%), however, there was a higher quantity of Na in the XPS measurement, indicating a diffusion gradient, as illustrated by Kim *et al.* and Kokubo *et al.* [201, 402]. Ti decreased in EDX (*ca.* 87 to 31 at.%), but remained constant in XPS (*ca.* 16 at.%),

also indicating titanate conversion, and matching relative quantities from Zárate *et al.* [439], through the aforementioned mechanism.

In comparison to the Anatase_MS and Rutile_MS microspheres, and their titanate-converted counterparts, the relative quantities of Na, O, and Ti, were substantially different to the Ti6Al4V_MS samples. Oxygen content pre- and post-titanate conversion for both EDX and XPS, remained approximately constant: Anatase from *ca.* 70 to 68 at.% (EDX) and *ca.* 78 to 73 at.% (XPS); and Rutile from *ca.* 69 to 70 at.% (EDX) and *ca.* 76 to 84 at.% (XPS), for pre- (_MS) and post-titanate converted (_MS NaTC) samples, respectively. There were marginal changes to the surface composition (XPS), probably due to titanate conversion occurring in the top few nm of the surface, whilst the mean composition through the microsphere (*ca.* 2 μm; EDX) remained constant. For both the anatase and rutile samples (_MS/_MS NaTC), Na content increased significantly post-titanate conversion (NaTC) for the XPS measurements: *ca.* 0 to 17 at.% and 0 to 10 at.% for Anatase_MS (NaTC) and Rutile_MS (NaTC) samples, respectively, whilst EDX remained < 1 at.% for both. This exemplified that the titanate conversion occurring in the top portion of the surface, however, was limited to just the surface, since low quantities are noted in EDX. A similar trend was seen for Ti, with similar values (*ca.* 30 at.%) detailed in EDX for both Anatase_MS and Rutile_MS pre- and post-titanate conversion, whilst the XPS values reduced for both: *ca.* 22 to 10 at.% and 25 to 7 at.% for Anatase_MS NaTC and Rutile_MS NaTC, respectively. This reduction is likely due to the top portion of the surface reacting with the NaOH solution to form the $HTiO_3^-$ species essential for the initial titanate formation, exemplifying the increase in Na and O content in XPS as a result. Once formed, and in agreement with the previously outlined hypothesis, this layer in conjunction with there being no free movement of Ti, resulted

in the inhibition of the titanate mechanism. Thus, limiting titanate formation to the top few nanometres of the surface.

Cumulatively, through understanding the reaction mechanism outlined, the diffusion processes occurring through these reactions, as well as data provided, it was clear how titanate growth was inhibited due to excessive O in the TiO_2 microspheres, and that there is a requirement for free Ti in order for further diffusion and conversion to proceed.

Despite titanate formation occurring chemically, there was no morphological evidence seen in the SEM micrographs (*Figure 5:30 vs. Figure 5:33*) of the TiO_2 (Anatase_MS NaTC and Rutile_MS NaTC) samples, which was linked to the growth of the sodium titanate nanocrystals due to the interplay of solution and substrate equilibrium reactions. Huang *et al.* hypothesised, and extended further than Kim *et al.*, the likely mechanistic growth of titanate structures [492]. Additional work by Zhao *et al.* [493], Lu *et al.* [494], and Mao *et al.* [495] have all focussed on the growth mechanism of titanate structures, however, due to differences in the methodology, particularly the chemical routes used: Zhao [493] utilised 8.5 mL tetrabutyl titanate in HCl/Neutral/NaOH conditions; Lu [494] investigated combined bismuth/sodium titanate structures through bismuth nitrate pentahydrate, TiO_2 and a NaOH mineraliser; whilst Mao [495] focussed on the growth of titanate structures using combined H_2O_2/NaOH solutions, which enhanced oxidation, it was difficult to specifically comment with regard to the present study. The growth mechanism was dependent on the presence of a Ti/oxide interface. Due to the presence of NaOH, the oxide layer present will react to form $Na_{2-x}(H_x)TiO_3$ (x = 1 or 0), which occurs inhomogeneously across the surface. This resulted in localised areas of increased dissolution and conversion, which enabled exposure of Ti, and thus resulted in further

oxidation and dissolution. In the case of TiO_2 (which was not observed by Huang *et al.* but of which the mechanism is hypothesised here), and despite inhomogeneous dissolution and conversion, the underlying layers were TiO_2 not Ti, and hence ultimately reached equilibrium once all of the underlying TiO_2 had converted to titanate, inhibiting further conversion. Furthermore, additional mechanisms involving the diffusion of OH^- in high concentration NaOH solutions could cause bulk TiO_2 to react to form $Ti_3O_7^{2-}$, however, again this process was ultimately diffusion limited, and the absence of free Ti limited subsequent reactions [492].

5.3.4 Summary

Currently, wet chemically produced titanate structures have been restricted to Ti-containing substrates due to the methodology, and its mechanism, employed. This chapter aimed to highlight this fundamental issue, through the generation of a platform methodology, in order to produce nanoporous titanate structures onto non-Ti containing substrates. Through combining DC magnetron sputtered Ti films, with the chemical method outlined by Kokubo *et al.* [189], nanoporous titanate structures were generated onto 316L SS for the first time. This result demonstrates the enhanced applicability of nanoporous titanate structures through this methodology, as well as the possibility of further modification through ion exchange reactions, since their chemical and structural properties are akin to titanate structures generated from bulk Ti (*Chapter 4*). Furthermore, the chemical and morphological difference noted between the titanate structures produced from different sputtering parameters highlights the potential tailorability of these structures for specific applications, if required.

It was noted in the initial study of titanate-converted Ti films that the degree of conversion was relatively small compared to the total Ti thickness used (*ca.* 4 μm),

hence the additional thickness study was conducted. Early indications from this study have demonstrated that the thickness of the sputtered Ti film can be reduced significantly whilst still producing chemically, structurally, and morphologically similar nanoporous titanate structures. This is particularly pertinent to biomedical coatings, since excess material can be problematic. Additionally, the critical thickness was also detailed, furthering the knowledge on the titanate mechanism.

Further to Ti thickness, an additional branch of the titanate mechanism, which had limited literature studies investigating it, was the effect of O content on titanate formation. Ultimately, this study gave the first insight into the inhibition of titanate formation due to varying Ti/TiO_2 substrate content, as well as proving titanate structures could be formed on Ti-containing microspheres. These initial observations exemplified the current consensus on the titanate formation mechanism, whilst broadening previously unknown branches of this mechanism. These findings would enable enhanced tailorability through modification of the sputtered Ti films, through the additional of TiO_2 multilayers, or similar.

The combination of the novel methodology outlined in this chapter, with the ionic substitution work detailed previously (*Chapter 4*), was utilised to investigate the effect of Ti thin films, as well as nanoporous titanate-converted and ionic-substituted films for corrosion inhibition of Mg (*Chapter 6*).

Chapter 6. Application of Titanate Surfaces on Mg for Corrosion Inhibition

6.1 Introduction

In this chapter, preliminary electrochemical and materials characterisation investigations were conducted in order to confirm the application of the novel DC magnetron sputtering and wet chemical conversion process, outlined in *Chapter 5*, to produce titanate films onto Mg substrates. Furthermore, investigations into how the various coatings generated, including their microstructure, affect the corrosion resistance of Mg substrates intended for biodegradation applications such as fracture fixation devices, were conducted. In addition to this, the utilisation of the ionic substitution methodology outlined in *Chapter 4*, was used to investigate the exchange of calcium into the titanate structure, which has been shown in the literature to inhibit Mg degradation. The main objective of this study was therefore to assess the degradation rate of native Mg substrates, and compare the effect on degradation measured through electrochemical corrosion investigations, through the application of Ti films alone; sodium titanate converted films; as well as calcium-substituted films.

6.2 Results

6.2.1 SEM and EDX

Changes in morphology were determined through SEM imaging of all samples in NB/NH and B/300 sample sets (*Figure 6:1* & *Figure 6:2*, respectively) as well as the Mg control (*Figure 6:1A insert*). The Mg control and the NB/NH Ti and B/300 Ti samples (*Figure 6:1A insert, Figure 6:1A,* & *Figure 6:2B,* respectively) exhibited relatively smooth morphologies with small cavities present. Marginal differences were noted between the samples but these were not significant and exemplify the step-coverage of magnetron sputtered coatings.

Cross-sectional images show an increase in the overall thickness of the coating from Ti to NaTC, on both the NB/NH (*Figure 6:1B & D*) and B/300 samples (*Figure 6:2B & D*) as well as the appearance of a bilayer in the coating formed of Ti (bottom) and titanate (top), distinguished by contrast in intensity and structure; the titanate was nanoporous in morphology compared to the columnar grown Ti coatings. The thicknesses of both the Ti and titanate portion of the coatings were quantified in *Table 6:1*, which showed a decrease in the thickness of the Ti layer in all titanate samples and a significant increase in total coating thickness due to the titanate growth. Furthermore, thicknesses of both NB/NH and B/300 Ti coatings in *Table 6:1* were close to the intended 500 nm coating thickness. The Ti layer revealed a consistent reduction in thickness from *ca*. 500 nm to *ca*. 300 nm for all titanate samples except for the B/300 CaTC (*Figure 6:2F*) samples, which reduced to *ca.* 380 nm. It was noted that the thickness of the titanate layer showed no variation between either sputtering parameters (NB/NH *vs.* B/300) and/or chemical character (NaTC *vs.* CaTC), with a range of thicknesses from *ca.* 0.82 μm on B/300 CaTC to *ca.* 1.42 μm on the B/300 NaTC sample.

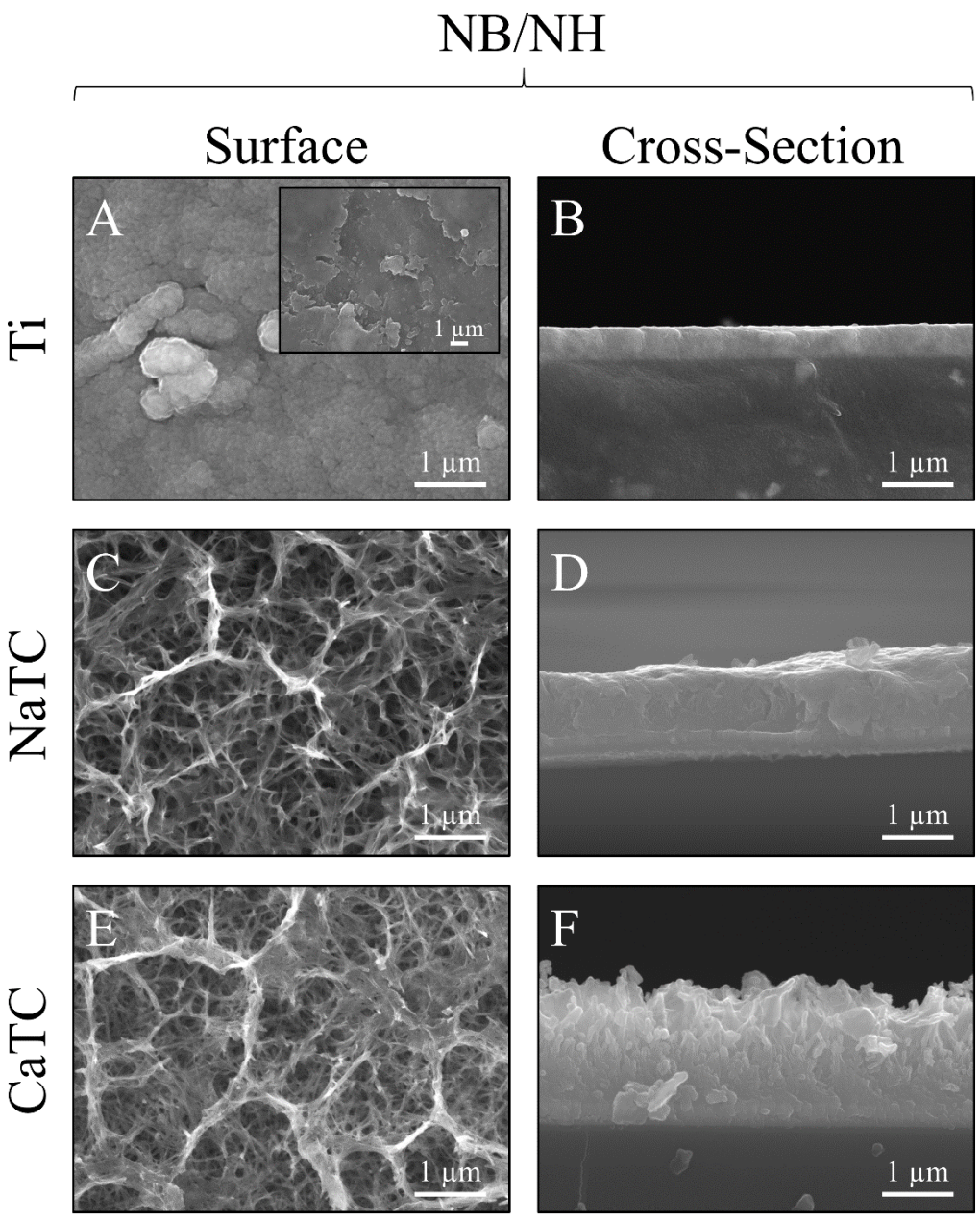

Figure 6:1. SEM Surface and cross-section micrographs with A) & B) NB/NH Ti; C) & D) NB/NH NaTC; and E) & F) NB/NH CaTC. Insert micrograph in A) is of the Mg control, for reference.

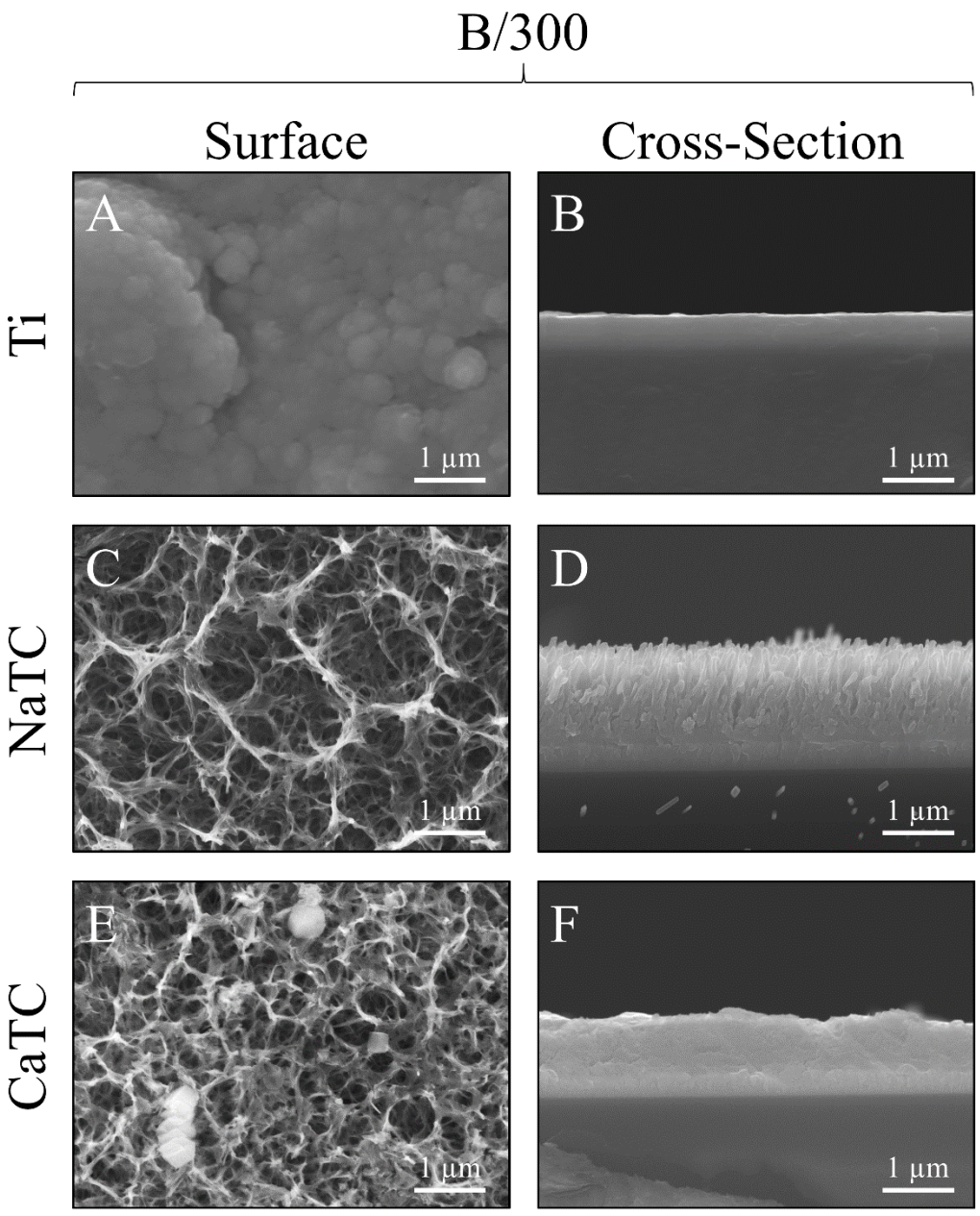

Figure 6:2. SEM Surface and cross-section micrographs with A) & B) B/300 Ti; C) & D) B/300 NaTC; and E) & F) B/300 CaTC.

Table 6:1. Ti coating and titanate thickness determined via SEM assessment. Error values are standard error; n = 5. NB/NH (No Substrate Bias/No Substrate Heating); B/300 (-100 V Bias/300 °C heating); Ti (just Ti coating); NaTC (sodium titanate converted); CaTC (calcium titanate converted).

Sample	Total Thickness / µm	Ti Thickness / µm	Titanate Thickness / µm
NB/NH Ti	0.52 ± 0.01	0.52 ± 0.01	N/A
NB/NH NaTC	1.23 ± 0.05	0.29 ± 0.02	0.96 ± 0.05
NB/NH CaTC	1.87 ± 0.12	0.30 ± 0.01	1.42 ± 0.11
B/300 Ti	0.48 ± 0.01	0.48 ± 0.01	N/A
B/300 NaTC	1.57 ± 0.03	0.38 ± 0.03	1.22 ± 0.02
B/300 CaTC	1.11 ± 0.03	0.29 ± 0.01	0.82 ± 0.02

Analysis of the elemental composition of NB/NH NaTC, NB/NH CaTC, B/300 NaTC and B/300 CaTC samples determined *via* EDX is summarised in *Table 6:2*. The O and Ti contents were similar for the NB/NH NaTC, NB/NH CaTC and B/300 NaTC samples, while the B/300 CaTC sample exhibited a higher Mg content at 31.5 at.%, correlating with decreased O and Ti contents. Both the NB/NH and B/300 NaTC samples demonstrated an increased Na content (8.0 and 7.1 at.%, respectively) with trace amounts (< 0.5 at.%) of Ca. However, the CaTC samples exhibited the inverse with low amounts (< 0.5 at.%) of Na and higher Ca contents (NB/NH = 4.8 at.%, B/300 = 3.1 at.%). Precipitates on the B/300 CaTC sample were found to be rich in Ca and O, as confirmed *via* EDX (*Figure 6:3*).

Table 6:2. EDX elemental data of titanate converted DC magnetron sputtered Ti films. Values given are mean values ± standard error (n = 5). All unconverted samples contained 100% Ti via EDX. NB/NH (No Substrate Bias/No Substrate Heating Ti coating); B/300 (-100 V Bias/300 °C heating Ti coating); NaTC (sodium titanate converted); CaTC (calcium titanate converted).

Sample ID	Element quantity / at.%				
	O	**Na**	**Mg**	**Ca**	**Ti**
NB/NH NaTC	60.2 ± 0.2	8.0 ± 0.2	7.9 ± 0.4	< 0.5	23.4 ± 0.2
NB/NH CaTC	64.2 ± 0.4	< 0.5	6.9 ± 0.2	4.8 ± 0.0	24.0 ± 0.4
B/300 NaTC	59.6 ± 0.6	7.1 ± 0.4	10.4 ± 1.5	< 0.5	22.6 ± 0.7
B/300 CaTC	53.8 ± 2.1	< 0.5	31.5 ± 4.3	3.1 ± 0.6	11.5 ± 1.7

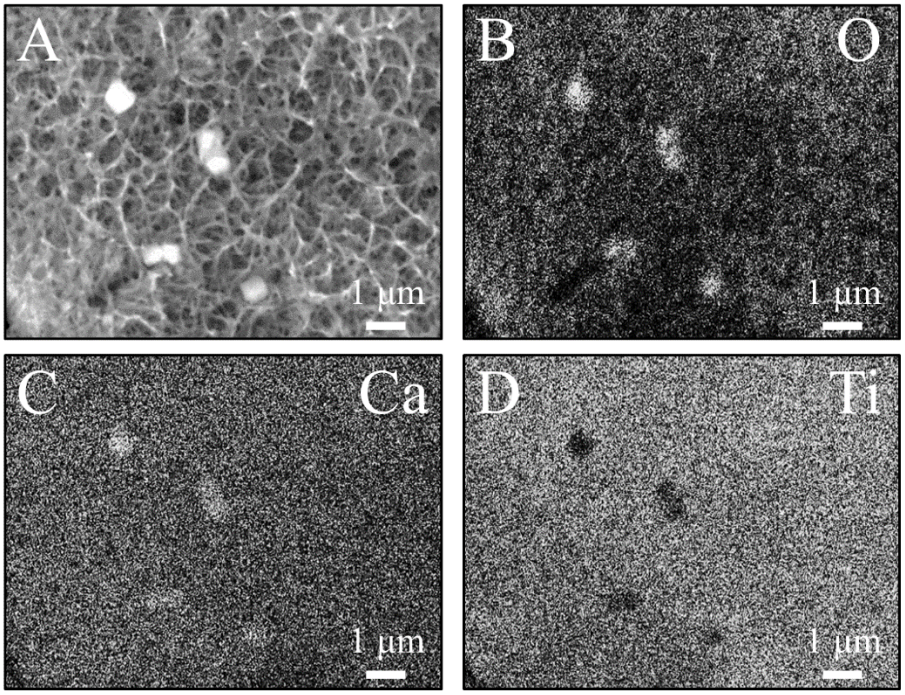

Figure 6:3. EDX mapping of precipitates on the B/300 CaTC sample, exhibiting increased intensities of Ca and O, with a reduction in Ti.

EDX mapping (*Figure 6:4*) of the samples suggested partial delamination had occurred in the coatings following wet chemical conversion, particularly for the B/300 NaTC (*Figure 6:4C*) and CaTC (*Figure 6:4D*) samples. Of the coatings produced, the NB/NH samples were least affected, with the NB/NH CaTC samples showing minimal delamination (< 0.1 %). Delamination data, quantified from ImageJ analysis of the SEM micrographs and summarised in *Table 6:3*, indicated the B/300 samples, particularly the CaTC sample, experienced a far higher degree of delamination in total area of delamination (*ca.* 40.3% *vs.* < 0.1%, respectively), and size of delaminated regions (*ca.* 3402.9 μm^2 *vs.* 238.4 μm^2, respectively), compared to the NB/NH CaTC coatings.

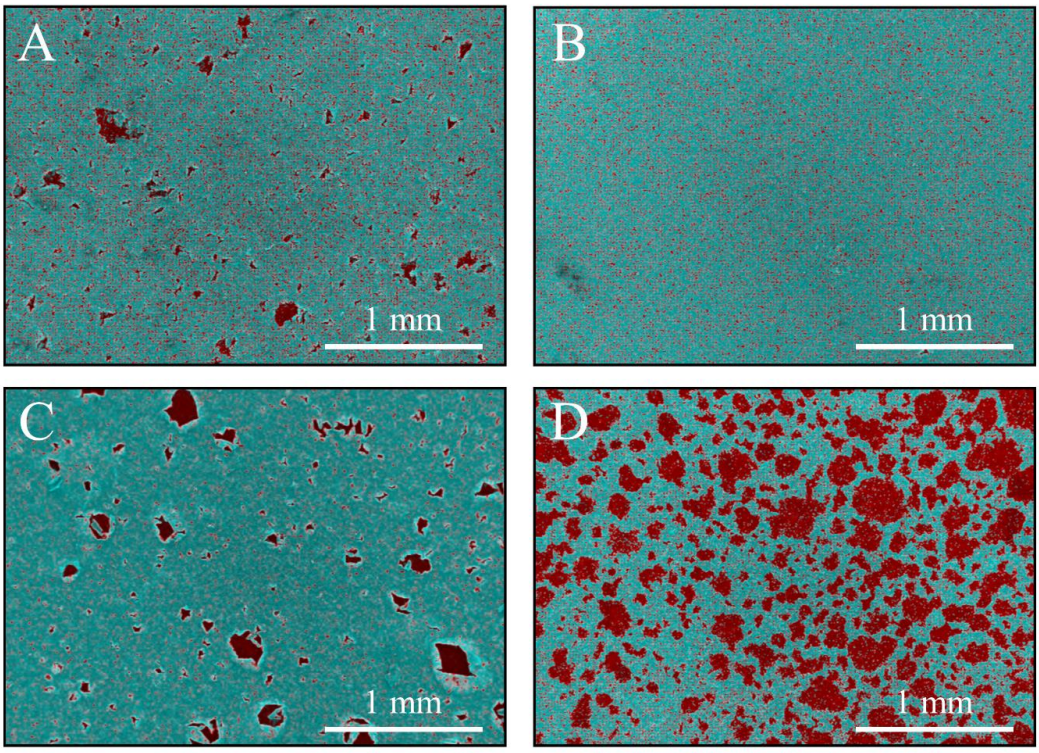

Figure 6:4. EDX Mapping of Mg (red) and Ti (blue) overlaying SEM images of delamination (Defined as the clear Mg regions (red) on the EDX micrographs) of A) NB/NH NaTC, B) NB/NH CaTC, C) B/300 NaTC and D) B/300 CaTC.

Table 6:3. ImageJ quantitative analysis for delamination of Titanate coatings on Mg substrates with values given as mean ± standard error (n = 5). NB/NH (No Substrate Bias/No Substrate Heating Ti coating); B/300 (-100 V Bias/300 °C heating Ti coating); NaTC (sodium titanate converted); CaTC (calcium titanate converted).

Sample ID	% Delamination (Delamination Area / Total Micrograph Area)	Frequency of Delaminated Regions / mm^{-2}	Average Area of Regions / μm^2
NB/NH NaTC	1.9 ± 0.7	46.0 ± 16.8	357 ± 20
NB/NH CaTC	< 0.1	0.5 ± 0.2	238 ± 47
B/300 NaTC	6.5 ± 1.1	40.1 ± 4.1	1429 ± 127
B/300 CaTC	40.3 ± 6.7	94.5 ± 5.6	3403 ± 382

6.2.2 XPS

XPS analysis (*Figure 6:5*) of high-resolution Ti 2p (*Figure 6:5B*), O 1s (*Figure 6:5C*), Mg 1s (*Figure 6:5D*), Na 1s (*Figure 6:5E*), and Ca 2p (*Figure 6:5F*) peaks demonstrated significant differences in peak deconvolutions, spectral shifts, and peak intensities, corresponding to alternative chemical structures produced. All survey

spectra (*Figure 6:5A*) detailed noticeable differences between the Ti coated (NB/NH Ti & B/300 Ti), sodium titanate converted (NB/NH NaTC & B/300 NaTC), and calcium ion exchanged (NB/NH CaTC & B/300 CaTC) samples. High-resolution spectra is shown in *Figure 6:5B-F*. The survey spectra was used to determine the elemental composition of the coatings, outlined in *Table 6:4*. All samples exhibited some Mg, despite the shallow penetration depth, except for the Ti coated samples. The comparison of NaTC and CaTC samples demonstrated high Na content in the NaTC samples becoming zero upon conversion to CaTC, with an associated increase in Ca content. The deconvoluted peaks are detailed in *Table 6:5* & *Table 6:6*.

The O 1s high-resolution scans (*Figure 6:5C*) for the Ti coated samples showed 3 constituent peaks corresponding to O^{2-} (Ti^{4+}—O; *ca.* 71.6%), OH^-/defective oxides (Ti—OH/Ti^{3+}—O/Ti^{2+}—O; *ca.* 18.8%), and H_2O (*ca.* 9.7%). Similar peaks were noted for the NaTC samples with the addition of a peak at 535.2 eV (*ca.* 9%) due to Na KLL Auger electrons. This peak reduced during the CaTC conversion, with 3 similar deconvoluted peaks to the Ti coated samples corresponding to O^{2-} (Ti^{4+}—O; *ca.* 23-43%), OH^-/defective oxides (Ti—OH/Ti^{3+}—O/Ti^{2+}—O; *ca.* 49-60%), and H_2O (*ca.* 8-16%), although the relative peak intensities/areas were different.

Ti 2p high-resolution analysis (*Figure 6:5B*) corroborated the O 1s findings, with the Ti coated samples (NB/NH Ti and B/300 Ti) exhibiting Ti in all 4 valence states; Ti^{4+} (2p 3/2 *ca.* 458.7 eV; *ca.* 51-64%), Ti^{3+} (2p 3/2 *ca.* 457.2 eV; *ca.* 13%), Ti^{2+} (2p 3/2 *ca.* 455.3 eV; *ca.* 5%), and Ti—Ti (2p 3/2 *ca.* 453.3 eV; *ca.* 17-31%). The number of deconvoluted peaks for Ti 2p doublets decreased to a single doublet for the NaTC (NB/NH NaTC and B/300 NaTC) and CaTC (NB/NH CaTC and B/300 CaTC) samples corresponding to Ti^{4+}/TiO_2 (2p 3/2 at *ca.* 458.3 eV); the CaTC samples

exhibited a shift (*ca.* 0.1-0.4 eV) to lower binding energies compared to NaTC samples.

The Na 1s region (*Figure 6:5E*) exhibited an asymmetric peak that resolved into 3 peaks at *ca.* 1071.5 eV (44-53%), *ca.* 1068.2 eV and 1071.5 eV (combined accounts for remaining peak area percentage) relating to Na—O and two Ti LMM Auger electron peaks, respectively for both NaTC samples. For both the Ti coated and CaTC samples, only two constituent peaks were present corresponding to the Ti LMM Auger peaks only. Three peaks were also present in the Ca 2p region (*Figure 6:5F*) for CaTC (NB/NH CaTC and B/300 CaTC) samples attributed to Ca 2p doublets (2p 3/2 *ca.* 347.0 eV; combined *ca.* 67 and 95% for NB/NH CaTC and B/300 CaTC samples, respectively) and Mg KLLb Auger electrons at 351.5 eV (33 and 5% for NB/NH CaTC and B/300 CaTC samples, respectively); a significant increase in the relative quantity of Mg KLL Auger electrons for the B/300 sample is noted.

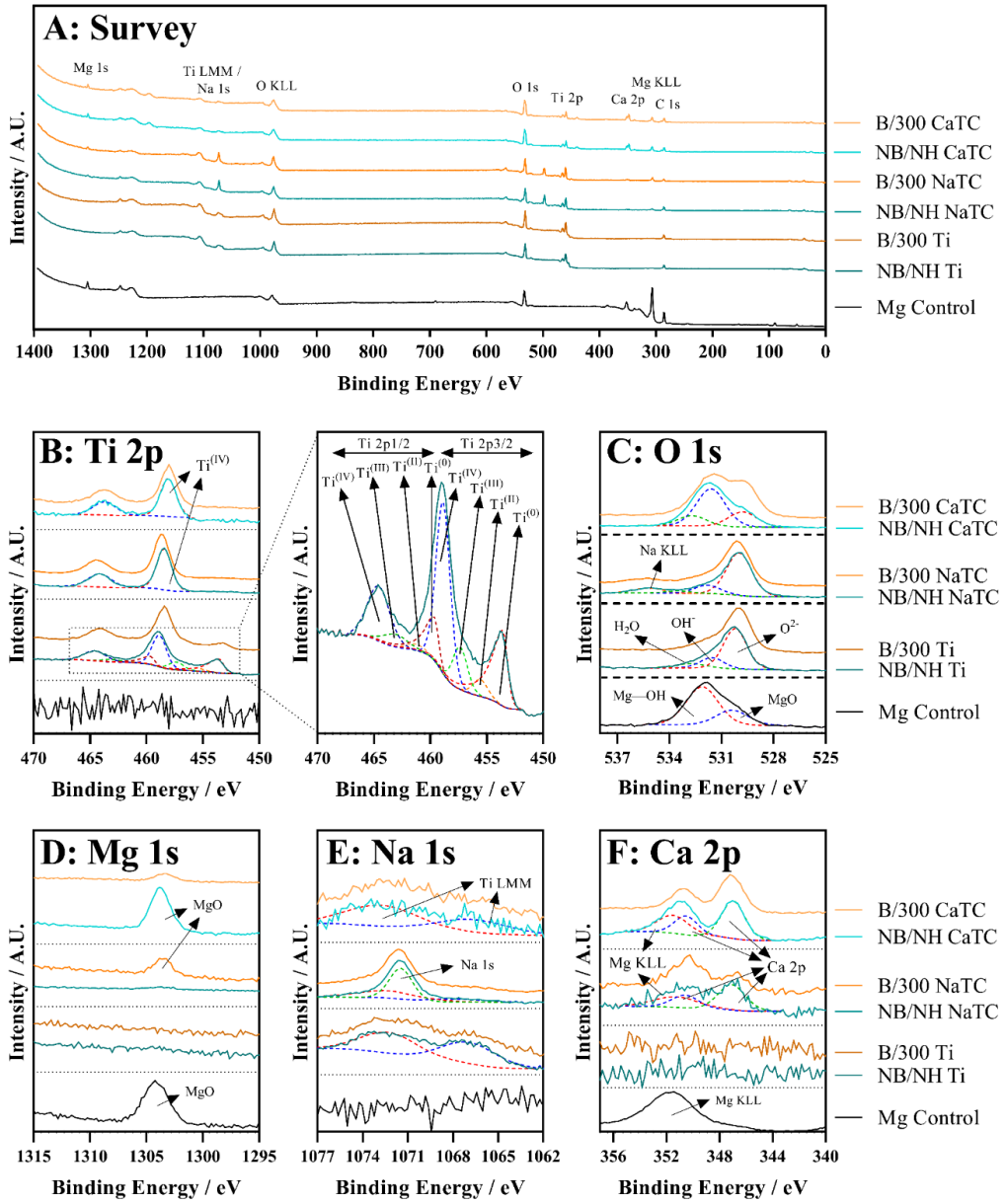

Figure 6:5. XPS survey and high-resolution spectra and corresponding peak deconvolutions of Ti coated (NB/NH Ti and B/300 Ti), sodium titanate converted (NB/NH NaTC and B/300 NaTC) and calcium ion exchanged (NB/NH CaTC and B/300 CaTC) samples. A) Survey, B) Ti 2p with inset spectra showing detailed deconvolutions for the NB/NH Ti sample, C) O 1s, D) Mg 1s, E) Na 1s, and F) Ca 2p elemental peaks.

Table 6:4. Surface element compositional analysis conducted via XPS survey spectra component fitting. Errors quoted are calculated area standard deviations using CasaXPS.

Sample ID	Elemental Composition / at.%				
	Mg	Ti	O	Na	Ca
Mg Control	40.2 ± 0.5	0	59.8 ± 0.5	0	0
NB/NH Ti	0	39.5 ± 0.4	60.5 ± 0.4	0	0
NB/NH NaTC	4.4 ± 0.4	18.0 ± 0.3	59.5 ± 0.6	16.5 ± 0.4	1.7 ± 0.2
NB/NH CaTC	27.0 ± 0.3	4.5 ± 0.2	54.7 ± 0.4	0	13.8 ± 0.4
B/300 Ti	0	31.2 ± 0.5	68.8 ± 0.5	0	0
B/300 NaTC	8.9 ± 0.3	17.5 ± 0.4	51.4 ± 0.9	15.3 ± 0.4	2.0 ± 0.2
B/300 CaTC	11.1 ± 0.3	16.3 ± 0.3	62.6 ± 0.5	0	16.3 ± 0.3

Table 6:5. XPS peak deconvolutions for the Mg control, NB/NH Ti and B/300 Ti samples.

Sample ID	Region	Peak Identity	Binding Energy / eV	Area / %	Reference(s)
Mg Control	O 1s	Mg—O	530.4	28.2	[496, 497]
		Mg—OH	532.1	71.8	[496, 497]
	Mg 1s	Mg—Mg	1303.3	32.7	[496, 497]
		Mg—O	1304.3	50.4	[496, 497]
		Mg—OH	1305.3	16.9	[496, 497]
NB/NH Ti	O 1s	O^{2-} (Ti^{4+}—O)	530.2	71.6	[215, 498]
		OH^{-} ($Ti^{3+/2+}$—O/Ti—OH)	531.5	18.8	[215, 498]
		H_2O (O—H)	532.7	9.7	[215, 498]
	Ti 2p 3/2	Ti—Ti	453.5	31.1	[499]
		Ti^{4+}—O	458.8	51.0	[499]
		Ti^{3+}—O	457.3	12.8	[499]
		Ti^{2+}—O	455.5	5.1	[499]
	Na 1s	Ti LMM	1066.8	51.3	[500]
		Ti LMM	1072.2	48.7	[500]
B/300 Ti	O 1s	O^{2-} (Ti^{4+}—O)	529.9	76.8	[215, 498]
		OH^{-} ($Ti^{3+/2+}$—O/Ti—OH)	531.5	17.6	[215, 498]
		H_2O (O—H)	532.6	6.7	[215, 498]
	Ti 2p 3/2	Ti—Ti	453.2	16.6	[499]
		Ti^{4+}—O	458.5	64.3	[499]
		Ti^{3+}—O	457.0	13.4	[499]
		Ti^{2+}—O	455.2	5.8	[499]
	Na 1s	Ti LMM	1072.4	66.1	[500]
		Ti LMM	1067.4	33.9	[500]

Table 6:6. XPS peak deconvolutions for the sodium and calcium titanate converted samples, NB/NH NaTC, NB/NH CaTC, B/300 NaTC and B/300 CaTC samples.

Sample ID	Region	Peak Identity	Binding Energy / eV	Area / %	Reference(s)
NB/NH NaTC	O 1s	Ti^{4+}—O	530.2	72.8	[215, 498]
		Ti^{3+}—O	531.5	14.5	[215, 498]
		Ti—OH	531.7	3.8	[215, 498]
		Na KLL	535.2	8.9	[387]
	Ti 2p 3/2	Ti^{4+}—O	458.5	66.7	[215, 498]
	Na 1s	Na—O	1071.5	53.2	[215]
		Ti LMM	1068.0 & 1072.2	46.8	[500]
	Ca 2p 3/2	Ca—O	347.0	95.6	[215]
		Mg KLLb	351.5	4.4	[496, 497]
	Mg 1s	Mg	1303.7	100.0	[496, 497]
B/300 NaTC	O 1s	Ti^{4+}—O	530.2	71.9	[215, 498]
		Ti^{3+}—O	531.6	13.4	[215, 498]
		Ti—OH	532.5	5.9	[215, 498]
		Na KLL	535.5	8.9	[387]
	Ti 2p	Ti^{4+}—O	458.5	66.7	[215, 498]
	Na 1s	Na—O	1071.6	44.2	[215]
		Ti LMM	1068.4 & 1072.6	55.8	[500]
	Ca 2p	Ca—O	346.7	35.2	[215, 498]
		Mg KLLb	350.3	64.8	[496, 497]
	Mg 1s	Mg 1s	1303.6	100.0	[496, 497]
NB/NH CaTC	O 1s	Ti^{4+}—O	529.8	23.9	[215, 498]
		Ti^{3+}—O	531.7	59.8	[215, 498]
		Ti—OH	532.7	16.4	[215, 498]
	Ti 2p 3/2	Ti^{4+}—O	458.1	66.7	[215]
	Na 1s	Ti LMM	1066.8 & 1072.7	100	[500]
	Ca 2p 3/2	Ca—O	347.0	66.8	[215, 498]
		Mg KLLb	351.5	33.2	[496, 497]
	Mg 1s	Mg 1s	1303.7	100.0	[496, 497]
B/300 CaTC	O 1s	Ti^{4+}—O	529.8	42.8	[215, 498]
		Ti^{3+}—O	531.7	49.0	[215, 498]
		Ti—OH	533.0	8.3	[215, 498]
	Ti 2p 3/2	Ti^{4+}—O	458.2	66.7	[215, 498]
	Na 1s	Ti LMM	1066.8 & 1072.7	100	[500]
	Ca 2p 3/2	Ca—O	347.0	95.1	[215, 498]
		Mg KLLb	351.0	4.9	[496, 497]
	Mg 1s	Mg 1s	1303.5	100.0	[496, 497]

6.2.3 XRD

XRD analysis (*Figure 6:6*) of the Mg control sample demonstrated peaks at *ca.* 32.2, 34.4, 36.6, 47.8 and 57.4° in 2θ, which was in good agreement with the ICDD database file for Mg (PDF 00-035-0821) regarding their peak position. However, the peak intensities revealed preferred orientation toward the (002) crystal plane. NB/NH Ti and B/300 Ti coatings exhibited the addition of small, broad peaks at 38.2 and 40.0° corresponding to the ICDD database file for α-Ti (PDF 00-044-1294) matching the (002) and (101) Ti planes, respectively. The NB/NH Ti coating also showed a bias toward the (002) plane, whilst the B/300 coating showed approximately equal intensities between the two plane orientations. Chemical treatment (both the NaTC and CaTC) of both the NB/NH and B/300 Ti sputtered coatings resulted in loss of Ti peaks, while Mg peaks remained unaltered. No titanate peaks were observed for any of the converted samples.

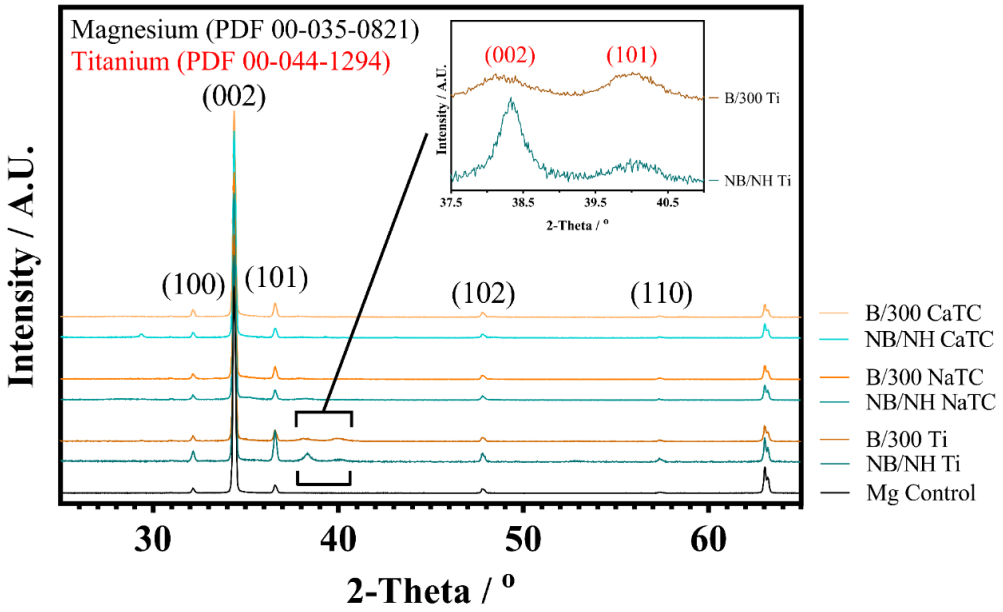

Figure 6:6. XRD spectra of all sample types including an insert zoomed in view of two Ti peaks present in both NB/NH Ti and B/300 Ti samples, with annotated crystal planes from Mg (ICDD PDF 00-035-0821; Black) and Ti (ICDD PDF 00-044-1294; Red).

6.2.4 Raman spectroscopy

Raman spectroscopy (*Figure 6:7*) of the NB/NH Ti samples contained bands corresponding to anatase/rutile mixed phases with bands at *ca.* 169 cm^{-1} distinct to the anatase structure, whilst bands at *ca.* 245, 417 and 600 cm^{-1} were from the combination of both [381-383]. NB/NH NaTC and B/300 NaTC samples both demonstrated a band at *ca.* 194 cm^{-1} attributed to the Na—O—Ti bending mode and bands at *ca.* 282 and 436 cm^{-1} characteristic of Na—O—Ti stretching modes [384]. The band at *ca.* 440 cm^{-1} was characteristic of Ti—O bending for 6-coordinated Ti [383]. The band at *ca.* 893 cm^{-1} was due to Ti—O stretching modes, while bands at 625 and 691 cm^{-1} were assigned to Ti—O—Ti octahedral [TiO_6] vibrations [383].

CaTC Raman spectras differed between the NB/NH and B/300 samples, with the NB/NH CaTC sample exhibiting bands associated with the underlying Mg substrate, as described above. However, both samples exhibited the presence of bands at *ca.* 185, 440 and 276 cm^{-1} corresponding to the Ca—O—Ti bending mode, Ca—O—Ti and O—Ti—O stretching modes, respectively [501, 502]. Additionally bands present at *ca.* 700 and 798 cm^{-1} were suggested to be due to Ti—O—Ti stretching modes, and *ca.* 870 cm^{-1} from the Ti—O stretching mode, which emerged within the broad band between 582-943 cm^{-1} [501, 502].

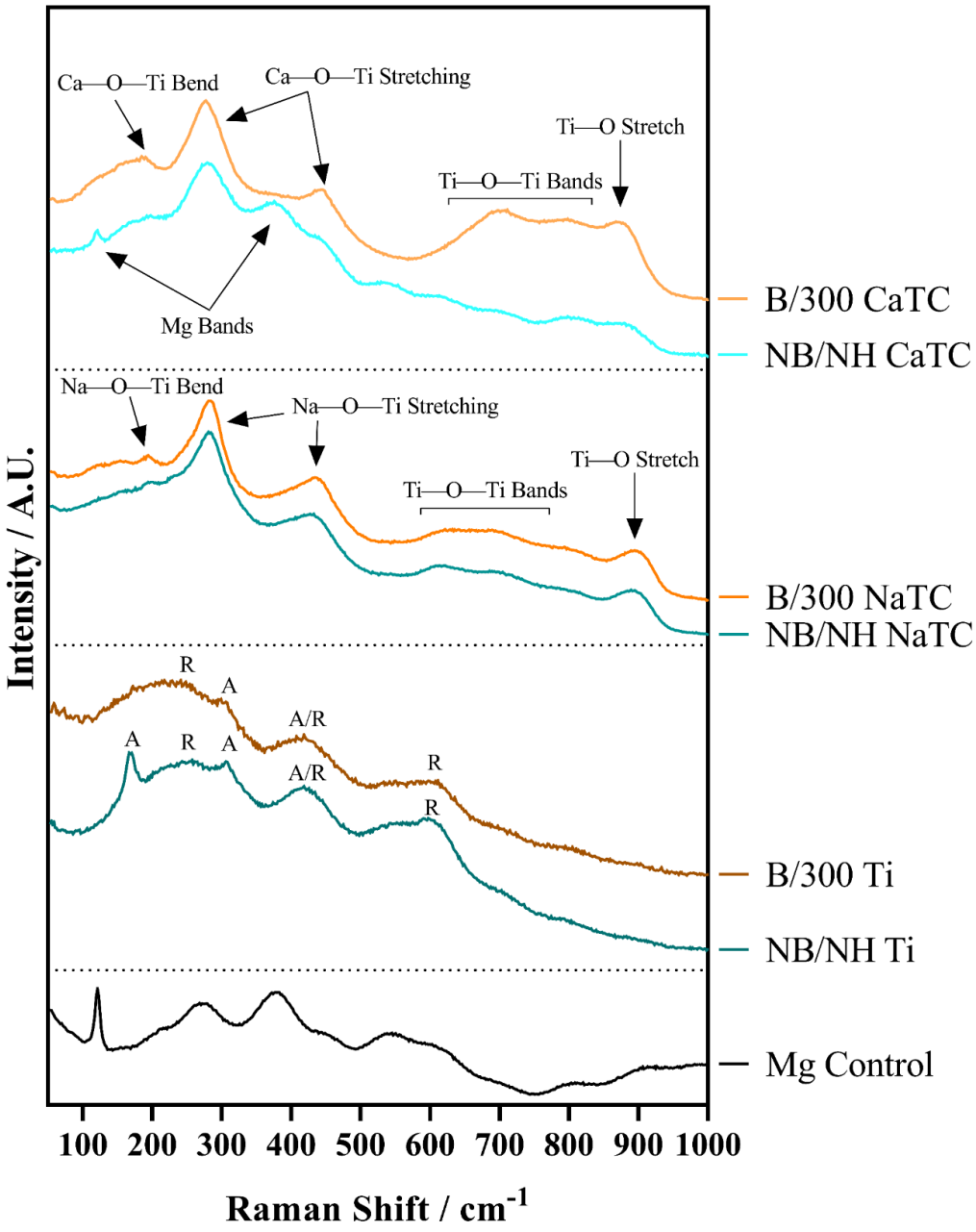

Figure 6:7. Raman spectra of all samples with annotated bands. For the NB/NH Ti and B/300 Ti samples, A = anatase and R = rutile.

6.2.5 Potentiodynamic Polarisation Analysis

Figure 6:8 demonstrated typical Tafel polarisation curves for the Ti-coated Mg samples (NB/NH Ti & B/300 Ti) and the titanate (NaTC & CaTC suffixes) converted samples, with quantitative corrosion values noted in *Table 6:7*. Samples that occupy the lower right quadrant on the graph relative to the Mg control had both lower

corrosion current density (i_{corr}) and higher corrosion potential and were thus relatively more stable within the solution with a lower tendency to corrode [503]. It was clear from the data presented that the NB/NH CaTC sample exhibited the lowest i_{corr} and highest E_{corr} values (*ca.* -1.327 V and 0.060 mA/cm^2, respectively) of the samples tested, particularly compared to the Mg control (*ca.* -1.488 V and 0.305 mA/cm^2, respectively, which exhibited the highest i_{corr} and lowest E_{corr} values). There were clear trends noted for the NB/NH samples, which showed an increase in E_{corr} values in the following order: Mg < Ti coated < NaTC < CaTC. A clear trend due to coating conditions was not observed for the i_{corr} values presented. However, the Ti coated samples, as well as all of the B/300 samples, performed less well compared to the Mg control (*ca.* 0.432 and 0.363 mA/cm^2 for the NB/NH Ti and B/300 Ti samples, respectively, compared to the Mg control at 0.305 mA/cm^2). The values for pure Mg have been compared with similar studies within the literature and are within an agreeable tolerance despite the variance in testing methodologies [504-511].

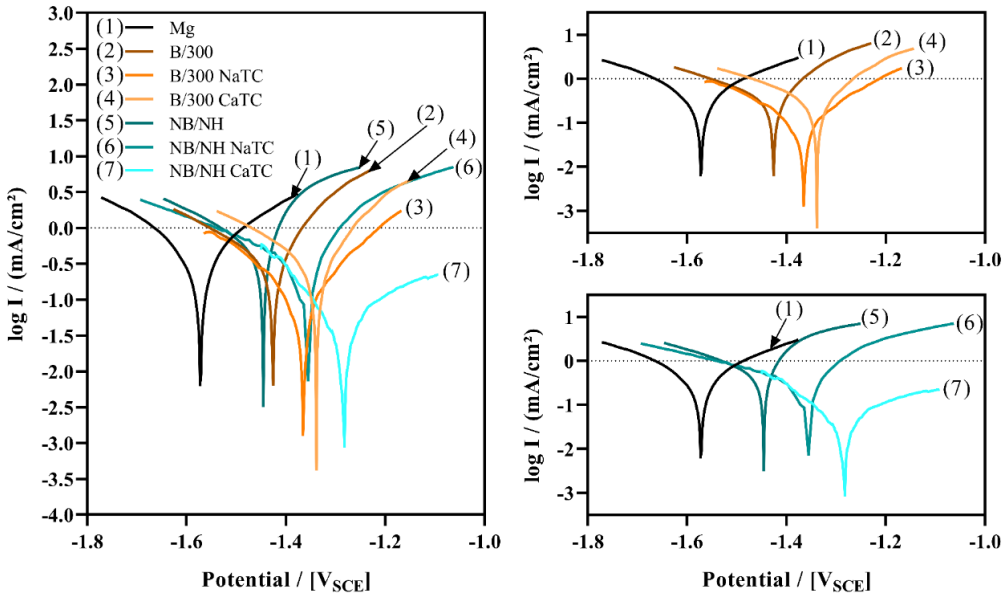

Figure 6:8. Representative Tafel plots from potentiodynamic polarisation curves of all coating samples in reference to Mg controls. Left-hand graph combines all samples, whilst the top right and bottom right graphs show localised regions of the B/300 and NB/NH samples, respectively.

Table 6:7. E_{corr} and i_{corr} values demonstrating the effect of coating on the degradation rate of Mg. Error values are standard error; n = 3.

Sample ID	Corrosion Potential, E_{corr} / (V)	Corrosion Current Density, i_{corr} / (mA.cm^{-2})	Polarisation Resistance, R_p / (Ω.cm^2)	Corrosion Rate, v_{corr} / (mm.y^{-1})
Mg	-1.49 ± 0.07	0.31 ± 0.09	155.8 ± 48.7	6.96 ± 0.01
NB/NH Ti	-1.48 ± 0.01	0.43 ± 0.14	128.8 ± 66.3	9.88 ± 0.01
NB/NH NaTC	-1.34 ± 0.07	0.22 ± 0.08	204.2 ± 63.5	5.10 ± 0.02
NB/NH CaTC	-1.33 ± 0.03	0.06 ± 0.01	625.4 ± 44.7	1.37 ± 0.01
B/300 Ti	-1.39 ± 0.03	0.36 ± 0.03	78.4 ± 0.7	8.29 ± 0.03
B/300 NaTC	-1.40 ± 0.03	0.38 ± 0.23	197.0 ± 100.6	8.79 ± 0.03
B/300 CaTC	-1.36 ± 0.02	0.43 ± 0.04	86.5 ± 9.6	9.93 ± 0.01

6.2.6 SEM of Electrochemically Degraded Samples

Following electrochemical corrosion, the morphological changes that occurred on the surface were explored *via* SEM analysis (see *Figure 6:9*). All samples exhibited cracking at the surface, with notable visual alteration to the surface roughness, likely generated through crevice or pitting corrosion. All titanate converted samples maintained discrete regions characteristic of titanate surfaces, with clear formation of

precipitates. The precipitates occurred in the form of nanoneedles rich in magnesium, chlorine, and oxygen, as detailed from EDX mapping (*Figure 6:10*), which were exemplified in the B/300 NaTC sample (*Figure 6:9D*), whilst nano-features rich in calcium, phosphorous, and oxygen were noted on the NB/NH NaTC sample (*Figure 6:9C*).

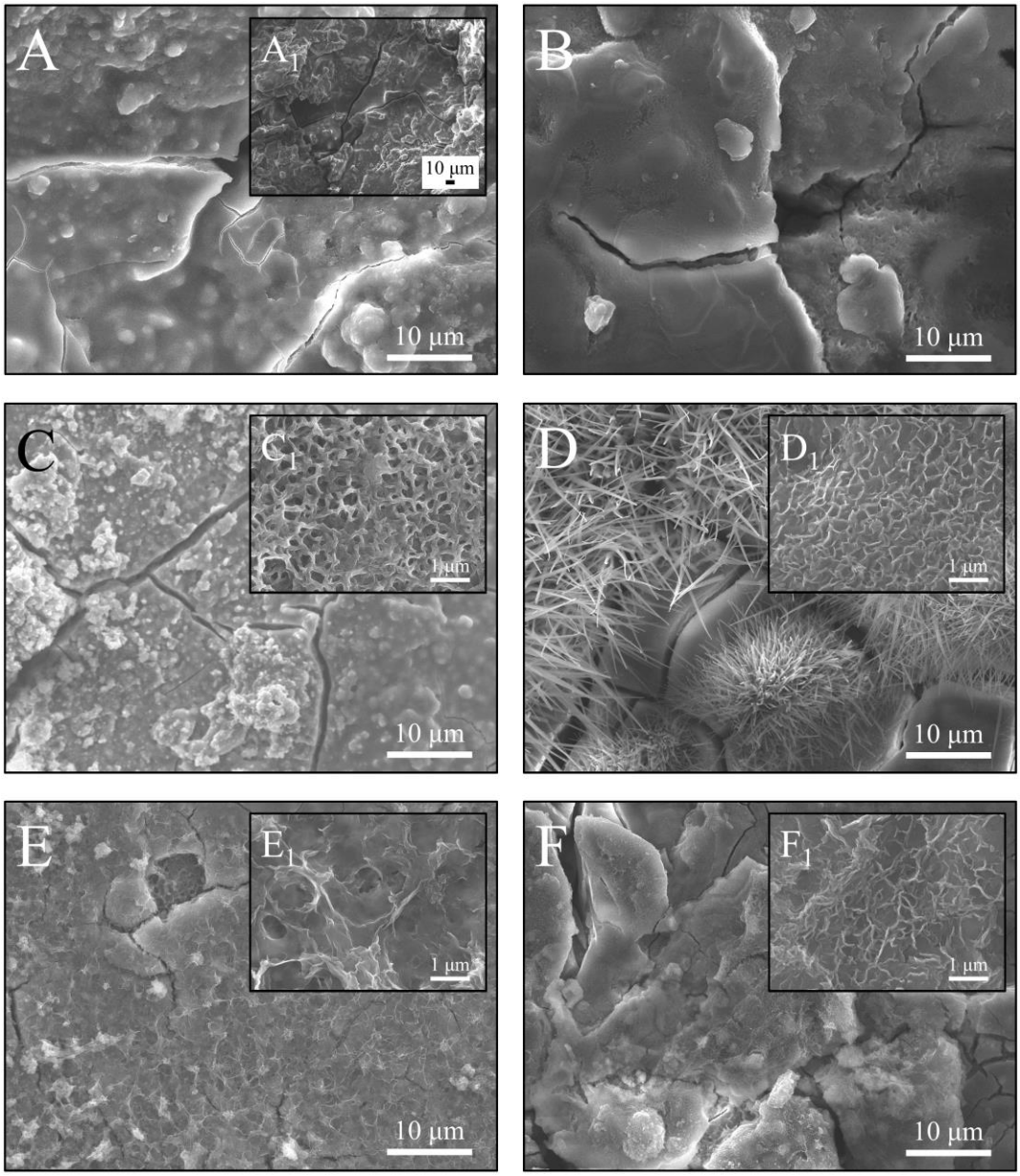

Figure 6:9. SEM micrographs of electrochemically degraded samples in DMEM. A) NB/NH Ti with insert A_1 = Mg; B) B/300 Ti; C) NB/NH NaTC; D) B/300 NaTC; E) NB/NH CaTC and F) B/300 CaTC. Micrographs A_1, C_1, D_1, E_1 and F_1 are all higher resolution areas of interest, particularly noting regions akin to nanoporous titanate structures.

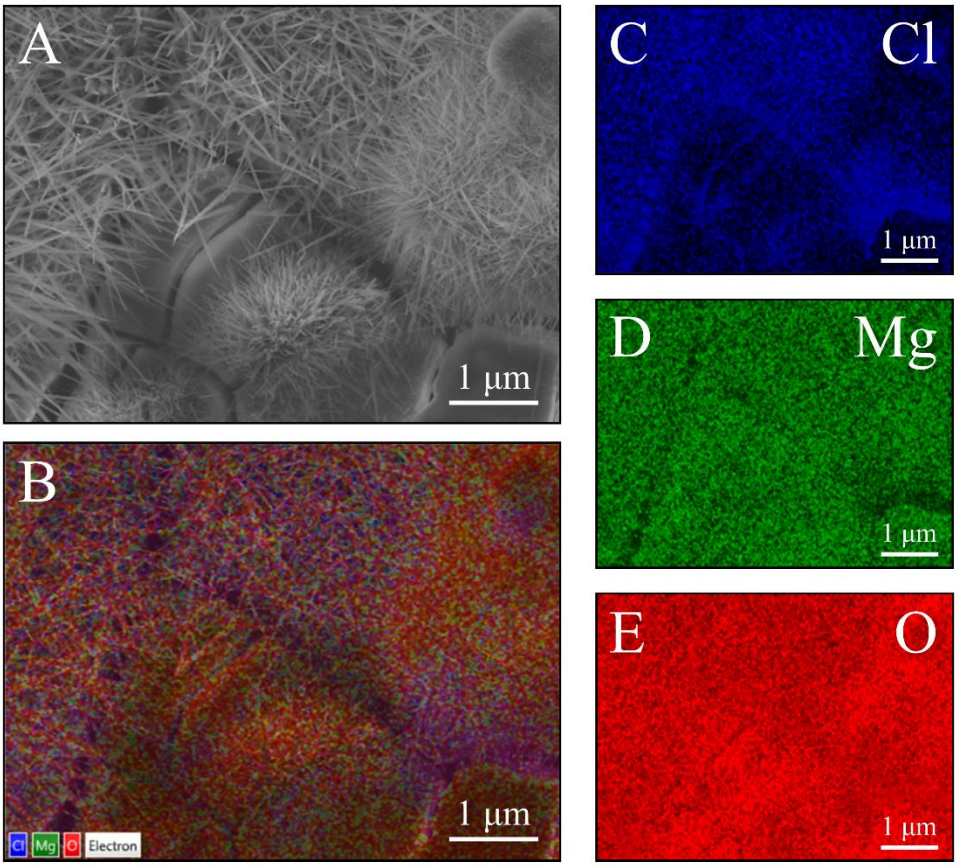

Figure 6:10. A) SEM micrograph and B) EDX mapping of 'nanowhiskers' noted in the B/300 NaTC sample post electrochemical degradation. The mapping suggests areas rich in C) Cl, D) Mg and E) O.

6.3 Discussion

6.3.1 Topographical, Structural and Compositional Analysis

6.3.1.1 DC Magnetron Sputtered Ti Coatings

Generation of a suitable barrier between Mg and the surrounding extracellular fluid is a complex and demanding challenge in order to mitigate additional necessary surgeries to remove non-degradable fixation devices. This study explored a novel approach for generating bioactive titanate layers onto biodegradable Mg, to facilitate use under *in vivo* corrosion conditions. Recent studies have investigated the potential of titanate layers for increased corrosion protection, such as the study conducted by Arumugam *et al.*, however, the substrate material utilised was a Ti-20Nb-13Zr alloy; a non-biodegradable material [512]. Their study demonstrated improved corrosion resistance of titanate converted surfaces, exemplifying their potential as a corrosion inhibition coating. To date, the presented work was the only such study of titanate coatings being used to modify the corrosion rate of Mg-based materials.

SEM micrographs of the Ti coated (NB/NH Ti and B/300 Ti; *Figure 6:1A* and *Figure 6:2A*, respectively) and native Mg discs (*Figure 6:1A insert*), demonstrated clear evidence of the magnetron sputtering methodology providing good step coverage, as detailed by Swann [347]. The structure of the Ti coating appeared to be columnar for all the NB/NH samples, as confirmed *via* XRD (*Figure 6:6*), with a preferential orientation in the (002) plane (Ti PDF 00-044-1294), characteristic of such coatings. However, the B/300 samples, exhibited a more equiaxed structure akin to bulk materials. This was due to the increased energy of deposited Ti species by the combination of higher bias and temperature.

There was good agreement between the characterisation techniques used to quantify the Ti coatings deposited on the Mg substrate, however, due to the shallow penetration depth of Raman and XPS, only the top passivated surface was detected

due to atmospheric exposure. Raman analysis (*Figure 6:7*) demonstrated clear anatase and rutile modes for both the NB/NH and B/300 Ti samples (similar to bands exhibited in studies by Exarhos [466], Ocana *et al.* [464], and Hsu *et al.* [465]), with the NB/NH sample exhibiting a preferred anatase structure, whilst the B/300 Ti showed a combination of anatase and rutile phases. This was expected since the atomic energy provided during the ion-bombardment process was higher in the B/300 sample due to the -100 V bias and 300 ^{o}C substrate heating, allowing atomic reordering to occur into the higher energy rutile phase, similar to the findings presented by Simionescu *et al.* [513]. These peaks were generated from Ti—O bonds, either through vibration, stretching or bending, and were clearly seen in the XPS spectra presented (*Figure 6:5*). The Ti found within the titania layer, which was due to the passivation of the Ti coating with air, was present in all of the possible valence states: Ti^{4+}, Ti^{3+}, Ti^{2+}, and Ti, however, preferential formation of the Ti^{4+} valence state, akin to TiO_2 (Anatase/Rutile) was noted. The Ti^{3+} valence state was statistically more likely, compared to the Ti^{2+} state due to thermodynamic favourability, as outlined by Hanawa *et al.* [467].

6.3.1.2 Sodium Titanate Conversion

SEM imaging of NB/NH and B/300 NaTC samples (*Figure 6:1C* and *Figure 6:2C*, respectively) revealed the characteristic nanoporous structure of sodium titanate expected from the chemical treatment used [514]. Successful conversion of the Ti sputtered surface to sodium titanate was supported by EDX (*Table 6:2*) and XPS analysis (*Figure 6:5* & *Table 6:4*), both confirming the presence of Na—O. The XPS analysis also showed a change in the quantity of deconvoluted Ti 2p doublet peaks, with four doublets of each oxidation state reduced to one doublet of Ti^{4+} at 458.5 eV (2p 3/2), characteristic of sodium titanate [210]. In addition, Raman spectra (*Figure 6:7*) of both NaTC samples exhibited bands expected of sodium titanate, as detailed

by Viana *et al.* [515] and Zhang *et al.* [459], further supporting successful conversion. SEM cross-sections (*Figure 6:1D* & *Figure 6:2D*) detailed two distinct layers in the coating: Ti coating and the sodium titanate structure. The increase in the total thickness of the coating suggested that the titanate structure grows from the Ti base, while the Ti coating reduces in thickness (as outlined in depth in *Chapter 5*). Providing evidence for a mass transport process in which the Ti diffuses through the forming titanate layer enabling titanate growth (*Figure 6:11*), which is also exemplified in *Chapter 4*. The thickness of the titanate layer was not limited by Ti thickness (> 0.5 μm), and thus the thickness of the sputtered Ti coating could be reduced further. This would allow a reduction in the coating time, improving the efficiency, and reducing the residual stress of the coating, which is partially dependent on thickness [516]. The disadvantage of residual Ti in the coating is the possibility of long term complications of residual Ti post-degradation [517] as well as galvanic corrosion occurring between Mg and Ti metals [518]. *Figure 6:11* demonstrates the change in coating thickness upon titanate conversion. Optimisation of the coating would involve the reduction of x_2 to zero, while maximising y_1 thickness *via* minimisation of x_1.

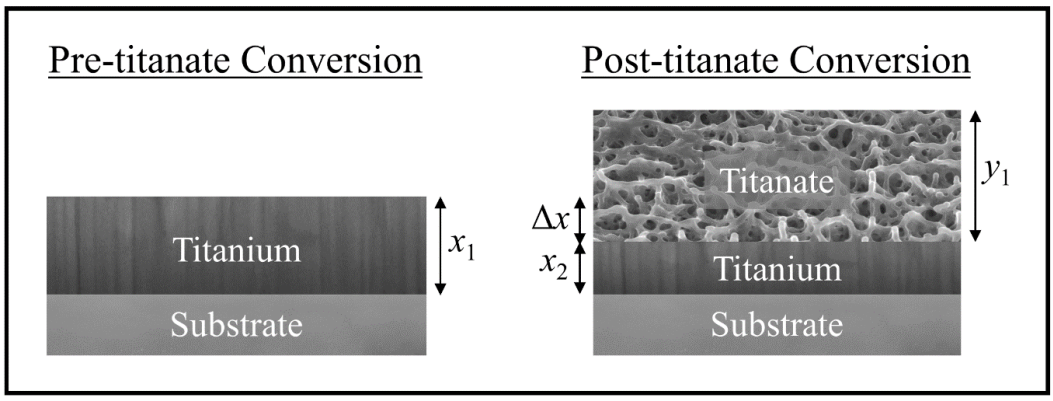

Figure 6:11. Schematic of the effect on coating thickness due to titanate conversion of the original titanium coating. x_1 is the original titanium coating thickness, x_2 is the post-titanate converted titanium thickness, Δx is the reduction in Ti thickness or penetration of the titanate layer, x_2 is the new Ti thickness, with y_1 being the thickness of the produced titanate layer

The presence of Ca in XPS and EDX elemental analysis (*Table 6:2*), detected in the NaTC samples, were due to Ca contamination of the NaOH used for hydrothermal conversion, which has been observed in sodium titanate synthesis [218]. Ca^{2+} bonds preferentially, due to increased electrostatic attraction, over Na^{+} within the titanate structure. Due to this attraction, Ca^{2+} does not release from the structure unless a subsequent hot water (80 ^{o}C) treatment is employed, therefore inhibiting subsequent apatite formation [218]. Despite this, the confirmation of a sodium titanate layer further highlighted the novel method for coating Mg substrates with an osteoconductive bioactive surface. It has been hypothesised that magnesium titanate may potentially form, due to the localised contact between the Ti and Mg surfaces in the presence of an alkaline aqueous environment: if Mg^{2+} ions were present in solution they would exchange with Na^{+} ions in the forming titanate due to preferential bonding of multivalent ions [519]. This however was not observed here, and suggested that the Mg substrate was passivated with an oxide/hydroxide layer in the presence of the high molarity NaOH (pH > 12), similar to the findings of Lips *et al.* [520], and Ismail *et al.* [521].

6.3.1.3 Calcium Ion exchange

EDX (*Table 6:2*) elemental compositions between NaTC and CaTC and XPS elemental analysis (*Table 6:4* & *Figure 6:5*) exemplified the replacement of Na^{+} content for Ca^{2+} in the CaTC samples, indicating successful conversion of sodium titante to calcium titante. XPS further supported this (*Table 6:4* & *Figure 6:5*) due to the loss of the Na 1s peak; the emergence of a clear Ca doublet; as well as distinct alteration in the realtive peak intensities of the O 1s deconvolutions due to a change in bonding from Ti—O—Na to Ti—O—Ca [210]. The inclusion of calcium within the titanate structure was intended to further inhibit Mg degradation, since literature

results have detailed the beneficial effect of Ca as an inclusion with Mg alloys [522], and as a surface coating (calcium orthophosphates, etc. [523]). Corrosion inhibition may occur through: the formation of Mg_2Ca intermediates, which is more efficient as an anode than α-Mg, since it will degrade preferentially, protecting the underlying Mg; or enhancing the formation of passivating oxides through solution treatments [524]. The SEM surface images (*Figure 6:1E* & *Figure 6:2E*) possessed the same nanoporous morphology as sodium titanate, whilst Raman analysis (*Figure 6:7*) demonstrated the same bands as the NaTC samples, indicative of the isomorphic ionic conversion from sodium to calcium titanate [57, 224].

The CaTC samples also exhibited precipitation on their surfaces (*Figure 6:1E* & *Figure 6:2E, Figure 6:3*), identified as being rich in Ca and O *via* EDX mapping (*Figure 6:3*) and XPS analysis (peak position 346.8 eV, from Yaseen *et al.* [525]), suggesting $Ca(OH)_2$ precipitation due to the low solubility of the $Ca(OH)_2$ solution used [525, 526]. This could potentially be resolved through further wash steps within the methodology, however, this may cause unecessary aqueous exposure to the Mg substrate. $CaCl_2$ has previously been used in calcium titanate synthesis [56], however, this was deliberately avoided in this study as the presence of Cl^- ions in solution accelerates Mg degradation [527]. $Ca(OH)_2$ has been used in dentistry to promote hard tissue growth in teeth from dissolution of Ca^{2+} and antimicrobial activity by increasing local pH [528]. Hence, the presence of this salt could be advantageous in the appropriate application [56, 517, 529].

6.3.2 Electrochemical Degradation Analysis

From the preliminary electrochemical degradation data presented, the NB/NH CaTC sample outperformed all other sample types tested. There was a marked increase of 0.16 V compared to the uncoated Mg sample, and an increase of 0.15 V on the Ti

coated sample alone. It was hypothesised by this thesis' author that the inclusion of calcium within the titanate structure may have enhanced the corrosion resistance [530, 531]. However, in both B/300 and NB/NH samples, this was clearly not the case with the corrosion potential, E_{corr}, which demonstrated no significant difference between the NaTC and CaTC samples. However, the E_{corr} results showed a clear trend for the NB/NH samples: Mg > NB/NH Ti > NB/NH NaTC > NB/NH CaTC.

On the NaTC samples (both NB/NH and B/300), there was a clear increase in the formation of calcium, phosphorous and oxygen rich regions during corrosion, likely from the DMEM solution used [506]. Titanates produced *via* aqueous chemical treatments have the ability to facilitate complex ion exchange reactions due to their ionic structure [226, 229, 532, 533], which over time, will form apatite both in SBF *in vitro* and extracellular fluid *in vivo*. This ability enables titanates to generate bone, enhancing the adhesion between the osseous-environment and the implant. Combining this property with a degradable material such as Mg, could enhance the bonding of the fracture fixation implant, enabling bone healing to occur at the interface of the fracture ends, whilst also facilitating a more controlled degradation of Mg. Ultimately, this endeavour may enable the mitigation of secondary surgery to remove fixation devices, which would benefit not only the patients' health, but also reduce the economic burden of such surgeries [299].

As described by Wei *et al.* [534], nanorods/nanowhiskers/nanoneedles; all names widely used in the literature for similar structures, can form from MgO and $Mg(OH)_2$, in addition to the more complex $Mg_2(OH)_3Cl{\cdot}4H_2O$. As noted in the NB/NH NaTC samples, there was clear formation of Mg, Cl, and O rich (*Figure 6:10*) nanoneedles on the samples' surface, potentially composed of $Mg_2(OH)_3Cl{\cdot}4H_2O$, although further

comprehensive analysis would be needed to confirm this due to the size of the structures present.

EDX mapping (*Figure 6:4*) of all titanate samples revealed cracking and partial delamination of the coatings to varying degrees. Delamination was due to the release of residual stresses within the Ti sputtered coatings upon conversion to titanate and poor interfacial strength between the coating and the Mg substrate, even with the use of magnetron sputtering, which is known for good film adhesion [330]. Comparison of relative delamination (*Table 6:3*) showed a higher degree of delamination present in the B/300 samples, attributed to the higher residual stresses present in those samples due to the B/300 sputtering parameters (seen previously in *Chapter 5*). The use of a bias voltage and higher temperature in the sputtering procedure results in higher energy bombardment of the surface by Ti ions, increasing the local temperature and the compressive stress of the coating upon cooling.

Both XPS (*Table 6:4*) and EDX (*Table 6:2*) elemental analyses showed the presence of Mg post conversion. As XPS is a surface analysis method, Mg content detected could have been solely due to delamination of the coating, exposing the substrate surface. The Mg content from EDX measurements was proportional to the degree of delamination, despite the increased penetration depth. The appearance of Mg bands in the Raman spectra for the NB/NH CaTC sample (*Figure 6:7*) suggested significant delamination of the coating as the Mg bands were not present in the other titanate sample spectra. Any degree of delamination is unfavourable for a coating intended to reduce the rate of degradation, as it not only exposes the substrate, but also could create crevices where pitting corrosion could occur.

6.3.3 Summary

In summary, the preliminary results demonstrated in this chapter have highlighted the successful application of titanate structures onto degradable Mg for the first time, as a potential corrosion inhibition surface. Although additional extensive studies are needed, as well as the need to address the interfacial bond strength issues outlined, these results should provide the building blocks to develop successful corrosion inhibition surfaces for fracture fixation applications. Furthermore, the ability to substitute cations into titanate-converted sputtered Ti films (demonstrated through the combination of the studies outlined in *Chapter 4 & Chapter 5*), achieved for the first time, further broadens the applicability of these structures, for a wide variety of medical and non-medical applications.

Chapter 7. Conclusions

7.1 Gallium Ion-Substitution for Potential Antibacterial Titanate Surfaces

Formation of gallium titanate surfaces through sequential hydrothermal NaOH, $Ga(NO_3)_3$ and subsequent heat treatments, was successful. Full characterisation of the produced gallium titanate surfaces was conducted, using FEG-SEM, RHEED, XRD, XPS, FTIR, EDX, Raman, and ICP methodologies. Significant morphological changes were demonstrated at high-resolution on titanium surfaces upon hydrothermal treatment in NaOH, ion exchange in $Ga(NO_3)_3$, and subsequent heat treatment. Furthermore, the antimicrobial and cytotoxic nature of the produced surfaces were assessed *via* Neutral red and LIVE/DEAD analyses. In addition to the Ga^{3+} ion's ability to substitute into the sodium titanate structure, the surface layer enables release of gallium ions into the surrounding environment. However, further testing against a wider range of relevant pathogens is required in order to demonstrate the concentrations of Ga^{3+} necessary for these surfaces to be clinically effective. It is also clear that the heat treatment conducted on the gallium titanate surface resulted in a more stable layer that released Ga ions at a slower rate: 2.76 compared to 0.68 ppm for S2: $Ga_2(TiO_3)_3$ and S3: $Ga_2(TiO_3)_3$-HT, respectively. Further to this, the incorporation of Ca/P ions on the surface was much lower on the heat treated surface (S3: $Ga_2(TiO_3)_3$-HT), generating a calcium deficient amorphous precipitate (Ca:P = 1.34), relative to crystalline HA as compared to the calcium rich (Ca:P = 1.71) precipitate deposited on the surface of S2: $Ga_2(TiO_3)_3$.

If additional assessments can indicate microbiological and further osteogenic efficacy, such surfaces may be suitable candidates as an orthopaedic alternative. The production design, which utilised low temperature Ga ion exchange reactions, will enable tailorable and cost effective antimicrobial surfaces that can potentially be used

to coat both surfaces and internal porosities of orthopaedic implants at commercial scales; a key design improvement.

7.2 Optimisation and Mechanistic Understanding of Titanate Formation

7.2.1 Optimisation and Conversion of DC Magnetron Sputtered Coatings

Presently, literature findings for biomedical titanates have been restricted to Ti-based substrate materials. Despite extensive innovation and success within this research avenue, the ability to translate titanate structures to alternative materials for biomedical applications has yet to be realised within the literature. The above results have demonstrated, for the first time, the translation of titanate structures onto alternative surfaces through a combinatorial DC magnetron sputtering and chemical conversion methodology, therefore, broadening the applicability of these surfaces for biomedical applications.

The findings demonstrated a converse trend to the original hypothesis, whereby more equiaxed films (NB/NH) produced the thickest titanate structures, due to the reduction in void area and void frequency/density negating oblique angle growth of the titanate structure, which was present in the columnar grown films. The combination of XRD and texture coefficient analysis demonstrated the successful production of graded films from columnar titanium, with preferred orientation in the (002) plane (NB/NH), to those more akin to equiaxed titanium (B/300). Furthermore, the titanate thicknesses produced ranged from 1.12 to 1.63 μm; thicker than those currently found within the literature. It was also found that the titanate structure did not fully convert the 4 μm Ti films, however, the total thickness of the films were greater than the initial Ti thickness, demonstrating outward titanate growth.

Both optical profilometry and AFM further confirmed the increased surface roughness values (S_a and R_a, respectively) from the non-titanate converted samples (*ca.* 23-40 and 26-33 nm, respectively) to the titanate converted samples (*ca.* 52-140

and 134-187 nm, respectively). Furthermore, there was a clear trend noted in the film adherence through both the pull-off tests, as well as the scratch adhesion tests. The NB/NH sample types exhibited the greatest film strength (*ca.* 42 MPa), with decreasing adherence noted for the higher T_c value films (B/300 had reduced to *ca.* 6 MPa). A similar trend was also noted for the titanate converted samples, with the titanate conversion itself resulting in a decrease in film adherence compared to the native sputtered film (e.g. the NB/NH and NB/NH_TC samples exhibited pull-off failure strengths of *ca.* 42 and 14 MPa, respectively). Scratch testing revealed similar trends for the film adhesion both pre- and post-titanate conversion. The NB/NH sample performed the best, with tensile cracking occurring at *ca.* 2.6 N compared to *ca.* 1.3 N for the B/300 sample. Spallation only occurred for the *in situ* heated samples at 2.9 and 1.6 N for the B/150 and B/300 samples, respectively. Following titanate conversion, all samples exhibited spallation prior to any tensile cracking or buckling, occurring between *ca.* 4.3 N for the NB/NH_TC sample to *ca.* 1.0 N for the B/300_TC sample.

7.2.2 Titanate Growth Mechanism Dependence on Ti Thickness

From the SEM observations, the Ti coatings exhibited good step coverage of the roughened substrates, with 50 – 500 nm coatings applied using a non-biased, non-internally heated sputtering run. Following titanate formation, only the 200 and 500 nm coatings produced the characteristic nanoporous ‘webbed’ titanate structures, whilst the 50 and 100 nm coatings generated nanocrystalline struts without the ‘webbing’. This was hypothesised to be due to the lack of free Ti in the coating, as opposed to the conventional diffusion limitation (Na and O) of the titanate mechanism.

Both XPS and XRD analyses confirmed the formation of titanate on all of the coatings tested, despite the morphological differences. Formation of broad, low

intensity nanocrystalline phases of titanate species were noted in the XRD at 24.2, 28.4 and 48.2° 2θ. From the XPS analysis, characteristic conversion from the four valence states of Ti (Ti^{4+}, Ti^{3+}, Ti^{2+}, Ti^{0}) in the Ti coatings, to just the Ti^{4+} state, characteristic of perovskite octahedral [TiO_6] complexes (O^{2-} at *ca.* 530 eV, and Ti 2p 3/2 at *ca.* 458.4 eV), as well as the formation of Na—O bonding (*ca.* 1071 eV) in the Na 1s core levels, indicated titanate structures had formed on all coatings, irrespective of thickness. Furthermore, the drop in Ti intensity in the XRD spectra, as well as previous findings on ΔTi thickness of titanate converted Ti films, illustrated the potential total, or partial, conversion of the Ti coating into titanate in the 50 nm coating.

7.2.3 Effect of Oxygen Content on Titanate Production

As evidenced from the data, successful formation of a titanate layer was produced on the Ti6Al4V microspheres, as previously hypothesised. Conversely, the formation of TiO_2 microspheres using anatase and rutile powder, resulted in no morphological nanoporous titanate growth, however, evidence of titanate formation *via* chemical analysis only in the XPS results, indicated minimal surface formation. Residual Na (< 1 at.%) *via* EDX was found on both of these samples, however, the low quantity evidenced the limitation of titanate formation due to O content in the substrate. The titanate formation mechanism was proposed to be a culmination of the material present and the ability for ions to diffuse through the structure. In the Ti6Al4V samples, there is an intrinsic passivated TiO_2 layer that forms (*ca.* 5 nm thick) due to atmospheric exposure. This is fundamental to the initial formation of the sodium titanate structures. Subsequent growth is driven through conversion of TiO_2 into titanate, whilst facilitating Na and O diffusion into the Ti structure to continue its growth. This mechanism is limited to the depth of Na diffusion (*ca.* 1 μm from the literature). For

the TiO_2 samples, Na and O are limited in their ability to diffuse into the material, since there is no free Ti available for conversion, therefore limiting the titanate growth only to the top surface.

7.3 Application of Titanate Surfaces on Mg for Corrosion Inhibition

Formation of nanoporous surface morphologies characteristic of titanate structures were achieved and determined *via* SEM (surface and cross-section) analysis. Despite the thickness of the Ti layer utilised in this study being thinner than the initial optimisation studies (*ca.* 500 nm *vs.* 4 μm), these surfaces demonstrated titanate structures of similar thicknesses (*ca.* 1.5 μm). This suggested that an equilibrium state has been achieved both through oxygen penetration and Ti depth (> 0.5 μm), to produce similar titanate thicknesses despite different Ti thickness.

Despite the preliminary data demonstrating the NB/NH CaTC sample provides corrosion protection for Mg substrates (E_{corr} = *ca.* -1.33 *vs.* -1.49 V; i_{corr} = *ca.* 0.06 *vs.* 0.31 $mA.cm^{-2}$, respectively), further work is necessary to address the issue of coating delamination, which was exhibited in the majority of samples tested, with the best performing sample type (NB/NH CaTC) exhibiting the lowest coating delamination. This can be achieved by either enhancing the interfacial strength of the coating with the Mg, or reducing the residual stress of the sputtered coatings.

Chapter 8. Future Work

In vitro cytocompatibility

The intended application of the produced titanate structures is for modifying orthopaedic implant material surfaces. However, broader applications may be sought due to the utilisation of alternative substrate materials. Therefore, *in vitro* assessments should be conducted to confirm the cytocompatibility of these structures for the appropriate application. For orthopaedic applications, culturing of MG63 (osteoblast-like cells) or Mesenchymal Stem Cells (MSCs; Pre-differentiated cells, which would be directed to specific cell lineages through material chemistry, mechanical stiffness, etc.) would be ideal for preliminary assessments. An initial cytotoxicity assessment of the converted sputtered films, through Neutral Red assays, should be conducted. Furthermore, early and late indicators of cellular proliferation and differentiation specific to osseous environments, such as Alkaline Phosphatase (ALP), Alamar Blue, and Osteocalcin will be useful for understanding cellular lineage stimulation for MSCs, or the efficacy for MG63 cells.

Further antibacterial assessment (gallium titanate)

During the gallium titanate investigations, I was fortunate enough to conduct a 2-week research placement at Aston University with Prof. Anthony C. Hilton, to understand how these surfaces interact with different bacterial types as an extension to the tests conducted in this thesis. It was discovered that the porous nature of the structures presented were not able to be fully characterised using the conventional Japanese film method (ISO 22196) conducted. However, there is no appropriate standard alternative within the literature to provide a comprehensive antibacterial assessment on roughened substrates. Although the results could not be used, it was discussed that future work should involve the development of a more universal

antibacterial assessment for both smooth and rough substrate surfaces. Co-culturing of bacterial and cellular testing may also be a possible line of enquiry.

Mechanical Properties of 3D structures

In this thesis, the mechanical investigation was solely conducted on 2D surfaces, using scratch testing (unidirectional) and pull off testing (tensile). However, implant surfaces and structures are required to survive 3D mechanical constraints, such as shear and torsional loads, meaning more comprehensive mechanical testing is required. To model the types of processes that occur *in vivo* post-implantation, tests such as nanoindentation and reciprocal wear tests would be useful to understand and model the forces induced, and how the coating behaviour changes during operation. Furthermore, more sophisticated testing, which simulates the *in vivo* environment during operation (appropriate aqueous surroundings, mechanical loads, temperature and pH variations, etc.), would be suitable once the initial mechanical assessment has been proved successful.

In-depth thickness investigations

One of the difficulties found in investigating the effect of thickness on the growth mechanism, was the ability to clearly characterise the cross-sectional growth and depth penetration *via* SEM/TEM; due to the delicate nature of the surfaces investigated, the characterisation techniques and substrate preparation methodologies used were sub-optimal. A separate investigation into appropriate techniques to characterise these structures, in extension to those already tested and failed, should be conducted. Furthermore, a more comprehensive understanding of the effect of depth changes when converting into titanate structures, as well as elucidating whether a certain optimal thickness can be achieved in order to fully convert the underlying Ti film, should be achieved.

Multilayers for optimal conversion

Following on from the concept of fully titanate-converted Ti films, additional investigations into the use of Ti/TiO_2 sputtered multilayers should be trialled in order to further confirm the mechanism of titanate formation. The hypothesis being that TiO_2 is essential for the initial formation and subsequent growth of the titanate structures, which interplays with the need for free Ti within the structure to further the conversion. By applying thin (*ca.* 10 nm) layers of Ti and TiO_2, one could theoretically achieve a fully titanate-converted coating. Furthermore, multilayers may provide a solution to the issue of delamination experienced, due to the ingress of NaOH underneath the Ti films during conversion, by increasing the substrate-coating adhesion.

Alternative implant materials

In extension to the fundamental work outlined in this thesis, alternative substrates such as polymeric medical materials should be investigated to further broaden the applicability of this process for a wide variety of material types. Due to the temperature measurements conducted in this thesis, further processing optimisation must be conducted in order to allow low T_g/T_m (<100 ^oC) polymeric materials to be utilised in this process. Furthermore, understanding of the adhesion of these films, and their subsequent conversion, must be investigated due to the thermal expansion coefficient discrepancies between the metallic films and polymeric substrates, to ascertain whether this combination is possible. If not, optimisation in order to enable this combination to be utilised must also be investigated, through appropriate surface modification, interlayers, etc., which will influence the adhesion properties.

References

[1] D.F. Williams, On the nature of biomaterials, Biomaterials 30(30) (2009) 5897-909.

[2] J. Black, Biological performance of materials: fundamentals of biocompatibility, CRC Press 2005.

[3] M. Navarro, A. Michiardi, O. Castano, J.A. Planell, Biomaterials in orthopaedics, Journal of the Royal Society Interface 5(27) (2008) 1137-58.

[4] O. Bostman, H. Pihlajamaki, Clinical biocompatibility of biodegradable orthopaedic implants for internal fixation: a review, Biomaterials 21(24) (2000) 2615-21.

[5] K.A. Egol, E.N. Kubiak, E. Fulkerson, F.J. Kummer, K.J. Koval, Biomechanics of locked plates and screws, Journal of Orthopaedic Trauma 18(8) (2004) 488-93.

[6] J. Charnley, Arthroplasty of the hip. A new operation, Lancet 1(7187) (1961) 1129-32.

[7] J. Jackson, Father of the modern hip replacement: Professor Sir John Charnley (1911–82), Journal of Medical Biography 19(4) (2011) 151-156.

[8] J. Charnley, The long-term results of low-friction arthroplasty of the hip performed as a primary intervention, Bone & Joint Journal 54(1) (1972) 61-76.

[9] NJR 16th Annual Report, National Joint Registry 2019.

[10] J.M. Aitken, Relevance of osteoporosis in women with fracture of the femoral neck, The BMJ 288(6417) (1984) 597-601.

[11] E.M. Curtis, R. van der Velde, R.J. Moon, J.P. van den Bergh, P. Geusens, F. de Vries, T.P. van Staa, C. Cooper, N.C. Harvey, Epidemiology of fractures in the United Kingdom 1988–2012: variation with age, sex, geography, ethnicity and socioeconomic status, Bone 87 (2016) 19-26.

[12] P.F. Gomez, J.A. Morcuende, Early attempts at hip arthroplasty: 1700s to 1950s, The Iowa Orthopaedic Journal 25 (2005) 25.

[13] S.R. Knight, R. Aujla, S.P. Biswas, Total hip arthroplasty-over 100 years of operative history, Orthopedic Reviews 3(2) (2011) 16.

[14] J. Charnley, Anchorage of the femoral head prosthesis to the shaft of the femur, The Journal of Bone and Joint Surgery 42-B(1) (1960) 28-30.

[15] J. Charnley, Low friction arthroplasty of the hip: theory and practice, Springer-Verlag 1979.

[16] L.A. Pruitt, A.M. Chakravartula, Mechanics of biomaterials: fundamental principles for implant design, Cambridge University Press 2011.

[17] S.H. Teoh, Fatigue of biomaterials: a review, International Journal of Fatigue 22(10) (2000) 825-837.

[18] M. Long, H. Rack, Titanium alloys in total joint replacement—a materials science perspective, Biomaterials 19(18) (1998) 1621-1639.

[19] A.L. Sabatini, T. Goswami, Hip implants VII: Finite element analysis and optimization of cross-sections, Materials & Design 29(7) (2008) 1438-1446.

[20] J. Alvarado, R. Maldonado, J. Marxuach, R. Otero, Biomechanics of hip and knee prostheses, Applications of Engineering Mechanics in Medicine, GED–University of Puerto Rico Mayaguez (2003) 1-20.

[21] M. Geetha, A. Singh, R. Asokamani, A. Gogia, Ti based biomaterials, the ultimate choice for orthopaedic implants–a review, Progress in Materials Science 54(3) (2009) 397-425.

[22] C. Oldani, A. Dominguez, Titanium as a biomaterial for implants, Recent Advances in Arthroplasty, InTechOpen 2012.

[23] H. Hermawan, D. Ramdan, J.R. Djuansjah, Metals for biomedical applications, Biomedical Engineering-From Theory to Applications, InTechOpen 2011.

[24] M.P. Staiger, A.M. Pietak, J. Huadmai, G. Dias, Magnesium and its alloys as orthopedic biomaterials: a review, Biomaterials 27(9) (2006) 1728-34.

[25] M.B. Nasab, M.R. Hassan, B.B. Sahari, Metallic biomaterials of knee and hip-A review, Trends in Biomaterials and Artificial Organs 24(1) (2010) 69-82.

[26] J.Y. Rho, L. Kuhn-Spearing, P. Zioupos, Mechanical properties and the hierarchical structure of bone, Medical Engineering & Physics 20(2) (1998) 92-102.

[27] F.G. Evans, Mechanical properties and histology of cortical bone from younger and older men, The Anatomical Record 185(1) (1976) 1-11.

[28] T.M. Keaveny, W.C. Hayes, A 20-year perspective on the mechanical properties of trabecular bone, Journal of Biomechanical Engineering 115(4B) (1993) 534-42.

[29] A. Wall, T. Board, The compressive behavior of bone as a two-phase porous structure, Journal of Bone and Joint Surgery 59(7) (1977) 954-962.

[30] C.H. Turner, Yield behavior of bovine cancellous bone, Journal of Biomechanical Engineering 111(3) (1989) 256-60.

[31] C.H. Turner, D.B. Burr, Basic biomechanical measurements of bone: a tutorial, Bone 14(4) (1993) 595-608.

[32] S. Morshed, K.J. Bozic, M.D. Ries, H. Malchau, J.M. Colford, Jr., Comparison of cemented and uncemented fixation in total hip replacement: a meta-analysis, Acta Orthopaedica 78(3) (2007) 315-26.

[33] I.S. Hage, R.F. Hamade, Structural micro processing of Haversian systems of a cortical bovine femur using optical stereomicroscope and MATLAB, ASME 2012 international mechanical engineering congress and exposition, American Society of Mechanical Engineers, 2012, pp. 595-601.

[34] M. Sundfeldt, L. V Carlsson, C. B Johansson, P. Thomsen, C. Gretzer, Aseptic loosening, not only a question of wear: a review of different theories, Acta Orthopaedica 77(2) (2006) 177-197.

[35] Y. Abu-Amer, I. Darwech, J.C. Clohisy, Aseptic loosening of total joint replacements: mechanisms underlying osteolysis and potential therapies, Arthritis Research & Therapy 9 Suppl 1(1) (2007) S6.

[36] B. Miletic, O. May, N. Krantz, J. Girard, G. Pasquier, H. Migaud, De-escalation exchange of loosened locked revision stems to a primary stem design: complications, stem fixation and bone reconstruction in 15 cases, Orthopaedics & Traumatology: Surgery & Research 98(2) (2012) 138-43.

[37] T. Albrektsson, P.-I. Brånemark, H.-A. Hansson, J. Lindström, Osseointegrated titanium implants: requirements for ensuring a long-lasting, direct bone-to-implant anchorage in man, Acta Orthopaedica Scandinavica 52(2) (1981) 155-170.

[38] R.M. Pilliar, Cementless implant fixation—toward improved reliability, Orthopedic Clinics of North America 36(1) (2005) 113-119.

[39] Y.C. Tsui, C. Doyle, T.W. Clyne, Plasma sprayed hydroxyapatite coatings on titanium substrates. Part 2: optimisation of coating properties, Biomaterials 19(22) (1998) 2031-43.

[40] A.A. Campbell, Bioceramics for implant coatings, Materials Today 6(11) (2003) 26-30.

[41] T.P.S. Sarao, H. Singh, H. Singh, R. Chhibbe, Thermal sprayed bioceramics coatings for metallic implants, Biomaterials Science: Processing, Properties, and Applications, The American Chemical Society 2011, p. 159.

[42] S. Bose, A.A. Vu, K. Emshadi, A. Bandyopadhyay, Effects of polycaprolactone on alendronate drug release from Mg-doped hydroxyapatite coating on titanium, Materials Science and Engineering C: Materials for Biological Applications 88 (2018) 166-171.

[43] E. Mohseni, E. Zalnezhad, A.R. Bushroa, Comparative investigation on the adhesion of hydroxyapatite coating on Ti–6Al–4V implant: A review paper, International Journal of Adhesion and Adhesives 48 (2014) 238-257.

[44] H. Zhou, F. Li, B. He, J. Wang, B. Sun, Effect of plasma spraying process on microstructure and microhardness of titanium alloy substrate, Journal of Thermal Spray Technology 17(2) (2008) 284-288.

[45] X.Y. Liu, P.K. Chu, C.X. Ding, Surface modification of titanium, titanium alloys, and related materials for biomedical applications, Mat Sci Eng R 47(3-4) (2004) 49-121.

[46] E. Tufekci, W.A. Brantley, J.C. Mitchell, D.W. Foreman, F.S. Georgette, Crystallographic characteristics of plasma-sprayed calcium phosphate coatings on Ti-6Al-4V, The International Journal of Oral & Maxillofacial Implants 14(5) (1999) 661-72.

[47] P.E. Purdue, P. Koulouvaris, B.J. Nestor, T.P. Sculco, The central role of wear debris in periprosthetic osteolysis, The Musculoskeletal Journal of Hospital for Special Surgery 2(2) (2006) 102-13.

[48] A. Aderem, D.M. Underhill, Mechanisms of phagocytosis in macrophages, Annual Review of Immunology 17(1) (1999) 593-623.

[49] F. Geissmann, M.G. Manz, S. Jung, M.H. Sieweke, M. Merad, K. Ley, Development of monocytes, macrophages, and dendritic cells, Science 327(5966) (2010) 656-61.

[50] H. Takadama, H.M. Kim, T. Kokubo, T. Nakamura, TEM-EDX study of mechanism of bonelike apatite formation on bioactive titanium metal in simulated body fluid, Journal of Biomedical Materials Research 57(3) (2001) 441-8.

[51] A. Chilvery, S. Das, P. Guggilla, C. Brantley, A. Sunda-Meya, A perspective on the recent progress in solution-processed methods for highly efficient perovskite solar cells, Science and Technology of Advanced Materials 17(1) (2016) 650-658.

[52] T. Kokubo, H.M. Kim, M. Kawashita, Novel bioactive materials with different mechanical properties, Biomaterials 24(13) (2003) 2161-75.

[53] T. Kokubo, T. Matsushita, H. Takadama, Titania-based bioactive materials, Journal of the European Ceramic Society 27(2-3) (2007) 1553-1553.

[54] T. Kokubo, Design of bioactive bone substitutes based on biomineralization process, Materials Science & Engineering C-Biomimetic and Supramolecular Systems 25(2) (2005) 97-104.

[55] T. Kokubo, S. Yamaguchi, Bioactive titanate layers formed on titanium and its alloys by simple chemical and heat treatments, The Open Biomedical Engineering Journal 9(1) (2015) 29-41.

[56] T. Kizuki, H. Takadama, T. Matsushita, T. Nakamura, T. Kokubo, Preparation of bioactive Ti metal surface enriched with calcium ions by chemical treatment, Acta Biomaterialia 6(7) (2010) 2836-42.

[57] T. Kizuki, T. Matsushita, T. Kokubo, Antibacterial and bioactive calcium titanate layers formed on Ti metal and its alloys, Journal of Materials Science: Materials in Medicine 25(7) (2014) 1737-46.

[58] S. Yamaguchi, T. Matsushita, T. Kokubo, A bioactive Ti metal with a Ca-enriched surface layer releases Mg ions, RSC Advances 3(28) (2013) 11274-11282.

[59] S. Yamaguchi, S. Nath, T. Matsushita, T. Kokubo, Controlled release of strontium ions from a bioactive Ti metal with a Ca-enriched surface layer, Acta Biomaterialia 10(5) (2014) 2282-9.

[60] L.L. Hench, J. Wilson, Surface-active biomaterials, Science 226(4675) (1984) 630-6.

[61] Y.T. Lee, G. Welsch, Young's modulus and damping of Ti6Al4V alloy as a function of heat treatment and oxygen concentration, Materials Science and Engineering: A 128(1) (1990) 77-89.

[62] S.S. da Rocha, G.L. Adabo, G.E. Henriques, M.A. Nobilo, Vickers hardness of cast commercially pure titanium and Ti6Al4V alloy submitted to heat treatments, Brazilian Dental Journal 17(2) (2006) 126-9.

[63] N. Poondla, T.S. Srivatsan, A. Patnaik, M. Petraroli, A study of the microstructure and hardness of two titanium alloys: Commercially pure and Ti6Al4V, Journal of Alloys and Compounds 486(1-2) (2009) 162-167.

[64] S. Kundu, S. Chatterjee, Interfacial microstructure and mechanical properties of diffusion-bonded titanium–stainless steel joints using a nickel interlayer, Materials Science and Engineering: A 425(1-2) (2006) 107-113.

[65] Y. Li, C. Yang, H. Zhao, S. Qu, X. Li, Y. Li, New developments of Ti-based alloys for biomedical applications, Materials 7(3) (2014) 1709-1800.

[66] A.T. Berman, J.S. Reid, D.R. Yanicko, Jr., G.C. Sih, M.R. Zimmerman, Thermally induced bone necrosis in rabbits. Relation to implant failure in humans, Clinical Orthopaedics and Related Research (186) (1984) 284-92.

[67] L.L. Hench, The story of Bioglass®, Journal of Materials Science: Materials in Medicine 17(11) (2006) 967-978.

[68] A. Tilocca, Models of structure, dynamics and reactivity of bioglasses: a review, Journal of Materials Chemistry 20(33) (2010) 6848-6858.

[69] L.L. Hench, J.M. Polak, Third-generation biomedical materials, Science 295(5557) (2002) 1014-7.

[70] R.H. Richards, J.D. Palmer, N.M. Clarke, Observations on removal of metal implants, Injury 23(1) (1992) 25-8.

[71] O. Bostman, H. Pihlajamaki, Routine implant removal after fracture surgery: a potentially reducible consumer of hospital resources in trauma units, Journal of Trauma and Acute Care Surgery 41(5) (1996) 846-9.

[72] F. Witte, V. Kaese, H. Haferkamp, E. Switzer, A. Meyer-Lindenberg, C.J. Wirth, H. Windhagen, In vivo corrosion of four magnesium alloys and the associated bone response, Biomaterials 26(17) (2005) 3557-63.

[73] C.E. Wen, M. Mabuchi, Y. Yamada, K. Shimojima, Y. Chino, T. Asahina, Processing of biocompatible porous Ti and Mg, Scripta Materialia 45(10) (2001) 1147-1153.

[74] R. Newnham, R. Wolfe, J. Dorrian, Structural basis of ferroelectricity in the bismuth titanate family, Materials Research Bulletin 6(10) (1971) 1029-1039.

[75] M. Itoh, R. Wang, Y. Inaguma, T. Yamaguchi, Y.J. Shan, T. Nakamura, Ferroelectricity induced by oxygen isotope exchange in strontium titanate perovskite, Physical Review Letters 82(17) (1999) 3540-3543.

[76] N. Barman, P. Singh, C. Narayana, K.B.R. Varma, Incipient ferroelectric to a possible ferroelectric transition in Te^{4+} doped calcium copper titanate ($CaCu_3Ti_4O_{12}$) ceramics at low temperature as evidenced by Raman and dielectric spectroscopy, AIP Advances 7(3) (2017) 035105.

[77] H.M. Kim, F. Miyaji, T. Kokubo, T. Nakamura, Preparation of bioactive Ti and its alloys via simple chemical surface treatment, Journal of Biomedical Materials Research 32(3) (1996) 409-17.

[78] H.M. Kim, F. Miyaji, T. Kokubo, T. Nakamura, Effect of heat treatment on apatite-forming ability of Ti metal induced by alkali treatment, Journal of Materials Science: Materials in Medicine 8(6) (1997) 341-7.

[79] Y.V. Kolen'ko, K.A. Kovnir, A.I. Gavrilov, A.V. Garshev, J. Frantti, O.I. Lebedev, B.R. Churagulov, G. Van Tendeloo, M. Yoshimura, Hydrothermal synthesis and characterization of nanorods of various titanates and titanium dioxide, The Journal of Physical Chemistry B 110(9) (2006) 4030-8.

[80] C.C. Tsai, H.S. Teng, Structural features of nanotubes synthesized from NaOH treatment on TiO2 with different post-treatments, Chemistry of Materials 18(2) (2006) 367-373.

[81] D. Arcos, A.R. Boccaccini, M. Bohner, A. Diez-Perez, M. Epple, E. Gomez-Barrena, A. Herrera, J.A. Planell, L. Rodriguez-Manas, M. Vallet-Regi, The relevance of biomaterials to the prevention and treatment of osteoporosis, Acta Biomaterialia 10(5) (2014) 1793-805.

[82] T. Kokubo, H.-M. Kim, M. Kawashita, T. Nakamura, REVIEW Bioactive metals: preparation and properties, Journal of Materials Science: Materials in Medicine 15(2) (2004) 99-107.

[83] S. Yamaguchi, S. Nath, Y. Sugawara, K. Divakarla, T. Das, J. Manos, W. Chrzanowski, T. Matsushita, T. Kokubo, Two-in-one biointerfaces—antimicrobial and bioactive nanoporous gallium titanate layers for titanium implants, Nanomaterials 7(8) (2017) 229.

[84] M. Niinomi, Metallic biomaterials, Journal of Artificial Organs 11(3) (2008) 105-10.

[85] R.R. Boyer, An overview on the use of titanium in the aerospace industry, Materials Science and Engineering: A 213(1-2) (1996) 103-114.

[86] A.K. Sachdev, K. Kulkarni, Z.Z. Fang, R. Yang, V. Girshov, Titanium for automotive applications: Challenges and opportunities in materials and processing, Jom-Us 64(5) (2012) 553-565.

[87] C.P. Bergmann, A. Stumpf, Biomaterials, Dental Ceramics, Springer 2013.

[88] D.M. Brunette, P. Tengvall, M. Textor, P. Thomsen, Titanium in medicine: material science, surface science, engineering, biological responses and medical applications, Springer 2012.

[89] C.N. Elias, J.H.C. Lima, R. Valiev, M.A. Meyers, Biomedical applications of titanium and its alloys, Jom-Us 60(3) (2008) 46-49.

[90] M. Niinomi, M. Nakai, Titanium-based biomaterials for preventing stress shielding between implant devices and bone, International Journal of Biomaterials 2011 (2011).

[91] J. Wolff, Das gesetz der transformation der knochen, A Hirshwald 1 (1892) 1-152.

[92] T. Lee, D. Taylor, Bone remodelling: should we cry Wolff?, Irish Journal of Medical Science 168(2) (1999) 102.

[93] W. Roux, Beitrage zur Morphologie der funktionellen Anpassung, Arch. Anat. Physiol. Anat. Abt. (1885) 120-185.

[94] T. Kusano, T. Seki, Y. Higuchi, Y. Takegami, Y. Osawa, N. Ishiguro, Preoperative canal bone ratio is related to high-degree stress shielding: A minimum 5-year follow-up study of a proximally HA-coated straight tapered titanium femoral component, The Journal of Arthroplasty 33(6) (2017) 1764-1769.

[95] V.P. Mantripragada, B. Lecka-Czernik, N.A. Ebraheim, A.C. Jayasuriya, An overview of recent advances in designing orthopedic and craniofacial implants, Journal of Biomedical Materials Research Part A 101(11) (2013) 3349-64.

[96] J. Heinrichs, T. Jarmar, M. Rooth, H. Engqvist, In vitro bioactivity of atomic layer deposited titanium dioxide on titanium and silicon substrates, Key Engineering Materials, Trans Tech Publications 2008, pp. 689-692.

[97] M. Jager, H.P. Jennissen, F. Dittrich, A. Fischer, H.L. Kohling, Antimicrobial and osseointegration properties of nanostructured titanium orthopaedic implants, Materials 10(11) (2017) 1302.

[98] K. de Groot, R. Geesink, C.P. Klein, P. Serekian, Plasma sprayed coatings of hydroxylapatite, Journal of Biomedical Materials Research 21(12) (1987) 1375-81.

[99] T.D. Driskell, Early history of calcium phosphate materials and coatings, Characterization and Performance of Calcium Phosphate Coatings for Implants, ASTM International 1994.

[100] L.C. Junqueira, J. Carneiro, R.O. Kelley, Basic histology: text & atlas, McGraw-Hill Education 2003.

[101] L. Getter, S.N. Bhaskar, D.E. Cutright, B. Perez, J.M. Brady, T.D. Driskell, M.J. O'Hara, Three biodegradable calcium phosphate slurry implants in bone, Journal of Oral Surgery 30(4) (1972) 263-8.

[102] K. Søballe, H. Brockstedt-Rasmussen, E.S. Hansen, C. Bünger, Hydroxyapatite coating modifies implant membrane formation: controlled micromotion studied in dogs, Acta Orthopaedica Scandinavica 63(2) (1992) 128-140.

[103] K. Søballe, E.S. Hansen, H. B-Rasmussen, P.H. Jørgensen, C. Bünger, Tissue ingrowth into titanium and hydroxyapatite-coated implants during stable and unstable mechanical conditions, Journal of Orthopaedic Research 10(2) (1992) 285-299.

[104] K. Soballe, E.S. Hansen, H. Brockstedt-Rasmussen, C. Bunger, Hydroxyapatite coating converts fibrous tissue to bone around loaded implants, The Journal of Bone and Joint Surgery 75(2) (1993) 270-8.

[105] M.A. Listgarten, Structure of surface coatings on teeth. A review, Journal of Periodontology 47(3) (1976) 139-47.

[106] J.-A. Epinette, M.T. Manley, Fifteen years of clinical experience with hydroxyapatite coatings in joint arthroplasty, Springer 2013.

[107] R.G. Geesink, Osteoconductive coatings for total joint arthroplasty, Clinical Orthopaedics and Related Research 395(395) (2002) 53-65.

[108] L.I. Havelin, L.B. Engesaeter, B. Espehaug, O. Furnes, S.A. Lie, S.E. Vollset, The Norwegian Arthroplasty Register: 11 years and 73,000 arthroplasties, Acta Orthopaedica Scandinavica 71(4) (2000) 337-53.

[109] J.A. D'antonio, W.N. Capello, M.T. Manley, R.G. Geesink, W.L. Jaffe, Hydroxyapatite femoral stems for total hip arthroplasty: 10–14 year follow-up, Fifteen Years of Clinical Experience with Hydroxyapatite Coatings in Joint Arthroplasty, Springer 2004, pp. 235-241.

[110] B. Ellison, N.A. Cheney, K.R. Berend, A.V. Lombardi, Jr., T.H. Mallory, Minimal stress shielding with a Mallory-Head titanium femoral stem with proximal porous coating in total hip arthroplasty, Journal of Orthopaedic Surgery and Research 4(1) (2009) 42.

[111] T.J. Callahan, J. Gantenberg, B.E. Sands, Calcium phosphate (Ca-P) coating draft guidance for preparation of Food and Drug Administration (FDA) submissions for orthopedic and dental endosseous implants, Characterization and performance of calcium phosphate coatings for implants, ASTM International 1994.

[112] G. Bolelli, I. Hulka, H. Koivuluoto, L. Lusvarghi, A. Milanti, K. Niemi, P. Vuoristo, Properties of WC-FeCrAl coatings manufactured by different high velocity thermal spray processes, Surf Coat Tech 247 (2014) 74-89.

[113] H. Herman, Plasma spray deposition processes, MRS Bulletin 13(12) (1988) 60-67.

[114] J.L. Ong, D.L. Carnes, K. Bessho, Evaluation of titanium plasma-sprayed and plasma-sprayed hydroxyapatite implants in vivo, Biomaterials 25(19) (2004) 4601-6.

[115] L.M. Sun, C.C. Berndt, C.P. Grey, Phase, structural and microstructural investigations of plasma sprayed hydroxyapatite coatings, Materials Science and Engineering: A 360(1-2) (2003) 70-84.

[116] S. Takeuchi, M. Ito, K. Takeda, Modeling of residual stress in plasma-sprayed coatings: Effect of substrate temperature, Surface and Coatings Technology 43-44(1) (1990) 426-435.

[117] X. Zheng, M. Huang, C. Ding, Bond strength of plasma-sprayed hydroxyapatite/Ti composite coatings, Biomaterials 21(8) (2000) 841-9.

[118] Y. Yang, K.-H. Kim, J.L. Ong, A review on calcium phosphate coatings produced using a sputtering process—an alternative to plasma spraying, Biomaterials 26(3) (2005) 327-337.

[119] S. Castiglioni, A. Cazzaniga, W. Albisetti, J.A. Maier, Magnesium and osteoporosis: current state of knowledge and future research directions, Nutrients 5(8) (2013) 3022-33.

[120] A. Flynn, The role of dietary calcium in bone health, Proceedings of the Nutrition Society 62(4) (2003) 851-8.

[121] P.J. Marie, M. Hott, D. Modrowski, C. De Pollak, J. Guillemain, P. Deloffre, Y. Tsouderos, An uncoupling agent containing strontium prevents bone loss by depressing bone resorption and maintaining bone formation in estrogen-deficient rats, Journal of Bone and Mineral Research 8(5) (1993) 607-15.

[122] P. Marie, M.-T. Garba, M. Hott, L. Miravet, Effect of stable strontium on bone metabolism in rats, Metals in Bone, Springer 1985, pp. 117-125.

[123] P.J. Marie, M. Hott, Short-term effects of fluoride and strontium on bone formation and resorption in the mouse, Metabolism 35(6) (1986) 547-51.

[124] E. Canalis, M. Hott, P. Deloffre, Y. Tsouderos, P.J. Marie, The divalent strontium salt S12911 enhances bone cell replication and bone formation in vitro, Bone 18(6) (1996) 517-23.

[125] S. Celotto, J. Pattison, J. Ho, A. Johnson, W. O'Neill, The economics of the cold spray process, The Cold Spray Materials Deposition Process, Elsevier 2007, pp. 72-101.

[126] N.R. White, Ion sources for use in ion-implantation, Nuclear Instruments and Methods in Physics Research Section B: Beam Interactions with Materials and Atoms 37-38 (1989) 78-86.

[127] H. Ryssel, I. Ruge, Ion implantation, Wiley-Blackwell 1986.

[128] J.F. Ziegler, Ion implantation science and technology, Elsevier 2012.

[129] G. Manivasagam, U.K. Mudali, R. Asokamani, B. Raj, Corrosion and microstructural aspects of titanium and its alloys as orthopaedic devices, De Gruyter, 2003.

[130] D.A. Armitage, R. Mihoc, T.J. Tate, D.S. McPhail, R. Chater, J.A. Hobkirk, L. Shinawi, F.H. Jones, The oxidation of calcium implanted titanium in water: A depth profiling study, Applied Surface Science 253(8) (2007) 4085-4093.

[131] R.A. Buchanan, E.D. Rigney, Jr., J.M. Williams, Wear-accelerated corrosion of Ti-6Al-4V and nitrogen-ion-implanted Ti-6Al-4V: mechanisms and influence of fixed-stress magnitude, Journal of Biomedical Materials Research 21(3) (1987) 367-77.

[132] T. Sundararajan, U.K. Mudali, K.G.M. Nair, S. Rajeswari, M. Subbaiyan, Electrochemical studies on nitrogen ion implanted Ti6Al4V alloy, Anti-Corrosion Methods and Materials 45(3) (1998) 162.

[133] K. Hohmuth, B. Rauschenbach, High fluence implantation of nitrogen ions into titanium, Materials Science and Engineering 69(2) (1985) 489-499.

[134] E. Leitao, C. Sa, R. Silva, M. Barbosa, H. Ali, Electrochemical and surface modifications on N+-ion implanted Ti-6A1-4V immersed in HBSS, Corrosion Science 37(11) (1995) 1861-1866.

[135] E. Leitao, R. Silva, M. Barbosa, Electrochemical and surface modifications on N+-ion implanted Ti-5Al-2.5 Fe immersed in HBSS, Corrosion Science 39(2) (1997) 377-383.

[136] T. Sundararajan, S. Rajeswari, M. Subbaiyan, U.K. Mudali, K. Nair, Effect of nitrogen ion implantation on the localized corrosion behavior of titanium modified type 316L stainless steel in simulated body fluid, Journal of Materials Engineering and Performance 8(2) (1999) 252-260.

[137] S.N. Nayab, F.H. Jones, I. Olsen, Effects of calcium ion-implantation of titanium on bone cell function in vitro, Journal of Biomedical Materials Research Part A 83(2) (2007) 296-302.

[138] D. Krupa, J. Baszkiewicz, J.A. Kozubowski, A. Barcz, J.W. Sobczak, A. Biliniski, M.D. Lewandowska-Szumiel, B. Rajchel, Effect of calcium-ion implantation on the corrosion resistance and biocompatibility of titanium, Biomaterials 22(15) (2001) 2139-51.

[139] S. Nayab, L. Shinawi, J. Hobkirk, T.J. Tate, I. Olsen, F.H. Jones, Adhesion of bone cells to ion-implanted titanium, Journal of Materials Science: Materials in Medicine 14(11) (2003) 991-7.

[140] S.N. Nayab, F.H. Jones, I. Olsen, Human alveolar bone cell adhesion and growth on ion-implanted titanium, Journal of Biomedical Materials Research Part A 69(4) (2004) 651-7.

[141] S.N. Nayab, F.H. Jones, I. Olsen, Effects of calcium ion implantation on human bone cell interaction with titanium, Biomaterials 26(23) (2005) 4717-27.

[142] T.R. Rautray, R. Narayanan, T.Y. Kwon, K.H. Kim, Surface modification of titanium and titanium alloys by ion implantation, Journal of Biomedical Materials Research Part B: Applied Biomaterials 93(2) (2010) 581-91.

[143] Y.T. Sul, The significance of the surface properties of oxidized titanium to the bone response: special emphasis on potential biochemical bonding of oxidized titanium implant, Biomaterials 24(22) (2003) 3893-907.

[144] M. Diefenbeck, T. Muckley, C. Schrader, J. Schmidt, S. Zankovych, J. Bossert, K.D. Jandt, M. Faucon, U. Finger, The effect of plasma chemical oxidation of titanium alloy on bone-implant contact in rats, Biomaterials 32(32) (2011) 8041-7.

[145] L.M. Bjursten, L. Rasmusson, S. Oh, G.C. Smith, K.S. Brammer, S. Jin, Titanium dioxide nanotubes enhance bone bonding in vivo, Journal of Biomedical Materials Research Part A 92(3) (2010) 1218-24.

[146] S. Minagar, J. Wang, C.C. Berndt, E.P. Ivanova, C. Wen, Cell response of anodized nanotubes on titanium and titanium alloys, Journal of Biomedical Materials Research Part A 101(9) (2013) 2726-39.

[147] Y. Shibata, D. Suzuki, S. Omori, R. Tanaka, A. Murakami, Y. Kataoka, K. Baba, R. Kamijo, T. Miyazaki, The characteristics of in vitro biological activity of titanium surfaces anodically oxidized in chloride solutions, Biomaterials 31(33) (2010) 8546-55.

[148] L. Xie, X. Liao, G. Yin, Z. Huang, D. Yan, Y. Yao, W. Liu, X. Chen, J. Gu, Preparation, characterization, in vitro bioactivity, and osteoblast adhesion of multi-level porous titania layer on titanium by two-step anodization treatment, Journal of Biomedical Materials Research Part A 98(2) (2011) 312-20.

[149] L. Zhao, S. Mei, P.K. Chu, Y. Zhang, Z. Wu, The influence of hierarchical hybrid micro/nano-textured titanium surface with titania nanotubes on osteoblast functions, Biomaterials 31(19) (2010) 5072-82.

[150] R. Zhou, D. Wei, H. Yang, S. Cheng, W. Feng, B. Li, Y. Wang, D. Jia, Y. Zhou, Osseointegration of bioactive microarc oxidized amorphous phase/TiO2 nanocrystals composited coatings on titanium after implantation into rabbit tibia, Journal of Materials Science: Materials in Medicine 25(5) (2014) 1307-1318.

[151] P. Li, C. Ohtsuki, T. Kokubo, K. Nakanishi, N. Soga, K. de Groot, The role of hydrated silica, titania, and alumina in inducing apatite on implants, Journal of Biomedical Materials Research Part A 28(1) (1994) 7-15.

[152] ISO 23317:2014 Implants for surgery - In vitro evaluation for apatite-forming ability of implant materials, ISO 2014, pp. 1-13.

[153] X. Lu, Y. Leng, Theoretical analysis of calcium phosphate precipitation in simulated body fluid, Biomaterials 26(10) (2005) 1097-108.

[154] S.A. Raina, B. Van Eerdenbrugh, D.E. Alonzo, H. Mo, G.G.Z. Zhang, Y. Gao, L.S. Taylor, Trends in the precipitation and crystallization behavior of supersaturated aqueous solutions of poorly water-soluble drugs assessed using synchrotron radiation, Journal of Pharmaceutical Sciences 104(6) (2015) 1981-1992.

[155] M. Bohner, J. Lemaitre, Can bioactivity be tested in vitro with SBF solution?, Biomaterials 30(12) (2009) 2175-2179.

[156] S. Kotani, Y. Fujita, T. Kitsugi, T. Nakamura, T. Yamamuro, C. Ohtsuki, T. Kokubo, Bone bonding mechanism of beta-tricalcium phosphate, Journal of Biomedical Materials Research Part A 25(10) (1991) 1303-15.

[157] T. Kokubo, H. Takadama, How useful is SBF in predicting in vivo bone bioactivity?, Biomaterials 27(15) (2006) 2907-2915.

[158] J.L. Gamble, Chemical anatomy, physiology, and pathology of extracellular fluid, Harvard University Press 1952.

[159] X.X. Wang, S. Hayakawa, K. Tsuru, A. Osaka, Bioactive titania-gel layers formed by chemical treatment of Ti substrate with a H2O2/HCl solution, Biomaterials 23(5) (2002) 1353-7.

[160] T. Peltola, M. Patsi, H. Rahiala, I. Kangasniemi, A. Yli-Urpo, Calcium phosphate induction by sol-gel-derived titania coatings on titanium substrates in vitro, Journal of Biomedical Materials Research Part A 41(3) (1998) 504-10.

[161] M. Jokinen, M. Patsi, H. Rahiala, T. Peltola, M. Ritala, J.B. Rosenholm, Influence of sol and surface properties on in vitro bioactivity of sol-gel-derived TiO2 and TiO2-SiO2 films deposited by dip-coating method, Journal of Biomedical Materials Research Part A 42(2) (1998) 295-302.

[162] J.M. Wu, S. Hayakawa, K. Tsuru, A. Osaka, Low-temperature preparation of anatase and rutile layers on titanium substrates and their ability to induce in vitro apatite deposition, Journal of the American Ceramic Society 87(9) (2004) 1635-1642.

[163] M. Uchida, H.M. Kim, T. Kokubo, S. Fujibayashi, T. Nakamura, Structural dependence of apatite formation on titania gels in a simulated body fluid, Journal of Biomedical Materials Research Part A 64(1) (2003) 164-70.

[164] X. Zhao, X. Liu, C. Ding, Acid-induced bioactive titania surface, Journal of Biomedical Materials Research Part A 75(4) (2005) 888-94.

[165] C.Y. Jimmy, J. Yu, J. Zhao, Enhanced photocatalytic activity of mesoporous and ordinary TiO2 thin films by sulfuric acid treatment, Applied Catalysis B: Environmental 36(1) (2002) 31-43.

[166] K. Takeuchi, L. Saruwatari, H.K. Nakamura, J.M. Yang, T. Ogawa, Enhanced intrinsic biomechanical properties of osteoblastic mineralized tissue on roughened titanium surface, Journal of Biomedical Materials Research Part A 72(3) (2005) 296-305.

[167] M.-H. Lee, I.-S. Park, K.-S. Min, S.-G. Ahn, J.-M. Park, K.-Y. Song, C.-W. Park, Evaluation of in vitro and in vivo tests for Surface-modified Titanium by H2SO4 and H2O2 Treatment, Metals and Materials International 13(2) (2007) 109.

[168] L.L. Hench, Ö. Andersson, Bioactive glasses, An Introduction to Bioceramics, World Scientific 1993, pp. 41-62.

[169] M.H. Lee, Biocompatibility of a modified metallic surface of pure Ti and Ti-6Al-4V alloy with the connective tissue of mouse, Met Mater-Korea 6(4) (2000) 373-379.

[170] M.-H. Lee, D.-J. Yoon, D.-H. Won, T.-S. Bae, F. Watari, Biocompatibility of surface treated pure titanium and titanium alloy byin vivo andin vitro test, Metals and Materials International 9(1) (2003) 35-42.

[171] B.I. Kim, M.H. Lee, W.Y. Chon, D.J. Yoon, T.S. Bae, H.H. Park, H.W. Cho, Biocompatibility of surface-treated pure titanium and Ti-6Al-4V alloy, Materials Transactions 42(12) (2001) 2590-2596.

[172] X. Lu, Z.F. Zhao, Y. Leng, Biomimetic calcium phosphate coatings on nitric-acid-treated titanium surfaces, Materials Science & Engineering C-Biomimetic and Supramolecular Systems 27(4) (2007) 700-708.

[173] D.K. Owens, R. Wendt, Estimation of the surface free energy of polymers, Journal of Applied Polymer Science 13(8) (1969) 1741-1747.

[174] M. Zenkiewicz, Comparative study on the surface free energy of a solid calculated by different methods, Polymer Testing 26(1) (2007) 14-19.

[175] W.A. Zisman, Relation of the equilibrium contact angle to liquid and solid constitution, ACS Publications 1964.

[176] C. Van Oss, R. Good, M. Chaudhury, The role of van der Waals forces and hydrogen bonds in "hydrophobic interactions" between biopolymers and low energy surfaces, Journal of Colloid and Interface Science 111(2) (1986) 378-390.

[177] C.J. Van Oss, M.K. Chaudhury, R.J. Good, Interfacial Lifshitz-van der Waals and polar interactions in macroscopic systems, Chemical Reviews 88(6) (1988) 927-941.

[178] A.W. Neumann, R. Good, C. Hope, M. Sejpal, An equation-of-state approach to determine surface tensions of low-energy solids from contact angles, Journal of Colloid and Interface Science 49(2) (1974) 291-304.

[179] D. Li, A.W. Neumann, Equation of state for interfacial-tensions of solid-liquid systems, Advances in Colloid and Interface Science 39 (1992) 299-345.

[180] L. Vitos, A.V. Ruban, H.L. Skriver, J. Kollar, The surface energy of metals, Surface Science 411(1-2) (1998) 186-202.

[181] X.B. Zhao, X.Y. Liu, J. You, Z.G. Chen, C.X. Ding, Bioactivity and cytocompatibility of plasma sprayed titania coating treated by sulfuric acid treatment, Surf Coat Tech 202(14) (2008) 3221-3226.

[182] U. Turkan, M. Guden, The effect of nitric acid surface treatment on CaP deposition of Ti6Al4V open-cell foams in SBF solution, Surf Coat Tech 205(7) (2010) 1904-1916.

[183] R.M. Pilliar, Porous-surfaced metallic implants for orthopedic applications, Journal of Biomedical Materials Research Part A 21(A1 Suppl) (1987) 1-33.

[184] L.F. Cooper, Y. Zhou, J. Takebe, J. Guo, A. Abron, A. Holmén, J.E. Ellingsen, Fluoride modification effects on osteoblast behavior and bone formation at TiO2 grit-blasted CP titanium endosseous implants, Biomaterials 27(6) (2006) 926-936.

[185] S. Ferraris, S. Spriano, G. Pan, A. Venturello, C. Bianchi, R. Chiesa, M. Faga, G. Maina, E. Verne, Surface modification of Ti–6Al–4V alloy for biomineralization and specific biological response: Part I, inorganic modification, Journal of Materials Science: Materials in Medicine 22(3) (2011) 533-545.

[186] M. Karthega, N. Rajendran, Hydrogen peroxide treatment on Ti–6Al–4V alloy: a promising surface modification technique for orthopaedic application, Applied Surface Science 256(7) (2010) 2176-2183.

[187] Y. Li, S. Zou, D. Wang, G. Feng, C. Bao, J. Hu, The effect of hydrofluoric acid treatment on titanium implant osseointegration in ovariectomized rats, Biomaterials 31(12) (2010) 3266-73.

[188] A. Sugino, C. Ohtsuki, K. Tsuru, S. Hayakawa, T. Nakano, Y. Okazaki, A. Osaka, Effect of spatial design and thermal oxidation on apatite formation on Ti–15Zr–4Ta–4Nb alloy, Acta Biomaterialia 5(1) (2009) 298-304.

[189] T. Kokubo, F. Miyaji, H.M. Kim, T. Nakamura, Spontaneous formation of bonelike apatite layer on chemically treated titanium metals, Journal of the American Ceramic Society 79(4) (1996) 1127-1129.

[190] R.R. Revie, H.H. Uhlig, Corrosion and corrosion control: an introduction to corrosion science and engineering, John Wiley & Sons 2008.

[191] T. Hurlen, W. Wilhelmsen, Passive behavior of titanium, Electrochimica Acta 31(9) (1986) 1139-1146.

[192] L.D. Arsov, C. Kormann, W. Plieth, In situ Raman spectra of anodically formed titanium dioxide layers in solutions of H2SO4, KOH, and HNO3, Journal of The Electrochemical Society 138(10) (1991) 2964-2970.

[193] A.R. Prusi, L.D. Arsov, The growth-kinetics and optical-properties of films formed under open circuit conditions on a titanium surface in potassium hydroxide solutions, Corrosion Science 33(1) (1992) 153-164.

[194] R.Z. LeGeros, J.P. LeGeros, Dense hydroxyapatite, An introduction to bioceramics, World Scientific 1993, pp. 139-180.

[195] T. Kokubo, S. Ito, M. Shigematsu, S. Sakka, T. Yamamuro, Mechanical-properties of a new type of apatite-containing glass ceramic for prosthetic application, Journal of Materials Science 20(6) (1985) 2001-2004.

[196] F. Miyaji, X. Zhang, T. Yao, T. Kokubo, C. Ohtsuki, T. Kitsugi, T. Yamamuro, T. Nakamura, Chemical treatment of Ti metal to induce its bioactivity, Bioceramics: Proceedings of the 7th International Symposium on Ceramics in Medicine, Elsevier, 1994, pp. 119-124.

[197] P. Tengvall, I. Lundström, Physico-chemical considerations of titanium as a biomaterial, Clinical Materials 9(2) (1992) 115-134.

[198] K.E. Healy, P. Ducheyne, The mechanisms of passive dissolution of titanium in a model physiological environment, Journal of Biomedical Materials Research Part A 26(3) (1992) 319-338.

[199] K. Healy, P. Ducheyne, Passive dissolution kinetics of titanium in vitro, Journal of Materials Science: Materials in Medicine 4(2) (1993) 117-126.

[200] T. Kokubo, S. Yamaguchi, Bioactive Ti metal and its alloys prepared by chemical treatments: state-of-the-art and future trends, Advanced Engineering Materials 12(11) (2010) B579-B591.

[201] H.M. Kim, F. Miyaji, T. Kokubo, S. Nishiguchi, T. Nakamura, Graded surface structure of bioactive titanium prepared by chemical treatment, Journal of Biomedical Materials Research Part A 45(2) (1999) 100-107.

[202] T. Ueno, N. Tsukimura, M. Yamada, T. Ogawa, Enhanced bone-integration capability of alkali- and heat-treated nanopolymorphic titanium in micro-to-nanoscale hierarchy, Biomaterials 32(30) (2011) 7297-308.

[203] N. Tsukimura, T. Ueno, F. Iwasa, H. Minamikawa, Y. Sugita, K. Ishizaki, T. Ikeda, K. Nakagawa, M. Yamada, T. Ogawa, Bone integration capability of alkali-and heat-treated nanobimorphic Ti–15Mo–5Zr–3Al, Acta Biomaterialia 7(12) (2011) 4267-4277.

[204] T. Sasaki, M. Watanabe, Y. Komatsu, Y. Fujiki, Layered hydrous titanium dioxide: Potassium ion exchange and structural characterization, Inorganic Chemistry 24(14) (1985) 2265-2271.

[205] H. Izawa, S. Kikkawa, M. Koizumi, Ion exchange and dehydration of layered [sodium and potassium] titanates, Na2Ti3O7 and K2Ti4O9, The Journal of Physical Chemistry 86(25) (1982) 5023-5026.

[206] T. Sasaki, K.M. Yu, Y. Fujiki, Protonated pentatitanate: Preparation, characterizations, and cation intercalation, Chemistry of Materials 4(4) (1992) 894-899.

[207] Y. Fujiki, Y. Komatsu, N. Ohta, A cesium immobilization from an aqueous-solution using the crystalline adsorber of hydrous titanium-dioxide fibers, Chemistry Letters 9(8) (1980) 1023-1026.

[208] J.M. Gold, M. Schmidt, S.G. Steinemann, XPS study of amino-acid adsorption to titanium surfaces, Helvetica Physica Acta 62(2-3) (1989) 246-249.

[209] S. Yamaguchi, H. Takadama, T. Matsushita, T. Nakamura, T. Kokubo, Cross-sectional analysis of the surface ceramic layer developed on Ti metal by NaOH-heat treatment and soaking in SBF, Journal of the Ceramic Society of Japan 117(1370) (2009) 1126-1130.

[210] H. Takadama, H.M. Kim, T. Kokubo, T. Nakamura, An X-ray photoelectron spectroscopy study of the process of apatite formation on bioactive titanium metal, Journal of Biomedical Materials Research Part A 55(2) (2001) 185-193.

[211] H.M. Kim, T. Himeno, M. Kawashita, J.H. Lee, T. Kokubo, T. Nakamura, Surface potential change in bioactive titanium metal during the process of apatite formation in simulated body fluid, Journal of Biomedical Materials Research Part A 67(4) (2003) 1305-1309.

[212] N.-b. Li, G.-y. Xiao, I.-H. Tsai, J.-h. Zhao, X. Chen, W.-h. Xu, Y.-p. Lu, Transformation of surface compositions of titanium during alkali and heat treatment with different vacuum degrees, New Journal of Chemistry (2018).

[213] R.J. Hunter, Zeta potential in colloid science: principles and applications, Academic Press 2013.

[214] P. Somasundaran, B. Markovic, Interfacial properties of calcium phosphates, Calcium phosphates in biological and industrial systems, Springer 1998, pp. 85-101.

[215] H. Takadama, H.-M. Kim, T. Kokubo, T. Nakamura, XPS study of the process of apatite formation on bioactive Ti–6Al–4V alloy in simulated body fluid, Science and Technology of Advanced Materials 2(2) (2001) 389.

[216] W.F. Neuman, M.W. Neuman, The chemical dynamics of bone mineral, The University of Chicago Press 1958.

[217] D.K. Pattanayak, S. Yamaguchi, T. Matsushita, T. Nakamura, T. Kokubo, Apatite-forming ability of titanium in terms of pH of the exposed solution, Journal of the Royal Society Interface 9(74) (2012) 2145-55.

[218] T. Kizuki, H. Takadama, T. Matsushita, T. Nakamura, T. Kokubo, Effect of Ca contamination on apatite formation in a Ti metal subjected to NaOH and heat treatments, Journal of Materials Science: Materials in Medicine 24(3) (2013) 635-44.

[219] T. Kawai, T. Kizuki, H. Takadama, T. Matsushita, H. Unuma, T. Nakamura, T. Kokubo, Apatite formation on surface titanate layer with different Na content on Ti metal, Journal of the Ceramic Society of Japan 118(1373) (2010) 19-24.

[220] C. Ammann, A. Brunner, C. Spirig, A. Neftel, Technical note: Water vapour concentration and flux measurements with PTR-MS, Atmospheric Chemistry and Physics 6(12) (2006) 4643-4651.

[221] S. Yamaguchi, H. Takadama, T. Matsushita, T. Nakamura, T. Kokubo, Preparation of bioactive Ti-15Zr-4Nb-4Ta alloy from HCl and heat treatments after an NaOH treatment, Journal of Biomedical Materials Research Part A 97(2) (2011) 135-44.

[222] Y. Okazaki, S. Rao, Y. Ito, T. Tateishi, Corrosion resistance, mechanical properties, corrosion fatigue strength and cytocompatibility of new Ti alloys without Al and V, Biomaterials 19(13) (1998) 1197-1215.

[223] S. Yamaguchi, H. Takadama, T. Matsushita, T. Nakamura, T. Kokubo, Apatite-forming ability of Ti–15Zr–4Nb–4Ta alloy induced by calcium solution treatment, Journal of Materials Science: Materials in Medicine 21(2) (2010) 439-444.

[224] S. Yamaguchi, T. Kizuki, H. Takadama, T. Matsushita, T. Nakamura, T. Kokubo, Formation of a bioactive calcium titanate layer on gum metal by chemical treatment, Journal of Materials Science: Materials in Medicine 23(4) (2012) 873-83.

[225] T. Kokubo, S. Yamaguchi, Biomineralization of metals using chemical and heat treatments, Biomineralization and Biomaterials, Elsevier 2016, pp. 339-364.

[226] A. Fukuda, M. Takemoto, T. Saito, S. Fujibayashi, M. Neo, S. Yamaguchi, T. Kizuki, T. Matsushita, M. Niinomi, T. Kokubo, Bone bonding bioactivity of Ti metal and Ti–Zr–Nb–Ta alloys with Ca ions incorporated on their surfaces by simple chemical and heat treatments, Acta Biomaterialia 7(3) (2011) 1379-1386.

[227] M. Tanaka, M. Takemoto, S. Fujibayashi, T. Kawai, S. Yamaguchi, T. Kizuki, T. Matsushita, T. Kokubo, T. Nakamura, S. Matsuda, Bone bonding ability of a chemically and thermally treated low elastic modulus Ti alloy: gum metal, Journal of Materials Science: Materials in Medicine 25(3) (2014) 635-43.

[228] S. Ferraris, S. Yamaguchi, N. Barbani, C. Cristallini, G.G. di Confiengo, J. Barberi, M. Cazzola, M. Miola, E. Vernè, S. Spriano, The mechanical and chemical stability of the

interfaces in bioactive materials: The substrate-bioactive surface layer and hydroxyapatite-bioactive surface layer interfaces, Materials Science and Engineering: C (2020) 111238.

[229] S. Yamaguchi, T. Matsushita, T. Nakamura, T. Kokubo, Bioactive Ti metal with Ca-enriched surface layer able to release Zn ion, Key Engineering Materials, Trans Tech Publ, 2013, pp. 547-552.

[230] D.W. Brett, A discussion of silver as an antimicrobial agent: Alleviating the confusion, Ostomy Wound Management 52(1) (2006) 34-41.

[231] D.J. Stickler, Biomaterials to prevent nosocomial infections: is silver the gold standard?, Current Opinion in Infectious Diseases 13(4) (2000) 389-393.

[232] B. Espehaug, L.B. Engesaeter, S.E. Vollset, L.I. Havelin, N. Langeland, Antibiotic prophylaxis in total hip arthroplasty. Review of 10,905 primary cemented total hip replacements reported to the Norwegian arthroplasty register, 1987 to 1995, The Journal of Bone and Joint Surgery 79(4) (1997) 590-5.

[233] L. Engesæter, S.A. Lie, B. Espehaug, O. Furnes, S.E. Vollset, L.I. Havelin, Antibiotic prophylaxis in total hip arthroplasty Effects of antibiotic prophylaxis systemically and in bone cement on the revision rate of 22,170 primary hip replacements followed 0-14 years in the Norwegian Arthroplasty Register, Acta Orthopaedica Scandinavica 74(6) (2003) 644-651.

[234] D. Campoccia, L. Montanaro, C.R. Arciola, The significance of infection related to orthopedic devices and issues of antibiotic resistance, Biomaterials 27(11) (2006) 2331-9.

[235] M. Stigter, K. de Groot, P. Layrolle, Incorporation of tobramycin into biomimetic hydroxyapatite coating on titanium, Biomaterials 23(20) (2002) 4143-4153.

[236] Y. Inoue, M. Uota, T. Torikai, T. Watari, I. Noda, T. Hotokebuchi, M. Yada, Antibacterial properties of nanostructured silver titanate thin films formed on a titanium plate, Journal of Biomedical Materials Research Part A 92(3) (2010) 1171-80.

[237] S.B. Lee, U. Otgonbayar, J.H. Lee, K.M. Kim, K.N. Kim, Silver ion-exchanged sodium titanate and resulting effect on antibacterial efficacy, Surf Coat Tech 205 (2010) S172-S176.

[238] S. Yamaguchi, P. Thi Minh Le, M. Ito, S.A. Shintani, H. Takadama, Tri-functional calcium-deficient calcium titanate coating on titanium metal by chemical and heat treatment, Coatings 9(9) (2019) 561.

[239] B.S. Atiyeh, M. Costagliola, S.N. Hayek, S.A. Dibo, Effect of silver on burn wound infection control and healing: review of the literature, Burns 33(2) (2007) 139-48.

[240] M.M. Cortese-Krott, M. Munchow, E. Pirev, F. Hessner, A. Bozkurt, P. Uciechowski, N. Pallua, K.D. Kroncke, C.V. Suschek, Silver ions induce oxidative stress and intracellular zinc release in human skin fibroblasts, Free Radical Biology and Medicine 47(11) (2009) 1570-7.

[241] F. Minandri, C. Bonchi, E. Frangipani, F. Imperi, P. Visca, Promises and failures of gallium as an antibacterial agent, Future Microbiology 9(3) (2014) 379-97.

[242] A. Cochis, B. Azzimonti, C. Della Valle, E. De Giglio, N. Bloise, L. Visai, S. Cometa, L. Rimondini, R. Chiesa, The effect of silver or gallium doped titanium against the multidrug resistant Acinetobacter baumannii, Biomaterials 80 (2016) 80-95.

[243] B. Kubista, T. Schoefl, L. Mayr, S. van Schoonhoven, P. Heffeter, R. Windhager, B.K. Keppler, W. Berger, Distinct activity of the bone-targeted gallium compound KP46 against osteosarcoma cells - synergism with autophagy inhibition, J Exp Clin Canc Res 36(1) (2017) 52.

[244] Y. Kaneko, M. Thoendel, O. Olakanmi, B.E. Britigan, P.K. Singh, The transition metal gallium disrupts Pseudomonas aeruginosa iron metabolism and has antimicrobial and antibiofilm activity, The Journal of Clinical Investigation 117(4) (2007) 877-88.

[245] T.J. Hall, T.J. Chambers, Gallium inhibits bone resorption by a direct effect on osteoclasts, Journal of Bone and Mineral Research 8(3) (1990) 211-216.

[246] D. Villers, E. Espaze, M. Coste-Burel, F. Giauffret, E. Ninin, F. Nicolas, H. Richet, Nosocomial Acinetobacter baumannii infections: microbiological and clinical epidemiology, Annals of Internal Medicine 129(3) (1998) 182-9.

[247] D. Baldoni, A. Steinhuber, W. Zimmerli, A. Trampuz, In vitro activity of gallium maltolate against Staphylococci in logarithmic, stationary, and biofilm growth phases: comparison of conventional and calorimetric susceptibility testing methods, Antimicrobial Agents and Chemotherapy 54(1) (2010) 157-63.

[248] O. Janson, S. Gururaj, S. Pujari-Palmer, M.K. Ott, M. Strömme, H. Engqvist, K. Welch, Titanium surface modification to enhance antibacterial and bioactive properties while retaining biocompatibility, Materials Science and Engineering: C 96 (2018) 272-279.

[249] P. Tengvall, E.G. Hornsten, H. Elwing, I. Lundstrom, Bactericidal properties of a titanium-peroxy gel obtained from metallic titanium and hydrogen peroxide, Journal of Biomedical Materials Research Part A 24(3) (1990) 319-30.

[250] W.Q. Yan, T. Nakamura, M. Kobayashi, H.M. Kim, F. Miyaji, T. Kokubo, Bonding of chemically treated titanium implants to bone, Journal of Biomedical Materials Research Part A 37(2) (1997) 267-75.

[251] S. Fujibayashi, T. Nakamura, S. Nishiguchi, J. Tamura, M. Uchida, H.M. Kim, T. Kokubo, Bioactive titanium: effect of sodium removal on the bone-bonding ability of bioactive titanium prepared by alkali and heat treatment, Journal of Biomedical Materials Research Part A 56(4) (2001) 562-70.

[252] S. Nishiguchi, S. Fujibayashi, H.M. Kim, T. Kokubo, T. Nakamura, Biology of alkali- and heat-treated titanium implants, Journal of Biomedical Materials Research Part A 67(1) (2003) 26-35.

[253] S. Nishiguchi, T. Nakamura, M. Kobayashi, H.M. Kim, F. Miyaji, T. Kokubo, The effect of heat treatment on bone-bonding ability of alkali-treated titanium, Biomaterials 20(5) (1999) 491-500.

[254] S. Nishiguchi, H. Kato, H. Fujita, M. Oka, H.M. Kim, T. Kokubo, T. Nakamura, Titanium metals form direct bonding to bone after alkali and heat treatments, Biomaterials 22(18) (2001) 2525-33.

[255] S. Nishiguchi, H. Kato, M. Neo, M. Oka, H.M. Kim, T. Kokubo, T. Nakamura, Alkali- and heat-treated porous titanium for orthopedic implants, Journal of Biomedical Materials Research Part A 54(2) (2001) 198-208.

[256] S. Nishiguchi, H. Kato, H. Fujita, H.M. Kim, F. Miyaji, T. Kokubo, T. Nakamura, Enhancement of bone-bonding strengths of titanium alloy implants by alkali and heat treatments, Journal of Biomedical Materials Research Part A 48(5) (1999) 689-96.

[257] T. Kokubo, S. Yamaguchi, Growth of novel ceramic layers on metals via chemical and heat treatments for inducing various biological functions, Frontiers in Bioengineering and Biotechnology 3 (2015) 176.

[258] K. Kawanabe, K. Ise, K. Goto, H. Akiyama, T. Nakamura, A. Kaneuji, T. Sugimori, T. Matsumoto, A new cementless total hip arthroplasty with bioactive titanium porous-coating by alkaline and heat treatment: Average 4.8-year results, Journal of Biomedical Materials Research Part B: Applied Biomaterials 90(1) (2009) 476-81.

[259] J. Mibe, A. Imakiire, T. Watanabe, T. Fujie, Results of total hip arthroplasty with bone graft and support ring for protrusio acetabuli in rheumatoid arthritis, Journal of Orthopaedic Science 10(1) (2005) 8-14.

[260] K. So, A. Kaneuji, T. Matsumoto, S. Matsuda, H. Akiyama, Is the bone-bonding ability of a cementless total hip prosthesis enhanced by alkaline and heat treatments?, Clinical Orthopaedics and Related Research® 471(12) (2013) 3847-3855.

[261] E. Garcia-Cimbrelo, A. Cruz-Pardos, R. Madero, M. Ortega-Andreu, Total hip arthroplasty with use of the cementless Zweymüller Alloclassic system: A ten to thirteen-year follow-up study, The Journal of Bone and Joint Surgery 85(2) (2003) 296-303.

[262] A.A. Shetty, R. Slack, A. Tindall, K.D. James, C. Rand, Results of a hydroxyapatite-coated (Furlong) total hip replacement: A 13- to 15-year follow-up, The Journal of Bone and Joint Surgery 87(8) (2005) 1050-4.

[263] P.B. de Witte, R. Brand, H.G. Vermeer, H.J. van der Heide, A.F. Barnaart, Mid-term results of total hip arthroplasty with the CementLess Spotorno (CLS) system, The Journal of Bone and Joint Surgery 93(13) (2011) 1249-55.

[264] E. Sariali, A. Mouttet, P. Mordasini, Y. Catonne, High 10-year survival rate with an anatomic cementless stem (SPS), Clinical Orthopaedics and Related Research® 470(7) (2012) 1941-9.

[265] C. Nourissat, J. Essig, G. Asencio, The cementless anatomic Benoist Girard (ABG) II total hip arthroplasty: A minimum 8-year follow-up study, Journal of Arthroplasty 28(4) (2013) 707-11.

[266] R.H. Wittenberg, R. Steffen, H. Windhagen, P. Bucking, A. Wilcke, Five-year results of a cementless short-hip-stem prosthesis, Orthopaedic Reviews 5(1) (2013) 4.

[267] S.S. Jameson, P.N. Baker, J. Mason, M. Rymaszewska, P.J. Gregg, D.J. Deehan, M.R. Reed, Independent predictors of failure up to 7.5 years after 35,386 single-brand cementless total hip replacements: A retrospective cohort study using National Joint Registry data, The Bone & Joint Journal 95B(6) (2013) 747-757.

[268] K.T. Makela, M. Matilainen, P. Pulkkinen, A.M. Fenstad, L. Havelin, L. Engesaeter, O. Furnes, A.B. Pedersen, S. Overgaard, J. Karrholm, H. Malchau, G. Garellick, J. Ranstam, A. Eskelinen, Failure rate of cemented and uncemented total hip replacements: register study of combined Nordic database of four nations, BMJ 348 (2014) 7592.

[269] N.O. Noiseux, W.J. Long, T.M. Mabry, A.D. Hanssen, D.G. Lewallen, Uncemented porous tantalum acetabular components: early follow-up and failures in 613 primary total hip arthroplasties, Journal of Arthroplasty 29(3) (2014) 617-620.

[270] W.T. Hoskins, R.J. Bingham, M. Lorimer, R.N. de Steiger, The effect of size for a hydroxyapatite-coated cementless implant on component revision in total hip arthroplasty: An analysis of 41,265 stems, Journal of Arthroplasty 35(4) (2020) 1074-1078.

[271] T. Albrektsson, C. Johansson, Osteoinduction, osteoconduction and osseointegration, European Spine Journal 10 Suppl 2(2) (2001) 96-101.

[272] M. Uchida, H.M. Kim, T. Kokubo, S. Fujibayashi, T. Nakamura, Effect of water treatment on the apatite-forming ability of NaOH-treated titanium metal, Journal of Biomedical Materials Research Part A 63(5) (2002) 522-30.

[273] M. Uchida, H.-M. Kim, T. Kokubo, T. Nakamura, Apatite-forming ability of titania gels with different structures, Bioceramics: Volume 12, World Scientific 1999, pp. 149-152.

[274] M. Uchida, H.M. Kim, T. Kokubo, T. Nakamura, Apatite-forming ability of sodium-containing titania gels in a simulated body fluid, Journal of the American Ceramic Society 84(12) (2001) 2969-2974.

[275] M. Wei, M. Uchida, H.M. Kim, T. Kokubo, T. Nakamura, Apatite-forming ability of CaO-containing titania, Biomaterials 23(1) (2002) 167-72.

[276] S. Fujibayashi, M. Neo, H.M. Kim, T. Kokubo, T. Nakamura, Osteoinduction of porous bioactive titanium metal, Biomaterials 25(3) (2004) 443-50.

[277] M. Takemoto, S. Fujibayashi, M. Neo, J. Suzuki, T. Matsushita, T. Kokubo, T. Nakamura, Osteoinductive porous titanium implants: effect of sodium removal by dilute HCl treatment, Biomaterials 27(13) (2006) 2682-91.

[278] A. Fukuda, M. Takemoto, T. Saito, S. Fujibayashi, M. Neo, D.K. Pattanayak, T. Matsushita, K. Sasaki, N. Nishida, T. Kokubo, T. Nakamura, Osteoinduction of porous Ti implants with a channel structure fabricated by selective laser melting, Acta Biomaterialia 7(5) (2011) 2327-36.

[279] M. Takemoto, S. Fujibayashi, M. Neo, J. Suzuki, T. Kokubo, T. Nakamura, Mechanical properties and osteoconductivity of porous bioactive titanium, Biomaterials 26(30) (2005) 6014-23.

[280] D.K. Pattanayak, T. Kawai, T. Matsushita, H. Takadama, T. Nakamura, T. Kokubo, Effect of HCl concentrations on apatite-forming ability of NaOH–HCl-and heat-treated titanium metal, Journal of Materials Science: Materials in Medicine 20(12) (2009) 2401-2411.

[281] D.K. Pattanayak, S. Yamaguchi, T. Matsushita, T. Kokubo, Effect of heat treatments on apatite-forming ability of NaOH- and HCl-treated titanium metal, Journal of Materials Science: Materials in Medicine 22(2) (2011) 273-8.

[282] D.K. Pattanayak, S. Yamaguchi, T. Matsushita, T. Kokubo, Nanostructured positively charged bioactive TiO2 layer formed on Ti metal by NaOH, acid and heat treatments, Journal of Materials Science: Materials in Medicine 22(8) (2011) 1803-1812.

[283] T. Kokubo, D.K. Pattanayak, S. Yamaguchi, H. Takadama, T. Matsushita, T. Kawai, M. Takemoto, S. Fujibayashi, T. Nakamura, Positively charged bioactive Ti metal prepared by

simple chemical and heat treatments, Journal of the Royal Society Interface 7(Suppl 5) (2010) 503-513.

[284] T. Kawai, M. Takemoto, S. Fujibayashi, H. Akiyama, S. Yamaguchi, D.K. Pattanayak, K. Doi, T. Matsushita, T. Nakamura, T. Kokubo, S. Matsuda, Osteoconduction of porous Ti metal enhanced by acid and heat treatments, Journal of Materials Science: Materials in Medicine 24(7) (2013) 1707-15.

[285] M. Takemoto, S. Fujibayashi, M. Neo, K. So, N. Akiyama, T. Matsushita, T. Kokubo, T. Nakamura, A porous bioactive titanium implant for spinal interbody fusion: An experimental study using a canine model, J Neurosurg-Spine 7(4) (2007) 435-443.

[286] S. Fujibayashi, M. Takemoto, M. Neo, T. Matsushita, T. Kokubo, K. Doi, T. Ito, A. Shimizu, T. Nakamura, A novel synthetic material for spinal fusion: A prospective clinical trial of porous bioactive titanium metal for lumbar interbody fusion, European Spine Journal 20(9) (2011) 1486-95.

[287] J. Ma, H.F. Wong, L.B. Kong, K.W. Peng, Biomimetic processing of nanocrystallite bioactive apatite coating on titanium, Nanotechnology 14(6) (2003) 619-623.

[288] M. Pourbaix, Electrochemical corrosion of metallic biomaterials, Biomaterials 5(3) (1984) 122-34.

[289] Y. Zheng, X. Gu, F. Witte, Biodegradable metals, Materials Science and Engineering: R: Reports 77 (2014) 1-34.

[290] J.D. Bronzino, J.B. Park, Biomaterials: Principles and applications, CRC Press 2002.

[291] M.T. Islam, R.M. Felfel, E.A. Abou Neel, D.M. Grant, I. Ahmed, K.M.Z. Hossain, Bioactive calcium phosphate–based glasses and ceramics and their biomedical applications: A review, Journal of Tissue Engineering 8 (2017) 1-16.

[292] C.C. Chen, J.Y. Chueh, H. Tseng, H.M. Huang, S.Y. Lee, Preparation and characterization of biodegradable PLA polymeric blends, Biomaterials 24(7) (2003) 1167-73.

[293] L.E. Freed, G. Vunjak-Novakovic, R.J. Biron, D.B. Eagles, D.C. Lesnoy, S.K. Barlow, R. Langer, Biodegradable polymer scaffolds for tissue engineering, Biotechnology 12(7) (1994) 689-93.

[294] R.K. Roeder, G.L. Converse, R.J. Kane, W.M. Yue, Hydroxyapatite-reinforced polymer biocomposites for synthetic bone substitutes, Jom-Us 60(3) (2008) 38-45.

[295] S. Ramakrishna, J. Mayer, E. Wintermantel, K.W. Leong, Biomedical applications of polymer-composite materials: a review, Composites Science and Technology 61(9) (2001) 1189-1224.

[296] J. Cheng, B. Liu, Y.H. Wu, Y.F. Zheng, Comparative in vitro study on pure metals (Fe, Mn, Mg, Zn and W) as biodegradable metals, Journal of Materials Science & Technology 29(7) (2013) 619-627.

[297] N.M. Yunos, R. Bellomo, D. Story, J. Kellum, Bench-to-bedside review: Chloride in critical illness, Critical Care 14(4) (2010) 226.

[298] E. Aghion, B. Bronfin, Magnesium alloys development towards the 21st century, Materials Science Forum, Trans Tech Publ, 2000, pp. 19-30.

[299] F. Witte, The history of biodegradable magnesium implants: A review, Acta Biomaterialia 6(5) (2010) 1680-1692.

[300] S.S. El-Rahman, Neuropathology of aluminum toxicity in rats (glutamate and GABA impairment), Pharmacological Research 47(3) (2003) 189-194.

[301] S. Hirano, K.T. Suzuki, Exposure, metabolism, and toxicity of rare earths and related compounds, Environmental Health Perspectives 104(Suppl 1) (1996) 85-95.

[302] B. Mordike, T. Ebert, Magnesium: properties—applications—potential, Materials Science and Engineering: A 302(1) (2001) 37-45.

[303] C. Fox, D. Ramsoomair, C. Carter, Magnesium: its proven and potential clinical significance, The South African Medical Journal 94(12) (2001) 1195-201.

[304] X.-N. Gu, Y.-F. Zheng, A review on magnesium alloys as biodegradable materials, Frontiers of Materials Science in China 4(2) (2010) 111-115.

[305] J. Vormann, Magnesium: nutrition and metabolism, Molecular Aspects of Medicine 24(1-3) (2003) 27-37.

[306] G. Song, A. Atrens, Understanding magnesium corrosion: A framework for improved alloy performance, Advanced Engineering Materials 5(12) (2003) 837-858.

[307] G. Song, A. Atrens, Recent insights into the mechanism of magnesium corrosion and research suggestions, Advanced Engineering Materials 9(3) (2007) 177-183.

[308] G. Baril, G. Galicia, C. Deslouis, N. Pebere, B. Tribollet, V. Vivier, An impedance investigation of the mechanism of pure magnesium corrosion in sodium sulfate solutions, Journal of the Electrochemical Society 154(2) (2007) C108-C113.

[309] J. Wang, J. Tang, P. Zhang, Y. Li, J. Wang, Y. Lai, L. Qin, Surface modification of magnesium alloys developed for bioabsorbable orthopedic implants: A general review, Journal of Biomedical Materials Research Part B: Applied Biomaterials 100(6) (2012) 1691-701.

[310] L.C. Li, J.C. Gao, Y. Wang, Evaluation of cytotoxicity and corrosion behavior of alkali-heat-treated magnesium in simulated body fluid, Surf Coat Tech 185(1) (2004) 92-98.

[311] Y. Al-Abdullat, S. Tsutsumi, N. Nakajima, M. Ohta, H. Kuwahara, K. Ikeuchi, Surface modification of magnesium by NaHCO3 and corrosion behavior in Hank's solution for new biomaterial applications, Materials Transactions 42(8) (2001) 1777-1780.

[312] K.S. Harsha, Principles of vapor deposition of thin films, Elsevier 2005.

[313] S. Berg, I.V. Katardjiev, Preferential sputtering effects in thin film processing, J Vac Sci Technol A 17(4) (1999) 1916-1925.

[314] H.H. Andersen, H.L. Bay, Sputtering yield measurements, Sputtering by Particle Bombardment I, Springer 1981, pp. 145-218.

[315] U. Conrad, H.M. Urbassek, Theoretical-study of preferential sputtering of isotopic systems at low fluence, Nucl Instrum Meth B 61(3) (1991) 295-301.

[316] S.i. Ogawa, T. Kouzaki, T. Yoshida, R. Sinclair, Interface microstructure of titanium thin-film/silicon single-crystal substrate correlated with electrical barrier heights, Journal of Applied Physics 70(2) (1991) 827-832.

[317] S. Iida, Observation of the surface and structure of very thin ti-film, Jpn J Appl Phys 2 29(2) (1990) 361-363.

[318] T. Tsuchiya, M. Hirata, N. Chiba, Young's modulus, fracture strain, and tensile strength of sputtered titanium thin films, Thin Solid Films 484(1-2) (2005) 245-250.

[319] J. Kong, H. Shen, B. Chen, Z. Li, W. Shi, W. Yao, Z. Qi, The abnormal structure of nanocrystalline titanium films prepared by DC sputtering, Thin Solid Films 207(1-2) (1992) 51-53.

[320] B. Window, Recent advances in sputter-deposition, Surf Coat Tech 71(2) (1995) 93-97.

[321] T. Godfroid, R. Gouttebaron, J.P. Dauchot, P. Leclere, R. Lazzaroni, M. Hecq, Growth of ultrathin Ti films deposited on SnO_2 by magnetron sputtering, Thin Solid Films 437(1-2) (2003) 57-62.

[322] N. Fujitsuka, J. Sakata, Y. Miyachi, K. Mizuno, K. Ohtsuka, Y. Taga, O. Tabata, Monolithic pyroelectric infrared image sensor using PVDF thin film, Sensors and Actuators A: Physical 66(1-3) (1998) 237-243.

[323] M.V.S. Ramakrishna, G. Karunasiri, P. Neuzil, U. Sridhar, W.J. Zeng, Highly sensitive infrared temperature sensor using self-heating compensated microbolometers, Sensors and Actuators A: Physical 79(2) (2000) 122-127.

[324] S.N. Wang, K. Mizuno, M. Fujiyoshi, H. Funabashi, J. Sakata, Thermal micropressure sensor for pressure monitoring in a minute package, Journal of Vacuum Science & Technology A: Vacuum Surfaces and Films 19(1) (2001) 353-357.

[325] H. Ljungcrantz, L. Hultman, J.E. Sundgren, S. Johansson, N. Kristensen, J.A. Schweitz, C.J. Shute, Residual-stresses and fracture properties of magnetron-sputtered Ti films on Si microelements, Journal of Vacuum Science & Technology A: Vacuum Surfaces and Films 11(3) (1993) 543-553.

[326] H.S. Vijaya, G.K. Muralidhar, G.N. Subbanna, G.M. Rao, S. Mohan, Characterization of titanium thin films prepared by bias assisted magnetron sputtering, Metallurgical and Materials Transactions B-Process Metallurgy and Materials Processing Science 27(6) (1996) 1057-1060.

[327] M.J. Jung, K.H. Nam, L.R. Shaginyan, J.G. Han, Deposition of Ti thin film using the magnetron sputtering method, Thin Solid Films 435(1-2) (2003) 145-149.

[328] T. Sonoda, A. Watazu, J. Zhu, W. Shi, K. Kato, T. Asahina, Structure and mechanical properties of pure titanium film deposited onto TiNi shape memory alloy substrate by magnetron DC sputtering, Thin Solid Films 459(1-2) (2004) 212-215.

[329] D.S.R. Krishna, Y. Sun, Effect of thermal oxidation conditions on tribological behaviour of titanium films on 316L stainless steel, Surf Coat Tech 198(1-3) (2005) 447-453.

[330] Y.L. Jeyachandran, B. Karunagaran, S.K. Narayandass, D. Mangalaraj, T.E. Jenkins, P.J. Martin, Properties of titanium thin films deposited by DC magnetron sputtering, Mat Sci Eng a-Struct 431(1-2) (2006) 277-284.

[331] V. Chawla, R. Jayaganthan, A.K. Chawla, R. Chandra, Microstructural characterizations of magnetron sputtered Ti films on glass substrate, Journal of Materials Processing Technology 209(7) (2009) 3444-3451.

[332] Y.Z. Jin, W. Wu, L. Li, J. Chen, J.Y. Zhang, Y.B. Zuo, J. Fu, Effect of sputtering power on surface topography of DC magnetron sputtered Ti thin films observed by AFM, Applied Surface Science 255(8) (2009) 4673-4679.

[333] T. Oya, E. Kusano, Effects of radio-frequency plasma on structure and properties in Ti film deposition by dc and pulsed dc magnetron sputtering, Thin Solid Films 517(20) (2009) 5837-5843.

[334] N. Arshi, J. Lu, C.G. Lee, J.H. Yoon, B.H. Koo, F. Ahmed, Thickness effect on properties of titanium film deposited by dc magnetron sputtering and electron beam evaporation techniques, Bulletin of Materials Science 36(5) (2013) 807-812.

[335] R. Álvarez, J.M. Garcia-Martin, A. García-Valenzuela, M. Macias-Montero, F. Ferrer, J. Santiso, V. Rico, J. Cotrino, A.R. Gonzalez-Elipe, A. Palmero, Nanostructured Ti thin films by magnetron sputtering at oblique angles, Journal of Physics D: Applied Physics 49(4) (2015) 045303.

[336] A.Y. Chen, Y. Bu, Y.T. Tang, Y. Wang, F. Liu, X.F. Xie, J.F. Gu, Deposition-rate dependence of orientation growth and crystallization of Ti thin films prepared by magnetron sputtering, Thin Solid Films 574 (2015) 71-77.

[337] C. Yang, B.L. Jiang, Z. Liu, J. Hao, L. Feng, Structure and properties of Ti films deposited by dc magnetron sputtering, pulsed DC magnetron sputtering and cathodic arc evaporation, Surf Coat Tech 304 (2016) 51-56.

[338] J. Dervaux, P.A. Cormier, P. Moskovkin, O. Douheret, S. Konstantinidis, R. Lazzaroni, S. Lucas, R. Snyders, Synthesis of nanostructured Ti thin films by combining glancing angle deposition and magnetron sputtering: A joint experimental and modeling study, Thin Solid Films 636 (2017) 644-657.

[339] A. Kavitha, K. Gunasekhar, T. Balakrishnan, Structural and electrochemical characterization of nanostructured titanium thin films prepared by DC magnetron sputtering with supported discharge, Iranian Journal of Science and Technology, Transactions A: Science 43(5) (2019) 2665-2671.

[340] H. Zhang, X. Li, J. Su, X. Wang, L. Ma, J. Xue, Y. Li, Z. Song, Modulation of columnar crystals of magnetron sputtered Ti thin films, Thin Solid Films 689 (2019) 137512.

[341] A. Roth, Vacuum technology, Elsevier 2012.

[342] B.W. Stuart, Deposition and characterisation of RF magnetron sputtered phosphate based glasses, University of Nottingham, 2017.

[343] J.G. Stark, H.G. Wallace, M. McGlashan, Chemistry data book, Murray London 1982.

[344] C.V. Thompson, Grain growth in thin films, Annual Review of Materials Science 20(1) (1990) 245-268.

[345] P. Lobl, M. Huppertz, D. Mergel, Nucleation and Growth in TiO2 Films Prepared by Sputtering and Evaporation, Thin Solid Films 251(1) (1994) 72-79.

[346] W.T. Xu, B.Q. Li, T. Fujimoto, I. Kojima, Suppressing the surface roughness and columnar growth of silicon nitride films, Surf Coat Tech 135(2-3) (2001) 274-278.

[347] S. Swann, Magnetron sputtering, Physics in Technology 19(2) (1988) 67.

[348] C. Phutela, N.T. Aboulkhair, C.J. Tuck, I. Ashcroft, The effects of feature sizes in selectively laser melted Ti-6Al-4V parts on the validity of optimised process parameters, Materials 13(1) (2020) 117.

[349] K.M.Z. Hossain, U. Patel, A.R. Kennedy, L. Macri-Pellizzeri, V. Sottile, D.M. Grant, B.E. Scammell, I. Ahmed, Porous calcium phosphate glass microspheres for orthobiologic applications, Acta Biomaterialia 72 (2018) 396-406.

[350] P.J. Kelly, R.D. Arnell, Magnetron sputtering: A review of recent developments and applications, Vacuum 56(3) (2000) 159-172.

[351] B.E. Aufderheide, 30.2 General Principles of Sputtering, in: A.A. Tracton (Ed.), Coatings Technology Handbook, 2006.

[352] D. Gonçalves, E.A. Irene, Fundamentals and applications of spectroscopic ellipsometry, Quimica Nova 25(5) (2002) 794-800.

[353] S. Zhang, L. Li, A. Kumar, Materials characterization techniques, CRC Press 2008.

[354] W.J. MoberlyChan, D.P. Adams, M.J. Aziz, G. Hobler, T. Schenkel, Fundamentals of focused ion beam nanostructural processing: Below, at, and above the surface, MRS Bulletin 32(5) (2007) 424-432.

[355] B.E. Warren, X-ray Diffraction, Courier Corporation 1969.

[356] C. Weidenthaler, Pitfalls in the characterization of nanoporous and nanosized materials, Nanoscale 3(3) (2011) 792-810.

[357] C. Giannini, M. Ladisa, D. Altamura, D. Siliqi, T. Sibillano, L. De Caro, X-ray diffraction: A powerful technique for the multiple-length-scale structural analysis of nanomaterials, Crystals 6(8) (2016) 87.

[358] G. Harris, X. Quantitative measurement of preferred orientation in rolled uranium bars, The London, Edinburgh, and Dublin Philosophical Magazine and Journal of Science 43(336) (1952) 113-123.

[359] H. Hantsche, Comparison of basic principles of the surface-specific analytical methods: AES/SAM, ESCA (XPS), SIMS, and ISS with X-ray microanalysis, and some applications in research and industry, Scanning 11(6) (1989) 257-280.

[360] F. Ramírez-Jiménez, A. Bashir, V. Villanueva, L. Villaseñor, M.A. Pérez, L. Urrutia, X-ray spectroscopy with PIN diodes, AIP Conference Proceedings, AIP, 2006, pp. 121-133.

[361] N. Gurker, M.F. Ebel, H. Ebel, Imaging XPS—A new technique, I—principles, Surface and Interface Analysis 5(1) (1983) 13-19.

[362] B.C. Smith, Fundamentals of Fourier transform infrared spectroscopy, CRC Press 2011.

[363] A. Ichimiya, P.I. Cohen, Reflection high-energy electron diffraction, Cambridge University Press 2004.

[364] S. Hasegawa, Reflection high-energy electron diffraction, Characterization of Materials (2012).

[365] J.R. Ferraro, Introductory Raman spectroscopy, Academic Press 2003.

[366] K.E. Jarvis, A.L. Gray, R.S. Houk, I. Jarvis, J. McLaren, J.G. Williams, Handbook of inductively coupled plasma mass spectrometry, Blackie Glasgow 1992.

[367] R. Danzl, F. Helmli, S. Scherer, Focus variation: A robust technology for high resolution optical 3D surface metrology, Strojniski Vestnik-Journal of Mechanical Engineering 57(3) (2011) 245-256.

[368] ISO 25178-2: Geometrical product specification (GPS)–surface texture–areal. Part 2: Terms, definitions and surface texture parameters. (2007)

[369] F.J. Giessibl, Advances in atomic force microscopy, Reviews of Modern Physics 75(3) (2003) 949-983.

[370] B.V.T. Hanby, B.W. Stuart, C. Grant, J. Moffat, J. Blissett, C. Gerada, M. Gimeno-Fabra, D.M. Grant, Dielectric breakdown of alumina thin films produced by pulsed direct current magnetron sputtering, Thin Solid Films 662 (2018) 145-154.

[371] W.-S. Lei, K. Mittal, Z. Yu, Adhesion measurement of coating on biodevices/implants, Progress in Adhesion and Adhesives 2 (2017) 351-379.

[372] ASTM D7234-19: Standard test method for pull-off strength of coatings using portable adhesion testers. (2009)

[373] S.J. Bull, Failure mode maps in the thin film scratch adhesion test, Tribology International 30(7) (1997) 491-498.

[374] S.J. Bull, Failure modes in scratch adhesion testing, Surf Coat Tech 50(1) (1991) 25-32.

[375] BS EN ISO, 20502:2016 Fine ceramics: Determination of adhesion of ceramic coatings by scratch testing. (2016)

[376] B.N. Popov, Corrosion engineering: Principles and solved problems, Elsevier 2015.

[377] ASTM International, F2129-19a: Standard test method for conducting cyclic potentiodynamic polarization measurements to determine the corrosion susceptibility of small implant devices. (2019)

[378] G. Repetto, A. del Peso, J.L. Zurita, Neutral red uptake assay for the estimation of cell viability/cytotoxicity, Nature Protocols 3(7) (2008) 1125-31.

[379] L. Boulos, M. Prevost, B. Barbeau, J. Coallier, R. Desjardins, LIVE/DEAD® BacLight™: application of a new rapid staining method for direct enumeration of viable and total bacteria in drinking water, Journal of Microbiological Methods 37(1) (1999) 77-86.

[380] A. Heydorn, A.T. Nielsen, M. Hentzer, C. Sternberg, M. Givskov, B.K. Ersboll, S. Molin, Quantification of biofilm structures by the novel computer program COMSTAT, Microbiology 146(10) (2000) 2395-2407.

[381] M. Shirpour, J. Cabana, M. Doeff, New materials based on a layered sodium titanate for dual electrochemical Na and Li intercalation systems, Energy & Environmental Science 6(8) (2013) 2538-2547.

[382] T.M.F. Marques, O.P. Ferreira, J.A.P. da Costa, K. Fujisawa, M. Terrones, B.C. Viana, Study of the growth of CeO2 nanoparticles onto titanate nanotubes, Journal of Physics and Chemistry of Solids 87 (2015) 213-220.

[383] R. Ma, K. Fukuda, T. Sasaki, M. Osada, Y. Bando, Structural features of titanate nanotubes/nanobelts revealed by Raman, X-ray absorption fine structure and electron diffraction characterizations, The Journal of Physical Chemistry B 109(13) (2005) 6210-4.

[384] M.A. Lillo-Rodenas, D. Cazorla-Amoros, A. Linares-Solano, Understanding chemical reactions between carbons and NaOH and KOH - An insight into the chemical activation mechanism, Carbon 41(2) (2003) 267-275.

[385] A. Dulda, Morphology controlled synthesis of α-GaO(OH) nanoparticles: Thermal conversion to Ga_2O_3 and photocatalytic properties, Advances in Materials Science and Engineering 2016 (2016).

[386] Y. Zhao, R.L. Frost, Raman spectroscopy and characterisation of α-gallium oxyhydroxide and β-gallium oxide nanorods, Journal of Raman Spectroscopy 39(10) (2008) 1494-1501.

[387] X. Sun, Y. Li, Synthesis and characterization of ion-exchangeable titanate nanotubes, Chemistry 9(10) (2003) 2229-38.

[388] M.H.A. Rehim, A.M. Youssef, H. Al-Said, G. Turky, M. Abdaly, Polyaniline and modified titanate nanowires layer-by-layer plastic electrode for flexible electronic device applications, RSC Advances 6(97) (2016) 94556-94563.

[389] Z.B. Bahsi, A. Buyukaksoy, S.M. Olmezcan, F. Simsek, M.H. Aslan, A.Y. Oral, A novel label-free optical biosensor using synthetic oligonucleotides from E. coli O157:H7: Elementary sensitivity tests, Sensors 9(6) (2009) 4890-900.

[390] T. Bezrodna, G. Puchkovska, V. Shymanovska, J. Baran, H. Ratajczak, IR-analysis of H-bonded H2O on the pure TiO2 surface, Journal of Molecular Structure 700(1-3) (2004) 175-181.

[391] R.P. Oleksak, W.F. Stickle, G.S. Herman, Aqueous-based synthesis of gallium tungsten oxide thin film dielectrics, Journal of Materials Chemistry C 3(13) (2015) 3114-3120.

[392] B.O. Aronsson, A. Krozer, J. Lausmaa, B. Kasemo, Commercially pure titanium and Ti6Al4V: XPS comparison between different commercial Ti dental implants and foils prepared by various oxidation procedures, Surface Science Spectra 4(1) (1996) 42-89.

[393] B. Bharti, S. Kumar, H.-N. Lee, R. Kumar, Formation of oxygen vacancies and Ti^{3+} state in TiO_2 thin film and enhanced optical properties by air plasma treatment, Scientific Reports 6 (2016) 32355.

[394] J.F. Moulder, W.F. Stickle, P.E. Sobol, K.D. Bomben, Handbook of X-ray photoelectron spectroscopy: A reference book of standard spectra for identification and interpretation of XPS data, Perkin-Elmer Co., Minnesota, U.S.A, 1995.

[395] R.A. Zarate, S. Fuentes, J.P. Wiff, V.M. Fuenzalida, A.L. Cabrera, Chemical composition and phase identification of sodium titanate nanostructures grown from titania by hydrothermal processing, Journal of Physics and Chemistry of Solids 68(4) (2007) 628-637.

[396] Q. Deng, Y. Gao, X. Xia, R. Chen, L. Wan, G. Shao, V and Ga co-doping effect on optical absorption properties of TiO_2 thin films, Journal of Physics: Conference Series, IOP Publishing, 2009, p. 12073.

[397] A. Surpi, E. Gothelid, T. Kubart, D. Martin, J. Jensen, Localised modifications of anatase TiO2 thin films by a Focused Ion Beam, Nuclear Instruments & Methods in Physics Research Section B-Beam Interactions with Materials and Atoms 268(19) (2010) 3142-3146.

[398] N.Y. Mostafa, Characterization, thermal stability and sintering of hydroxyapatite powders prepared by different routes, Materials Chemistry and Physics 94(2-3) (2005) 333-341.

[399] M.M. Can, G.H. Jaffari, S. Aksoy, S.I. Shah, T. Firat, Synthesis and characterization of $ZnGa_2O_4$ particles prepared by solid state reaction, Journal of Alloys and Compounds 549 (2013) 303-307.

[400] N. Eliaz, N. Metoki, Calcium phosphate bioceramics: A review of their history, structure, properties, coating technologies and biomedical applications, Materials 10(4) (2017) 334.

[401] Z. Xu, M. Li, X. Li, X. Liu, F. Ma, S. Wu, K.W. Yeung, Y. Han, P.K. Chu, Antibacterial activity of silver doped titanate nanowires on Ti implants, ACS Applied Materials & Interfaces 8(26) (2016) 16584-94.

[402] T. Kokubo, T. Matsushita, H. Takadama, T. Kizuki, Development of bioactive materials based on surface chemistry, Journal of the European Ceramic Society 29(7) (2009) 1267-1274.

[403] B. Alhalaili, R. Bunk, R. Vidu, M.S. Islam, Dynamics contributions to the growth mechanism of Ga_2O_3 thin film and NWs enabled by Ag Catalyst, Nanomaterials 9(9) (2019) 1272.

[404] L.A. Xue, Y. Chen, R.J. Brook, The influence of ionic radii on the incorporation of trivalent dopants into BaTiO3, Materials Science and Engineering: B 1(2) (1988) 193-201.

[405] C.Y. Kim, T. Sekino, K. Niihara, Synthesis of bismuth sodium titanate nanosized powders by solution/sol–gel process, Journal of the American Ceramic Society 86(9) (2003) 1464-1467.

[406] M. Mohammadi, D. Fray, Semiconductor TiO_2–Ga_2O_3 thin film gas sensors derived from particulate sol–gel route, Acta Materialia 55(13) (2007) 4455-4466.

[407] K. Thamaphat, P. Limsuwan, B. Ngotawornchai, Phase characterization of TiO_2 powder by XRD and TEM, Kasetsart Journal (Natural Science) 42(5) (2008) 357-361.

[408] J. Chen, G. Zou, H. Hou, Y. Zhang, Z. Huang, X. Ji, Pinecone-like hierarchical anatase TiO_2 bonded with carbon enabling ultrahigh cycling rates for sodium storage, Journal of Materials Chemistry A 4(32) (2016) 12591-12601.

[409] B.C. Viana, O.P. Ferreira, A.G. Souza, J. Mendes, O.L. Alves, Structural, morphological and vibrational properties of titanate nanotubes and nanoribbons, Journal of the Brazilian Chemical Society 20(1) (2009) 167-175.

[410] L.L. Marciniuk, P. Hammer, H.O. Pastore, U. Schuchardt, D. Cardoso, Sodium titanate as basic catalyst in transesterification reactions, Fuel 118 (2014) 48-54.

[411] R. Rao, A.M. Rao, B. Xu, J. Dong, S. Sharma, M.K. Sunkara, Blueshifted Raman scattering and its correlation with the [110] growth direction in gallium oxide nanowires, Journal of Applied Physics 98(9) (2005) 094312.

[412] Y. Gao, Y. Bando, T. Sato, Y. Zhang, X. Gao, Synthesis, Raman scattering and defects of β-Ga_2O_3 nanorods, Applied Physics Letters 81(12) (2002) 2267-2269.

[413] Y.Y. Zhao, R.L. Frost, W.N. Martens, Synthesis and characterization of gallium oxide nanostructures via a soft-chemistry route, Journal of Physical Chemistry C 111(44) (2007) 16290-16299.

[414] J. Shah, P. Ratnasamy, M.L. Carreon, Influence of the nanostructure of gallium oxide catalysts on conversion in the green synthesis of carbamates, Catalysts 7(12) (2017) 372.

[415] S. Ramesh, C. Tan, M. Hamdi, I. Sopyan, W. Teng, The influence of Ca/P ratio on the properties of hydroxyapatite bioceramics, International Conference on Smart Materials and Nanotechnology in Engineering, International Society for Optics and Photonics, 2007, p. 64233A.

[416] J. Faure, A. Balamurugan, H. Benhayoune, P. Torres, G. Balossier, J.M.F. Ferreira, Morphological and chemical characterisation of biomimetic bone like apatite formation on alkali treated Ti6Al4V titanium alloy, Materials Science & Engineering C-Biomimetic and Supramolecular Systems 29(4) (2009) 1252-1257.

[417] P. Collery, B. Keppler, C. Madoulet, B. Desoize, Gallium in cancer treatment, Critical Reviews in Oncology/Hematology 42(3) (2002) 283-96.

[418] J.E. Chandler, H.H. Messer, G. Ellender, Cytotoxicity of gallium and indium ions compared with mercuric ion, Journal of Dental Research 73(9) (1994) 1554-9.

[419] M.A. Getzlaf, E.A. Lewallen, H.M. Kremers, D.L. Jones, C.A. Bonin, A. Dudakovic, R. Thaler, R.C. Cohen, D.G. Lewallen, A.J. van Wijnen, Multi-disciplinary antimicrobial strategies for improving orthopaedic implants to prevent prosthetic joint infections in hip and knee, Journal of Orthopaedic Research 34(2) (2016) 177-86.

[420] H.J. Busscher, M. Rinastiti, W. Siswomihardjo, H.C. van der Mei, Biofilm formation on dental restorative and implant materials, Journal of Dental Research 89(7) (2010) 657-65.

[421] J. Raphel, M. Holodniy, S.B. Goodman, S.C. Heilshorn, Multifunctional coatings to simultaneously promote osseointegration and prevent infection of orthopaedic implants, Biomaterials 84 (2016) 301-314.

[422] A.R. Yazdi, M. Towler, The effect of the addition of gallium on the structure of zinc borate glass with controlled gallium ion release, Materials & Design 92 (2016) 1018-1027.

[423] R. Chakraborty, A. Dey, A.K. Mukhopadhyay, Loading rate effect on nanohardness of soda-lime-silica glass, Metallurgical and Materials Transactions A 41(5) (2010) 1301-1312.

[424] L. Kernazhitsky, V. Shymanovska, T. Gavrilko, V. Naumov, L. Fedorenko, V. Kshnyakin, J. Baran, Laser-excited excitonic luminescence of nanocrystalline TiO_2 powder, Ukranian Journal of Physics 59(3) (2014) 248-255.

[425] P.J. Kelly, R.D. Arnell, Development of a novel structure zone model relating to the closed-field unbalanced magnetron sputtering system, Journal of Vacuum Science & Technology A: Vacuum Surfaces and Films 16(5) (1998) 2858-2869.

[426] T. Ungár, Microstructural parameters from X-ray diffraction peak broadening, Scripta Materialia 51(8) (2004) 777-781.

[427] T. Hanawa, S. Hiromoto, A. Yamamoto, D. Kuroda, K. Asami, XPS characterization of the surface oxide film 316L stainless steel samples that were located in quasi-biological environments, Materials Transactions 43(12) (2002) 3088-3092.

[428] C.R. Clayton, Y.C. Lu, A bipolar model of the passivity of stainless-steel: The role of Mo addition, Journal of the Electrochemical Society 133(12) (1986) 2465-2473.

[429] A.R. Brooks, C.R. Clayton, K. Doss, Y.C. Lu, On the role of Cr in the passivity of stainless-steel, Journal of the Electrochemical Society 133(12) (1986) 2459-2464.

[430] C.C. Shih, C.M. Shih, Y.Y. Su, L.H.J. Su, M.S. Chang, S.J. Lin, Effect of surface oxide properties on corrosion resistance of 316L stainless steel for biomedical applications, Corrosion Science 46(2) (2004) 427-441.

[431] B.S. Kang, Y.T. Sul, S.J. Oh, H.J. Lee, T. Albrektsson, XPS, AES and SEM analysis of recent dental implants, Acta Biomaterialia 5(6) (2009) 2222-9.

[432] S. Takemoto, M. Hattori, M. Yoshinari, E. Kawada, Y. Oda, Corrosion behavior and surface characterization of titanium in solution containing fluoride and albumin, Biomaterials 26(8) (2005) 829-37.

[433] W.-C. Peng, Y.-C. Chen, J.-L. He, S.-L. Ou, R.-H. Horng, D.-S. Wuu, Tunability of p- and n-channel TiO_x thin film transistors, Scientific Reports 8(1) (2018) 9255.

[434] T. Ohsaka, F. Izumi, Y. Fujiki, Raman-spectrum of Anatase, TiO_2, Journal of Raman Spectroscopy 7(6) (1978) 321-324.

[435] M. Lubas, J.J. Jasinski, M. Sitarz, L. Kurpaska, P. Podsiad, J. Jasinski, Raman spectroscopy of TiO_2 thin films formed by hybrid treatment for biomedical applications, Spectrochimica Acta Part A: Molecular and Biomolecular Spectroscopy 133 (2014) 867-71.

[436] C. Bloed, J. Vuong, A. Enriquez, S. Raghavan, I. Tran, S. Derakhshan, H. Tavassol, Oxygen vacancy and chemical ordering control oxygen evolution activity of $Sr_{2-x}Ca_xFe_2O_{6-\delta}$ Perovskites, ACS Applied Energy Materials 2(9) (2019) 6140-6145.

[437] U. Diebold, T. Madey, TiO_2 by XPS, Surface Science Spectra 4(3) (1996) 227-231.

[438] P. Krishnan, M. Liu, P.A. Itty, Z. Liu, V. Rheinheimer, M.-H. Zhang, P.J. Monteiro, E.Y. Liya, Characterization of photocatalytic TiO_2 powder under varied environments using near ambient pressure X-ray photoelectron spectroscopy, Scientific Reports 7 (2017) 43298.

[439] R.A. Zarate, S. Fuentes, A.L. Cabrera, V.M. Fuenzalida, Structural characterization of single crystals of sodium titanate nanowires prepared by hydrothermal process, Journal of Crystal Growth 310(15) (2008) 3630-3637.

[440] H.L. Wang, S. Zhang, Y.B. Li, D. Sun, Bias effect on microstructure and mechanical properties of magnetron sputtered nanocrystalline titanium carbide thin films, Thin Solid Films 516(16) (2008) 5419-5423.

[441] S. Konstantinidis, J.P. Dauchot, A. Hecq, Titanium oxide thin films deposited by high-power impulse magnetron sputtering, Thin Solid Films 515(3) (2006) 1182-1186.

[442] A.G. Dirks, R.A.M. Wolters, A.E.M. Deveirman, Columnar microstructures in magnetron-sputtered refractory-metal thin-films of tungsten, molybdenum and W-Ti-(N), Thin Solid Films 208(2) (1992) 181-188.

[443] P. Patsalas, C. Charitidis, S. Logothetidis, The effect of substrate temperature and biasing on the mechanical properties and structure of sputtered titanium nitride thin films, Surf Coat Tech 125(1-3) (2000) 335-340.

[444] T. Selinder, G. Larsson, U. Helmersson, S. Rudner, Resputtering effects on the stoichiometry of $YBa_2Cu_3O_x$ thin films, Journal of Applied Physics 69(1) (1991) 390-395.

[445] I. Petrov, L. Hultman, J.E. Sundgren, J.E. Greene, Polycrystalline Tin films deposited by reactive bias magnetron sputtering: Effects of ion-bombardment on resputtering rates, film composition, and microstructure, Journal of Vacuum Science & Technology A: Vacuum Surfaces and Films 10(2) (1992) 265-272.

[446] N. Martin, D. Baretti, C. Rousselot, J.Y. Rauch, The effect of bias power on some properties of titanium and titanium oxide films prepared by RF magnetron sputtering, Surf Coat Tech 107(2-3) (1998) 172-182.

[447] J.A. Thornton, Influence of apparatus geometry and deposition conditions on the structure and topography of thick sputtered coatings, Journal of Vacuum Science and Technology 11(4) (1974) 666-670.

[448] R. Messier, A.P. Giri, R.A. Roy, Revised structure zone model for thin-film physical structure, Journal of Vacuum Science & Technology A: Vacuum Surfaces and Films 2(2) (1984) 500-503.

[449] J. Musil, S. Kadlec, V. Valvoda, R. Kuzel, R. Cerny, Ion-assisted sputtering of tin films, Surf Coat Tech 43-4(1-3) (1990) 259-269.

[450] S. Craig, G.L. Harding, Effects of argon pressure and substrate-temperature on the structure and properties of sputtered copper-films, Journal of Vacuum Science & Technology 19(2) (1981) 205-215.

[451] M. Andritschky, F. Guimaraes, V. Teixeira, Energy deposition and substrate heating during magnetron sputtering, Vacuum 44(8) (1993) 809-813.

[452] B.G. Priyadarshini, M. Kumar Gupta, S. Ghosh, M. Chakraborty, S. Aich, Role of substrate bias during deposition of magnetron sputtered Ni, Ti and Ni–Ti thin films, Surface Engineering 29(9) (2013) 689-694.

[453] H. Zhao, J. Xie, A. Mao, A. Wang, Y. Chen, T. Liang, D. Ma, Effects of heating mode and temperature on the microstructures, electrical and optical properties of molybdenum thin films, Materials 11(9) (2018) 1634.

[454] B.H. Wu, Y. Yu, J. Wu, I. Shchelkanov, D.N. Ruzic, N. Huang, Y.X. Leng, Tailoring of titanium thin film properties in high power pulsed magnetron sputtering, Vacuum 150(150) (2018) 144-154.

[455] H. Wang, Y.-K. Lai, R.-Y. Zheng, Y. Bian, K.-Q. Zhang, C.-J. Lin, Tuning the surface microstructure of titanate coatings on titanium implants for enhancing bioactivity of implants, International journal of nanomedicine 10 (2015) 3887.

[456] K. Kanaya, S. Okayama, Penetration and energy-loss theory of electrons in solid targets, Journal of Physics D: Applied Physics 5(1) (1972) 43.

[457] K.B. Devi, K. Singh, N. Rajendran, Synthesis and characterization of nanoporous sodium-substituted hydrophilic titania ceramics coated on 316L SS for biomedical applications, Journal of Coatings Technology and Research 8(5) (2011) 595-604.

[458] T. Kasuga, M. Hiramatsu, A. Hoson, T. Sekino, K. Niihara, Titania nanotubes prepared by chemical processing, Advanced Materials 11(15) (1999) 1307.

[459] Z. Zhang, J.B. Goodall, S. Brown, L. Karlsson, R.J. Clark, J.L. Hutchison, I. Rehman, J.A. Darr, Continuous hydrothermal synthesis of extensive 2D sodium titanate ($Na_2Ti_3O_7$) nano-sheets, Dalton Transactions 39(3) (2010) 711-714.

[460] K. Aniołek, M. Kupka, A. Barylski, Characteristic of oxide layers obtained on titanium in the process of thermal oxidation, Archives of Metallurgy and Materials 61(2) (2016) 853-856.

[461] E. McCafferty, J.P. Wightman, An X-ray photoelectron spectroscopy sputter profile study of the native air-formed oxide film on titanium, Applied Surface Science 143(1-4) (1999) 92-100.

[462] C.J. Boxley, H.S. White, C.E. Gardner, J.V. Macpherson, Nanoscale imaging of the electronic conductivity of the native oxide film on titanium using conducting atomic force microscopy, Journal of Physical Chemistry B 107(36) (2003) 9677-9680.

[463] D.A.H. Hanaor, C.C. Sorrell, Review of the anatase to rutile phase transformation, Journal of Materials Science 46(4) (2011) 855-874.

[464] M. Ocana, J.V. Garcia-Ramos, C.J. Serna, Low-temperature nucleation of rutile observed by Raman spectroscopy during crystallization of TiO_2, Journal of the American Ceramic Society 75(7) (1992) 2010-2012.

[465] L. Hsu, R. Rujkorakarn, J. Sites, C. She, Thermally induced crystallization of amorphous-titania films, Journal of Applied Physics 59(10) (1986) 3475-3480.

[466] G.J. Exarhos, High temperature Raman studies of phase transitions in thin film dielectrics, MRS Online Proceedings Library Archive 48 (1985).

[467] T. Hanawa, K. Asami, K. Asaoka, Repassivation of titanium and surface oxide film regenerated in simulated bioliquid, Journal of Biomedical Materials Research Part A 40(4) (1998) 530-8.

[468] V. Prabu, P. Karthick, A. Rajendran, D. Natarajan, M.S. Kiran, D.K. Pattanayak, Bioactive Ti alloy with hydrophilicity, antibacterial activity and cytocompatibility, RSC Advances 5(63) (2015) 50767-50777.

[469] V. Rodríguez-González, S. Obregón-Alfaro, L. Lozano-Sánchez, S.-W. Lee, Rapid microwave-assisted synthesis of one-dimensional silver–$H_2Ti_3O_7$ nanotubes, Journal of Molecular Catalysis A: Chemical 353 (2012) 163-170.

[470] C.E. Bamberger, G.M. Begun, Sodium titanates: stoichiometry and Raman spectra, Journal of the American Ceramic Society 70(3) (1987) C-48-C-51.

[471] N. Murthy, Techniques for analyzing biomaterial surface structure, morphology and topography, Surface Modification of Biomaterials, Elsevier 2011, pp. 232-255.

[472] A.S. Fawzy, M.A. Amer, An in vitro and in vivo evaluation of bioactive titanium implants following sodium removal treatment, Dental Materials 25(1) (2009) 48-57.

[473] D. Ricci, P.C. Braga, Recognizing and avoiding artifacts in AFM imaging, Atomic Force Microscopy, Springer 2004, pp. 25-37.

[474] Y.G. Shen, Y.W. Mai, Q.C. Zhang, D.R. McKenzie, W.D. McFall, W.E. McBride, Residual stress, microstructure, and structure of tungsten thin films deposited by magnetron sputtering, Journal of Applied Physics 87(1) (2000) 177-187.

[475] W.C. Wagner, K. Asgar, W.C. Bigelow, R.A. Flinn, Effect of interfacial variables on metal-porcelain bonding, Journal of Biomedical Materials Research 27(4) (1993) 531-537.

[476] D.-M. Liu, Q. Yang, T. Troczynski, Sol–gel hydroxyapatite coatings on stainless steel substrates, Biomaterials 23(3) (2002) 691-698.

[477] R.C. Vega-Moron, G.A.R. Castro, D.V. Melo-Maximo, J.V. Mendez-Mendez, L. Melo-Maximo, J.E. Oseguera-Pena, A. Meneses-Amador, Adhesion and mechanical properties of Ti films deposited by DC magnetron sputtering, Surf Coat Tech 349 (2018) 1137-1147.

[478] Y. Tian, S. Fujibayashi, S. Yamaguchi, T. Matsushita, T. Kokubo, S. Matsuda, In vivo study of the early bone-bonding ability of Ti meshes formed with calcium titanate via chemical treatments, Journal of Materials Science: Materials in Medicine 26(12) (2015) 271.

[479] Y.P. Guo, N.H. Lee, H.J. Oh, C.R. Yoon, K.S. Park, S.C. Jung, S.J. Kim, The growth of oriented titanate nanotube thin film on titanium metal flake, Surf Coat Tech 202(22-23) (2008) 5431-5435.

[480] T. Kokubo, Apatite formation on surfaces of ceramics, metals and polymers in body environment, Acta Materialia 46(7) (1998) 2519-2527.

[481] T. Kokubo, S. Yamaguchi, Novel bioactive titanate layers formed on Ti metal and its alloys by chemical treatments, Materials 3(1) (2010) 48-63.

[482] N. Erdman, R. Campbell, S. Asahina, Precise SEM cross section polishing via argon beam milling, Microscopy Today 14(3) (2006) 22-25.

[483] G. Battiston, R. Gerbasi, Film thickness determination by grazing incidence diffraction, 1996, pp. 225-244.

[484] A. Zomorrodian, A. Mesarwi, N.J. Wu, A. Ignatiev, XPS oxygen line broadening in lead zirconium titanate and related materials, Applied Surface Science 90(3) (1995) 343-348.

[485] V.V. Atuchin, V.G. Kesler, N.V. Pervukhina, Z. Zhang, Ti 2p and O 1s core levels and chemical bonding in titanium-bearing oxides, Journal of Electron Spectroscopy and Related Phenomena 152(1-2) (2006) 18-24.

[486] J. Xie, X. Wang, Y. Zhou, Understanding formation mechanism of titanate nanowires through hydrothermal treatment of various Ti-containing precursors in basic solutions, Journal of Materials Science & Technology 28(6) (2012) 488-494.

[487] Y.-Y. Won, D. Ramkrishna, Revised formulation of Fick's, Fourier's, and Newton's laws for spatially varying linear transport coefficients, ACS Omega 4(6) (2019) 11215-11222.

[488] H. Nakajima, M. Koiwa, Diffusion in Titanium, ISIJ International 31(8) (1991) 757-766.

[489] R. Schaub, E. Wahlstrom, A. Ronnau, E. Lagsgaard, I. Stensgaard, F. Besenbacher, Oxygen-mediated diffusion of oxygen vacancies on the TiO_2(110) surface, Science 299(5605) (2003) 377-9.

[490] P. Ouyang, G. Mi, P. Li, L. He, J. Cao, X. Huang, Non-isothermal oxidation behavior and mechanism of a high temperature near-alpha titanium alloy, Materials 11(11) (2018) 2141.

[491] H. Mehrer, Diffusion in solids: fundamentals, methods, materials, diffusion-controlled processes, Springer Science & Business Media 2007.

[492] X.W. Huang, Z.J. Liu, Growth of titanium oxide or titanate nanostructured thin films on Ti substrates by anodic oxidation in alkali solutions, Surf Coat Tech 232 (2013) 224-233.

[493] B. Zhao, L. Lin, D.N. He, Phase and morphological transitions of titania/titanate nanostructures from an acid to an alkali hydrothermal environment, Journal of Materials Chemistry A 1(5) (2013) 1659-1668.

[494] R. Lu, J. Yuan, H.L. Shi, B. Li, W.Z. Wang, D.W. Wang, M.S. Cao, Morphology-controlled synthesis and growth mechanism of lead-free bismuth sodium titanate nanostructures via the hydrothermal route, Crystengcomm 15(19) (2013) 3984-3991.

[495] Y. Mao, M. Kanungo, T. Hemraj-Benny, S.S. Wong, Synthesis and growth mechanism of titanate and titania one-dimensional nanostructures self-assembled into hollow micrometer-scale spherical aggregates, The Journal of Physical Chemistry B 110(2) (2006) 702-10.

[496] S. Feliu, C. Maffiotte, J.C. Galván, A. Pardo, M. Concepcion Merino, R. Arrabal, The application of X-ray photoelectron spectroscopy in understanding corrosion mechanisms of magnesium and Mg-Al alloys, Open Surface Science Journal 3 (2011) 1-14.

[497] Y. Bouvier, B. Mutel, J. Grimblot, Use of an Auger parameter for characterizing the Mg chemical state in different materials, Surf Coat Tech 180 (2004) 169-173.

[498] R. Shvab, E. Hryha, L. Nyborg, Surface chemistry of the titanium powder studied by XPS using internal standard reference, Powder Metallurgy 60(1) (2017) 42-48.

[499] M.C. Biesinger, B.P. Payne, B.R. Hart, A.P. Grosvenor, N.S. McIntryre, L.W. Lau, R.S. Smart, Quantitative chemical state XPS analysis of first row transition metals, oxides and hydroxides, Journal of Physics: Conference Series, IOP Publishing, 2008, p. 012025.

[500] N.R.A. Rahman, L. Muniandy, F. Adam, A. Iqbal, E.P. Ng, H.L. Lee, Detailed photocatalytic study of alkaline titanates and its application for the degradation of methylene blue (MB) under solar irradiation, Journal of Photochemistry and Photobiology A: Chemistry 375 (2019) 219-230.

[501] P. McMillan, N. Ross, The Raman-spectra of several orthorhombic calcium-oxide perovskites, Physics and Chemistry of Minerals 16(1) (1988) 21-28.

[502] U. Balachandran, N.G. Eror, Laser-induced Raman-scattering in calcium titanate, Solid State Communications 44(6) (1982) 815-818.

[503] E.A. Noor, A.H. Al-Moubaraki, Corrosion behavior of mild steel in hydrochloric acid solutions, International Journal of Electrochemical Science 3(7) (2008) 806-818.

[504] J. Degner, F. Singer, L. Cordero, A.R. Boccaccini, S. Virtanen, Electrochemical investigations of magnesium in DMEM with biodegradable polycaprolactone coating as corrosion barrier, Applied Surface Science 282 (2013) 264-270.

[505] R.Z. Xu, X.B. Yang, P.H. Li, K.W. Suen, S. Wu, P.K. Chu, Electrochemical properties and corrosion resistance of carbon-ion-implanted magnesium, Corrosion Science 82 (2014) 173-179.

[506] S.N. Dezfuli, Z.G. Huan, J.M.C. Mol, M.A. Leeflang, J. Chang, J. Zhou, Influence of HEPES buffer on the local pH and formation of surface layer during in vitro degradation tests of magnesium in DMEM, Progress in Natural Science-Materials International 24(5) (2014) 531-538.

[507] V. Wagener, S. Virtanen, Protective layer formation on magnesium in cell culture medium, Materials Science & Engineering C: Materials for Biological Applications 63 (2016) 341-51.

[508] X. Gu, Y. Zheng, S. Zhong, T. Xi, J. Wang, W. Wang, Corrosion of, and cellular responses to Mg–Zn–Ca bulk metallic glasses, Biomaterials 31(6) (2010) 1093-1103.

[509] Y.Y. Yang, C. Michalczyk, F. Singer, S. Virtanen, A.R. Boccaccini, In vitro study of polycaprolactone/bioactive glass composite coatings on corrosion and bioactivity of pure Mg, Applied Surface Science 355 (2015) 832-841.

[510] M.B. Kannan, H. Khakbaz, A. Yamamoto, Understanding the influence of HEPES buffer concentration on the biodegradation of pure magnesium: An electrochemical study, Materials Chemistry and Physics 197 (2017) 47-56.

[511] V. Wagener, S. Virtanen, Influence of electrolyte composition (simulated body fluid vs. Dulbecco's Modified Eagle's medium), temperature, and solution flow on the biocorrosion behavior of commercially pure Mg, Corrosion 73(12) (2017) 1413-1422.

[512] M.K. Arumugam, M.A. Hussein, A.Y. Adesina, N. Al-Aqeeli, In vitro corrosion and bioactivity performance of surface-treated Ti-20Nb-13Zr alloys for orthopedic applications, Coatings 9(5) (2019).

[513] O.G. Simionescu, C. Romanitan, O. Tutunaru, V. Ion, O. Buiu, A. Avram, RF magnetron sputtering deposition of TiO_2 thin films in a small continuous oxygen flow rate, Coatings 9(7) (2019) 442.

[514] H.-M. Kim, H. Takadama, T. Kokubo, S. Nishiguchi, T. Nakamura, Formation of a bioactive graded surface structure on Ti–15Mo–5Zr–3Al alloy by chemical treatment, Biomaterials 21(4) (2000) 353-358.

[515] B.C. Viana, O.P. Ferreira, A.G. Souza, A.A. Hidalgo, J. Mendes, O.L. Alves, Alkali metal intercalated titanate nanotubes: A vibrational spectroscopy study, Vibrational Spectroscopy 55(2) (2011) 183-187.

[516] H. Oettel, R. Wiedemann, Residual stresses in PVD hard coatings, Surf Coat Tech 76(1-3) (1995) 265-273.

[517] T. Kokubo, S. Yamaguchi, Simulated body fluid and the novel bioactive materials derived from it, Journal of Biomedical Materials Research Part A 107(5) (2019) 968-977.

[518] A.M. Fekry, R.M. El-Sherif, Electrochemical corrosion behavior of magnesium and titanium alloys in simulated body fluid, Electrochimica Acta 54(28) (2009) 7280-7285.

[519] S. Spriano, S. Yamaguchi, F. Baino, S. Ferraris, A critical review of multifunctional titanium surfaces: New frontiers for improving osseointegration and host response, avoiding bacteria contamination, Acta Biomaterialia 79 (2018) 1-22.

[520] K. Lips, P. Schmutz, M. Heer, P.J. Uggowitzer, S. Virtanen, Electrochemical corrosion investigation on Mg alloy AZ91: Description of critical parameters and their influence on the mechanisms of attack on NRC type alloys, Materials and Corrosion 55(1) (2004) 5-17.

[521] K.M. Ismail, S. Virtanen, Electrochemical behavior of magnesium alloy AZ31 in 0.5 M KOH solution, Electrochem Solid St 10(3) (2007) 9-11.

[522] N.T. Kirkland, N. Birbilis, J. Walker, T. Woodfield, G.J. Dias, M.P. Staiger, In-vitro dissolution of magnesium–calcium binary alloys: Clarifying the unique role of calcium additions in bioresorbable magnesium implant alloys, Journal of Biomedical Materials Research Part B: Applied Biomaterials 95(1) (2010) 91-100.

[523] S.V. Dorozhkin, Calcium orthophosphate coatings on magnesium and its biodegradable alloys, Acta Biomaterialia 10(7) (2014) 2919-34.

[524] T.S. Narayanan, I.-S. Park, M.-H. Lee, Surface modification of magnesium and its alloys for biomedical applications: Modification and coating techniques, Elsevier 2015.

[525] S.A. Yaseen, G.A. Yiseen, Z. Li, Elucidation of calcite structure of calcium carbonate formation based on hydrated cement mixed with graphene oxide and reduced graphene oxide, ACS Omega 4(6) (2019) 10160-10170.

[526] B. Athanassiadis, L.J. Walsh, Aspects of solvent chemistry for calcium hydroxide medicaments, Materials 10(10) (2017).

[527] M. Esmaily, J.E. Svensson, S. Fajardo, N. Birbilis, G.S. Frankel, S. Virtanen, R. Arrabal, S. Thomas, L.G. Johansson, Fundamentals and advances in magnesium alloy corrosion, Progress in Materials Science 89 (2017) 92-193.

[528] J.J. Morrier, G. Benay, C. Hartmann, O. Barsotti, Antimicrobial activity of $Ca(OH)_2$ dental cements: an in vitro study, The Journal of Endodontics 29(1) (2003) 51-4.

[529] Z. Li, X. Gu, S. Lou, Y. Zheng, The development of binary Mg-Ca alloys for use as biodegradable materials within bone, Biomaterials 29(10) (2008) 1329-44.

[530] R. Harrison, D. Maradze, S. Lyons, Y. Zheng, Y. Liu, Corrosion of magnesium and magnesium–calcium alloy in biologically-simulated environment, Progress in Natural Science: Materials International 24(5) (2014) 539-546.

[531] A.B. Khiabani, A. Ghanbari, B. Yarmand, A. Zamanian, M. Mozafari, Improving corrosion behavior and in vitro bioactivity of plasma electrolytic oxidized AZ91 magnesium alloy using calcium fluoride containing electrolyte, Materials Letters 212 (2018) 98-102.

[532] M. Ravelingien, S. Mullens, J. Luyten, V. Meynen, E. Vinck, C. Vervaet, J.P. Remon, Thermal decomposition of bioactive sodium titanate surfaces, Applied Surface Science 255(23) (2009) 9539-9542.

[533] Y. Okuzu, S. Fujibayashi, S. Yamaguchi, K. Yamamoto, T. Shimizu, T. Sono, K. Goto, B. Otsuki, T. Matsushita, T. Kokubo, S. Matsuda, Strontium and magnesium ions released from bioactive titanium metal promote early bone bonding in a rabbit implant model, Acta Biomaterialia 63 (2017) 383-392.

[534] Q. Wei, C. Lieber, Solution-based synthesis of magnesium oxide nanorods, MRS Online Proceedings Library Archive 581 (1999).